

Optical Spectroscopy of Spin Ladders

Inaugural - Dissertation

zur

Erlangung des Doktorgrades
der Mathematisch-Naturwissenschaftlichen Fakultät
der Universität zu Köln

vorgelegt von

Marco Sascha Windt

aus Vechta (Niedersachsen)

Köln, Dezember 2002

Berichterstatter:

Prof. Dr. A. Freimuth
Priv.-Doz. Dr. G.S. Uhrig

Vorsitzender der Prüfungskommission: Prof. Dr. L. Bohatý

Tag der mündlichen Prüfung: 14. Februar 2003

Contents

1	Introduction	3
2	Low-Dimensional Quantum Magnets	7
2.1	Some Basics	7
2.2	Antiferromagnetic Heisenberg Chains	12
2.2.1	Elementary Excitations	13
2.2.2	Alternating Chains and Spin-Peierls Transition	17
2.2.3	Doping of Chains	21
2.3	Ladders: Bridge between 1D and 2D	24
2.3.1	Even- and Odd-Leg Ladders	26
2.3.2	Interpretation of Susceptibility Data	29
2.3.3	Elementary Excitations: Triplets vs. Spinons	33
2.4	Telephone-Number Compounds	36
2.4.1	Crystal Structure of $(\text{Sr},\text{La},\text{Ca})_{14}\text{Cu}_{24}\text{O}_{41}$	36
2.4.2	Charge Carriers	40
2.4.3	Spin Gaps	41
2.4.4	Superconductivity	44
2.4.5	Optical Studies	45
3	Optical Spectroscopy	51
3.1	Dielectric Function and its Determination	51
3.2	Typical Units	56
3.3	Bimagnon-Plus-Phonon Absorption	57
3.3.1	Experimental Evidence	57
3.3.2	Basic Idea	60
4	Experimental Setup	63
4.1	Fourier Spectroscopy	63
4.1.1	Calculating the Spectra	66
4.1.2	Problems to Take Care of	69
4.2	Sample Preparation	80

5	Bound States and Continuum in Undoped Ladders	87
5.1	First Predictions	87
5.2	Experimental Results	93
5.2.1	Reflectance	93
5.2.2	Transmittance	95
5.2.3	Optical Conductivity	102
5.2.4	Subtraction of the Electronic Background	107
5.3	Comparison with Calculations	117
5.3.1	Jordan-Wigner Fermions and Continuous Unitary Transformations .	118
5.3.2	DMRG Results: Continuum and the Influence of a Cyclic Exchange	126
5.3.3	Resemblance to the $S=1$ Chain	132
6	Doped Ladders	139
6.1	Sharp Raman Peak in $\text{Sr}_{14}\text{Cu}_{24}\text{O}_{41}$	140
6.2	Infrared Spectra of $\text{Sr}_{14}\text{Cu}_{24}\text{O}_{41}$	144
7	Conclusions	157
	References	161
	List of Publications	176
	Acknowledgements	179
	Abstract	180
	Zusammenfassung	181

Chapter 1

Introduction

Transition-metal oxides exhibit a vast panopticum of remarkable phenomena such as ordered states of spin, charge, and orbitals. These states along with the corresponding low-energy excitations are particularly interesting in low dimensions. For instance the unconventional superconductivity in the two-dimensional (2D) cuprates gave a special boost to the field of low-dimensional quantum magnets. The undoped parent compounds contain stacked layers of CuO_2 , which are supposed to be the best representations of 2D square-lattice Heisenberg antiferromagnets (AF) discovered so far. Since the spin of the involved Cu^{2+} ions is just $1/2$ and since the number of neighbors on the square lattice is rather small, strong quantum fluctuations emerge that hinder long-range order. These fluctuations most likely play an important role in explaining high-temperature superconductivity, that arises upon doping with charge carriers. Up to now, numerous ideas have been published but still no single theory can explain all the strange findings such as the linear temperature dependence of the resistivity in the normal state, the pseudo gap, or the origin of the pairing mechanism itself. Not even the exact ground state of the undoped 2D square-lattice Heisenberg AF with spin $S = 1/2$ is known so far.¹ However, analytical, semianalytical, and numerical techniques suggest AF long-range order with reduced staggered magnetization compared to the classical value. A comprehensive review on corresponding calculations is given in reference [1].

As a consequence of the difficulties in 2D, the quest for other materials containing one- and two-dimensional copper-oxide structures yielded a whole bunch of new magnetic features. 1D systems, for instance, provide a good testing ground to verify theoretical models that are exactly solvable. Moreover, numerical calculations on clusters with many sites can be counterchecked. To name but two examples, the spin- $1/2$ chain compound Sr_2CuO_3 or the first inorganic spin-Peierls substance CuGeO_3 inspired much research activity. Even a step closer to the two-dimensional problem are spin ladders with a topology somewhere in-between 1D and 2D. By adding more and more chains to each ladder, the dimensional crossover can be approached. To stay within the ladder terminology, each chain gets labelled as a *leg*, accordingly with perpendicular *rungs* in-between (see figure 1.1). Early calculations demonstrated that this crossover does not evolve smoothly. Instead, the physics strongly depends on if there is an even or an odd number of legs involved [2].

¹The finite inter-layer coupling in the real materials induces long-range Néel order below an ordering temperature of typically 300 to 400 K.

The theoretical study by Dagotto et al. published in 1992 predicted superconductivity in two-leg ladders upon doping with holes [3]. Two holes that are close-by show a tendency to occupy the same rung, which means that there is an attractive interaction. Sigrist et al. found that the order parameter exhibits *d*-wave-like symmetry, which resembles the high- T_c cuprates [4]. After all, superconductivity was finally discovered in the doped two-leg ladder system $\text{Sr}_{0.4}\text{Ca}_{13.6}\text{Cu}_{24}\text{O}_{41.84}$ by Uehara et al. in 1996 [5]. They applied high pressures of 3 and 4.5 GPa and found superconducting onset temperatures of 12 and 9 K, respectively. Yet it is not clear if the predicted mechanism is indeed responsible for the observed superconductivity. An alternative explanation is that the couplings simply get more two-dimensional under pressure.

Two-leg ladders with $S = 1/2$ exhibit a spin-liquid ground state with triplets as the elementary excitations. The triplet dispersion shows a gap [3], which is contrary to both 1D Heisenberg chains and odd-leg ladders that have gapless excitation spectra. The so-called telephone-number compounds $(\text{Sr},\text{La},\text{Ca})_{14}\text{Cu}_{24}\text{O}_{41}$ provide excellent realizations of two-leg spin ladders, which are composed of the same corner-sharing plaquettes as the 2D cuprates. High-quality single crystals of various compositions are available, which were grown in mirror furnaces using the travelling-solvent-floating-zone method [6–8]. Apart from the ladder subcell, there is a second incommensurate subcell of spin chains. Holes doped into the compounds are expected to reside mainly in the chains [9], and charge ordering occurs within the chains of $\text{Sr}_{14-x}\text{Ca}_x\text{Cu}_{24}\text{O}_{41}$ for $x \leq 5$ [10].

In general, infrared spectroscopy is one of the most popular spectroscopic techniques in solid-state physics. The breakthrough was the development of Fourier spectrometers, which provide many advantages over conventional dispersive spectrometers in the infrared range. By now, sophisticated devices are commercially available and can be found in many physics and chemistry labs. The use of infrared spectroscopy to study magnetic excitations proved already successful for the undoped 2D cuprates. The concept of phonon-assisted bimagnon absorption in combination with spin-wave theory [11, 12] is able to explain the sharp peak measured around 0.4 eV [13] in terms of an *almost* bound state of two magnons, which here is called a “bimagnon”. Yet there are additional sidebands at higher energies, which still cause a lot of discussion [14, 15]. In spin ladders we observe similar infrared spectra, i.e. *two* sharp peaks and a further high-energy contribution. Thus it is interesting to ask if there could be a *real* bound state in spin-ladder compounds.

For this quest of bound states in spin ladders, infrared spectroscopy is particularly suitable compared to other standard spectroscopic techniques. For instance the bound-state energies are quite high in cuprate ladders, which renders the quest for this state quite challenging by means of neutrons. Raman scattering is sensitive to excitations with vanishing total momentum, but the bound state only emerges at higher momenta. Infrared absorption is also restricted to $k_{tot} = 0$ excitations, but since the phonon participating in the phonon-assisted magnetic absorption provides momentum according to $0 = k_{tot} = k_{ph} + k_{mag}$, it rather measures a weighted average of the magnetic spectrum over the whole Brillouin zone.

In fact, the complete magnetic infrared spectrum could unambiguously be explained in cooperation with the theoretical groups of Uhrig et al. from the University of Cologne and Kopp et al. from the University of Augsburg. The double peaks are indeed due to a bound state of two triplets, whereas the sidebands could be identified with the multi-triplet continuum. Such bound states in spin ladders have already been predicted before



Figure 1.1: Example of a small cluster of a two-leg ladder with 10 rungs. Contrary to our experimental setup, this ladder is illuminated by two separate light sources [28].

[16–23], but we were able to report the first experimental verification [24]. In addition to this remarkable result, the comparison of theory and experiment also yields the set of coupling constants along the legs and along the rungs. We could demonstrate that the inclusion of a four-spin cyclic exchange into the Hamiltonian is necessary to accurately reproduce the measured spectra *and* the spin-gap value determined by neutron scattering [25] at the same time [26].

The concept of binding is fundamental in physics [27]. Here, we discuss 1D quantum antiferromagnets, in which there are elementary excitations that carry a fractional spin of $S = 1/2$, the so called spinons. In most systems, spinons are not free but confined and form bound states with $S = 1$, i.e. triplets. The two-triplet bound state that we have identified in the infrared spectra thus can be viewed as a bound state of bound states. To illustrate the phenomenon of binding one can draw a parallel to, for instance, the Coulomb interaction that binds electrons and atomic nuclei to form atoms.² Afterwards the interaction is mainly saturated, but there might still be some contribution left, that e.g. leads to the formation of higher-order bound states, namely molecules tied together by covalent bonds. The next hierarchy is then the formation of a solid by means of the van-der-Waals interaction. Other examples are for instance electrons and holes that bind to excitons and further on to biexcitons, or in the field of high-energy physics: quarks, hadrons, and nuclei.

Scope of this Thesis

The excitement surrounding ladder compounds was originally triggered by theoretical predictions of (i) the existence of a spin gap in the undoped phase and (ii) a transition to a superconducting state upon hole doping [3]. Both predictions have been sufficiently

²Actually, the spin-spin interaction that leads to the formation of these magnetic bound states can be traced back to the Coulomb interaction as well.

confirmed, and since 1992 a large amount of maybe 1000 papers on spin ladders has been published. However, many aspects are still not clear. In particular, no other analysis of the *magnetic* infrared spectra incorporating the mandatory transmittance measurements on thin samples has been reported so far to our knowledge.

In chapter 2 some basics on low-dimensional quantum magnets and their elementary excitations are discussed. After treating uniform and alternating Heisenberg chains, the Heisenberg ladders as a bridge between 1D and 2D are introduced. Afterwards the readers attention is turned to the telephone-number compounds $(\text{Sr},\text{La},\text{Ca})_{14}\text{Cu}_{24}\text{O}_{41}$, which represent the most widely studied series of spin ladders.

In optical spectroscopy we probe the linear response of solids to an applied electric field. This as well as the concept of phonon-assisted two-magnon absorption are briefly summarized in chapter 3, before in chapter 4 details on the experimental setup are presented, which was put into operation within the framework of this thesis.

The infrared spectra of undoped telephone-number compounds are the subject of chapter 5. In comparison with theoretical results it is possible to unambiguously identify the signature of a bound state of two triplets and a multi-triplet continuum. The inclusion of a cyclic exchange in the analysis enhances the agreement between theory and experiment and reproduces the spin gap measured by neutron scattering. Thus the importance of this exchange term for a minimal model to describe spin ladders is verified. The analysis yields the complete set of the three relevant exchange couplings. The temperature dependence of the phonon-assisted magnetic absorption is discussed, and the relationship between the $S = 1/2$ two-leg ladder and the $S = 1$ chain is analyzed.

Chapter 6 deals with the effect of charge-carrier doping on the optical spectra. In $\text{Sr}_{14}\text{Cu}_{24}\text{O}_{41}$, charge ordering in the chain subsystem modulates the exchange coupling along the ladders and thus leads to additional superstructure. Further mechanisms are discussed that may explain some of the features in the doped compounds which are absent in the undoped compounds of chapter 5.

Chapter 2

Low-Dimensional Quantum Magnets

In the following, low-dimensional antiferromagnets (AF) and their elementary excitations are discussed. At first some basics are given, and then the attention is focussed on the 1D chain. Afterwards more detail on the current state of spin-ladder research is presented. Finally, the “telephone-number” compounds are introduced, which take the center stage in this thesis.

2.1 Some Basics

The dimensionality of magnetic systems plays a crucial role when it comes to long-range ordering, phase transitions, spin gaps or low-energy excitations. At first there is the conventional dimension of the *magnetic* lattice $d = 1, 2, 3$, that corresponds to chains, planes, and 3D models. Below, notations like $d = 2$ and 2D are used as a synonym. But also the number n of spin components (x, y, z) has to be considered. The parameter n is called the spin dimensionality and is always to be distinguished from d . It is e.g. possible to have a 3D model with spin operators that just have one component along the z axis. This would be the 3D Ising model with $d = 3$ and $n = 1$. For a given spin dimensionality $n > 1$ one may in addition vary the number of *interacting* spin components described by

Spin Dimensionality	Interacting Components	Name of Model
$n = 3$ $\mathbf{S}^2 = S_x^2 + S_y^2 + S_z^2$	$J_x = J_y = J_z$ $J_x = J_y; J_z = 0$ $J_z; J_x = J_y = 0$	Isotropic Heisenberg XY Z
$n = 2$ $\mathbf{S}^2 = S_x^2 + S_y^2$	$J_x = J_y$ $J_y; J_x = 0$	Planar Planar Ising
$n = 1$ $\mathbf{S}^2 = S_z^2$	J_z	Ising

Table 2.1: Classification of model systems. The different \mathbf{S}^2 spin operators are given in the left column. Note that the magnetic lattice dimension is not specified. In fact, all the models may occur in 1, 2, or 3D. Based on references [29, 30].

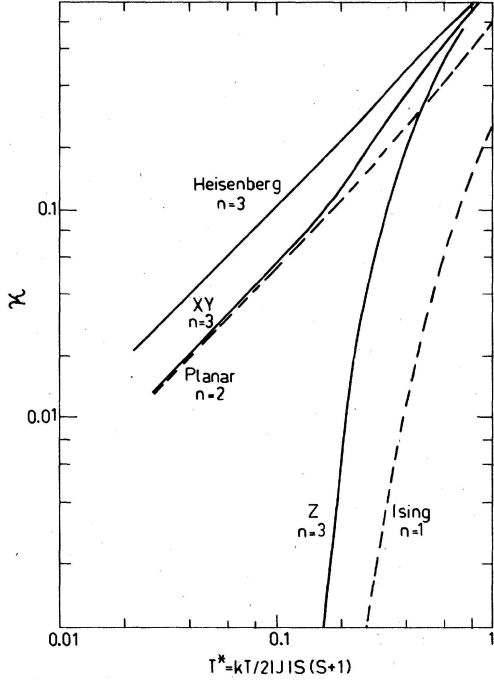


Figure 2.1: Inverse correlation length along the chain axis for different $d = 1$ chain models versus a reduced temperature T^* . At high temperatures, all $n = 3$ models approach the isotropic Heisenberg limit. The calculations were performed within the classical spin formalism. Note that the classical Ising results are equal to the quantum-mechanical $S = 1/2$ case. Reproduced from reference [30].

the exchange constants J_x , J_y , and J_z , as illustrated in table 2.1. Of these models, the Ising, Heisenberg, and XY models are probably the most popular ones. But of course there are more possible combinations not listed in the table. For instance in three spin dimensions and for $J_x \neq J_y \neq J_z$ one gets the anisotropic Heisenberg or XYZ model.

To further illuminate this classification, one can e.g. have a look at the inverse correlation length (see figure 2.1) and discuss the difference between the XY and the planar model in 1D. In the XY model the interaction between the spins only has components within the xy plane, whereas the spins themselves are free to rotate in all three directions. In the planar model, however, the spins are confined to the xy plane. At low temperatures the difference between the two models is not that significant. In the high-temperature limit the XY model approaches the 1D isotropic Heisenberg model. This is due to the thermal motion of the spins, which introduces a nonzero expectation value of the spin component along the z axis, even though $J_z = 0$.

The isotropic Heisenberg model is often applicable to metal ions with open $3d$ shells. In particular, it frequently describes systems with Cu^{2+} ($S=1/2$) or Mn^{2+} ($S=5/2$) ions rather well.¹ In all the models next-nearest-neighbor interactions are often neglected. The reason is that in most considered materials the coupling is predominantly caused by superexchange, which is of extremely short range ($J \propto r^{-n}$, $n > 12$) [32]. But the superexchange is also very sensitive to the actual bond angle. 180° bonds lead to strong AF exchange, whereas the exchange across 90° bonds is typically weak and ferromagnetic according to the Goodenough-Kanamori-Anderson (GKA) rules [33].

In three spatial dimensions ($d = 3$) most magnetic systems develop long-range order if only the temperature is sufficiently low. And this holds true independently from the spin

¹However, on the basis of ESR data it has recently been demonstrated that the exchange within 1D CuO_2 chains is strongly anisotropic [31].

dimensionality. The case of $n=3$ with just nearest-neighbor interactions can be described by the general Heisenberg Hamiltonian

$$\mathcal{H} = \sum_i J_x S_i^x S_{i+1}^x + J_y S_i^y S_{i+1}^y + J_z S_i^z S_{i+1}^z. \quad (2.1)$$

Here again, S^x , S^y , and S^z denote the components of the spin operator $\mathbf{S} = (S^x, S^y, S^z)$, whereas J_x , J_y , and J_z are the interactions for the different spin components, respectively. In this convention, positive values of J are used for antiparallel coupling of neighboring spins, i.e. antiferromagnetic coupling, whereas $J < 0$ means ferromagnetic coupling. Probably one of the best representations of a 3D Heisenberg antiferromagnet with spin $S = 1/2$ is KNiF_3 . This is a prototype system with 180° superexchange paths and a perovskite structure [34].

The spin itself is another crucial quantity that determines the system. Quantum-mechanically the spin is represented by operators with quantum numbers $S = 1/2, 1, 3/2, 2$, and so on. The crossover towards “classical” spin *vectors* is equal to $S \rightarrow \infty$. In this case the eigenvalue of the operator $\mathbf{S}^2 = S_x^2 + S_y^2 + S_z^2$, which is $S(S+1)\hbar^2$, can be replaced by $S^2\hbar^2$. Quantum fluctuations disappear and the so-called Néel state becomes the ground state (see figure 2.2). In a bipartite lattice there are two sublattices A and B with, for instance, just spin-up and spin-down sites, respectively. In the absence of frustration there is AF interaction only between A and B spins. If there is any interaction *within* a sublattice, it is supposed to be ferromagnetic. Every deviation from this scenario is then called frustration. MnO is an example of Néel order in three dimensions with $T_N = 122$ K [35]. As already mentioned above, the spin of the magnetic Mn^{2+} ion is $S = 5/2$ and thus substantially larger than the quantum limit of $S = 1/2$.

More generally, all states that show finite sublattice magnetizations $\langle \mathbf{S}_A \rangle - \langle \mathbf{S}_B \rangle \neq 0$ are labelled Néel states [36]. Therefore this definition also includes ferrimagnets. Above the critical Néel temperature T_N the order breaks down, and the system becomes paramagnetic. However, below T_N one axis gets singled out even if there is no intrinsically favored direction within the crystal, which would be called an easy axis. This singled-out direction is not imposed externally, and such a phenomenon is called spontaneous symmetry breaking [27]. The Goldstone theorem states that in all cases with broken *continuous* symmetries there are excitations with arbitrarily low energy [37]. These excitations are called massless Goldstone bosons.

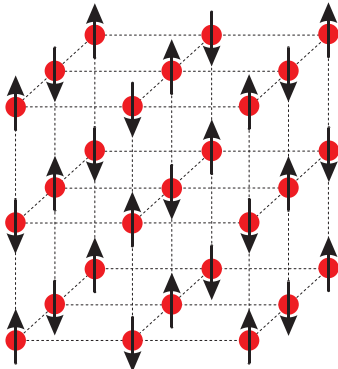


Figure 2.2: Classical Néel state in three dimensions of the magnetic lattice ($d = 3$). The AF lattice of the magnetic ions is face-centered cubic (fcc), whereas the corresponding paramagnetic lattice is simple cubic (sc).

In 1D chains, on the other hand, there is no long range order above $T = 0$, regardless of the spin dimension. Only the Ising chain exhibits order right *at* zero temperature. Whether there is an ordered state in two lattice dimensions depends on the symmetry of the Hamiltonian. The planar Ising model, for instance, orders at finite temperatures [38], whereas Mermin and Wagner proved in their classical letter [39] that for isotropic Heisenberg chains and planes with finite-range exchange interactions there cannot be spontaneous ordering at any finite temperature.² Thermal excitations disorder the spins already at infinitesimally low temperatures. Yet at $T = 0$ in the 2D square lattice the effect of zero-point quantum fluctuations is not strong enough [41], and thus the phase transition occurs exactly at zero temperature. Another example is the XY model in 2D. Kosterlitz and Thouless showed that no long-range order of the conventional type exists [42]. Nevertheless, there is a state below a critical temperature T_{KT} that is characterized by a so-called *topological* order of spin vortices. Pairs of metastable vortices and antivortices are closely bound and eventually become free above the phase transition at T_{KT} . The mean magnetization is zero for all temperatures [43]. However, such a Kosterlitz-Thouless phase transition does not occur in the isotropic 2D Heisenberg model [42]. To sum up the occurrences of phase transitions at finite temperatures depending on the different spin and lattice dimensions, table 2.2 gives an overview of exemplary models for all combinations of d and n .

	$d = 1$	$d = 2$	$d = 3$
Ising ($n = 1$)	○	✓	✓
XY ($n = 2$)	○	KT	✓
Heisenberg ($n = 3$)	○	○	✓

Table 2.2: Presence (✓) or absence (○) of a transition to conventional long-range order of exemplary models at finite temperatures. The Kosterlitz-Thouless transition to topological order is denoted by (KT). Based on reference [29].

The thermodynamic behavior of magnets can be treated with mean-field (MF) theory, which is the simplest way to describe collective phenomena [44]. Nevertheless it has been successful to qualitatively describe magnetic phase transitions in 3D systems. For lower lattice dimensions, though, it appears to be inadequate since e.g. it predicts states of long-range order regardless of d . MF theory rather applies to classical magnets, and the actual critical temperatures T_c always lack behind the calculated MF values of $\theta = zJS(S+1)/3k_B$ [29]. The parameter z is called magnetic coordination number and denotes the amount of nearest-neighbor spins. The discrepancy between T_c and θ increases when spin fluctuations get more important. As a rule of thumb, these fluctuations become more important upon

- (i) lowering the lattice dimension d ,
- (ii) increasing the spin dimension n ,
- (iii) reducing the involved spin values,

²Essentially the same approach was used one year later by Hohenberg to exclude superfluidity at $T > 0$ in one and two dimensions [40].

- (iv) decreasing the number of nearest-neighbor spins z , or finally
- (v) enhancing frustration.

The last point is particularly obvious in a triangular plaquette as sketched in figure 2.3a. There is no possible solution for the three neighboring spins to get aligned antiferromagnetically. However, the 2D triangular lattice indeed does exhibit long-range order. In the classical limit the ground state is a Néel state with the spins arranged at 120° to each other in *three* ferromagnetic sublattices (see figure 2.3b). But even in the quantum limit of $S = 1/2$ there probably exists an ordered Néel ground state with a sublattice magnetization of as much as 50 to 60% of the classical value [45, 46]. The quite large magnetic coordination number of $z = 6$ helps to stabilize the system against extra fluctuations due to frustration. The situation is different for the Kagomé lattice with a lower value of $z = 4$ (figure 2.3c). Calculations indicate that there is no planar AF long-range order down to zero temperature [46, 47]. In general, such systems with no extensive magnetic order at $T = 0$ are called spin liquids. In analogy to *real* liquids there is, at the most, short-range order. The Kagomé system shows rather unusual properties, but the frustrated $S=1/2$ chain with antiferromagnetic exchange is an exemplary spin liquid. In AF chains frustration always emerges as soon as a further AF coupling between next-nearest-neighbor spins is present.

The notion of spin liquids was first proposed by Anderson. He also introduced the corresponding resonating valence bond (RVB) state that is contrary to the classical Néel state [48, 49]. In zeroth order the RVB model assumes a ground state consisting of nearest-neighbor singlet pairs. Higher-order corrections then allow the singlet pairs to move or “resonate”, which makes this insulating singlet state more stable [49]. The actual state of the system is a linear superposition of such valence-bond singlets, corresponding to all possible pairings of sites into singlets with appropriate weight factors [50]. At this juncture it is sufficient to consider only bonds from one sublattice to the other. A simple visualization of such a product state in 1D is attempted in figure 2.4.

One of the main characteristics of RVB states is the absence of long-range order. Therefore it is not surprising that the above mentioned factors that enhance spin fluctuations just as much favor the RVB state. For instance, rough estimates of the energies yield for the Néel case $E_{\text{Néel}} = -S^2 z J / 2$ per spin and accordingly $E_{\text{RVB}} = -S(S+1)J/2$ for the

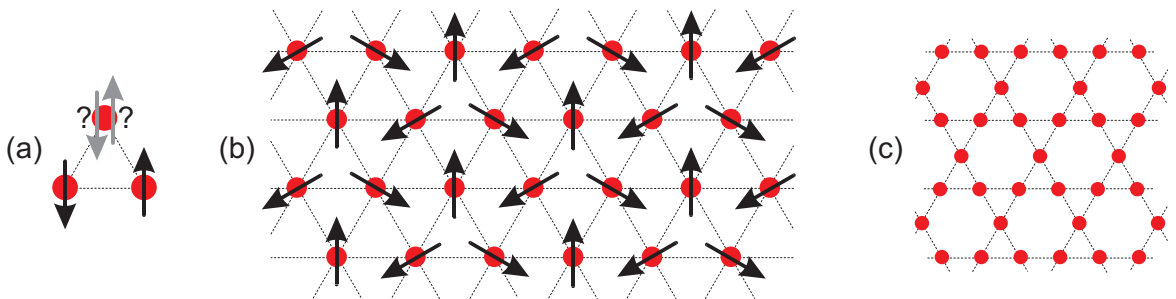


Figure 2.3: (a) Illustration of the no-win situation on a triangular plaquette with anti-ferromagnetic coupling. This frustrated arrangement enhances spin fluctuations. (b) Nevertheless, the triangular lattice does exhibit a Néel ground state with three ferromagnetic sublattices. (c) An example of a spin liquid without long-range order is the Kagomé lattice.

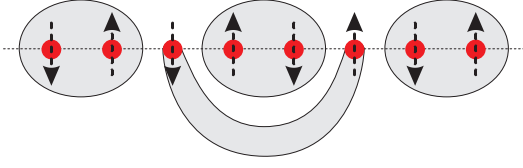


Figure 2.4: Sketch of a possible RVB product state in 1D. The spin arrows might be misleading since in fact the singlets do not favor any direction.

RVB case [36]. Hence larger values of the spin coordination number z swiftly promote the classical limit. Increasing the spin has the same effect, though not as drastically. When the size of the superposed singlets in the RVB state stays finite, there will be a spin gap in the excitation spectrum. The gap energy then corresponds to the energy required to break up the “cheapest” singlet. However, in the case of infinitely large bonds also the Néel state can be described as a superposition of appropriate RVB states. With increasing bond length Monte Carlo simulations on the square lattice in reference [50] indicate disordered RVB states of very low energy. That shows that the RVB state gets competitive to a gapless Néel state with Goldstone excitations. Thus the difference between both types of states vanishes as soon as infinite-range singlets are included.

2.2 Antiferromagnetic Heisenberg Chains

From the above it becomes clear that the ground state of an antiferromagnetic 1D spin system is of exotic nature with quantum fluctuations impeding magnetic order. Theoretical physics dealt with such systems since the early days of quantum mechanics as a simple model for many-body effects. The Hamiltonian of the Heisenberg spin chain can be written as

$$\mathcal{H} = J \sum_i (\mathbf{S}_i \mathbf{S}_{i+1} + \alpha \mathbf{S}_i \mathbf{S}_{i+2}). \quad (2.2)$$

The second term accounts for next-nearest-neighbor interactions. Therefore, with increasing the parameter α frustration gets enhanced. In the following, at first the frustration is switched off, i.e. $\alpha = 0$. The classical ground state of the ferromagnetic case ($J < 0$) is simply the parallel alignment of all spins. However, in the AF case it is easy to demonstrate that the classical Néel state cannot be the ground state. With the help of raising and lowering operators

$$S^\pm = S^x \pm iS^y \quad (2.3)$$

the Hamiltonian 2.2 (still with $\alpha = 0$) can be rewritten as

$$\mathcal{H} = J \sum_i \left[\frac{1}{2} (S_i^+ S_{i+1}^- + S_i^- S_{i+1}^+) + S_i^z S_{i+1}^z \right]. \quad (2.4)$$

The mentioned classical ground state $|\psi\rangle$ would very well satisfy the spin-test relation

$$S_i^z |\psi\rangle = \pm S |\psi\rangle, \quad (2.5)$$

but it is obvious that the inner bracket of Hamiltonian 2.4, applied to the Néel version of $|\psi\rangle$, transposes the spins of neighboring sites. Therefore the Néel state is not an exact eigenstate of the AF Hamiltonian.

Without frustration the model is exactly solvable, and the ground-state wave function of the Heisenberg chain with $S = 1/2$ was already determined by Bethe back in 1931 [51, 52]. Using Bethe's solution it was Hulthén [53] who first calculated the exact ground-state energy eight years later for the AF case as

$$E_G = -N (\ln 2 - 1/4). \quad (2.6)$$

Explicit results for other physical quantities emerged slowly at first and only faster since around 1960. Of course interest in this model began to spread as soon as the first AF chain compounds became available. The total spin of the ground state is zero. Yet this state is somewhere in-between the Néel and the RVB state. The missing sublattice magnetization and the pronounced local singlet character of the wave function place it close to the RVB description. But as in the Néel state there is no excitation gap, and there are strong AF correlations since the decay follows a power-law [36].

As soon as frustration is allowed in the AF chain by increasing α , the RVB state gains ground in this contest. Many calculations were carried out for $S = 1/2$: In the case of $\alpha = 1/2$, which is known as the Majumdar-Gosh point, the ground state is a dimer state consisting of a product of merely nearest-neighbor singlets [54–57]. It is two-fold degenerate and characterized by an excitation gap as well as the exponential decay of the spin correlation. In particular, the two-point correlation function $\langle \mathbf{S}_i \cdot \mathbf{S}_j \rangle$ vanishes whenever $|i - j| \geq 2$, i.e. there is no correlation between adjacent singlets. The ground state energy amounts to $E_0 = -3/8J$ per spin as proven by van den Broek for infinite chains [58]. But there has to be a transition somewhere on the way from the gapless state at $\alpha = 0$ to the pure RVB state with gap at $\alpha = 1/2$. Numerical calculations yield rather precise values [59, 60]. At first, the excitation spectrum stays continuous but at the critical point of $\alpha = 0.24116(7)$ the energy gap finally emerges [60]. In section 5.3.3 more detail on the phase diagram of the chain is presented.

2.2.1 Elementary Excitations

Now the attention is turned to the excitations themselves. Before 1981, the excitations of $S = 1/2$ chains were generally assumed to be triplet spin-wave states with momentum k and spin $S = 1$ [61]. At least this was expected because of the situation in three-dimensional AF systems, where excitations are equal to delocalized spin flips with $\Delta S = \pm 1$. However, Faddeev and Takhtajan introduced the *spinon* with spin $S = 1/2$ as the true elementary excitation in 1D [62].³ Later, Haldane spoke of topological soliton excitations [64], since a spinon can be pictured as a movable domain wall within the chain, that separates two degenerate ground-state configurations. This image even works for Néel and RVB types of ground states. The Néel case is depicted in the top panel of figure 2.5.

³It was already in 1979 that Andrei and Lowenstein discovered the spinon in a different context. They diagonalized the Hamiltonian of the Gross-Neveu model and found excitations with spin $1/2$ that only get excited in pairs, and they called these excitations *spinors* [63]. The Heisenberg model was not mentioned, but they used a modified Bethe ansatz which also holds true for the Heisenberg AF. All the spinon credit is usually booked to Faddeev's and Takhtajan's account, though.

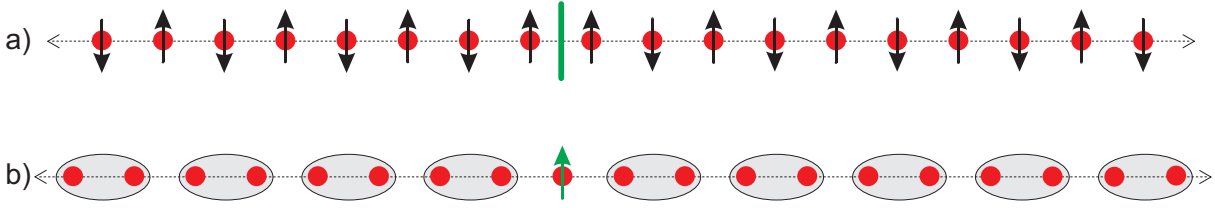


Figure 2.5: Representation of spinons as domain walls. The momentum of the sketched excitations is “ $k = \pi$ ”. Panel (a) represents the Néel case, and panel (b) the RVB case. In contrast to figure 2.4 on page 12, here the misleading spin arrows within the RVB singlets are omitted. Note that spinons can only be excited in pairs.

The spin of $1/2$ can be recognized especially in the RVB representation (figure 2.5b) due to the single unpaired spin. Both pictures are to be understood as oversimplifications, though. The RVB state for instance consists of singlets of different range, whereas the idealized Néel state does not exist anyway because of the fluctuations. Moreover, the spinon is not only the simple domain wall of figure 2.5, but it polarizes the environment. This leads to some sort of polarization cloud [27].

Depending on if there is an even or odd number of spins, the total spin of the chain is either integer or half-odd integer. In chains with an odd number of sites there always has to exist at least one spinon. Actually, whether the total spin is integer or half-odd integer is a fundamental property of the system and cannot be changed by any excitation. Although the spinon indeed is the elementary excitation, a single spinon would change the total spin by $1/2$, and thus the excitation of a single spinon is not allowed. Instead, always *two* spinons are created simultaneously. In the Néel case it is easier to excite two spinons close to each other because all the spins in-between have to be flipped around. And in the RVB state a singlet gets excited to a triplet, which directly yields two adjacent spinons.⁴ Afterwards there is almost no confinement anymore that would tend to keep the spinons close-by. In fact, there is an interaction due to the polarization clouds, but the larger the distance between the spinons gets, the smaller the interaction is. This is meant by speaking of *asymptotically free* spinons.

Also important to note is that spinons cannot be gapless excitations in dimensions higher than one.⁵ Domain walls are always objects of dimension $d - 1$ when the lattice dimension is d . But this means that the energy gets proportional to L^{d-1} with L being the linear size of the system. Always when $d \geq 2$, the energy exceeds all limits with increasing system size. This is not reasonable for elementary excitations [36].

The next step is to calculate the momentum or wave vector k of the spinons. For each eigenfunction $|\psi\rangle$ the quantum number k is defined by the relation

$$T|\psi\rangle = e^{ik}|\psi\rangle, \quad (2.7)$$

where T is the operator that translates the entire chain by one lattice spacing [61]. To gain the dispersion of a single spinon one could for instance test the varying “ground-state

⁴Of course this is only true for the pure RVB state. In case of long-range bonds the two spinons are separated right away.

⁵Actually, this point is still under discussion. For instance Moessner and Sondhi claim that there are gapped spinons in the 2D triangular lattice [65].

energies” of an odd-number chain with respect to different momenta. At this point, the naive picture of figure 2.5 for spinons as local domain walls breaks down. For values of k smaller than π the domain wall gets delocalized and sort of smears out. The corresponding wavelength of the spinon is $\lambda = 2\pi/k$. Therefore a state with vanishing momentum will occupy the whole length of the chain and the notion of a domain wall is obsolete. The first dispersion relation for the AF $S = 1/2$ chain was calculated by des Cloizeaux and Pearson [61], long before the spinons were invented. Their result was

$$\frac{E_L(k)}{J} = \frac{\pi}{2} |\sin(k)|. \quad (2.8)$$

These spin-wave states are now understood to be a superposition of two spinons. The wave vector of two spinons is equal to the sum of both the single values $k = k_1 + k_2$. Thus there is always one free parameter when a double spinon with total momentum k is excited, and the real excitation spectrum will actually be a two-spinon continuum. The lower boundary is given by the equation from above whereas the upper boundary corresponds to two spinons with:

$$\frac{E_U(k)}{J} = \pi |\sin(k/2)|. \quad (2.9)$$

The continuum between lower boundary E_L and upper boundary E_U is marked as shaded area in the left panel of figure 2.6. By now, there are nice experimental verifications

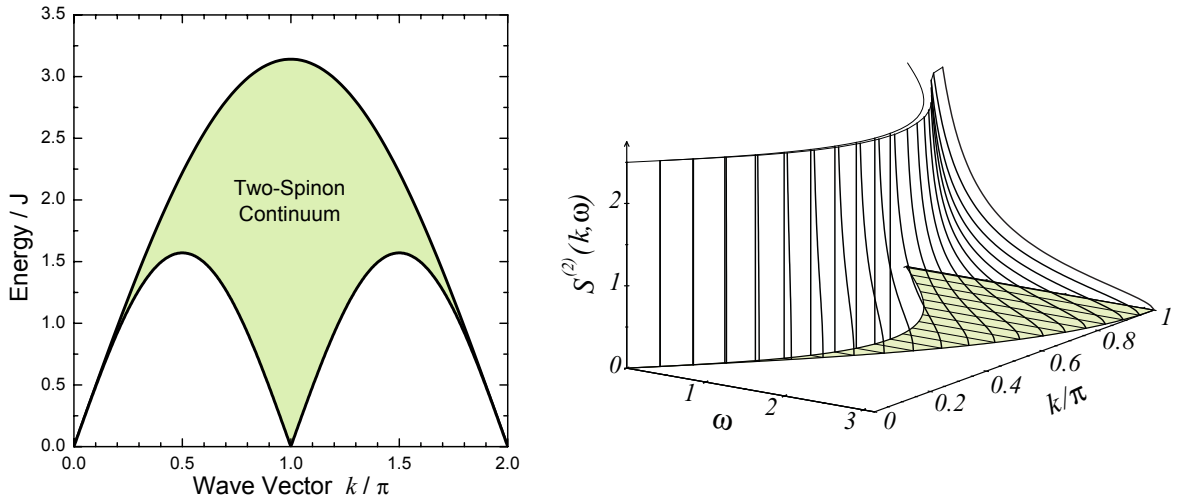


Figure 2.6: **Left** panel: Two-spinon continuum as shaded area between the boundaries of equations 2.8 and 2.9. The unit of the wave vector is in fact π/a , where a is the lattice constant. But as usual, a is set to unity. **Right** panel: Exact result of the dynamical structure factor $S(k, \omega)$ at $T = 0$ reproduced from reference [66]. Here ω denotes the energy as is common in spectroscopy (see section 3.2). Again the continuum is marked as shaded area. But contrary to the left panel only momenta up to $k = \pi$ are shown. The intensity plotted along the upright axis diverges at the lower boundary of the continuum and approaches zero without any discontinuity at the upper boundary.

by means of inelastic neutron scattering, which is the experiment of choice to check dispersions. KCuF_3 for instance turned out to be an appropriate candidate for the $S = 1/2$ AF Heisenberg chain [67]. This compound shows 3D long-range order below $T_N \approx 39$ K but exhibits almost ideal 1D chains above this temperature [68].

Measured scattering intensities are always weighted by the dynamical structure factor $S(k, E)$, and especially in the case of continua it is not clear where to expect neutrons without model calculations.⁶ Finally, Tennant et al. measured KCuF_3 [68, 70] and compared their intensities with calculations in the low-energy and zero-temperature limit by Schulz [71]. They measured along a line in the energy-momentum plane, as indicated in figure 2.7a, and found excellent agreement of their spectrum with the model data (figure 2.7b). As theoretical tools evolved further, the approximate structure factor used so far got replaced by exact results in 1997. The data of Karbach et al. [66] is shown in the right panel of figure 2.6. Again drawn as shaded area is the two-spinon continuum from the left panel, and the upright axis represents the dynamical structure factor. At the lower boundary the intensity diverges, whereas it approaches zero continuously at the upper boundary. The latter point actually marks the main difference compared to the older approximation which reveals a discontinuity at the upper boundary. But there is yet another interesting statement in the paper of Karbach et al. [66]. With the aid of sum rules it is possible to calculate that the two-spinon excitations account for approximately 73% of the *total* intensity in $S(k, E)$. The rest of the overall spectral weight is due to excitations of more than two spinons. In the next section about spin-Peierls systems a nice experimental mapping of a complete spinon continuum is presented.

What happens in AF chains when the spin is larger than $1/2$? One of the first points to clarify is the occurrence of a spin gap between the ground state and the first excited state. It was Haldane who used a semiclassical approach and predicted that Heisenberg chains with integer spins do exhibit energy gaps and thus are significantly different from half-odd-integer chains that show gapless excitation spectra [64]. The latter was already

⁶In the case of inelastic neutron scattering the momentum and the energy of the incident neutrons are changed. The intensity I of neutrons with energy dE' that is scattered into the solid angle $d\Omega$ is directly proportional to the scattering cross section: $I \propto \frac{d^2\sigma}{d\Omega dE'}$. This cross section again is proportional to the dynamical structure factor $S^{\alpha\beta}(\mathbf{k}, E)$. Here, \mathbf{k} and E mean the *changes* of momentum and energy in the scattering process and thus are equivalent to momentum and energy of the observed excitation. The parameters α and β denote the x, y and z components of the spin operator. In Heisenberg systems with no spin anisotropy the structure factor vanishes for all $\alpha \neq \beta$. Often the structure factor is also called spectral density or scattering function. Finally, the intensity is related to the Fourier transform of the spin-spin correlation function $\langle S_0^\alpha(t=0) \cdot S_{\mathbf{R}}^\beta(t) \rangle$. The stronger the correlation the more peak intensity can be expected. This can be deduced from the van Hove scattering function [69]. For simplicity, just contributions parallel to the z direction are considered, i.e. $\alpha = \beta = z$

$$I \propto \frac{d^2\sigma}{d\Omega dE'} \propto S^{zz}(\mathbf{k}, E) \propto \sum_{\mathbf{R}} \int_{-\infty}^{\infty} e^{i\mathbf{k}\cdot\mathbf{R} - iEt/\hbar} \langle S_0^z(0) \cdot S_{\mathbf{R}}^z(t) \rangle dt. \quad (2.10)$$

Neutron scattering hence measures directly the space-time Fourier transform of the (time-dependent) two-spin correlation function. Following the fluctuation-dissipation theorem, the structure factor furthermore is proportional to the imaginary part of the dynamical susceptibility $\chi''(\mathbf{k}, E)$ times the Bose distribution

$$S^{\alpha\beta}(\mathbf{k}, E) \propto \chi''(\mathbf{k}, E) \frac{1}{1 - e^{-E/k_B T}}. \quad (2.11)$$

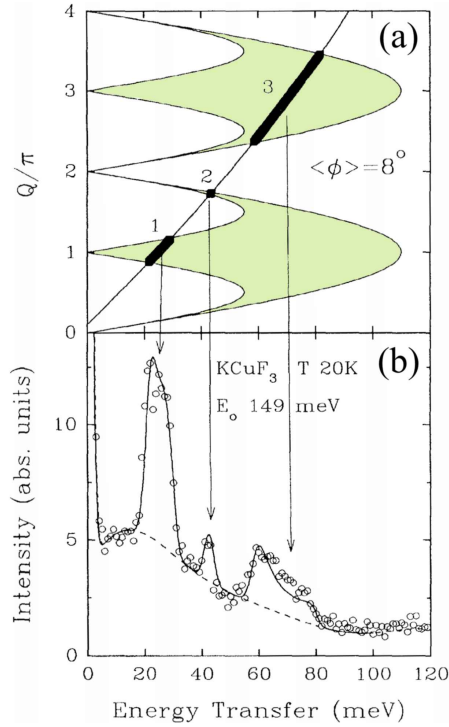


Figure 2.7: Neutron scattering data of KCuF_3 reproduced from reference [70]. **(a)** This continuum is equivalent to the one in the left panel of figure 2.6, though turned by 90° . The measurement was performed along the given line. Scattering intensity is observed when this line intersects with the continuum states as indicated by bold lines. **(b)** The resulting three features at the corresponding energies can clearly be seen in the spectrum. The dashed line denotes the fit to the background. The line shape is reproduced very well by the model fit using the calculated dynamical structure factor. The temperature was 20 K and thus it is interesting to note that the 1D quantum effects are dominant well below the 3D ordering temperature of $T_N \approx 39\text{ K}$. Yet there is no drastic change up to 200 K except for the usual weakening and broadening of the features.

proven in reference [72]. Rigorous evidence for the meanwhile called Haldane gap was given later by Affleck et al. in reference [73]. As a consequence of a topological term in the field-theoretical formulation of the problem, the spinons are bound when the spin is integer. This leads to well defined, spin-wave-like modes that are separated from the ground state by the Haldane gap [70].

2.2.2 Alternating Chains and Spin-Peierls Transition

The model of the alternating Heisenberg chain is a straightforward generalization of the so far discussed uniform chain. Now the spin-spin interaction alternates between the two values J_1 and J_2 from bond to bond along the chain. In real systems this may be the consequence of the crystallographic structure such as different superexchange paths or just alternating distances between neighboring spin sites (see figure 2.8). The insulating magnetic salt $(\text{VO})_2\text{P}_2\text{O}_7$ (VOPO) is an example [74, 75] although there was some confusion in early papers, where VOPO was mistaken for a spin-ladder compound.⁷ Further candidates are CsV_2O_5 [80] and the organic compounds $(\text{CH}_3)_2\text{CHNH}_3\text{CuCl}_3$ [81] as well as $\text{Cu}_2(\text{C}_5\text{H}_{12}\text{N}_2)_2\text{Cl}_4$ [82]. But again, it is difficult to extract the correct magnetic configuration from the available data. For example, the calculated susceptibilities of *different*

⁷VOPO (vanadyl pyrophosphate) has been widely considered to be a candidate for a two-leg AF Heisenberg spin ladder with legs running along the a axis [76–78]. However, more recent results from inelastic neutron scattering on powder samples [79] were inconsistent with the ladder model. Finally, neutron data on single crystals published somewhat later [74] verified that VOPO is instead an AF Heisenberg chain system with alternating couplings along the b axis. Thus the chains run perpendicular to the assumed ladders. The magnetic V^{4+} ions have spin $1/2$, and there is weak ferromagnetic interchain coupling. In general, it is difficult to distinguish between the two models from static susceptibility or neutron data of powder samples.

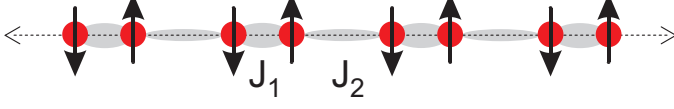


Figure 2.8: Example of an alternating chain. The interaction J_1 within a dimer is stronger than the interaction J_2 between the dimers. The lattice spacing is doubled compared to the uniform chain.

spin models often agree that much that all of them reproduce the experimental data better than the agreement between different measurements of the same compound [82]. Accurate calculations of the magnetic susceptibility and of the specific heat for different systems were given by Johnston et al. [83].

The new magnetic Hamiltonian has reduced translational symmetry due to the dimerization, and just including nearest-neighbor interactions it reads as follows

$$\mathcal{H} = \sum_{i=1}^{N/2} (J_1 \mathbf{S}_{2i-1} \mathbf{S}_{2i} + J_2 \mathbf{S}_{2i} \mathbf{S}_{2i+1}). \quad (2.12)$$

It is common to define an inter-dimer coupling parameter $\lambda = J_2/J_1$ with $0 \leq \lambda \leq 1$. In the case of unity one simply gets the isotropic chain with gapless excitations, and for vanishing λ the system is reduced to uncoupled dimers. Then a gap occurs which is equivalent to the breakup of a single dimer⁸ and thus $E_{gap} = J_1$. In-between there is the regime of coupled AF dimers in a singlet $S = 0$ ground state with a gap to the lowest $S = 1$ triplet excitation. A continuum of excitations sets in at $2E_{gap}$. Both the triplet gap and the continuum edge were observed in CuGeO_3 by means of inelastic neutron scattering [84] (see below). Analytical results can be derived using perturbation theory about the isolated dimer limit, i.e. $\lambda = 0$. But real systems often are closer to the critical point of the uniform chain. VOPO for instance has a value of $\lambda = 0.8$ [74]. And copper germanate (CuGeO_3), which is discussed below, exhibits an λ around 0.95 [85, 86].

Another approach is to distort the uniform chain in terms of the distortion parameter $\delta = \frac{1-\lambda}{1+\lambda}$. With the average value of $\tilde{J} = \frac{J_1+J_2}{2}$ the alternating couplings become

$$J_1 = \tilde{J}(1 + \delta) \quad \text{and} \quad J_2 = \tilde{J}(1 - \delta). \quad (2.13)$$

Finally, the Hamiltonian 2.12 can be rewritten as

$$\mathcal{H} = \tilde{J} \sum_i (1 + (-1)^i \delta) \mathbf{S}_i \mathbf{S}_{i+1}. \quad (2.14)$$

Cross et al. [87] as well as Black et al. [88] discuss such weak dimerization and following their approach, which involves a Jordan-Wigner transformation⁹, the gap energy is

$$\lim_{\delta \rightarrow 0} \frac{E_{gap}}{\tilde{J}} \propto \frac{\delta^{2/3}}{\sqrt{|\ln \delta|}}. \quad (2.15)$$

⁸The Hamiltonian of a single dimer reads $\mathcal{H} = J \mathbf{S}_1 \mathbf{S}_2 = \frac{J}{2}(\mathbf{S}_1 + \mathbf{S}_2)^2 - \frac{3J}{4}$. Therefore one finds a singlet energy of $E_S = -3J/4$ and a triplet energy of $E_T = E_S + J = 1/4J$.

⁹The Jordan-Wigner transformation [89] allows to map a one-dimensional $S = 1/2$ system exactly onto interacting fermions without spin.

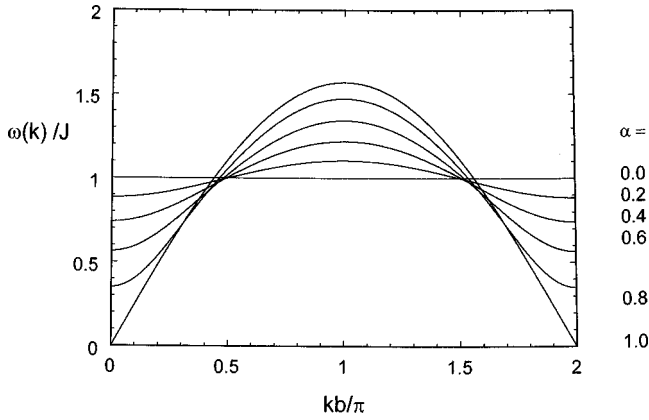


Figure 2.9: Spinon dispersion of an alternating chain for different inter-dimer couplings $\lambda = J_2/J_1$ [91]. Note that in the figure α is equal to λ . When comparing the result of the uniform chain at $\lambda = 1$ with the former spinon dispersion on page 15, one has to keep in mind that here the lattice spacing b is doubled. Therefore the dispersion for the uniform chain given here is equal to the first arc of the lower boundary of figure 2.6(left). Again, the energy is denoted by $E = \hbar\omega$ with \hbar set to unity.

Contrary to the intrinsically dimerized compounds described so far, alternating chains may also arise as a result of the spin-Peierls effect. In this case the spin chains are not isolated anymore but instead a coupling to the phonons of the complete lattice has to be included. A spatial dimerization of the ionic positions along the chain yields alternating interaction strengths and results in the lowering of the magnetic ground state energy. But as usual this advantage has to be paid for by an increase of lattice energy. The corresponding phonon contribution to the energy dominates at large distortions. An equilibrium will be reached at the lowest possible ground state energy. The spontaneous dimerization that occurs with decreasing temperature at T_{SP} is known as the spin-Peierls effect. In fact, a second-order phase transition occurs at T_{SP} . And since the lattice instability is driven by magnetic interactions, this transition is called magneto-elastic. The resulting *magnetic* Hamiltonian is equal to the given alternating chain Hamiltonian (equation 2.12 or 2.14). But when the temperature is decreased even further, a new equilibrium will be adopted and the dimerization gets stronger. Therefore λ becomes inherently temperature dependent.

The first inorganic example of a spin-Peierls compound is CuGeO_3 , which was discovered in 1993 [90]. The crystals are light blue, similar to “Wick Blau” ®, the German brand of Vicks cough drops. So far no other inorganic system has been proven to exhibit a spontaneous dimerization. The transition occurs at $T_{SP} = 14$ K, and below this temperature the magnetic susceptibility rapidly drops for all three directions to small constant values. However, the role of competing next-nearest-neighbor (NNN) interactions was discussed as an extension of the model in order to explain the susceptibility data. The frustration has the effect of increasing the transition temperature [85]. The admixture of NNN coupling was estimated to be somewhere between 0.24 and 0.36 [85, 86] and thus possibly beyond the critical value of 0.2412 at which a gap would occur even without dimerization (see page 13).

Dispersion relations of the magnetic excitations were presented in reference [91, 92]. The calculations were based on a combination of the Lanczos algorithm and multiple-precision numerical diagonalization to determine perturbation series to high order. In figure 2.9 the result is shown for a number of different inter-dimer couplings $\lambda = J_2/J_1$. Of course, the $\lambda = 1$ dispersion has to be equivalent to the uniform-chain result. The

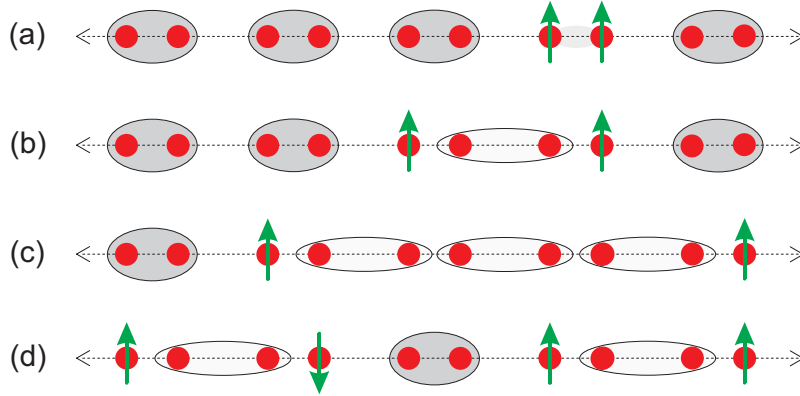


Figure 2.10: Spinon confinement. (a) Excitation of a local triplet. (b) The two spins can move away from each other at the cost of building weakly coupled dimers in-between. Two spinons are formed. (c) The potential energy rises further the more weak dimers are formed. (d) For large distances it is energetically favorable to create another pair of spinons compared to a situation with a large number of weak dimers. The total spin of the excitation is still $S = 1$. Based on reference [27].

dimer limit of $\lambda = 0$ yields just a straight line with an energy gap of J_1 . Without dispersion the excitation cannot move along the chain, and thus the excited triplet stays localized. By switching on the coupling between the dimers, which means increasing λ , the gap energy gets smaller. At the same time the excitation can hop as a whole from dimer to dimer, and the bandwidth of the dispersion increases. Both the spins that form the triplet can also separate, and we get two spinons. But there is an important difference to the asymptotically free spinons of the uniform chain. The corresponding mechanism is illustrated in figure 2.10: As soon as the spinons move away from each other, new singlet dimers are formed in-between. But the coupling is weaker because the spin sites are further apart compared to the initial dimers. In terms of energy this configuration is unfavorable, and the situation gets worse the more weak dimers are formed. Hence the energy increases with distance d , and there is a potential $V(d)$ that tries to keep the spinons nearby. The spinons are bound, and their movement is hampered by this new confinement. From a certain distance on it gets “cheaper” to excite a new pair of spinons than to build further weak dimers. Energetically this corresponds to $2E_{gap}$, where the energy is sufficient to excite two triplets.

A dimerization of the chain thus binds spinons to pairs [17, 93]. The total spin of such a bound spinon is either $S = 0$ for a singlet or $S = 1$ for a triplet. These two types of excitations both yield a well defined excitation branch. The energy of the triplet is lower than the singlet energy. Strictly speaking, the spinons are not the elementary excitations anymore due to the binding. Instead the triplet spinon pairs get labelled to be the new elementary excitations. This appears naturally from the point of view of isolated dimers discussed above.

Both branches are located below the continuum, that still is present in the dimerized chain. The continuum has to emerge from two unbound excitations, which can be regarded as either two triplets, two spinons, or two pairs of spinons. Due to spin-rotation symmetry the gap of the continuum is twice the elementary triplet gap [17]. But there is also another

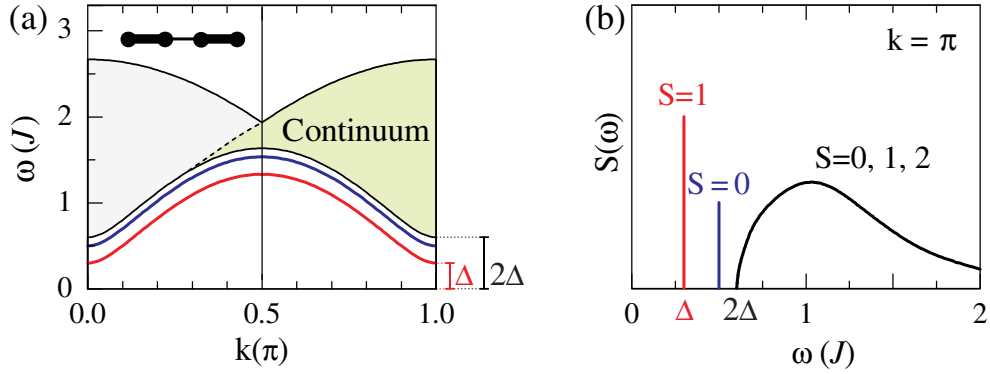


Figure 2.11: Sketch of the dispersion and the spectral density of the dimerized chain, reproduced from reference [27]. (a) The bottom curve shows the elementary branch of the triplet. Just above is the singlet branch. The shape of the continuum can be derived from the spinon continuum of the uniform chain (see page 15) or by taking all possible combinations of two triplets. The dashed line is a guide to the eye to indicate the “uniform” continuum (right area), although now with a gap. Due to the doubling of the unit cell the Brillouin zone is cut in half at $k = \pi/2$. Hence the “right” continuum is mirrored or folded back along the $k = \pi/2$ line, and the “left” area emerges. The complete continuum is the combined area of both contributions. When the dimerization is weak there won’t be much intensity from the “left” area. Δ and 2Δ denote the gaps to the elementary triplet and to the continuum, respectively. (b) Structure factor or spectral density at momentum $k = \pi$. Of course, with neutrons only $S = 1$ excitations are accessible.

way of interpreting the singlet branch. If one prefers to choose the triplet picture without the concept of spinons, at least two triplets have to be excited to yield a singlet state. This would be a bound state of two triplets with antiparallel alignment.

The excitation spectrum of the alternating chain with the two branches of bound states and the continuum is sketched in the left panel of figure 2.11. The right panel illustrates the spectral densities at momentum $k = \pi$ with two sharp peaks stemming from the bound states. The triplet peak and the continuum of CuGeO_3 were measured with neutrons [84], as discussed above. The continuum had already been mapped before by Arai et al. [94]. Their impressive plot is presented in figure 2.12. However, the resolution had not yet been high enough to see the triplet bound state. And since dimerization is low in CuGeO_3 the continuum resembles the one of the uniform chain, but of course the spin gap is present. With neutrons it is not possible to measure $S = 0$ singlet excitations. Such excitations at momentum $k = 0$ are accessible by inelastic Raman scattering [95–97]. In Figure 2.13 the Raman spectrum of CuGeO_3 is plotted. The sharp peak is clearly visible but not separated from the weak continuum that follows.

2.2.3 Doping of Chains

So far, no doping of charge carriers or magnetic impurities has been discussed. The simplest possibility is to replace some spins by spinless impurities, such as it occurs by doping with Zn^{2+} ions. The effect is quite similar for a variety of different spin models and is caused mainly by short-distance physics. A small percentage of vacancies rapidly

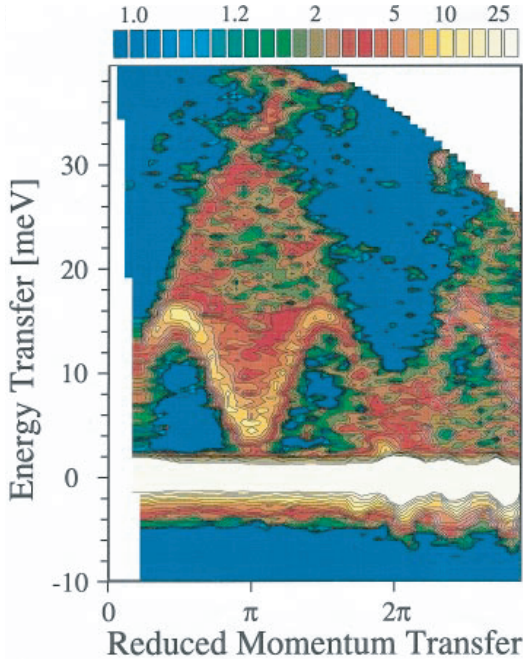


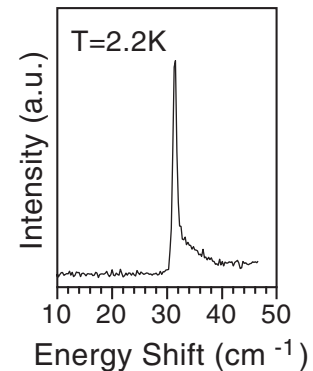
Figure 2.12: Map of the dynamical structure factor of CuGeO_3 , measured with inelastic neutron scattering at 10 K by Arai et al. [94]. The dimerization in CuGeO_3 is quite small and thus the left “mirror” intensity of figure 2.11 is not present. Therefore the continuum resembles the spinon continuum of the uniform chain. The arcs of the lower boundary are very distinct. Since these arcs do not reach all the way down to zero energy the gap is verified. Also the upper boundary of the continuum is according to expectations. Due to the resolution of the measurement the triplet bound state is not separated from the continuum but was verified later in reference [84].

destroys spin gaps, and their presence induces enhanced AF correlations nearby [98, 99]. Again, CuGeO_3 is a fruitful example [100–103]. The explanation acts on the assumption of localized spinons near the doped vacancies that interact with each other through weak effective AF couplings. This interaction will get stronger the more Zn is doped into the system. Calculations demonstrated that these localized states form a low energy band in the spectrum, which appears inside the original spin gap of dimerized chains and also of the spin ladders discussed in the next section [104].

Charge-Carrier Doping

Much effort has been spent to describe the copper-oxide planes of superconducting cuprates which are doped with holes. Fortunately, the concepts can often be applied to other Cu-O systems as well. Let us start from the undoped case. The Cu^{2+} ion possesses nine electrons in the $3d$ shell. The degeneracy of the $3d$ orbitals is lifted by the crystal field, resulting in a single hole in the $d_{x^2-y^2}$ orbital. This leads to a half-filled band

Figure 2.13: Raman spectrum of CuGeO_3 reproduced from figure 1 of reference [97], yet simplified and rearranged. Inelastic photon scattering is sensitive to $S = 0$ excitations. Thus the sharp peak arises from the singlet bound state. The subsequent continuum is not separated from this peak, though.



of $d_{x^2-y^2}$ orbitals within the crystal. Accordingly, band structure calculations predicted a non-magnetic metallic state [105], which is in clear contrast to the insulating gap of the order of 1.5 eV observed in optical spectra [106–108]. This failure of band theory is due to the large on-site Coulomb repulsion U that forces the electrons to avoid double occupancy of a single orbital. In this situation the electrons are strongly correlated.

When further holes get doped into copper-oxide spin systems, *effective* Cu^{3+} ions are created with spin $S = 0$. In fact, no real Cu^{3+} ions occur but instead hybridization between copper and oxygen strongly binds a hole to a central Cu^{2+} ion and its surrounding oxygen ions. This leads to the formation of a local singlet which is well-known as the Zhang-Rice singlet [109]. Overlap between neighboring sites allows for hopping of electrons and thus the singlet can move. The Zhang-Rice singlet corresponds to a *spinless* fermion moving in the background of Cu spins without doubly occupied sites. It represents an *empty* site or hole, respectively, in the copper lattice. The kinetics of holes in the background of an $S = 1/2$ Heisenberg AF can be described by the t - J model, which is an effective low-energy model for single or multi-band Hubbard models. The parameter t denotes the site-hopping matrix element. The AF exchange is then given by

$$J = 4t^2/U \quad (2.16)$$

with U being the already mentioned on-site Coulomb repulsion. In the t - J approach this repulsion is assumed to be larger than the hopping: $U \gg t$. At exactly half filling of the band the charge excitations are gapped, and the low-energy degrees of freedom are purely magnetic. In this case the t - J model reduces to the standard Heisenberg model.

In 2D the Hubbard model as well as the t - J model have not been solved exactly, and not even the ground states are entirely known so far. A lot of numerical calculations on finite clusters were performed, but the complexity grows outrageously with cluster size. The computation of a 32-site cluster within the t - J model already requires to handle matrices with dimensions of up to 3×10^8 [110]. That is the reason why the probing question whether there is superconductivity in these models has not been answered satisfactorily to date.

In 1D, however, the low-energy properties of many gapless quantum systems can be described by the exactly solvable Luttinger model [111]. The class of models that can be mapped onto so-called Luttinger liquids includes the 1D Hubbard model away from half-filling and thus also the 1D t - J model. One of the key properties is the spin-charge separation: instead of quasiparticles like in Fermi liquids, collective excitations of charge (with no spin) and spin (with no charge) are formed, that move independently and even at different velocities. Just recently our group found evidence for this phenomenon in the Bechgaard salts by measuring the electrical and thermal conductivity [112].

Another interesting effect is the occurrence of charge ordering in doped chains. $\text{Sr}_{14}\text{Cu}_{24}\text{O}_{41}$ for instance is inherently doped with charge carriers. The nominal hole count yields six holes per formula unit, and the holes are expected to reside mainly within the sublattice of the CuO_2 chains. Nücker et al. estimated the distribution of holes at room temperature via x-ray absorption spectroscopy [9]. They found approximately 5.2 holes in the chains, whereas 0.8 holes are located within the other sublattice, which includes layers of spin ladders. This telephone-number compound will be discussed in greater detail later on. Below the temperature of approximately 200 K a superstructure occurs due to charge ordering in the chains. Regnault et al. used inelastic neutron scattering and proposed a

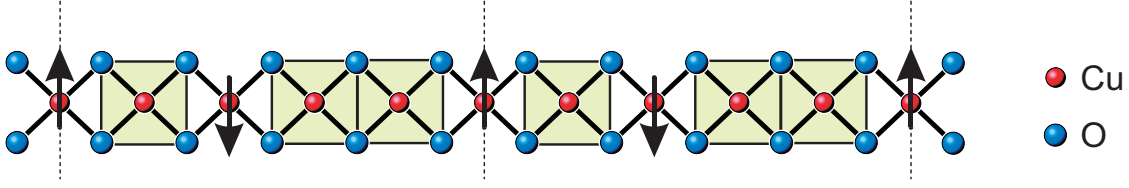


Figure 2.14: The charge ordering in the chains of $\text{Sr}_{14}\text{Cu}_{24}\text{O}_{41}$ produces a superstructure with the periodicity of five lattice spacings. The squares denote Zhang-Rice singlets.

model of interacting AF dimers with intra- and interdimer distances equal to 2 and ≈ 3 times the distance between neighboring copper ions [113]. This implies that almost no charge carriers are left within the ladders at low temperatures. A possible illustration of such an arrangement is sketched in figure 2.14. The holes are drawn as squares to symbolize Zhang-Rice singlets. AF dimers are formed between spins that are separated by a single hole. The dimers are separated by *two* holes from each other, which leads to only weak magnetic exchange. The charge order in $\text{Sr}_{14}\text{Cu}_{24}\text{O}_{41}$ is discussed in greater detail in chapter 6.

2.3 Ladders: Bridge between 1D and 2D

The humble survey of 1D chains demonstrated that a great deal of the rich phenomena are understood after a long period of research. The important models are solved and experiments support the theoretical results. The 2D square-lattice Heisenberg AF is far from this state. Some hope is associated with the ladders that topologically are situated between one and two dimensions. One can start with a single chain, or leg, and successively couple further chains to it, until finally the square lattice is approached. Neither in Heisenberg chains, nor in the 2D square-lattice there is a spin gap for $S = 1/2$. The corresponding ground states are of spin-liquid and AF type, respectively. And of course it is very instructive to examine what happens in-between, both in theory and experiment. This section is chiefly based on the comprehensive reviews on ladders presented in reference [2] by Dagotto and Rice, and in reference [114] by Dagotto.

AF Heisenberg ladders with two and three legs, respectively, are sketched in figure 2.15. The exchange coupling along the legs is labelled as J_{\parallel} , and J_{\perp} denotes the rung coupling. The Hamiltonian of the simplest case with just two legs reads

$$\mathcal{H} = \sum_i \{ J_{\parallel} (\mathbf{S}_{1,i} \mathbf{S}_{1,i+1} + \mathbf{S}_{2,i} \mathbf{S}_{2,i+1}) + J_{\perp} \mathbf{S}_{1,i} \mathbf{S}_{2,i} \}. \quad (2.17)$$

The first two terms represent the interaction between neighboring spins along the two legs, and the last term takes care of the interaction within each rung. The first index of each spin operator denotes the leg number, whereas the second index counts the rungs (confer top panel of figure 2.15). Reference [3] might be regarded as the starting point of the recent interest in ladder physics. The early calculations on two-leg ladders with $J_{\perp} \gg J_{\parallel}$, usually called the strong-coupling limit, found a finite spin gap. This came as a surprise since the limiting cases of 1D chains and 2D planes are both gapless, yet it is easy to comprehend in the strong-coupling limit. Here the rungs interact only weakly

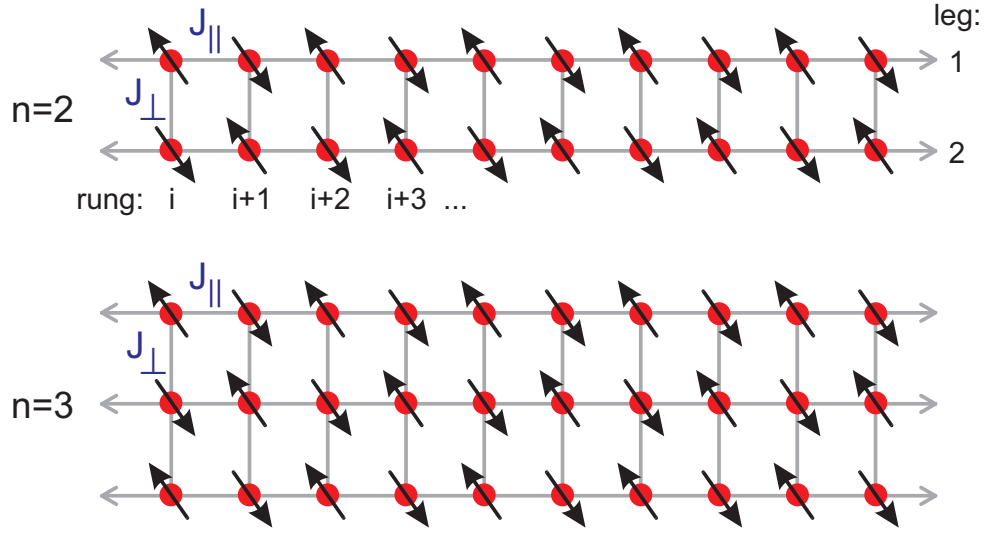


Figure 2.15: Sketch of AF Heisenberg ladders with $n = 2$ and 3 legs. The coupling along the legs is J_{\parallel} , whereas the rung exchange is J_{\perp} . Compared to the former pictures the spin arrows are tilted for readability. But in the Heisenberg model the spin is isotropic anyway, and thus no quantization axis is favored. Moreover, the spin-liquid ground states do not favor any orientation.

with each other and the dominant configuration is a product state of independent singlets on each rung. Thus the total spin is zero and the elementary excitation is the breakup of one singlet to a spin-1 triplet. The ground-state energy of an *isolated* rung singlet is $-3/4 J_{\perp}$, the corresponding value of the triplet state is $+J_{\perp}/4$. Therefore the spin gap, which is the energy needed to excite the first triplet, is simply J_{\perp} . The small coupling along the chains allows for hopping of the triplet along the ladder. As a consequence, dispersion arises and a triplet band is formed with the dispersion relation [115]

$$E(k) = J_{\perp} + J_{\parallel} \cos k + \frac{3 J_{\parallel}^2}{4 J_{\perp}} \quad \text{for } J_{\perp} \gg J_{\parallel} \quad (2.18)$$

and a downsized spin gap of

$$E_{\text{gap}} = J_{\perp} - J_{\parallel} + \frac{3 J_{\parallel}^2}{4 J_{\perp}}. \quad (2.19)$$

This implies that in the strong-coupling limit the gap is primarily a measure of the rung interaction J_{\perp} , whereas the triplet bandwidth $W = 2J_{\parallel}$ is determined by the leg coupling. The question is of course whether the gap survives when the leg coupling gets stronger. In reference [115] evidence was found that indeed there is a nonzero gap in two-leg spin-1/2 ladders for *any* finite rung coupling $J_{\perp} > 0$. A crosscheck indicated that spin-wave theory is less appropriate for ladder systems, since it incorrectly predicts a gapless dispersion for all non-vanishing rung couplings.

The other extreme to treat ladders is the limit with $J_{\perp} \ll J_{\parallel}$. Here the properties are mainly determined by the legs, and one gets a system of weakly interacting Heisenberg chains. In particular, asymptotically free spinons become the elementary excitations again

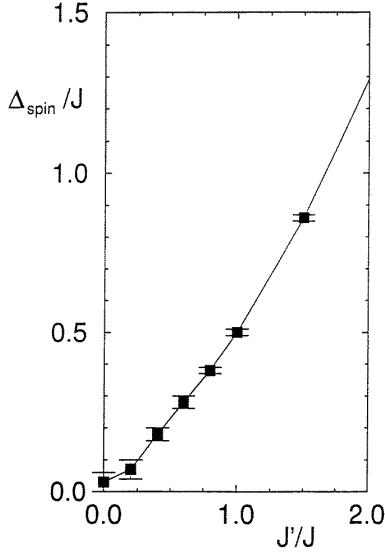


Figure 2.16: Spin-gap energy (here: Δ_{spin}) versus rung coupling ($J' = J_{\perp}$) of $S = 1/2$ two-leg ladders with both axes in units of the leg coupling ($J = J_{\parallel}$). At zero rung coupling ($J'=0$) the chain limit with vanishing gap is approached. For all finite rung couplings there is a spin gap. Numerical data on small clusters was extrapolated to the bulk limit in reference [115]. The figure itself is copied from reference [114], though. Basically the same values were calculated later by Greven et al. using a refined Monte Carlo algorithm [116].

upon vanishing rung coupling. Also in this limit, there is no spin gap and excitations of arbitrarily low energy are possible. However, chains are critical systems. In this situation even small perturbations may qualitatively change the properties of the ground state. Therefore it is not astonishing that a spin gap immediately opens as soon as J_{\perp} becomes nonzero [16]. Numerical results based on Lanczos and Monte-Carlo techniques support this result, and in the isotropic limit of $J_{\parallel} = J_{\perp}$ the gap energy reaches $E_{\text{gap}} \approx 0.5 J_{\perp}$ [115]. The corresponding values of E_{gap} over a wide range of coupling ratios are plotted in figure 2.16. A further confirmation is given in reference [117] and also in reference [118], where DMRG calculations¹⁰ in the isotropic limit provide $E_{\text{gap}} = 0.504 J_{\perp}$. In the ladder compounds discussed in this thesis, one may expect J_{\parallel} and J_{\perp} to be of similar size since the Cu–O bond lengths are comparable (see section 2.4.1).¹¹ Thus it is not sufficient to study weak- and strong-coupling limits alone. Unfortunately, perturbative methods in the isotropic regime of $J_{\parallel} = J_{\perp}$ are quite challenging because there is no small parameter to guide expansions. Nevertheless, since the spin gap is present for all coupling ratios except for $J_{\perp} = 0$, the physics of the two-leg ladder is said to be dominated by the strong-coupling limit with nearly decoupled rungs. Hence calculations are frequently carried out in the strong-coupling limit with the hope that the results won't change qualitatively in the isotropic limit.

2.3.1 Even- and Odd-Leg Ladders

Increasing the number of legs is not just an academic issue, for there actually are materials with more than two legs. For instance the compounds of the homologous series $\text{Sr}_n\text{Cu}_{n+1}\text{O}_{2n+1}$, discovered in 1991 by Hiroi et al. [120], contain ladder structures with $n+1$ legs each [121].¹² Figure 2.17 shows the copper-oxide sheets of SrCu_2O_3 and $\text{Sr}_2\text{Cu}_3\text{O}_5$

¹⁰DMRG is short for **d**ensity **m**atrix **r**enormalization **g**roup, see section 5.3.2.

¹¹Deviations from $J_{\parallel} = J_{\perp}$ may arise because the Madelung potentials of the O ions on the rungs and on the legs are different.

¹²In most cases the notation $\text{Sr}_{m-1}\text{Cu}_{m+1}\text{O}_{2m}$ with $m = 3, 5, 7, \dots$ is used, which yields doubled indices. Accordingly, the number of legs is then equal to $\frac{m+1}{2}$.

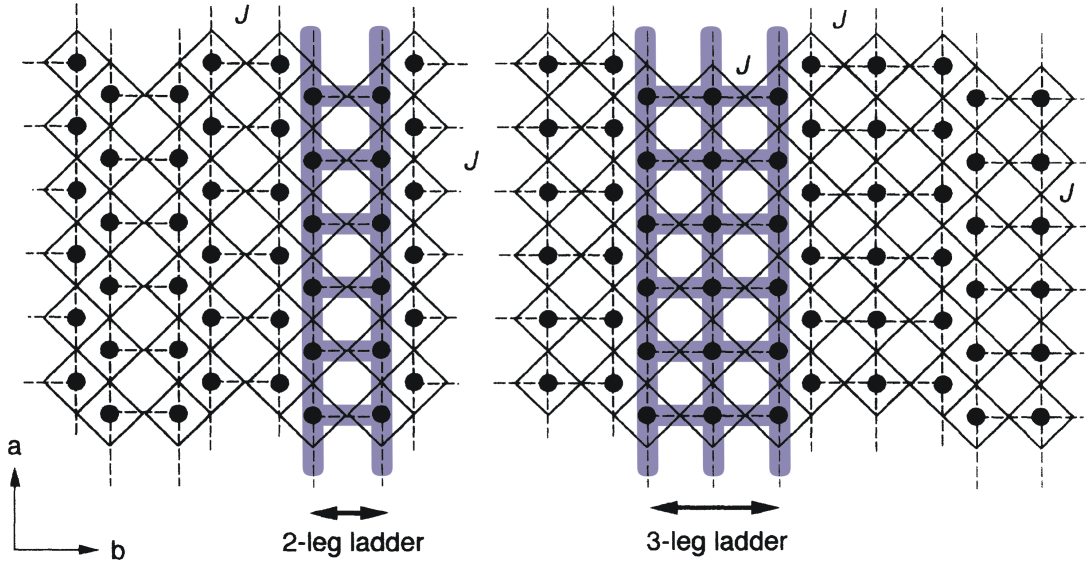


Figure 2.17: Schematic view of the two-leg ladder compound SrCu_2O_3 (**left**) and the three-leg counterpart $\text{Sr}_2\text{Cu}_3\text{O}_5$ (**right**). Black circles represent the copper ions and the oxygen ions are located at the corners of the tilted squares. Within the ladders there is strong AF coupling, whereas between adjacent ladders the coupling J_{trellis} is weakly ferromagnetic and frustrated. The two-leg configuration is usually denoted as a trellis layer. Within the ladders the CuO_4 squares are in corner-sharing arrangement, whereas they share edges in-between adjacent ladders. Reproduced from reference [119].

with two-leg and three-leg ladders, respectively. The two-leg configuration is called a trellis layer. The exchange between adjacent ladders is ferromagnetic and rather weak due to the 90° Cu–O–Cu bonds. Moreover, the triangular arrangement of the Cu ions between the ladders leads to frustration. Therefore the corresponding coupling constant J_{trellis} is usually negligible, and the ladders in the trellis structure can be considered as magnetically decoupled. The difficult synthesis of this series of compounds is only possible at high pressures, though. So far only reasonable samples for $n = 1$ and 2 have been produced but at least “contaminations” of phases with more legs have been reported [120]. More recently, Sekar et al. reported the fabrication of the four-leg ladder compound $\text{La}_2\text{Cu}_2\text{O}_5$ [122] and of the five-leg ladder $\text{La}_8\text{Cu}_7\text{O}_{19}$ [123].

As long as the number of legs stays *even*, the physics of two-leg ladders should qualitatively be preserved. In particular the gap is expected to survive in all even-leg ladders. This behavior can easily be explained in the strong-coupling limit. As before, the decoupled rungs form singlets since the ground state of an even number of $S = 1/2$ spins has zero total spin. The first possible excitation again is to promote a rung singlet to a triplet state. The gap has to decrease with n such that the limit of a gapless 2D plane can be achieved. However, the magnitude will remain nonzero for any finite and even number of legs, which is supported by several calculations [117, 118, 124, 125]. And at least for the case of four-leg ladders the existence of a gap of approximately half the two-leg value is well established.

The situation changes completely when the number of legs becomes *odd*. Then the behavior at low energies rather resembles that of a single chain. Namely there is no spin gap, and the spin-spin correlations decay slowly following a power law. Again the strong-coupling picture is helpful. In this limit it is possible to map the three-leg ladder onto a single chain, since both systems are in the same universality class [126]. Each rung can be diagonalized exactly, which leads to an $S = 1/2$ doublet ground state as well as doublet and quadruplet excited states. Thus the ground state now consists of spin-1/2 states on each rung. A small leg coupling J_{\parallel} will generate an effective interaction J_{eff} between these states. As a consequence the ground-state properties of the three-leg ladder in the strong-coupling limit are essentially equal to a spin-1/2 Heisenberg chain with renormalized exchange J_{eff} . In particular, the spin gap vanishes. This argument can easily be generalized to any odd-leg ladder. Since there is just as well no spin gap in the other limit of decoupled legs with $J_{\perp}/J_{\parallel} = 0$, it is reasonable to expect a vanishing gap at any intermediate coupling ratio. A rigorous proof of this conjecture was presented by Rojo in 1996 [127]. His arguments hold not only for spin-1/2 but for any half-odd-integer spin.

The fundamental difference between even- and odd-leg ladders can also be discussed on the basis of an argument used by Haldane for the 2D square lattice [128]. A topological term governs the long-wavelength ($=$ small k) dynamics of the 2D Heisenberg model. This term is similar to the one that is responsible for the already mentioned difference between integer and half-odd integer spin chains. The former exhibit the Haldane gap, the latter don't. However, when this expression is applied to n -leg ladders, one can find that for odd n the topological term does not vanish. The system becomes effectively one-dimensional and remains gapless. In contrast, the term exactly cancels out in the case of even n . The gap survives and scales as $E_{\text{gap}} \propto e^{-n}$ [129].

Apart from the quest for gaps, there should as well be a distinct difference in the spin-spin correlation functions. White et al. used a DMRG approach and calculated $\langle \mathbf{S}_i \cdot \mathbf{S}_j \rangle$ correlations for $n = 2, 3$ and 4-leg ladders [118]. The corresponding results are presented in figure 2.18. The spin-spin correlations of a two-leg ladder (left panel) decline fast following an exponential decay. In the case of four legs the decay is still exponential but not as fast. The $n = 3$ ladder clearly shows a much slower power-law decay (right panel). Moreover, the behavior resembles the 1D-chain decay quite well. Based on these findings, a RVB picture is developed in reference [118]. Accordingly, even-leg ladders are spin liquids that exhibit a short-range RVB ground state with exponentially decaying correlations and a spin gap. Odd-leg ladders, however, exhibit *long*-range RVB ground states, power-law correlations and no gap. A further study based on the RVB concept is given by Sierra et al. in reference [130]. They find that the RVB description of two-leg ladders even survives upon hole doping up to a certain critical value. Away from the strong-coupling limit, the short-range singlets have to be accompanied by some longer-range singlets to account for correlation lengths of about three lattice spacings [118, 131].

One possible probe for the occurrence of magnetic ordering is muon spin relaxation (μSR). Actually, μSR is the most sensitive technique to investigate the absence of static magnetic order in the ground state of two-leg ladders. Kojima et al. performed measurements on SrCu_2O_3 and $\text{Sr}_2\text{Cu}_3\text{O}_5$ and indeed found no magnetic order in the two-leg system down to 20 mK. Instead, field fluctuations did not vanish, which is in good agreement with the nonmagnetic ground state of a spin liquid [132]. The three-leg ladder

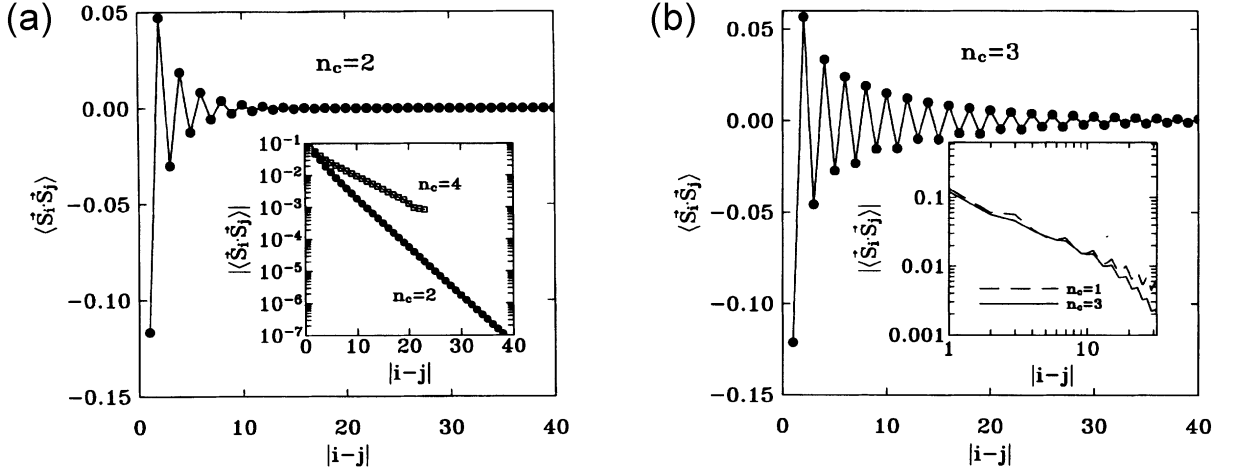


Figure 2.18: Spin-spin correlations $\langle \hat{S}_i \cdot \hat{S}_j \rangle$ versus distance $|i-j|$, with sites i and j located on the top leg. (a) Correlations of the two-leg ladder. The semilog plot in the inset clearly shows the exponential decay for $n = 2$ and 4 legs. (b) Three-leg ladder. Here the log-log inset demonstrates the similar power-law decays of the chain and the three-leg ladder. The deviation from pure power-law behavior at large distances is due to finite-size artefacts. Reprinted from reference [118].

compound, however, does exhibit magnetic ordering below approximately 52 K. Kojima et al. deduced a random freezing of moments rather than true Néel order, which might be the sign of a spin-glass type of ordering [133]. A spin-liquid state can definitely be excluded for this compound on grounds of the data. Similar phenomena were observed in compounds with quasi-1D chains where the small inter-chain interactions give rise to 3D ordering at sufficiently low temperatures.

2.3.2 Interpretation of Susceptibility Data

Whether there is a spin gap or not has to have an effect on the susceptibility, too. Frischmuth et al. performed a Monte Carlo loop algorithm [134] and were able to calculate susceptibilities for ladders of up to six legs (figure 2.19). In the limit of low temperatures the susceptibility χ per rung of odd-leg ladders remains approximately constant as in the single chain. Ladders with an even number of legs show an exponential drop of χ , which indicates a gap in the excitation spectrum. The gap energy decreases substantially with increasing n (see right panel of figure 2.19).

Measurements are available from Azuma et al. [119] as shown in figure 2.20. In the left panel one can easily recognize the signature of a spin gap in SrCu_2O_3 . A small Curie contribution has been subtracted as is common for such measurements. This component might be assigned to a contribution from 0.26% of free Cu^{2+} spins due to imperfections or impurity phases. After subtraction there is a continuous decrease of χ over a wide temperature range. The thin solid line represents a fit to the data using the equation

$$\chi(T) = \frac{\alpha}{\sqrt{T}} e^{-E_{\text{gap}}/T}, \quad (2.20)$$

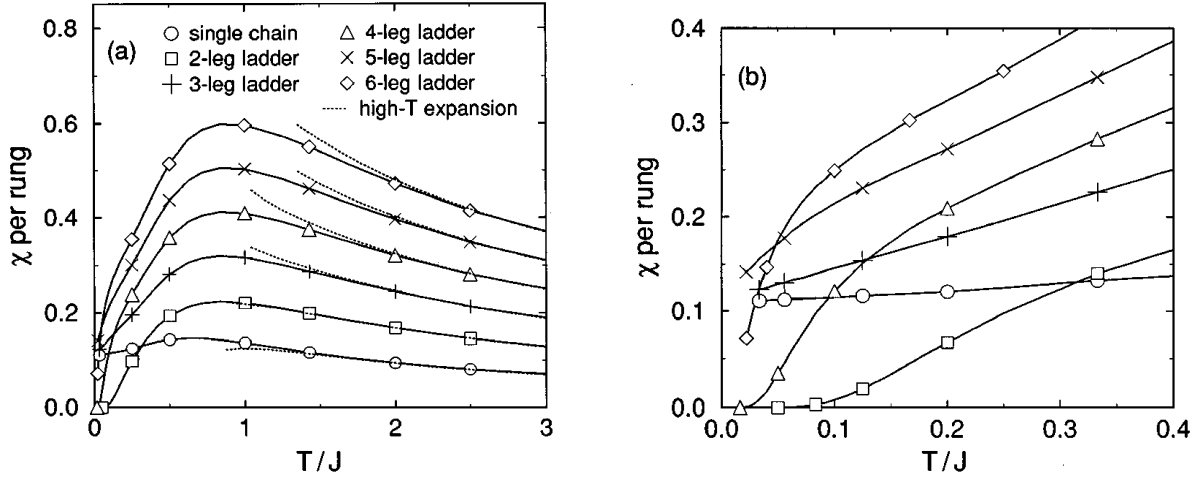


Figure 2.19: Magnetic susceptibility χ per rung as a function of temperature for a single chain and Heisenberg ladders of up to six legs. Frischmuth et al. used a Monte Carlo loop algorithm for the isotropic case of $J_{\parallel} = J_{\perp}$. To distinguish the curves some data points are marked by symbols. In the **right** panel the low-temperature regime is magnified. Here, the different character of odd- and even-leg systems is obvious. The latter exhibit a spin gap whereas odd-leg ladders are gapless. Reproduced from reference [134].

which was calculated by Troyer et al. for the strong-coupling limit [135]. The constant α depends on the dispersion of the first excitation and the fit yielded the gap value of $E_{\text{gap}} = 420$ K. This is in rough agreement with the expectation of $E_{\text{gap}} \approx J_{\perp}/2$ if it is assumed that the coupling is similar in magnitude to its 2D copper-oxide counterpart with $J \approx 1200$ K [114]. However, an investigation by means of nuclear magnetic resonance (NMR) revealed a larger spin gap of 680 K [136]. The right panel of figure 2.20 shows the corresponding susceptibility of $\text{Sr}_2\text{Cu}_3\text{O}_5$. Again, a small Curie contribution has been subtracted. The corrected susceptibility steadily decreases upon reducing the temperature but remains at a large finite value at low temperatures. This is in unambiguous contrast to SrCu_2O_3 and supports the assumption that this three-leg compound indeed exhibits no spin gap.

An extensive analysis of the very susceptibility data of SrCu_2O_3 measured by Azuma et al. [119] was undertaken by Johnston in reference [137]. He challenges the usually assumed isotropic coupling ratio of $J_{\perp} = J_{\parallel}$ and also the magnitude of approximately 1200 K inferred from 2D cuprates. He used calculations from Barnes and Riera [78] and stated that, instead, the experimental data from reference [119] can accurately be fitted with a leg coupling twice as large as the rung coupling ($J_{\parallel}/J_{\perp} \gtrsim 2$). Accordingly, the fit yields a value of $J_{\parallel} \gtrsim 2000$ K, which is considerably larger than in 2D cuprates like La_2CuO_4 .

Susceptibility measurements on 1D cuprate chains like Sr_2CuO_3 and SrCuO_2 [138] support the conjecture that the lower dimensionality promotes a larger coupling. A quite accurate determination of the coupling constant in Sr_2CuO_3 was performed by means of optical spectroscopy. At first, Suzuura et al. measured the infrared absorption [139]. Later, Lorenzana and Eder were able to explain the spectrum by means of phonon-assisted

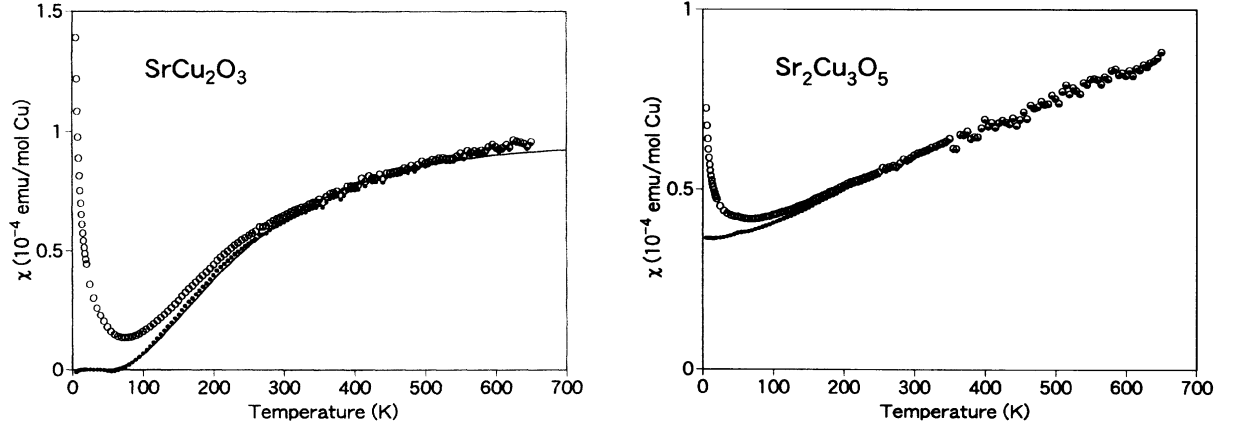


Figure 2.20: Susceptibility χ versus temperature of SrCu_2O_3 (left) and $\text{Sr}_2\text{Cu}_3\text{O}_5$ (right) as measured by Azuma et al. [119]. Open circles represent the raw data, while the data after subtraction of the Curie component is plotted as closed circles. The solid line in the left panel indicates the fit to the data according to equation 2.20 with an assumed spin gap of 420 K for SrCu_2O_3 .

two-spinon absorption [140] (see figure 3.3 on page 59).¹³ The analysis of Sr_2CuO_3 yielded a considerably large value of $J = 2850$ K. The occurrence of large couplings in low dimensions even seems to hold when the different Cu–O bond lengths are taken into account. A theoretical investigation by Mizuno et al. involving Madelung potentials [141] explains this difference by increased hopping elements in 1D and moreover proposes anisotropic couplings in these cuprate ladders. For systems like SrCu_2O_3 and $\text{Sr}_{14}\text{Cu}_{24}\text{O}_{41}$ they predict J_{\parallel} greater than J_{\perp} by approximately 10%. But this small difference is not sufficient to explain the unexpectedly strong anisotropy proposed by Johnston (see also reference [133]).

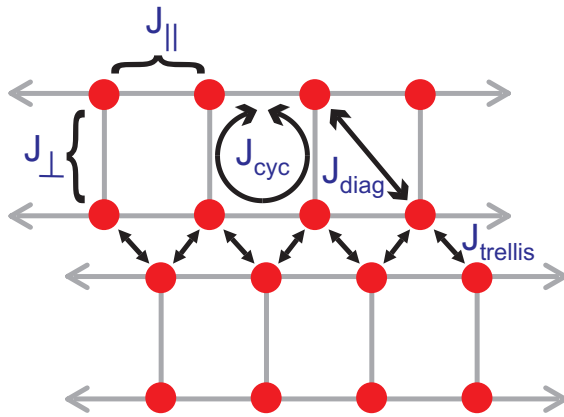


Figure 2.21: Sketch of exchange couplings within two-leg ladder systems. The cyclic exchange J_{cyc} is around basic plaquettes of the ladder. Next-nearest-neighbor spins on adjacent legs are coupled across the diagonal by J_{diag} , and the coupling between neighboring ladders is denoted as J_{trellis} .

¹³The approach of phonon-assisted multimagnon absorption by Lorenzana and Sawatzky [11, 12] is also one of the foundations of this thesis as discussed in section 3.3.

To make the observed data compatible with the rather expected isotropic coupling ratio, Brehmer et al. suggested the inclusion of a four-spin cyclic exchange in 1999 [142] (see also reference [143]). This type of interaction is sketched in figure 2.21. The corresponding four-spin term is known to be relevant for the 2D cuprates. A cyclic coupling emerges as a correction to the Heisenberg Hamiltonian in order t^4/U^3 from a t/U expansion of the one-band Hubbard model [144]. It is expected to be the dominant correction within the more realistic three-band description of the 2D CuO_2 planes since in this case the cyclic permutation of four spins on a plaquette can take place without double occupancy [26, 145]. To illustrate this, one might for instance think of the cyclic permutation of four atoms in solid ^3He [146, 147]. In a naive approach, this process obviously takes less energy than exchanging only *two* neighboring atoms. This is because just in the latter case the surrounding atoms have to be displaced considerably.

High-resolution neutron scattering experiments on the 2D cuprate La_2CuO_4 exhibit a magnon dispersion at the zone boundary that cannot be described within a nearest-neighbor Heisenberg model [148]. It has been argued that the inclusion of a cyclic spin exchange of about 20% would reproduce this dispersion [149]. In the case of two-leg ladders, even a moderate amount of J_{cyc} substantially reduces the spin gap (see section 5.3.2). It always influences the determination of the major two-spin couplings. The value of J_{\parallel}/J_{\perp} deduced e.g. from the susceptibility data is reduced if $J_{cyc} \neq 0$ is considered in the analysis. One may think of J_{cyc} disturbing the singlet states on the rungs, which leads to some sort of frustration. Consequently, the effect of J_{\perp} gets smaller. Thus the value of J_{\perp} has to be scaled up in order to get reasonable fits of χ [150]. Or the other way round, increasing J_{cyc} has a somehow similar effect on a fit of χ as increasing J_{\parallel} .

Mizuno et al. refined their analysis of SrCu_2O_3 mainly based on Madelung potentials [141] by means of exact diagonalization of small clusters. They also included terms with cyclic and diagonal exchange (see figure 2.21) into their Hamiltonian [150, 151]. The outcome was a slightly larger value of $J_{\parallel}/J_{\perp} \approx 1.3$ than before (1.1 in reference [141]) with a nonzero $J_{cyc} \approx 0.1J_{\parallel}$.¹⁴ The effect of J_{diag} accounts for less than one percent and hence is not important. These values are in good agreement with the parameters that we have determined from the optical conductivity of $(\text{La,Ca})_{14}\text{Cu}_{24}\text{O}_{41}$ [26], as presented in chapter 5.3.2.

Matsuda et al. took up this suggestion and fitted their neutron data of the ladder compound $\text{La}_6\text{Ca}_8\text{Cu}_{24}\text{O}_{41}$ both ways [25]. First, they fitted their measured spectra in the same conventional way with $J_{cyc} = 0$ as already done in reference [152] for $\text{Sr}_{14}\text{Cu}_{24}\text{O}_{41}$. In this way they gained several points of the dispersion relation of the lowest-energy excitation. Afterwards, they applied a Lanczos method to fit these points without inclusion of J_{cyc} . This analysis again yielded an anisotropic ratio of $J_{\parallel}/J_{\perp} = 2$. A corresponding analysis including a nonzero cyclic exchange, yet with *fixed* ratio of $J_{\parallel}/J_{\perp} := 1$, also yielded a fit of the dispersion of essentially the same quality as before. The according cyclic exchange constant is $\tilde{J}_{cyc} \approx 0.15J_{\perp} \approx 190$ K with the main two-spin couplings

¹⁴Note that the ratio of $J_{\parallel}/J_{\perp} \approx 1.1$ calculated by Mizuno et al. without J_{cyc} is close to unity [141], but this almost isotropic ratio does *not* yield reasonable fits of the susceptibility data. However, the slightly larger value of 1.3 [150, 151], calculated upon inclusion of a nonzero $J_{cyc} \approx 0.1J_{\parallel}$, indeed does yield excellent fits of $\chi(T)$ [151], and the ratio is still considerably smaller than the value of $J_{\parallel}/J_{\perp} \approx 2$ by Johnston in reference [137].

$$J_{\parallel} = J_{\perp} \approx 1300 \text{ K}.^{15}$$

Many different model Hamiltonians can fit the same experimental $\chi(T)$ data of ladder compounds exhibiting a gap. Apart from the cyclic exchange, also the diagonal coupling J_{diag} and the coupling $J_{trellis}$ between different ladders in the trellis lattice stand to reason (see figure 2.21). Both couplings are expected to be weak and ferromagnetic. However, the susceptibility calculated by Johnston et al. [133] is quite insensitive to both parameters and an inclusion is not needed to get persuasive fits to the measured $\chi(T)$ of SrCu_2O_3 from Azuma et al. [119, 133]. Another exchange path is between one ladder and the other two ladders located directly above and below. This stacked configuration leads to a J_{stack} and in contrast to the former two couplings, the fits of Johnston et al. are quite sensitive to the value of J_{stack} . Yet only small contributions of approximately $0.01J_{\parallel}$ can fit the data, and thus J_{stack} may as well be neglected.

The cyclic exchange survives as the most important candidate to improve the modelling of spin ladders. Optical spectroscopy offers a quite powerful tool to contribute to the quest for the proper set of couplings. Our results deduced from measurements on undoped telephone-number compounds in comparison with calculations will be presented in section 5.3. By including a cyclic exchange into the analysis, we find $J_{\parallel}/J_{\perp} \approx 1.25 - 1.35$, $J_{\perp} \approx 1370 - 1580 \text{ K}$, and $J_{cyc}/J_{\perp} = 0.20 - 0.27$ [26].

2.3.3 Elementary Excitations: Triplets vs. Spinons

To get a better idea of the elementary excitation of the two-leg ladder, again it is helpful to have a look at the two limits, which has already been broached above. In the strong-coupling limit, as depicted in the top panel of figure 2.22, the ladder exhibits a spin-liquid ground state of independent singlets. In this RVB state the first possible excitation is the breakup of a single rung singlet at the expense of $E_{gap} = J_{\perp}$. This type of isolated triplet excitation has no dispersion but a finite value of J_{\parallel} will allow for hopping to other rungs. The excitation gets spread out and becomes a so-called dressed triplet. The dispersion gets finite, and the gap decreases. In the other limit of uncoupled chains (bottom panel of figure 2.22) there is no gap, and the spinons are asymptotically free. Yet as soon as a rung coupling is switched on, the spinons get bound. The reason might be illustrated as follows: The further away the spinons are from each other, the more rungs in-between are occupied by parallel spins (bottom panel of figure 2.22). This arrangement is unfavorable and potential energy increases with the distance between the spinons. Since the realistic coupling regime is located somewhere between these two extremes, it is not clear right from the start which concept is suited better. Either dressed triplets or two bound spinons are reasonable entry points, and as usual the truth might be somewhere in-between. From now on, mostly the term triplet will be used. Sometimes the elementary excitation is also labelled as magnon in the literature.

The dispersion relation in the strong-coupling limit [115, 126],

$$E(k) \approx J_{\perp} + J_{\parallel} \cos k \quad \text{for } J_{\perp} \gg J_{\parallel}, \quad (2.21)$$

¹⁵There are several ways of defining the actual cyclic-exchange term. To compare values of J_{cyc} from different groups, it is important to pay attention to scaling factors. For instance values of Matsuda et al. in reference [25] have to be multiplied by a factor of two, i.e. $J_{cyc} = 2\tilde{J}_{cyc} \approx 0.30J_{\perp}$, before comparing with the results of Nunner et al. [26] (see chapter 5.3.2).

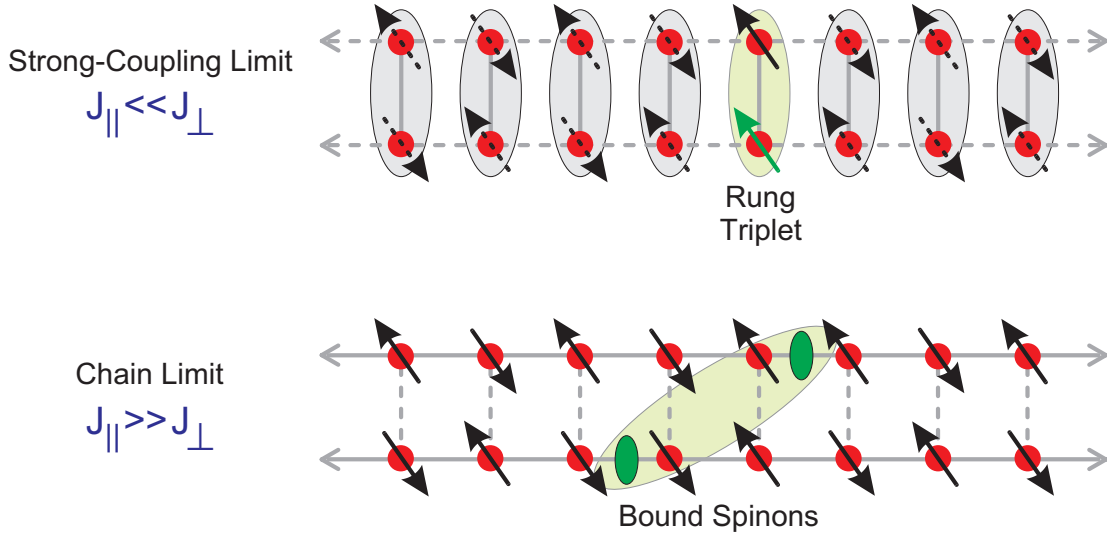


Figure 2.22: Illustration of the elementary excitation of a two-leg ladder. The **top** panel demonstrates the strong coupling or dimer limit, which yields an RVB ground state. The spins within each rung singlet are dashed. When a single rung singlet gets promoted to a triplet, it can hop to neighboring rungs due to the small J_{\parallel} . In the chain limit of the **bottom** panel, though, we are back to the spinon picture. Each of the two spinons (or domain walls) is indicated by a blotch. As soon as a small interchain or rung coupling is introduced, the spinons get bound together. The above illustration offers an intuitive explanation: The larger the distance between the spinons the more parallel spins are created on the rungs in-between. Similar but less intuitive arguments can be found within the RVB picture. After all, the elementary excitation of a ladder can be visualized either as a dressed triplet or as two bound spinons.

has already been given in equation 2.18. The minimum of the triplet band is hence located at $k = \pi$. This just means that the gap energy is to be found at the boundary of the Brillouin zone. Using quantum Monte Carlo simulations, Barnes and Riera presented dispersion relations for several coupling ratios already in 1994 [78]. Johnston et al. reproduced their calculations on slightly larger clusters [133], and figure 2.23 shows the corresponding data. Also included in the plot are the strong-coupling result from Barnes et al. [78] as well as the lower boundary of the spinon continuum of the isolated chain for comparison. For all the ladder couplings the band minimum is located at $k = \pi$, and also the maximum survives at $k \approx \pi/2$ at least up to isotropic coupling. It is quite remarkable that the ratio of maximum and minimum energy E_{max}/E_{gap} of the triplet band is strongly related to the coupling ratio J_{\perp}/J_{\parallel} . This function, which is shown in figure 2.24, enables estimates of coupling ratios for instance from neutron scattering data. A similar analysis was used by Eccleston et al. to deduce a value of $J_{\perp}/J_{\parallel} = 0.55$ from neutron data of $\text{Sr}_{14}\text{Cu}_{24}\text{O}_{41}$ [152]. However, there is no cyclic exchange included here, and a nonzero J_{cyc} would yield different dispersions and hence different sets of coupling constants. Experimentally, E_{gap} can be determined rather accurately with neutron scattering, but in the cuprate ladders E_{max} is of the order of 200 meV and therefore difficult to measure even with spallation sources.

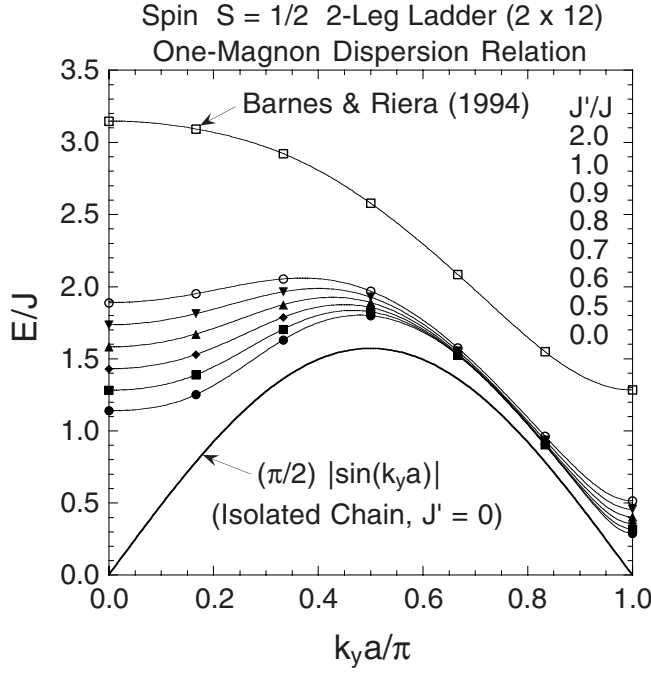


Figure 2.23: One-triplet dispersion relations for different values of J_{\perp}/J_{\parallel} , calculated by exact diagonalization using the Lanczos algorithm. Here again the notation $J = J_{\parallel}$ and $J' = J_{\perp}$ was chosen and the wave vector k_y is parallel to the legs. The data for $J_{\perp}/J_{\parallel} = 2$ was calculated using the same algorithm as by Barnes and Riera [78]. The lower boundary of the spinon continuum of the isolated chain ($J_{\perp} = 0$) is shown for comparison. Solid curves are fits to the data points. Reproduced from reference [133].

The triplet branch is not the only feature of the excitation spectrum. There is also a continuum of excitations at higher energies. Since the nature of the elementary excitations is not unambiguous, the continuum can be interpreted either as stemming from two or more triplets or stemming from four or more spinons. The corresponding intensity at high energies is not to be neglected in the discussion of e.g. neutron data. Since counts are low at the upper band edge of the triplet dispersion, which is close to or within the continuum, the deduction of coupling ratios as described above might be misleading. But there is even more. As in the alternating chain, an attractive potential exists in two-leg ladders between the elementary excitations that leads to bound states. Usually such bound states yield distinct features in different kinds of spectra. However, the dispersion of bound states and the continuum as well as their implications for infrared spectra is

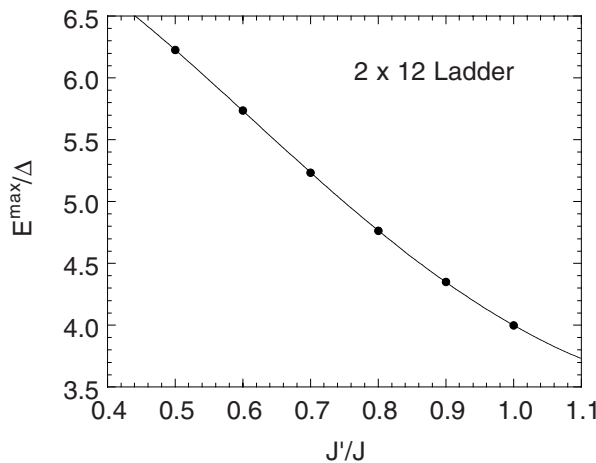


Figure 2.24: Ratio of the maximum to the minimum one-triplet energy E_{max}/E_{gap} versus coupling ratio J_{\perp}/J_{\parallel} . Reproduced from reference [133].

left for detailed discussion in chapter 5. Afterwards chapter 6 deals with the effect of charge-carrier doping on spin ladders.

2.4 Telephone-Number Compounds

In the early days of ladder research, $(\text{VO})_2\text{P}_2\text{O}_7$ was one of the best candidates for an actual ladder compound. However, VOPO was proven to be a Heisenberg chain instead [74] as stated above. The series of $\text{Sr}_n\text{Cu}_{n+1}\text{O}_{2n+1}$ in fact does supply spin ladders, even with more than two legs. The growth of these compounds is quite challenging, though, since high pressure is necessary. In addition, hole doping has not been achieved so far, and hence no superconductivity could be found. In this thesis measurements of the so-called telephone-number compounds are presented. The series $(\text{Sr},\text{La},\text{Ca})_{14}\text{Cu}_{24}\text{O}_{41}$ provides excellent samples of two-leg ladders in a trellis configuration of spin-1/2 copper ions. One of the major advantages of the telephone-number compounds is that they can be grown under ambient pressure. Moreover, the use of the travelling-solvent-floating-zone (TSFZ) method in image furnaces provided large rods of single crystals [6–8], even large enough for neutron measurements. The crystals are black and typically insulating with semiconducting temperature dependence of the dc resistivity. With increasing Ca content an insulator-to-metal transition occurs [153]. The overall amount of charge carriers can be adjusted by doping, although it is not straightforward to judge where exactly the holes are located within the structure. The predicted superconductivity was in fact verified in Ca doped systems under high pressure [5, 154].

2.4.1 Crystal Structure of $(\text{Sr},\text{La},\text{Ca})_{14}\text{Cu}_{24}\text{O}_{41}$

The initial synthesis was reported by McCarron et al. in 1988 [155]. At first, needles of $\text{Sr}_{14-x}\text{Ca}_x\text{Cu}_{24}\text{O}_{41}$ were unintentionally produced as some sort of contamination of the actually wanted high- T_c cuprates. Yet x-ray measurements on these needles yielded two incommensurate sublattices, which penetrate each other. Compounds of this kind are referred to as composite crystals. This configuration aroused the authors' curiosity and prompted them to eliminate the superconducting phase instead. Two weeks later, Siegrist et al. submitted their report on a different range of substitutions including lanthanum and yttrium [156]. In all cases the telephone-number compounds contain stacked layers of two-leg Cu_2O_3 ladders as well as 1D CuO_2 chains, which both run along the crystallographic c axis. In both layers, each copper ion is centered within four oxygen ions. These CuO_4 plaquettes are oriented in different manners, though, as described below. Between these alternating layers there always is a sheet of Sr, La or Ca. Figure 2.25 shows the corresponding 3D plot of the entire structure, which illustrates the overall layered configuration. But the chain and the ladder layers do not belong to the same structural unit since the orthorhombic sublattices are incommensurate along the c axis. The lattice parameters of these structures are equal along a and b axis, respectively, and they read $a \approx 11.3 \text{ \AA}$ and $b \approx 12.6 \text{ \AA}$. Along the c direction, the chain system exhibits a smaller unit cell with $c_{\text{chain}} \approx 2.75 \text{ \AA}$, whereas the ladder value is $c_{\text{ladder}} \approx 3.9 \text{ \AA}$ [8]. This means that $7c_{\text{ladder}} \approx 10c_{\text{chain}}$ as demonstrated in figure 2.26. Since the intermediate layers of $(\text{Sr},\text{La},\text{Ca})$ belong to the ladder sublattice, it makes sense to rewrite the struc-

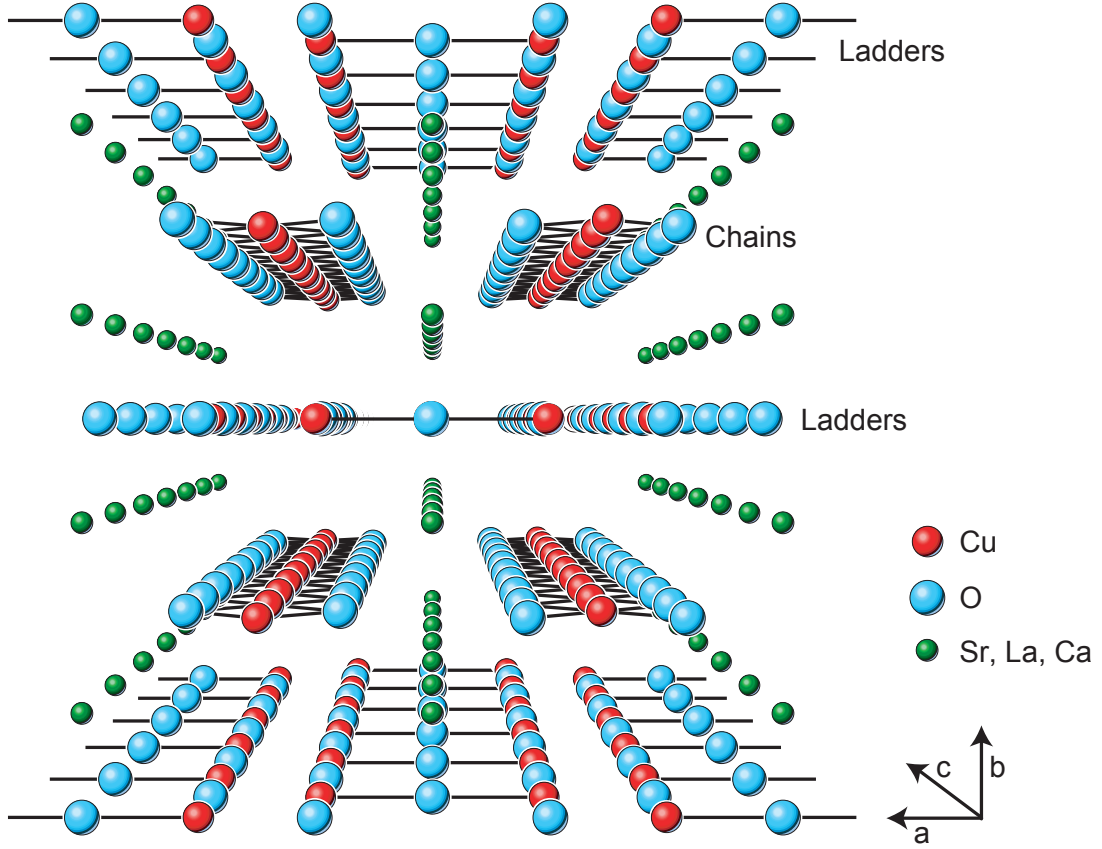


Figure 2.25: 3D visualization of the crystal structure of $(\text{Sr,La,Ca})_{14}\text{Cu}_{24}\text{O}_{41}$ [158]. The two-leg ladders and the 1D chains are both oriented parallel to the c axis, yet located in different layers. These layers are stacked along the b axis and separated by sheets consisting of Sr, Ca, or La. Different ions within this third type of layers are statistically distributed among the sites.

ture as $[(\text{Sr,Ca,La})_2\text{Cu}_2\text{O}_3]_7 (\text{CuO}_2)_{10}$. But this large unit cell is just an approximation because there still is a slight mismatch between the two sublattices. The superconducting compound $\text{Sr}_{0.4}\text{Ca}_{13.6}\text{Cu}_{24}\text{O}_{41+\delta}$ for instance exhibits a mismatch of approximately 0.18% [157].

Within the Cu_2O_3 layers, adjacent ladders are close to each other, but magnetically the ladders are effectively decoupled just as in $\text{Sr}_n\text{Cu}_{n+1}\text{O}_{2n+1}$ (see discussion in section 2.3.2). Along the zigzag boundary between neighboring ladders, the CuO_4 plaquettes share edges as already shown in figure 2.17. Within the ladders themselves, the CuO_4 plaquettes are corner-sharing, and thus the copper ions are coupled via 180° Cu–O–Cu bonds. According to the Goodenough-Kanamori-Anderson (GKA) rules [33], this configuration produces strong AF couplings along the legs and along the rungs. The CuO_2 chains in the other sublattice consist of edge-sharing CuO_4 plaquettes, and the 90° Cu–O–Cu bonds produce weak ferromagnetic couplings within the chains. Carter et al. fitted the susceptibility of $\text{La}_4\text{Sr}_2\text{Ca}_8\text{Cu}_{24}\text{O}_{41}$ and indeed found a ferromagnetic chain coupling of $J_{\text{chain}} = -20$ K [159]. However, the sign of the coupling is not that clear just from the configuration since, for instance, CuGeO_3 contains the same type of 1D

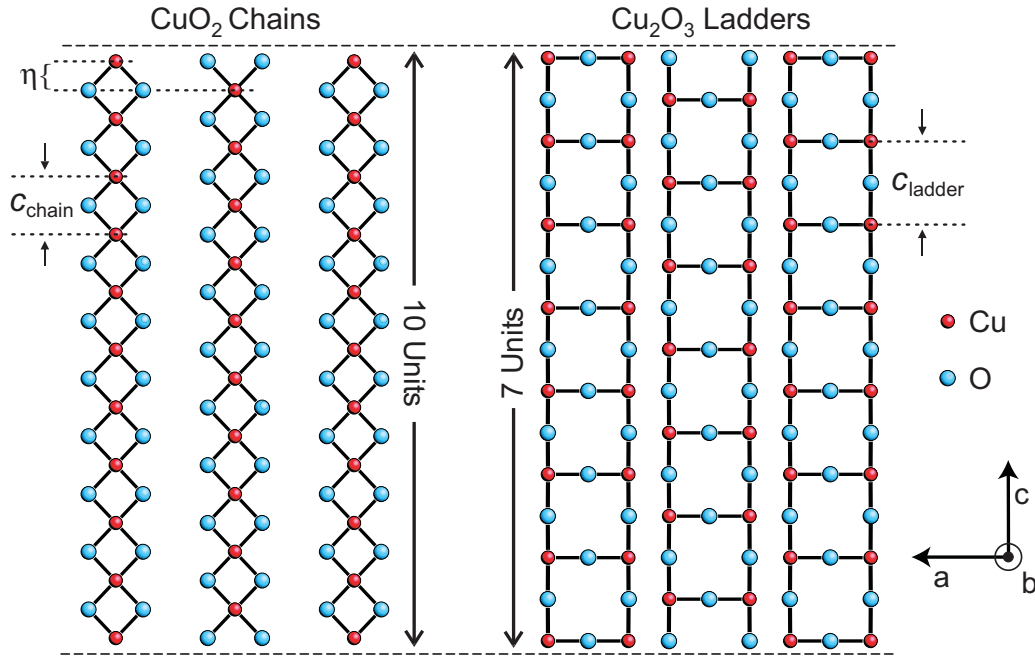


Figure 2.26: CuO₂ chains and Cu₂O₃ ladders in the ac planes of (Sr,La,Ca)₁₄Cu₂₄O₄₁ [158] are incommensurate. 10 chain units in the **left** panel approximately sum up to 7 ladder units in the **right** panel, i.e. $10c_{\text{chain}} \approx 7c_{\text{ladder}}$. For Ca content $x \geq 5$, the standard displacement between neighboring chains is $\eta = c_{\text{chain}}/2$.

chains and exhibits AF coupling instead.¹⁶ Telephone-number compounds with a smaller La concentration show AF exchange in the chains, yet in company with hole doping, Zhang-Rice singlets, and charge ordering in the chain subsystem. More detail is given later on.

A quite precise crystal-structure analysis of a strongly Ca-doped system was performed by Ohta et al. by means of neutron and x-ray measurements [162]. The studied compound Sr_{0.4}Ca_{13.6}Cu₂₄O₄₁ is of special interest because superconductivity was first reported for this member of the series. The most remarkable unveiled feature is an interplay between the two subsystems, which modulates the structure incommensurably. Some of the copper ions on the ladders are coordinated to neighboring oxygen ions of the chain system, forming tetragonal CuO₅ pyramids. This new “apical” oxygen leads to reduced equatorial bonds compared to the other ladder bonds. The left panel of figure 2.27 shows a ladder layer of the ac plane. Also included are those oxygen ions from the chain subsystem which act as apical ones. They are plotted as large shaded circles. The right panel contains a corresponding view of the bc plane. Here the dashed lines indicate the long bonds between the two subsystems. It is also shown that the deflection of the oxygen ions in the chains due to this interplay is larger than the structural effect on the ladders. This difference might be owing to the fact that the chains are isolated from each other, whereas the zigzag

¹⁶Magnitude and sign of the 90° exchange are quite sensitive to small deviations from 90° [160] because then the two involved oxygen-2p orbitals are not orthogonal anymore. In CuGeO₃ the angle is $\approx 98^\circ$ [90] and also neighboring Ge ions have a significant influence [161]. These so-called side groups allow “detours” for the holes, and both effects finally lead to AF instead of ferromagnetic exchange.

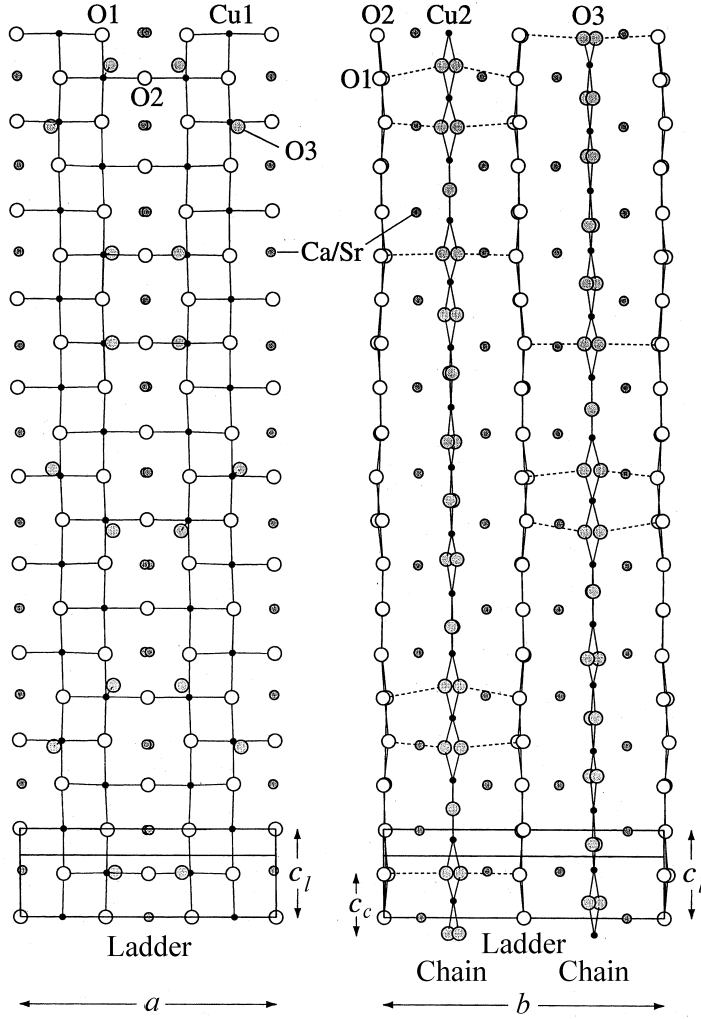


Figure 2.27: Modulated structure of $\text{Sr}_{0.4}\text{Ca}_{13.6}\text{Cu}_{24}\text{O}_{41}$. The **left** panel shows the projection of the ladder layer within the ac plane. Black dots denote the copper ions, small shaded circles stand for Ca or Sr, and large open circles are the oxygen ions of the ladders. The large shaded circles represent those oxygen ions from the chain subsystem that lead to the formation of tetragonal CuO_5 pyramids. One part of these ions belongs to the neighboring chain layer from above, the other part is from the chain layer below. The **right** panel provides a projection of the bc plane. Black solid lines are the short bonds within the ladders and chains, whereas the dashed bonds run between these two subsystems. The Cu ions of the ladders are entirely hidden by the oxygen ions. Based on reference [162].

geometry of the ladders is rather rigid [162]. Nevertheless this modulation may have a drastic effect on the magnetic excitation spectrum [163], as discussed in chapter 6.

The overall modulation of distances in this Ca-rich phase is more pronounced than in the Sr-rich phase [162]. Moreover, when the Ca doping x in $\text{Sr}_{14-x}\text{Ca}_x\text{Cu}_{24}\text{O}_{41}$ is less than five, new superstructure reflections occur, which can be attributed to a slight shift of the chains against each other [8, 164]. This means that the displacement η between neighboring chains deviates from the value $c_{\text{chain}}/2$ (see figure 2.26). Another effect stems from the smaller size of the Ca ions compared to Sr. The unit-cell volume decreases by 9.5% upon increasing the Ca content from $x = 0$ up to $x = 12$ [6, 8]. The corresponding reduction of the lattice parameters is moderate along the a and c direction with no more than 2%. However, the b axis is considerably compressed by 6.6%, which meets expectations because of the stacked structure along the b direction. This explains the stronger modulation in the Ca-rich phase. It is also the reason why the single crystals of the Ca series, and of the $x = 0$ compound as well, cleave easily perpendicular to the b axis. Another comprehensive x-ray analysis of $\text{Sr}_{13.44}\text{Bi}_{0.56}\text{Cu}_{24}\text{O}_{41}$ was presented by Frost-Jensen et al. [165].

2.4.2 Charge Carriers

The approach of parts of the oxygen ions from the chains to the ladders supports the idea that holes move from the charge reservoir of the chains to the conductive ladders with increasing Ca content (see also the corresponding calculations by Mizuno et al. in reference [166]). This is supported by the slight shrinking of the bond lengths within the ladder when pyramids are formed with apical oxygens from the chains. Such reduction of Cu–O bond lengths is a general feature of increased hole concentration [162]. A similar change of bond lengths was observed in $\text{YBa}_2\text{Cu}_3\text{O}_{6+z}$ ($0 \leq z \leq 1$), where apical oxygen ions move towards Cu ions on the CuO_2 sheet with increasing oxygen content [167].

Although the dc resistivity of $\text{Sr}_{14}\text{Cu}_{24}\text{O}_{41}$ is semiconducting up to room temperature [153], the average formal oxidation state of the copper ions is +2.25. This compound is therefore “self-doped” with holes, and there is a total of six holes per formula unit, equivalent to six holes per 24 copper ions. However, the holes are assumed to reside mainly within the chains [9, 159]. Bond-valence-sum calculations by Kato et al. also propose such an unequal hole distribution [153]. Substituting Ca^{2+} for Sr^{2+} does not change the average formal valence at all, yet the resistivity decreases accompanied by a gradual disappearance of semiconducting behavior [153]. Osafune et al. observed a transfer of spectral weight from the high- to the low-energy region in the optical conductivity upon Ca substitution [168]. Based on this result they as well suggest a redistribution of charges from the chains to the ladders with increasing Ca content. More details on this study is given below. At room temperature Nücker et al. measured polarized x-ray absorption spectra and estimated approximately 5.2 holes in the chains and accordingly 0.8 holes in the ladders per formula unit [9], as noted already in section 2.2.3. In figure 2.28 the numbers of holes per subcell are plotted for $\text{Sr}_{14-x}\text{Ca}_x\text{Cu}_{24}\text{O}_{41}$ versus the Ca content x . It can be seen that the actual redistribution of holes is rather small since for $x = 12$ there are still no more than 1.1 holes in the ladders. The polarized x-ray absorption yields one of the most direct views on the hole distribution between ladders and chains. Unfortunately, so far no data is available for low temperatures.

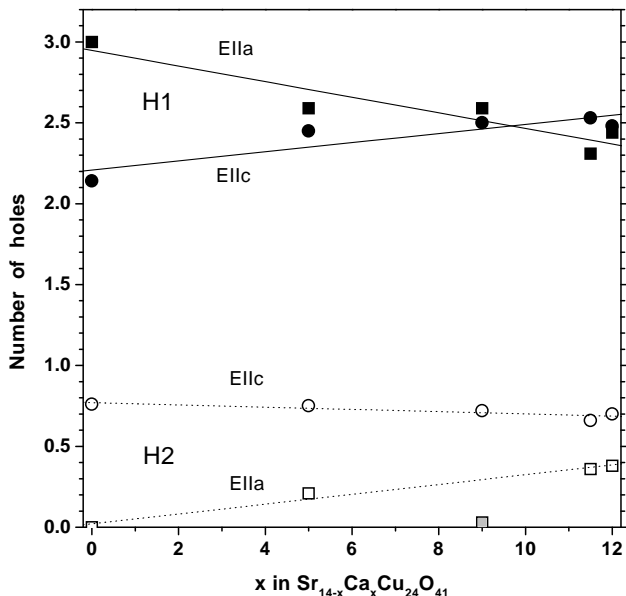


Figure 2.28: Hole count per formula unit for $\text{Sr}_{14-x}\text{Ca}_x\text{Cu}_{24}\text{O}_{41}$ derived from polarized x-ray absorption [9]. Contributions labelled as H1 represent doped holes in the chains, whereas H2 can be attributed to the ladders. The complete number of holes for each subcell is the sum of the contributions of both polarizations. Thus for $x = 0$ there are 5.2 holes in the chains and 0.8 holes in the ladders.

Each hole located in the chains is expected to create a non-magnetic Zhang-Rice singlet [109]. Since $\text{Sr}_{14}\text{Cu}_{24}\text{O}_{41}$ is insulating, the charge carriers are not only confined to the chains but presumably they are also localized and thus do not contribute to the dc conductivity. But as soon as the holes get released into the ladders by Ca doping, they are assumed to become more mobile. Hence the ladders are expected to provide the charge transport. The decreased mobility in the chains can be visualized by mainly two effects. First, in the pure 1D case already a single impurity renders the chain insulating. In addition, the exchange constants are smaller in the chains, which implies that the hopping matrix elements are substantially larger in the ladders.

Carter et al. found a crossover to more insulating behavior in the dc resistivity of $\text{Sr}_{14}\text{Cu}_{24}\text{O}_{41}$ below $T \approx 250$ K and interpreted this as an onset of charge ordering [159]. The charge-ordering temperature T_{CO} , as well as the overall resistivity, decrease with increasing Ca doping. The occurrence of charge ordering was also reported by other groups using neutron diffraction [113, 169], x-ray scattering [170], and thermal expansion [171]. Further support was presented by Kataev et al. who studied single crystals with Ca contents from $x = 0$ to 12 by means of electron spin resonance (ESR) [10]. They found the onset of charge order in the chains at $T_{\text{CO}} = 200$ K for $x = 0$, 170 K ($x = 2$), and 80 K ($x = 5$). There was no signature of charge ordering anymore for larger Ca contents. A recent x-ray diffraction measurement by Fukuda et al. provided clear evidence that the charge order in the chains of $\text{Sr}_{14}\text{Cu}_{24}\text{O}_{41}$ exhibits a periodicity of five chain units [172] (see also figures 2.30 and 6.2). The effect of charge ordering on the magnetic excitation spectrum is discussed in section 6.1.

Another important dopant is La^{3+} , which indeed does change the average valence of the copper ions. The series $\text{La}_y\text{Ca}_{14-y}\text{Cu}_{24}\text{O}_{41}$, for instance, supplies an excellent possibility to study the effect of charge carriers. A La content of $y = 6$ would yield a system without any holes at all.¹⁷ Unfortunately, it seems that single-phase crystals of this very interesting compound have not been synthesized so far, although several publications claim this very composition. Ammerahl et al. were able to grow high-quality crystals with $y = 5$ [7] and $y = 5.2$ [173], but it was not possible for them to obtain single-phase crystals with $y > 5.6$. Hence they speculate that the real solubility limit of La is somewhere between $y \approx 5.6$ and 6 [7]. The lattice parameters slightly increase by no more than roughly 1% with increasing the La content from $y = 2$ to 5.6. Yet there is another distinct feature in the x-ray patterns. Above the La concentration of $y \approx 5$ the sharp reflections from the chain subcell vanish. Instead new superstructure reflections occur, which are diffuse with streaks along the a direction. This gives strong evidence for one-dimensional disorder in the chain subcell. All the chains get slightly displaced along the c axis, each chain with a different magnitude. Yet to explain the superstructure, neighboring chains probably are, on average, displaced similarly [8].

2.4.3 Spin Gaps

An NMR study of polycrystalline $\text{Sr}_{14-x}\text{Ca}_x\text{Cu}_{24}\text{O}_{41}$ by Kumagai et al. claimed that the spin gap of the ladder system gets smaller with increasing Ca content x and finally disappears around $x = 13$ [174]. The reduction of the spin gap is not directly related to

¹⁷Of course this is only true when there are indeed 41 oxygen ions per formula unit. What is more, the formula $\text{X}_{14}\text{Cu}_{24}\text{O}_{41}$ does not represent the *true* stoichiometry of the incommensurate compounds.

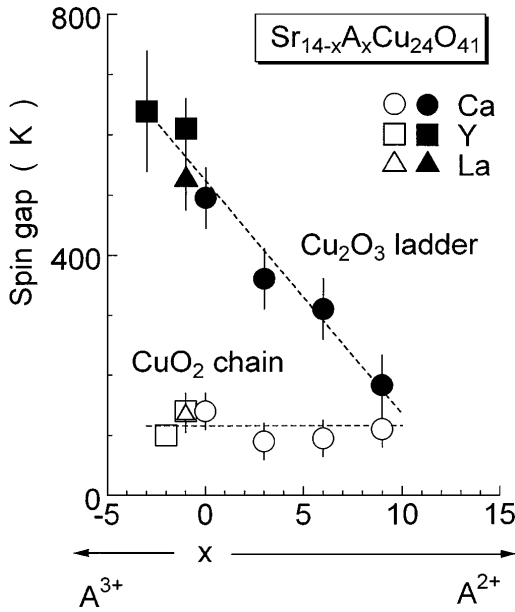


Figure 2.29: Dependence of the spin gaps of chains and ladders on doping in $\text{Sr}_{14-x}\text{A}_x\text{Cu}_{24}\text{O}_{41}$ as deduced from NMR. Black symbols represent the ladder values, whereas open symbols stand for the chain gaps. Reproduced from reference [174].

the geometrical changes since this would produce the opposite effect. The reason is that mainly the Cu–O bonds along the c axis get distorted after the formation of pyramids [162]. The bond angle thus deviates slightly from 180° , which should considerably reduce the leg coupling J_{\parallel} . Yet an increased ratio of J_{\perp}/J_{\parallel} would lead to a *larger* gap (see figure 2.16). The instead deduced reduction is hence not attributed to structural changes with growing Ca content, but Kumagai et al. claim that it is rather due to the actual hole doping into the ladders. The spin gap of $\text{Sr}_{14}\text{Cu}_{24}\text{O}_{41}$ measured by NMR has the value of 470 K [174], which is considerably higher than e.g. the value of 380 K by Eccleston et al. measured via neutron scattering [152]. The determination of the spin gap is more direct by means of neutron scattering. This method e.g. allows to measure the gap at low temperatures, whereas in NMR the gap is deduced from the temperature dependence of the nuclear spin relaxation rate or the Knight shift measured over a large temperature range. But for instance the hole distribution between chains and ladders might be temperature dependent and thus also the gap energy. Opposite to the effect of Ca substitution, the spin gap increases with La^{3+} and Y^{3+} substitutions for Sr^{2+} . This makes sense since the trivalent substitution reduces the hole concentration of the whole system.

Due to the large spin gap, the ladders are magnetically inert below room temperature, and the magnetism is basically dominated by the chains. Yet with NMR Kumagai et al. also found a spin gap of 140 K for the chains [174], which is in agreement with the susceptibility results of Carter et al. [159]. Eccleston et al. as well detected magnetic excitations at the slightly lower energy of approximately 120 K, again by means of inelastic neutron scattering [175]. These authors assigned this feature to a spin gap of the chains, too. The complete dependence of the gaps upon substitution measured via NMR is shown in figure 2.29. The chain gap is almost unaffected, whereas the ladder gap strongly depends on the effective doping of the ladder. Similar results were reported by Magishi et al., who performed NMR measurements on single crystals of $\text{Sr}_{14-x}\text{Ca}_x\text{Cu}_{24}\text{O}_{41}$ [176]. They as well find a reduction of the ladder gap upon Ca substitution, yet with the difference of a flattened decrease at high Ca levels. The gap also persists up to $x = 11.5$, for

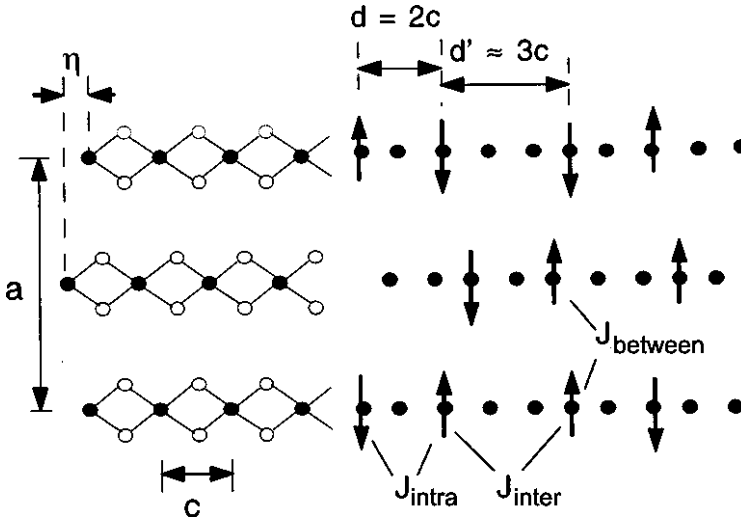


Figure 2.30: Schematic representation of a chain array in $\text{Sr}_{14}\text{Cu}_{24}\text{O}_{41}$. η is the relative displacement between neighboring chains. The black dots without spin in the right panel represent nonmagnetic Zhang-Rice singlets. The dimer size d is two chain lattice spacings, while the interdimer distance d' is three spacings. Reproduced from reference [113].

which superconductivity was reported (see below). On the other hand, Mayaffre et al. argued that for $x = 12$ the spin gap collapses under high pressure of 3.1 GPa, where superconductivity sets in at 5 K [177]. High-pressure NMR measurements by Mito et al. found a robust spin gap up to 1.7 GPa for the same Ca content, though [178]. Inelastic neutron scattering yields a different scenario. Katano et al. found *no* dependence of the ladder spin gap between Ca contents of $x = 0$ and 11.5 [179]. But they do find that the gap energy decreases with temperature.

A gap in 1D chains that are expected to exhibit weak ferromagnetic coupling seems surprising. But this gap might be interpreted on the assumption that dimers are formed as soon as a sufficient amount of holes is present. In this case the holes lead to a non-magnetic ground state of the chains, and E_{gap} is the energy to break up a single spin dimer, i.e. to excite one local singlet to a triplet. After all, the ferromagnetic exchange found by Carter et al. [159] was measured on La-substituted compounds with just a few holes. In the (Sr,Ca) series, though, the Zhang-Rice singlets due to the holes render about half of the copper sites non-magnetic in the chains.

A possible resulting configuration with AF couplings and localized holes has already been illustrated in figure 2.14 on page 24. In this scenario the dimers are formed by next-nearest-neighbor spins, which are separated by a localized Zhang-Rice singlet, and neighboring dimers are separated by two Zhang-Rice singlets. The exchange between next-nearest neighbors proceeds via non-orthogonal orbitals and is antiferromagnetic, which explains the formation of singlets. The coupling is of course smaller than for a 180° Cu–O–Cu bond, which is the reason why the gap in the chains is smaller than in the ladders. Experimentally, the value for $\text{Sr}_{14}\text{Cu}_{24}\text{O}_{41}$ was determined to be $J_{\text{intra}} \approx 120$ K [113] or ≈ 130 K [169]. It is not settled so far whether the *interdimer* coupling J_{inter} is AF or ferromagnetic. Regnault et al. for instance claim a ferromagnetic J_{inter} of approximately -13 K [113] as sketched in figure 2.30. Matsuda et al. state an AF J_{inter} of $\approx +9$ K [169]. However, both neutron studies yielded in addition a considerable AF exchange *between* neighboring chains of $J_{\text{between}} \approx 20$ K (Regnault) as well as ≈ 9 K (Matsuda). This interchain coupling explains the appearance of long-range magnetic order below $T_N = 2.5$ K for $x = 12$ [10].

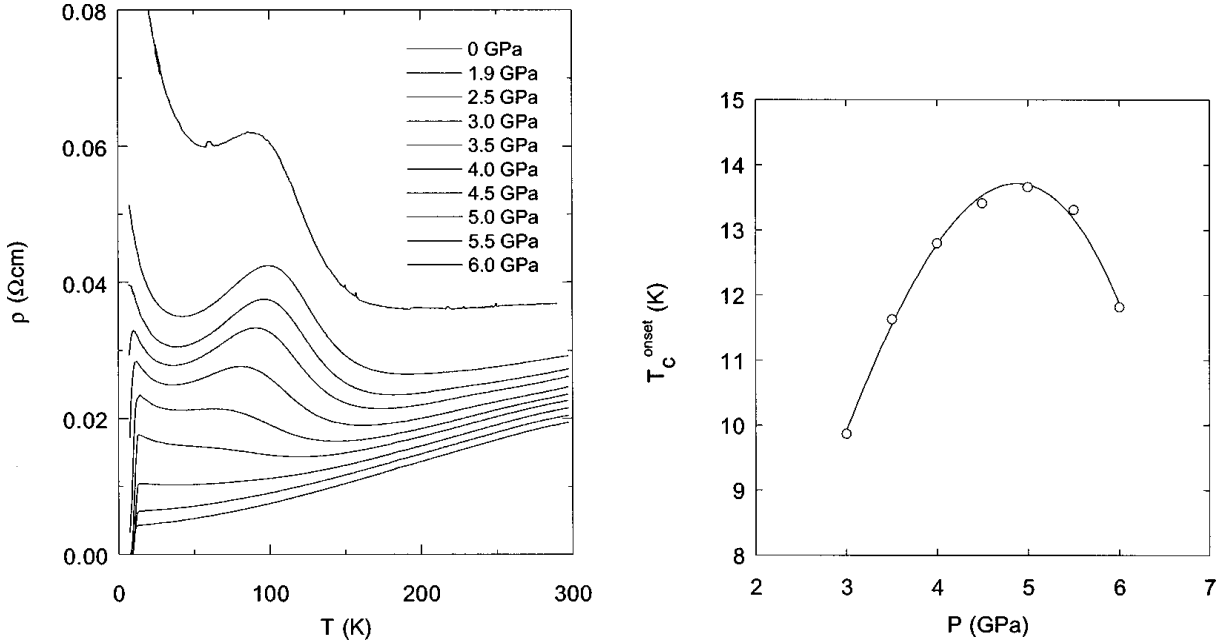


Figure 2.31: Superconductivity in $\text{Sr}_{0.4}\text{Ca}_{13.6}\text{Cu}_{24}\text{O}_{41+\delta}$. The **left** panel shows $\rho(T)$ at various pressures. There is a low-pressure hump around 100 K that was found for any Ca content of $x \geq 13$. This hump disappears above 5 GPa. Superconductivity sets in at a pressure of 3 GPa. In the **right** panel the onset transition temperature T_c^{onset} is plotted as a function of pressure. Reproduced from reference [157].

2.4.4 Superconductivity

The first report on superconductivity in the Ca-rich compound $\text{Sr}_{0.4}\text{Ca}_{13.6}\text{Cu}_{24}\text{O}_{41.84}$ by Uehara et al. in 1996 [5] marked the vital breakthrough of ladder physics and also of the telephone-number compounds. This series provides the only copper-oxide superconductors *without* 2D planes known so far. This theoretically expected yet long-awaited discovery was confirmed two years later by Isobe et al. [157]. High pressures of several GPa are necessary to induce the crossover from semiconducting resistivity $\rho(T)$ to metallic behavior. The optimal pressure of around 5 GPa leads to a superconducting transition temperature of $T_c \approx 13$ K. The $\rho(T)$ data from Isobe et al. is presented in the left panel of figure 2.31. The typical drop at T_c is clearly visible in the high-pressure curves. The right panel demonstrates the dependence of T_c on the pressure. The shape of the curve resembles the well known equivalent of the high- T_c cuprates, if only the pressure is replaced by the hole concentration. It is of course very important to verify that the state of the crystal remains unchanged under pressure and at low temperatures. Therefore Isobe et al. also measured the crystal structure by x-ray diffraction. There were no significant changes in the peak profile except for peak shifts due to lattice compression and the usual slight broadening. They found a single weak extra peak above 3 GPa, though, and an anisotropy of the compression. The b axis shrinks by a respectable 0.7% per GPa, while the c and especially the a axis remain almost constant over the entire range of applied pressures. This again indicates hard binding within the layers and soft one in-between the layers. But there is no phase transition at least up to 9 GPa and down to 7 K.

It is still not clear why such high pressures and Ca contents are necessary for the emergence of superconductivity. Ca produces additional “chemical” pressure comparable to real pressure and both criteria enhance the redistribution of holes from the chains to the ladders (see also reference [180]). However, if only enough holes were the key for superconductivity, less Ca and higher pressure should do as well. But Isobe et al. found no onset of superconductivity in $\text{Sr}_4\text{Ca}_{10}\text{Cu}_{24}\text{O}_{41}$ up to 8.5 GPa. They conclude that the Ca doping enhances the 2D character of the ladder layers since both the a and the c axis shrink by nearly the same percentage, while pressure essentially leaves the a axis unchanged. Ca doping hence increases the interaction between neighboring ladders and superconductivity appears only after the system acquired more 2D character. Strictly speaking, a single ladder cannot support superconductivity for $T > 0$, i.e. higher-dimensional interactions are always a necessary ingredient [40].

Soon after the first discovery of superconductivity at Ca content $x = 13.6$, for $x = 11.5$ a lower transition temperature of 6.5 K at an optimal pressure of 4.5 GPa was reported by Nagata et al. [154]. Resistivity measurements on a single crystal revealed that the ratio of ρ_a/ρ_c decreases from approximately 85 at ambient pressure to as low as approximately 15 at 4.5 GPa. This result supports an increasing 2D character and thus a dimensional crossover upon applied pressure [181]. This is in contrast to the arguments given above regarding the lattice constants. The already mentioned high-pressure NMR measurements by Mayaffre et al. on $\text{Sr}_2\text{Ca}_{12}\text{Cu}_{24}\text{O}_{41}$ demonstrated that the spin gap existing at ambient pressure collapses under 3.1 GPa, where superconductivity sets in. But Mito et al. found a robust spin gap by means of NMR up to 1.7 GPa [178]. And Katano et al. performed inelastic neutron scattering on a single crystal with $x = 11.5$ and found no significant change of the gap at all compared to $\text{Sr}_{14}\text{Cu}_{24}\text{O}_{41}$ [179]. This result did not even change significantly under a pressure of 2.1 GPa [182].

Thus several open questions remain. First of all, the discussion is still open whether there is “real” ladder superconductivity, which just occurs when there are enough carriers in the ladders via increasing Ca content and pressure. The alternative would be a mechanism close to the 2D type since under pressure a crossover to 2D character with increased interladder (and presumably inter-chain) hopping occurs. In addition, it is still controversial whether superconductivity occurs in the presence of a spin gap in the ladders or not.

2.4.5 Optical Studies

Osafune et al. measured the reflectivity of $\text{Sr}_{14-x}\text{Ca}_x\text{Cu}_{24}\text{O}_{41}$ for $x = 0$ to 11 at room temperature [168]. The optical conductivity $\sigma_1(\omega)$ was calculated using a Kramers-Kronig analysis (see section 3.1). The result is plotted in figure 2.32, showing a remarkable dependence on x for polarization of the electric field parallel to the legs. Osafune et al. analyzed the data under the assumption that metallic properties have to be ascribed to holes in the ladders, whereas holes in the chains have to be localized. Under this assumption, the low-frequency Drude-like contribution allows to estimate the number of “free” carriers in the ladders.

As with La^{3+} , also Y^{3+} reduces the total amount of holes in the system, and thus the spectrum for Y content $x = 3$ is typical of an insulator. At low frequencies there are just phonon peaks and the electronic excitations show a gap. At around 2 eV a characteris-

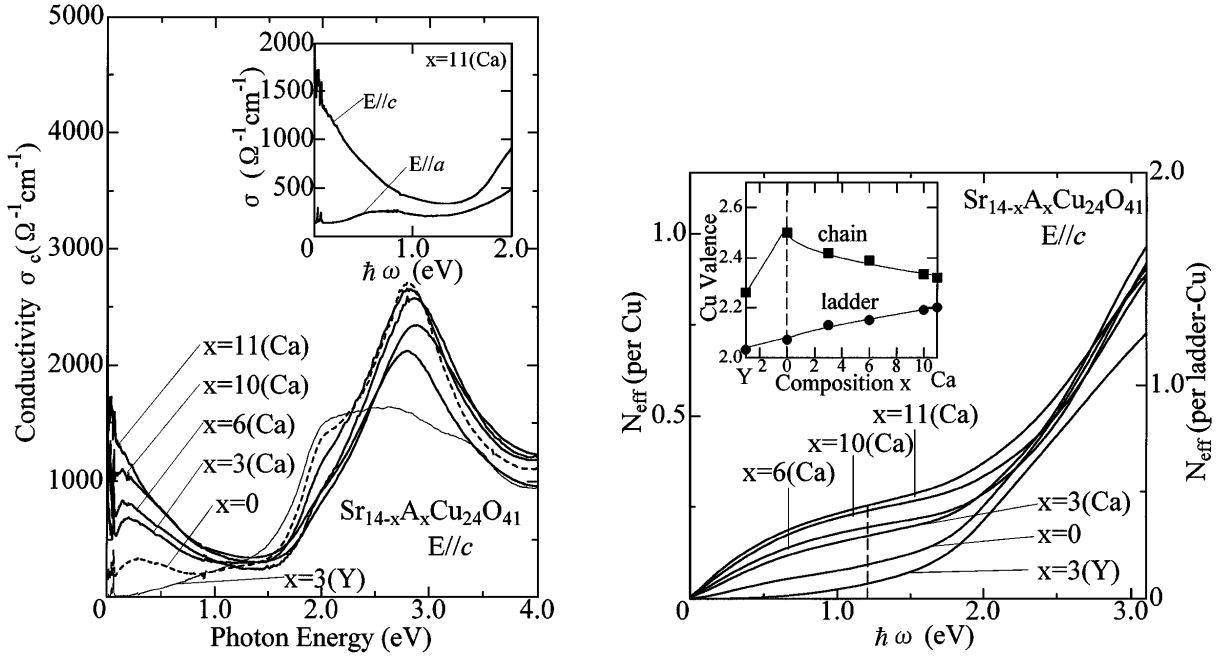


Figure 2.32: Left panel: Optical conductivity $\sigma_c(\omega)$ along the c axis for various compositions of $\text{Sr}_{14-x}\text{A}_x\text{Cu}_{24}\text{O}_{41}$. The data was obtained via Kramers-Kronig transformation of the reflectance spectra. With increasing Ca content spectral weight is transferred from the charge-transfer peak to energies below 1.2 eV. In addition, a distinct peak at 3 eV is present for $\text{Sr}_{14-x}\text{Ca}_x\text{Cu}_{24}\text{O}_{41}$. The inset illustrates the highly anisotropic conductivities along a - and c -axis, respectively. The **right** panel shows the effective number of electrons versus energy. The deduced copper valence in both subsystems is plotted in the inset. This is based on the assumption that the low-frequency metallic contribution is solely due to the ladders. Reproduced from reference [168].

tic peak occurs, that is most probably due to charge-transfer (CT) excitations between copper- $3d$ and oxygen- $2p$ states. This is commonly observed in undoped high- T_c cuprates. On moving to $\text{Sr}_{14}\text{Cu}_{24}\text{O}_{41}$ and further to $\text{Sr}_{14-x}\text{Ca}_x\text{Cu}_{24}\text{O}_{41}$, the conductivity in the low-energy region increases, whereas the CT spectral weight at 2 eV decreases. Obviously there is already a small density of free carriers showing up in $\text{Sr}_{14}\text{Cu}_{24}\text{O}_{41}$. Osafune et al. ascribe the low-energy contribution to the ladders since the carriers are expected to be more mobile in the ladders than in the chains. In (quasi) 1D systems like the ladders, localization of carriers is easily possible in case of disorder. However, the energy scale of this localization would be low, and the material can recover metallic features at optical frequencies [168]. But there is yet another feature arising in $\text{Sr}_{14}\text{Cu}_{24}\text{O}_{41}$, namely a pronounced peak is formed at approximately 3 eV. In this system there has to be an average of six charge carriers per unit cell. This contribution was assigned by Osafune et al. to the holes in the chains, which are supposed to be strongly localized (see also reference [166]). The peak is then due to excitations of these charges, and less weight of this peak with increasing Ca content thus means less holes in the chains. But in this scenario the remaining holes in the chains stay localized for all x up to 11.

A sum-rule analysis yielded the effective number of electrons that contribute to the conductivity up to the energy $E = \hbar\omega$. The results are reproduced in the right panel

of figure 2.32. Above approximately 2.5 eV there is no strong dependence on doping, and thus the redistribution of spectral weight mainly takes place below this energy. This implies that it is mostly the CT weight that is shifted to the low-energy region. This is essentially the same as seen when 2D cuprates get doped [106]. It follows that holes are doped into that structural unit that is a CT insulator in $\text{Sr}_{11}\text{Y}_3\text{Cu}_{24}\text{O}_{41}$ with CT energy gap of 2 eV, and that the doped hole density increases with Ca content. As Ca does not change the average valence, a redistribution of holes from the chains to the ladders should be induced under the assumption that the chains are insulating. Therefore the increased low-energy conductivity is a consequence of increased carrier density in the ladders and not a consequence of originally localized carriers becoming mobile within the chains. Osafune et al. also determine the Cu valence, which directly yields the hole density, for both ladders and chains separately. The inset of the right panel suggests a hole transfer upon doping. Mizuno et al. studied the optical conductivity by exact diagonalization of small clusters [166] and provided a consistent explanation of the optical spectra measured by Osafune et al. [168]. However, to study the actual hole distribution, the technique of polarized x-ray absorption is more direct and does not rely on that many assumptions. The data of Nücker et al. shows that there is only a marginal redistribution of holes upon increasing the Ca content [9] (see figure 2.28).

Two years later Osafune et al. reported low-temperature results for $x = 8$ and 11 [183]. At first they measured the dc resistivity as shown in figure 2.33a. The crystal with Ca content of $x = 8$ is semiconducting between 10 and 300 K, and the ratio ρ_a/ρ_c is almost constant (see inset). The situation for $x = 11$ is different, though. The low-temperature resistivity is still semiconducting, yet ρ_c exhibits metallic temperature dependence above $T_0 \approx 100$ K. Along the a axis, the slope of the resistivity shows a gradual change of sign at $T^* \approx 250$ K. As a consequence there exists a region between 100 and 250 K where ρ_c is metallic ($d\rho_c/dT > 0$) but ρ_a is semiconducting ($d\rho_a/dT < 0$). Accordingly, the anisotropy ρ_a/ρ_c is enhanced in this regime.

Panel (b) of figure 2.33 presents the a -axis optical conductivity for $x = 11$. σ_a is dominated by several optical phonons below 700 cm^{-1} , which are superposed on an electronic background. Upon lowering the temperature, spectral weight at low frequencies is transferred to the higher energy region. This behavior is reminiscent of the pseudogap of underdoped high- T_c cuprates, which has been seen in the interplane conductivity [110, 184]. The energy scale of approximately 600 cm^{-1} (≈ 860 K) is quite large as well, and the other specimen with $x = 8$ exhibits an even larger pseudogap of 1100 cm^{-1} (≈ 1600 K). The opening of the pseudogap with lowering the temperature causes a reduction of σ_{DC} , which matches the semiconducting behavior of $\rho_a(T)$. Osafune et al. speculate that the pseudogap signals the pair formation of doped holes in the ladder [183].

On the other hand, the spectrum along the c axis is dominated by a low-frequency peak that rapidly grows upon lowering the temperature (figure 2.33c). It is not a metallic Drude peak since it is both too narrow and centered at a finite frequency of $\approx 50 \text{ cm}^{-1}$. Osafune et al. interpret this peak as a result of spatially ordered hole pairs or even a pinned charge-density wave (CDW) of hole pairs. The deepening of the pseudogap in σ_a appears to correlate with the peak in σ_c . Therefore it is reasonable to suppose that hole pairs are formed, which produces the pseudogap, and at the same time a collective oscillation of an ordered array of such hole pairs forms a peak in σ_c . In this scenario the number of hole pairs within the ladder increases with decreasing temperature. The pairs readily

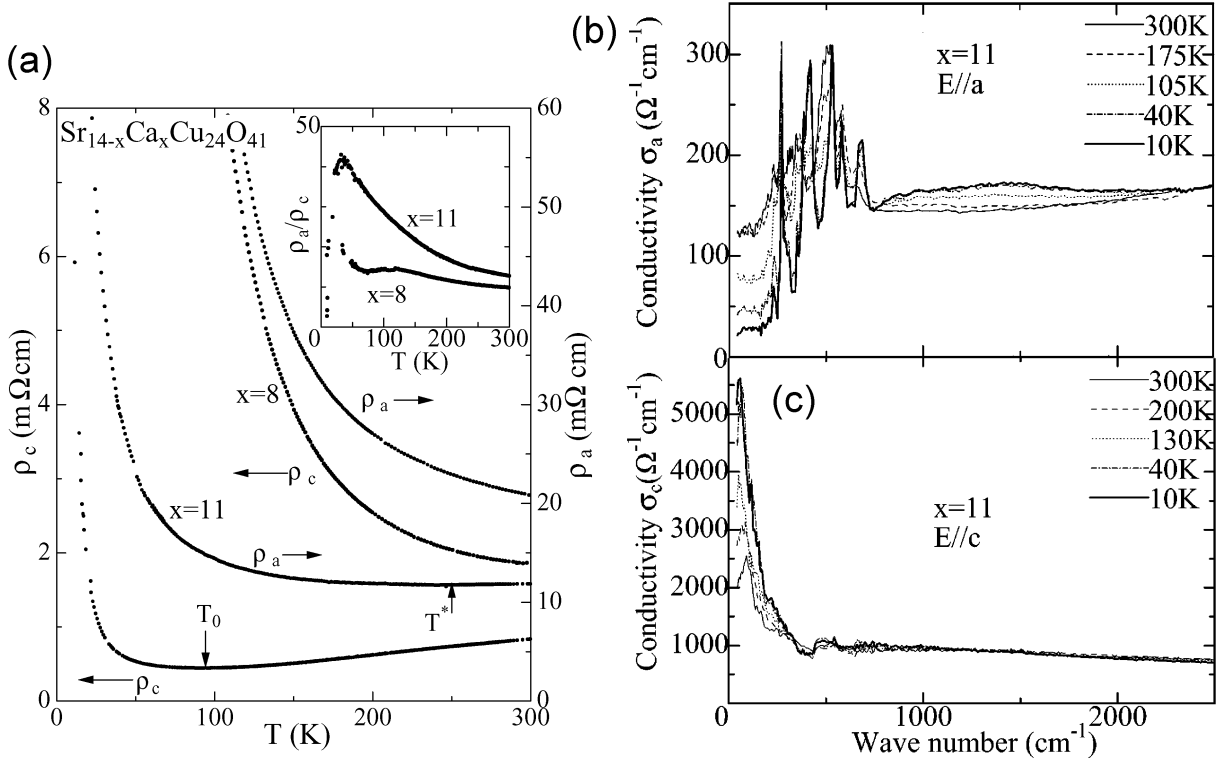


Figure 2.33: (a) T dependence of the dc resistivities along a and c axis, respectively, of $\text{Sr}_{14-x}\text{Ca}_x\text{Cu}_{24}\text{O}_{41}$ with $x = 8$ and 11 . The characteristic temperatures T_0 and T^* , where $d\rho/dT$ changes sign, are indicated by arrows for $x = 11$. The anisotropy ρ_a/ρ_c is plotted in the inset. (b) Optical conductivity of the a axis for $x = 11$. At low temperatures there is a suppression of conductivity below approximately 600 cm^{-1} similar to the pseudogap of underdoped high- T_c cuprates. The sharp peaks stem from optical phonons. (c) Optical conductivity of the c axis for $x = 11$. With lowering the temperature a sharp peak grows rapidly. It is located at the finite frequency of probably 50 cm^{-1} and might be due to a pinned charge-density wave (CDW). Reproduced from reference [183], yet simplified.

form a short-range charge ordering which is locally pinned by impurities or other lattice imperfections. The charge order in the ladder then becomes longer ranged with lower temperature as indicated by the narrowing of the peak and its growing spectral weight. But there is no phase transition to true long-range order [183]. At low temperatures the pinned charge carriers do not contribute to the dc resistivity. At higher temperature the hole pairs can dissociate into single holes by thermal excitations. For Ca content $x = 11$ also the CDW itself may be depinned by thermal fluctuations. In this case both the CDW and dissociated holes contribute to the “metallic” ρ_c .

The independent optical study of samples with $x = 0, 5$, and 12 by Ruzicka et al. led to a similar proposal of a CDW of paired holes at low temperatures [185, 186]. They report a pseudogap-like behavior along the c direction for $x = 12$. In general, a CDW of hole pairs is not surprising at all since it is well known from theoretical calculations that superconductivity and charge ordering are competing states in doped two-leg ladders [2, 3, 187].

Summary: Telephone-number compounds still offer a great deal of interesting questions. However, all the basic expectations for a two-leg ladder were in fact verified. This includes the spin gap as well as the triplet dispersion. Large high-quality crystals are available, and the ladders can be doped with charge carriers. Superconductivity was found, and so far no other copper oxide is known to become superconducting that does not contain 2D square planes. The interplay between the ladders and the incommensurate chains is still not completely understood, though. The proper set of exchange couplings is still lacking, including the value of the cyclic exchange. The magnetic and charge ordering in the chains is challenging, and the superconductivity is rather difficult to probe due to the necessary high pressure. Especially the issue of the coupling constants in connection with the first proof of bound states will be addressed in this thesis. A further topic will be the impact of incommensurability and charge ordering on the spin dynamics of the ladders.

Chapter 3

Optical Spectroscopy

3.1 Dielectric Function and its Determination

The main task in optical spectroscopy is to determine the dielectric function $\varepsilon(\mathbf{k}, \omega)$ of a system since it is closely related to the microscopic electronic properties of solids.¹ In general, this function depends on the frequency ω as well as on the wave vector \mathbf{k} , and it is a complex tensor of second rank. One can determine ε by probing the response of the present charges by applying a weak disturbance in form of an external electric field. When light hits the sample, the wavelength of the applied electric field is very large compared to typical lattice spacings. Since the wave vector is inversely proportional to the wavelength, only $\mathbf{k} \approx 0$ phenomena can be studied with optical spectroscopy. For instance, visible light exhibits wave vectors of the order of 10^5 cm^{-1} , whereas typical Brillouin zones extend to the order of 10^8 cm^{-1} . This fact is of fundamental importance for solid-state spectroscopy and plays a dominant role in the selection rules of optical transitions. Thus in the following, the momentum dependence of the considered quantities may be neglected. Often other functions are used instead of $\varepsilon(\omega)$, namely the refractive index $n(\omega)$ along with the extinction coefficient $k(\omega)$, or the optical conductivity $\sigma(\omega)$. Yet all these functions are directly related to the dielectric function as shown below.

With the advance of efficient lasers it is now quite common to observe nonlinear optical effects. We are rather interested in the linear response to a weak disturbance, though. One of the most fundamental response functions is the dielectric function that connects the displacement field \mathbf{D} to the incident electric field by²

$$\mathbf{D}(\omega) = \varepsilon(\omega) \mathbf{E}(\omega). \quad (3.1)$$

Actually, linear response theory is formulated in time and space. But since the response is generally frequency and momentum dependent, it is more appropriate to consider the Fourier transforms. More precisely, $\varepsilon(\mathbf{k}, \omega)$ is the Fourier transform of the general response function $\varepsilon(\mathbf{r}, \mathbf{r}', t, t')$ that connects $\mathbf{D}(\mathbf{r}, t)$ with the field $\mathbf{E}(\mathbf{r}', t')$ existing at all other positions and all earlier times.

¹Comprehensive introductions to the wide field of optical spectroscopy can be found for instance in references [188–190].

²The cgs system will be used as is common in many textbooks on spectroscopy.

The next fundamental response function is the dielectric susceptibility $\chi_e(\omega)$, which can be expressed as

$$\chi_e(\omega) = \frac{\varepsilon(\omega) - 1}{4\pi}. \quad (3.2)$$

Then the polarization $\mathbf{P}(\omega)$ as response to the electric field reads

$$\mathbf{P}(\omega) = \chi_e(\omega) \mathbf{E}(\omega). \quad (3.3)$$

The third important response function is the optical conductivity $\sigma(\omega)$, which occurs in the frequency-dependent version of Ohm's law

$$\mathbf{j}(\omega) = \sigma(\omega) \mathbf{E}(\omega) \quad (3.4)$$

connecting the induced current density \mathbf{j} to the electric field \mathbf{E} . It is important to note, though, that here \mathbf{E} denotes the *total* electric field. Thus it includes not only the applied external field but also the induced local fields. The relation between the dielectric function and the optical conductivity is

$$\frac{4\pi i}{\omega} \sigma(\omega) = \varepsilon(\omega) - 1. \quad (3.5)$$

From this equation it becomes obvious that all the relevant functions presented here are indeed complex, as for instance

$$\varepsilon(\omega) = \varepsilon_1(\omega) + i\varepsilon_2(\omega) \quad \text{and} \quad \sigma(\omega) = \sigma_1(\omega) + i\sigma_2(\omega). \quad (3.6)$$

Using this convention, equation 3.5 splits into

$$\sigma_1(\omega) = \frac{\omega}{4\pi} \varepsilon_2(\omega) \quad \text{and} \quad \sigma_2(\omega) = \frac{\omega}{4\pi} [1 - \varepsilon_1(\omega)]. \quad (3.7)$$

The distinction between real and complex parts of each quantity is easy in the DC case of vanishing frequency. Then σ_1 , for instance, describes free charges that can move over arbitrary distances in response to the DC field, whereas σ_2 (or ε_1) describes bound charges. These charges are bound to equilibrium positions and only get deflected to new equilibrium positions by the DC field, which is the reason for the polarization. In the case of an AC field this distinction blurs. The free charges do not move arbitrarily far any more but oscillate back and forth with the frequency of the field. And the bound charges no longer come to rest but also oscillate at the field frequency. If the frequency is sufficiently low, i.e. lower than typical scattering rates $1/\tau$, plasma and oscillator frequencies, the distinction can still be preserved, yet on rather different grounds. The free charges respond in phase with the field, i.e. $\sigma(\omega)$ is predominantly real. On the contrary, the bound charges oscillate rather out of phase, i.e. $\varepsilon(\omega)$ is now predominantly real. At higher frequencies even this difference does not hold any more. Thus at optical frequencies of up to 10^{15} Hz the distinction between free and bound charges is entirely a conventional one [35]. But it still holds true that σ_1 describes dissipative losses, which means the absorption of the system. Since we want to probe low-energy excitations, $\sigma_1(\omega)$ is the quantity we will be most interested in.

Both $\varepsilon(\omega)$ and $\sigma(\omega)$ are not only complex but, in general, also tensors of second rank. Nevertheless, the real part of the dielectric tensor is symmetric even for an anisotropic

medium. Hence it is always possible to find a set of axes, the so-called principal dielectric axes, such that the real dielectric tensor can be put into diagonal form. The conductivity tensor, that is proportional to the imaginary dielectric tensor, is also symmetric and can be diagonalized. However, the directions of the principal axes of the real dielectric and conductivity tensors are not generally the same. But the two sets of principal axes do coincide for crystals with symmetry at least as high as orthorhombic [190]. In the following, only such systems are considered. In this case the three remaining diagonal elements can be measured independently by using polarized light. Hence we will neglect the tensor nature of ε and σ from now on and consider just scalars.

There is a further set of variables commonly used to describe the response of a system, namely the complex refractive index

$$N(\omega) = n(\omega) + ik(\omega) \quad (3.8)$$

consisting of the usual refractive index $n(\omega)$ and the extinction coefficient $k(\omega)$. The relation to the dielectric function is given by

$$\varepsilon_1(\omega) = n^2(\omega) - k^2(\omega) \quad \text{and} \quad \varepsilon_2(\omega) = 2n(\omega)k(\omega). \quad (3.9)$$

Due to the requirement of causality, the real and imaginary parts of a response function are not independent. Instead they are related by Kramers-Kronig relations. The one linking ε_1 and ε_2 reads [190]

$$\varepsilon_1(\omega) - 1 = \frac{2}{\pi} \mathcal{P} \int_0^\infty \frac{\omega' \varepsilon_2(\omega')}{\omega'^2 - \omega^2} d\omega'. \quad (3.10)$$

Since there is a divergence for $\omega' = \omega$, \mathcal{P} refers to the principal value of the integral.

But the most important question is not answered so far. It is how one can actually extract the real part of the optical conductivity from the measured quantities, namely the transmittance $T(\omega)$ and the reflectance $R(\omega)$. In many cases only $R(\omega)$ is available. For instance metals exhibit such high absorptions, that already thicknesses of $0.1 \mu\text{m}$ are sufficient to block any measurable transmittance. But $R(\omega)$ yields only one parameter for each frequency, which is not sufficient to determine the *two* components of any response function. In fact, there is indeed a second information stemming from the reflectance at normal incidence. This is the phase shift $\phi_r(\omega)$ that the light experiences during reflection from the sample surface. The so-called complex reflectance directly yields $\varepsilon(\omega)$ according to

$$\sqrt{R(\omega)} e^{i\phi_r(\omega)} = \frac{1 - \sqrt{\varepsilon(\omega)}}{1 + \sqrt{\varepsilon(\omega)}}. \quad (3.11)$$

With standard spectrometers this phase shift cannot be measured directly, though. There are several cures for this under-determined equation. One possibility is to use ellipsometry. This technique uses elliptically polarized light and its reflectance at a finite angle of incidence. A measurement yields two components and thus allows to directly determine the response function for any measured frequency. Although ellipsometers are quite common to probe thin films on a surface, there are several problems. One is that we usually measure sample surfaces smaller than 1 mm^2 . Therefore it is difficult to obtain reasonable signal-to-noise ratios at the necessary large angles of incidence. In addition, the actual

alignment is very challenging when a cryostat has to be used for low temperatures. The commonly used technique is rather the standard reflectance measurement at normal incidence over a wide range of frequencies with a subsequent Kramers-Kronig analysis to gain the missing phase shift. The according transform reads [190]

$$\phi_r(\omega) = -\frac{2\omega}{\pi} \mathcal{P} \int_0^\infty \frac{\ln \sqrt{R(\omega')}}{\omega'^2 - \omega^2} d\omega'. \quad (3.12)$$

A Kramers-Kronig analysis requires the knowledge of $R(\omega)$ for all frequencies from zero to ∞ . Therefore it is always necessary to extrapolate the data to both low and high frequencies. Errors may in particular arise close to the borders of the measured frequency range.

But there is another way to determine the second quantity and thus to circumvent the problems of a Kramers-Kronig analysis. Since we measure insulators in a frequency regime above the phonons and below the band gap (see section 5.2.1), the overall absorption is quite low. This allows us to measure not only the reflectance but also the transmittance $T(\omega)$. We still need to prepare thin samples of thicknesses from several 100 μm down to less than 10 μm , but we can directly calculate any response function once R and T are known for a certain frequency. The only remaining parameter we have to determine is the exact thickness d of the transmittance sample. The according equations read [191, 192]

$$T(\omega) = \frac{(1 - R(\omega))^2 \Phi}{1 - (R(\omega) \Phi)^2}, \quad (3.13)$$

$$R(\omega) = \frac{(n(\omega) - 1)^2 + k^2(\omega)}{(n(\omega) + 1)^2 + k^2(\omega)} \quad (3.14)$$

$$\Phi(\omega) = e^{-2\omega k(\omega) d / c} = e^{-\alpha(\omega) d} \quad (3.15)$$

where $\alpha(\omega)$ denotes the absorption coefficient, and c the vacuum velocity of light. Note that $R(\omega)$ means the single bounce reflectance and hence needs to be measured on samples thick enough so that there is no contribution from light reflected from the back face of the sample. Equation 3.13 is obtained for a sample with parallel faces by adding up the intensities of all multiply reflected beams incoherently, i.e. by neglecting interference effects. Experimentally, this condition is realized either if the sample faces are not perfectly parallel or by smoothing out the Fabry-Perot interference fringes by means of Fourier filtering (see page 72). In practice there is usually no choice between a Kramers-Kronig analysis of $R(\omega)$ data or the combined R and T measurements. When the absorption is high, the large $\alpha(\omega)$ together with the exponential function in equation 3.15 will lead to vanishing transmittances in equation 3.13.³ However, when the absorption is low it is almost impossible to extract these small values of $\alpha(\omega)$ from the reflectance data with subsequent Kramers-Kronig analysis.

³Actually, this equation is a generalization of the well known Lambert's law

$$I(d) = I_0 e^{-\alpha d}, \quad (3.16)$$

that completely neglects any reflectance effects. I_0 is the initial intensity and $I(d)$ is its reduced value after traversing a thickness d within the sample.

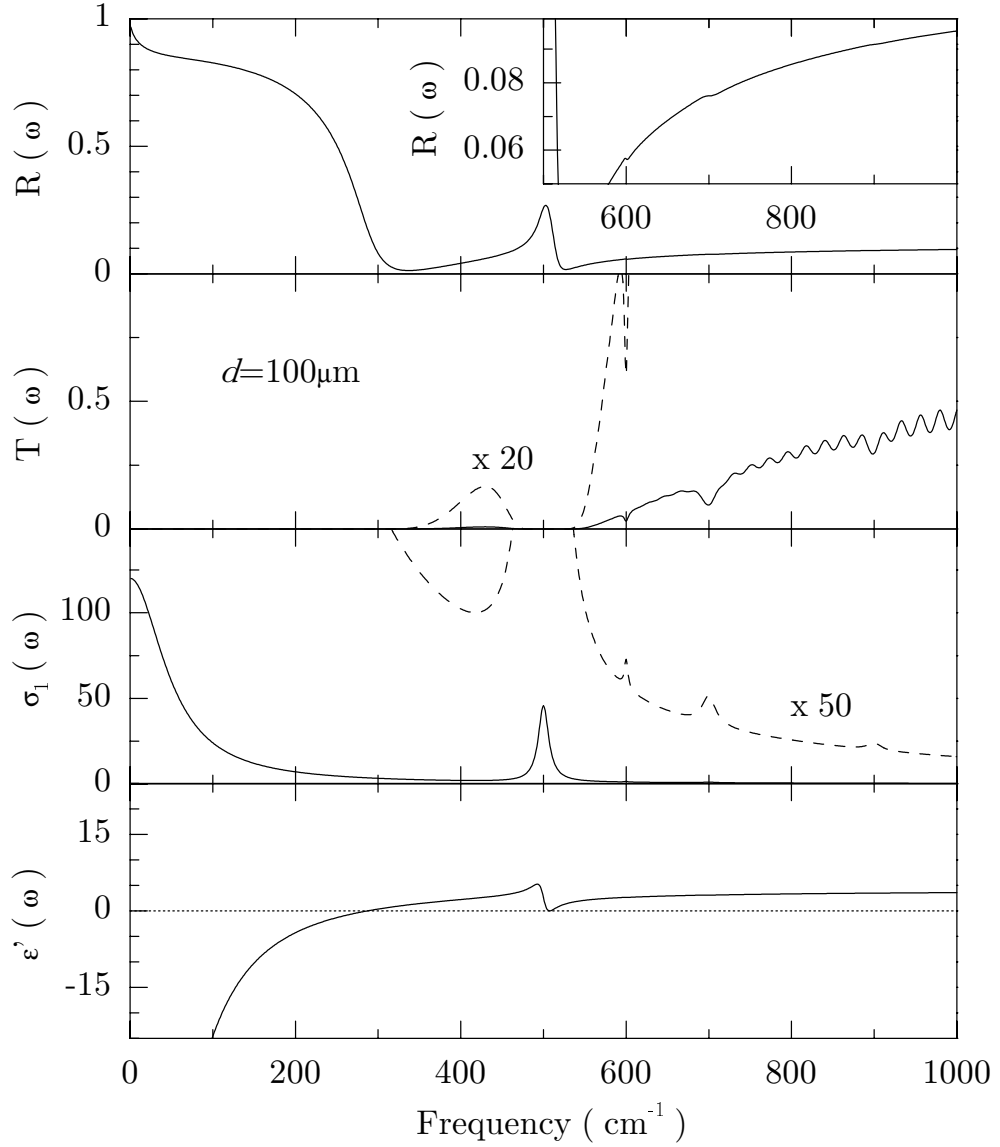


Figure 3.1: Drude-Lorentz simulation of an exemplary system with five different contributions. First there is a weak metallic Drude part at zero frequency, then a weak phonon at 500 cm^{-1} , and finally three further very weak excitations at 600 , 700 , and 900 cm^{-1} . For the transmittance sample a thickness of $100 \mu\text{m}$ was assumed. The inset in the upper panel shows the very weak features in $R(\omega)$ on a larger scale. In the T and σ_1 panels the dashed lines show the data multiplied by the given factors. ε' denotes the real part of the dielectric function. Reproduced from reference [110].

In order to illustrate this point, simulations of $R(\omega)$, $T(\omega)$, $\sigma_1(\omega)$, and $\varepsilon_1(\omega)$ are plotted in figure 3.1. The underlying model system includes a weak metallic contribution at $\omega = 0$, a weak phonon at 500 cm^{-1} , and three very weak features⁴ at 600 , 700 , and 900 cm^{-1} . For the transmittance sample a thickness of $100 \mu\text{m}$ was assumed. The metallic excitation and the phonon can easily be determined from $R(\omega)$, whereas $T(\omega)$

⁴The units of cm^{-1} are defined in the next section.

is so small that a measurement is almost hopeless. Exactly the opposite is true for the weaker absorptions. Their fingerprint in $R(\omega)$ is rather vague and will be lost in the noise of a real experiment. Yet in the transmittance spectrum they are clearly visible. The high-frequency region with larger values of T is dominated by Fabry-Perot fringes, which are due to multiple reflections within the sample. These fringes can be smoothed away, but then of course the resolution of the experiment is reduced. Obviously, the exponential dependence on d and α requires a delicate choice of the proper sample thickness.

The simulation uses the so-called Drude-Lorentz model, which is the classical theory of absorption and dispersion. It assumes a set of several oscillators that cause the response to light. One can for instance consider an atom with electrons bound to the nucleus in much the same way as a small mass can be bound to a large mass by a spring. The motion of the electron is then described by a typical equation of motion

$$m \frac{d^2 \mathbf{r}}{dt^2} + m\Gamma \frac{d\mathbf{r}}{dt} + m\omega_o^2 \mathbf{r} = -e\mathbf{E}_{local} \quad (3.17)$$

where m is the electron mass, $-e$ is the electron charge, Γ denotes damping, and ω_o is the oscillator frequency. The field \mathbf{E}_{local} is the local electric field that acts on the electron as a driving force. Here the small force stemming from the interaction with the magnetic field of the light is neglected. The Lorentz force $-e\mathbf{v} \times \mathbf{H}/c$ is indeed negligible since the velocity of the electrons is small compared with c . To describe the conduction electrons of a metal, one simply has to omit the restoring force $m\omega_o^2 \mathbf{r}$ because the electrons are not bound anymore. This is the Drude part of the model. It is surprising how many properties of real crystals can actually be described by such a simple idea. For more details on the Drude-Lorentz model and its derived response functions the reader is referred to references [189, 190, 193].

3.2 Typical Units

At this point, some general remarks are necessary on the units that occur in the following. In optical spectroscopy, it is common to use a rather sloppy terminology. Namely the *angular* frequency ω is not given in s^{-1} but instead in wave numbers ν with the unit cm^{-1} . To avoid confusion, the conventional frequency in Hz will be labelled as f . With Planck's constant $\hbar = h/2\pi$, the energy is directly proportional to the frequency: $E = \hbar\omega = hf$. Hence the frequency is basically an effective energy scale. The definition of the wave number ν is quite simple as it is the reciprocal value of the wavelength λ . Then the wave number is just the frequency f divided by the speed of light c :

$$\nu = \frac{1}{\lambda} = \frac{f}{c}. \quad (3.18)$$

This is very convenient because it avoids huge numbers. For instance, mid-infrared light with $\lambda = 4 \mu\text{m}$ has a frequency of $f = 75 \text{ THz}$ but a wave number of just 2500 cm^{-1} . The other common energy scale is given in units of eV. The energy is related to ν via

$$E = hf = hc\nu. \quad (3.19)$$

The most important conversion is directly from cm^{-1} to eV and vice versa. For practical use it is helpful to remember that

- 1 eV corresponds to 8066 cm^{-1} .

The last major energy unit is the temperature in K. Since $E = k_B T$, where k_B is Boltzmann's constant, one gets that

- 1 cm^{-1} corresponds to 1.439 K, and
- 1 meV corresponds to 11.60 K.

Note that in the following the wave-number symbol ν usually does not emerge any more. Instead, it is common to use the angular-frequency symbol ω along with units of cm^{-1} to describe an effective energy scale. Finally, table 3.1 gives an overview of typical frequency ranges.

	$\omega \text{ (cm}^{-1}\text{)}$	$\lambda \text{ (}\mu\text{m)}$	$E \text{ (eV)}$
ultraviolet (UV)	25 000 - 100 000	0.4 - 0.01	3.1 - 12
visible (VIS)	12 500 - 25 000	0.8 - 0.4	1.5 - 3.1
near infrared (NIR)	4000 - 12 500	2.5 - 0.8	0.5 - 1.5
mid infrared (MIR)	400 - 4000	25 - 2.5	0.05 - 0.5
far infrared (FIR)	4 - 400	2500 - 25	$0.5 \times 10^{-3} - 0.05$

Table 3.1: Comparison of different frequency ranges. The boundaries are not standardized, though.

3.3 Bimagnon-Plus-Phonon Absorption

3.3.1 Experimental Evidence

The mid-infrared absorption of undoped 2D cuprates exhibits interesting features that are still not completely understood. Measurements by Perkins et al. on La_2CuO_4 and three other single-layer cuprates revealed a sharp peak at around 0.4 eV ($\approx 3200 \text{ cm}^{-1}$) in all the systems [13]. Associated with this main peak, further high-energy sidebands occur. The upper left panel of figure 3.2 shows the absorption data of La_2CuO_4 . Note that a linear background was subtracted from the initial data. Perkins et al. initially ascribed the main peak to an exciton, but Lorenzana and Sawatzky provided a meanwhile accepted interpretation in terms of bimagnon-plus-phonon (BIMP) absorption in the frame of conventional spin-wave theory [11, 12]. The corresponding fit is included as a dashed line in the figure. Obviously, the sidebands cannot be explained within conventional spin-wave theory. Similar features were reported by Grüninger et al. in the bilayer system $\text{YBa}_2\text{Cu}_3\text{O}_6$ [14, 196] as shown in the right panel of figure 3.2. At 4 K there is again a sharp peak followed by other high-frequency contributions. Also in this system the main peak is well described by BIMP absorption and spin-wave theory.

But there are further confirmations of this concept. For instance in the 2D $S = 1$ system La_2NiO_4 , the *complete* line shape can be reproduced [12, 194] because there is no additional high-frequency weight. This compound is isostructural to La_2CuO_4 yet with a larger spin. In the lower left panel of figure 3.2 the absorption is plotted together with the

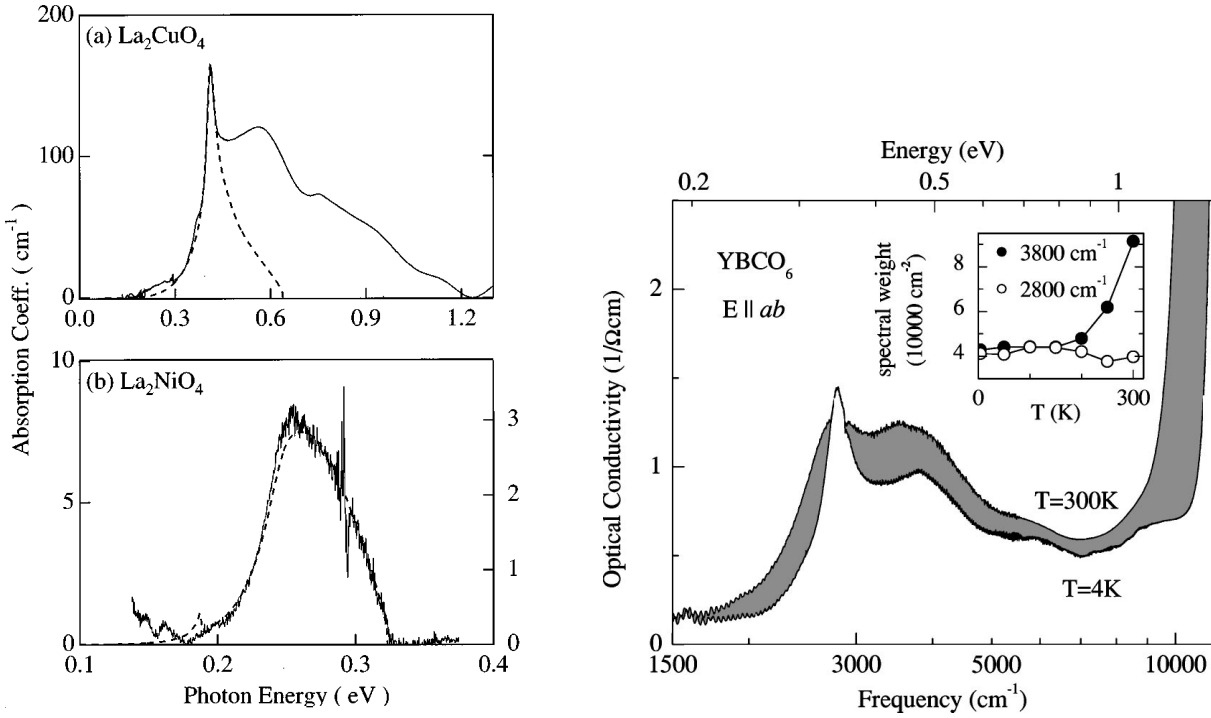


Figure 3.2: Infrared absorption spectra of different systems. **Upper left** panel: 2D $S = 1/2$ single-layer compound La_2CuO_4 (solid line) at 10 K as measured by Perkins et al. [13, 194, 195]. Dashed lines indicate the theoretical results by Lorenzana and Sawatzky [11, 12]. **Lower left** panel: 2D $S = 1$ compound La_2NiO_4 at 10 K, as well measured by Perkins et al. [194, 195] along with the according BIMP results. Note that in both panels a linear background was subtracted. **Right** panel: Optical conductivity σ_1 of $\text{YBa}_2\text{Cu}_3\text{O}_6$ at 4 and 300 K measured by Grüninger et al. [14]. The inset shows the experimental temperature dependence of the spectral weights of the 2800 and 3800 cm^{-1} peaks.

theoretical results. The same holds true for the 1D $S = 1/2$ chain Sr_2CuO_3 [139, 140], as shown in the left panel of figure 3.3. Good agreement between observed and calculated spectra was achieved in 1D because the according two-spinon treatment already takes care of the quantum fluctuations. In the case of La_2NiO_4 the agreement is excellent since quantum fluctuations beyond spin-wave theory obviously are small enough already for $S = 1$. In the intermediate case of the 2D cuprates with $S = 1/2$, only the main peak is well described (upper left panel of figure 3.2). The considerable weight of the sidebands above this peak is beyond conventional spin-wave theory. In $\text{YBa}_2\text{Cu}_3\text{O}_6$ this weight even grows with temperature as well as with doping [14]. Above 200 K, the line shape shows a remarkable change, as can be seen in the right panel of figure 3.2. The main peak broadens although its total weight is unaffected. Yet the sidebands dramatically increase, and at 300 K the peak around 3800 cm^{-1} already doubles its weight. The weights of both the peaks versus temperature are plotted in the inset. A similar temperature dependence was also reported for La_2CuO_4 [195] and $\text{Sr}_2\text{CuO}_2\text{Cl}_2$ [191, 195]. In the right panel of figure 3.3, the comparison of these three 2D cuprates with the theoretical BIMP result reveals that the infrared features are indeed intrinsic to the 2D Cu–O planes. Note that all data sets were adjusted so that the main peaks match.

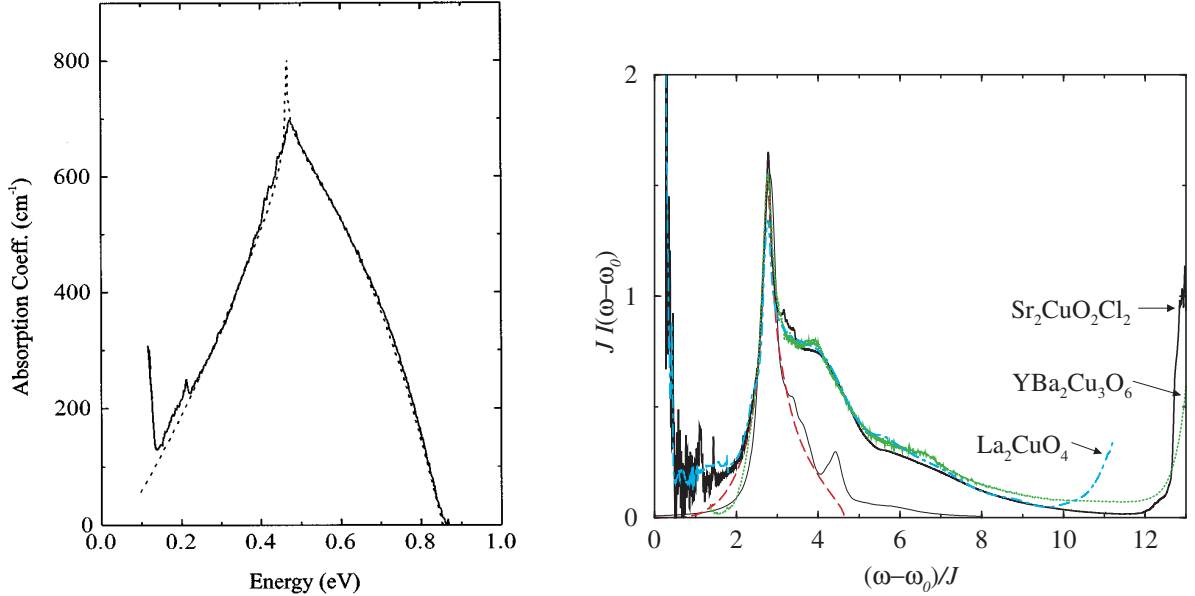


Figure 3.3: **Left** panel: Absorption of the 1D $S = 1/2$ chain Sr_2CuO_3 at $T=32$ K as reported by Suzuura et al. [139]. The dashed line is the theoretical curve of phonon-assisted two-spinon absorption as given by Lorenzana and Eder [140]. **Right** panel: Intensities of experimental absorptions for three different 2D cuprates. The data sets were scaled so that the main peaks coincide. $\text{Sr}_2\text{CuO}_2\text{Cl}_2$ (solid) and La_2CuO_4 (dot-dashed) were measured by Perkins et al. [13]. The $\text{YBa}_2\text{Cu}_3\text{O}_6$ data (solid) is from Grüninger et al. [196]. The dashed line was calculated by Lorenzana et al. using spin-wave theory and reproduces the main peaks of all measurements [15]. The thin line denotes results of the exact diagonalization of a 32-site cluster. Reproduced from reference [15].

But an explanation of the sidebands still remains elusive. Several interpretations in terms of multi-magnon-plus-phonon absorption [11, 12], $d-d$ transitions [194], and charge-transfer excitons [197] were proposed. Grüninger et al. challenge these approaches and suggest that a full account of the infrared data in the undoped cuprates has to include quantum fluctuations beyond spin-wave theory [14]. The magnetic origin of the high-energy features was demonstrated by means of infrared and Raman measurements under high pressure by Struzhkin et al. [198]. In this context it is surprising that the exact diagonalization result of Lorenzana et al. (thin solid line in the right panel of figure 3.3) does *not* show a strong high-energy contribution [15]. This might be related to the cluster size of 32 sites, or to a missing term in the Hamiltonian. Lorenzana et al. claimed [15] that a cyclic spin-exchange term might increase the high-energy weight (see also section 5.3.2). However, their result for the so-called first moment, which is the “center of mass” frequency of the spectral weight, is smaller than observed experimentally. Hence there is still high-energy weight missing. $S = 1/2$ ladders exhibit many similarities to the 2D cuprates, yet calculations are a lot easier. The hope to shine some light upon this challenging high-energy contribution provided the first intention for us to investigate the telephone-number compounds, which are described in section 2.4.1. In chapter 5 it is shown that we indeed found a large high-energy weight in the ladders, which as well exhibits a strong temperature dependence.

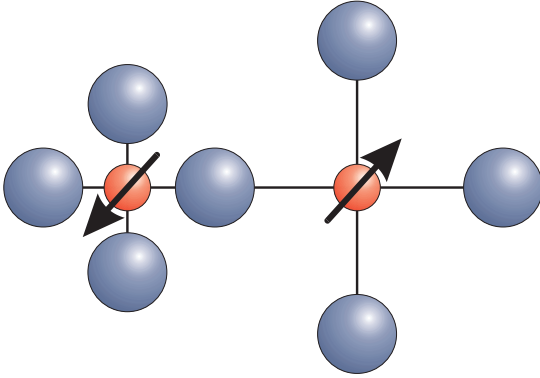


Figure 3.4: Breathing phonon mode that breaks the inversion symmetry of the copper sites. This phonon stretches the bonds between the copper (small spheres) and the oxygen ions (large spheres). Other examples for the spin ladder are given in figure 5.32 on page 131.

3.3.2 Basic Idea

How is it possible to measure magnetic excitations with light at all? The magnetic part of the electromagnetic wave is usually not responsible for the interaction with solids. Therefore magnetic dipole transitions will be neglected in the following. Considering electric dipole transitions only, it is not possible to excite any state that would lead to a change of the total spin. Hence it is not allowed to excite just a single spin wave, magnon, or triplet. From spin conservation alone, the lowest order process would be to excite *two* magnons with a total spin of zero. But infrared absorption of two magnons is still not allowed in the tetragonal structure of the 2D cuprates. This is because in a typical two-magnon excitation the presence of a center of inversion inhibits any asymmetric displacement of charge, and hence the associated *electric* dipole moment vanishes. The situation changes if phonons are taken into account. In a process in which one phonon and two magnons are absorbed, the symmetry of the lattice is effectively lower. In this case the process becomes weakly allowed.⁵ Lorenzana and Sawatzky presented the first calculations on the actual line shape stemming from this kind of absorption [11, 12]. They considered the 2D copper-oxide layers, but the generalization of the results to other magnetically ordered insulators is not difficult.

An example of a very effective symmetry-breaking phonon is sketched in figure 3.4. This Cu–O bond-stretching mode is also called a breathing mode. But phonons do not only break the symmetry, they also contribute momentum. Only the combined momentum $k_{total} = k_{ph} + k_{2magnon}$ has to be zero in order to be infrared active. Hence the infrared bimagnon-plus-phonon absorption is a weighted average over magnetic excitations from the entire Brillouin zone, and the phonons provide some sort of “momentum bath”. Due to energy conservation, the energy scale of the observed magneto-elastic peaks will be shifted by the energy $\hbar\omega_{ph}$ of the phonon. Neglecting a possible dispersion of the phonon mode is usually justified because only optical phonons come into question and because in the cuprates the exchange constants are large compared to $\hbar\omega_{ph}$. Typically, just Einstein phonons without any dispersion are assumed.

The first step for determining the line shape and the spectral weight of the absorption

⁵The early roots of this ansatz date back to optical measurements of Newman and Chrenko on NiO in 1959 [199]. The observed absorption band at 0.24 eV was interpreted in terms of the combined absorption of two magnons and one phonon by Mizuno and Koide five years later [200].

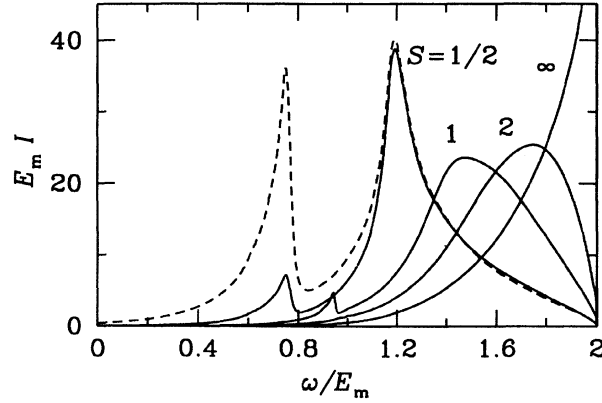


Figure 3.5: Line shape of the BIMP absorption in a 2D square-lattice Heisenberg AF for different values of the spin. The dashed line denotes a particular approximation in the case of $S = 1/2$. The second peak at lower frequencies is an artefact. The energy scale is given in units of the magnon energy E_m at the zone boundary. Reproduced from reference [12].

is to consider the dependence of the exchange constants both on the external electric field \mathbf{E} of the photon and on the displacements \mathbf{u} of the oxygen ions. Thus $J \equiv J(\mathbf{E}, \mathbf{u})$ [11, 12, 14]. The phonons modulate the inter-site hopping and the on-site energies on both Cu and O sites. Expanding $J(\mathbf{E}, \mathbf{u})$ to order $d^2 J/d\mathbf{E}d\mathbf{u}$ entails the coupling of a photon to a phonon and two neighboring spins. This determines how to integrate the spin response in the Brillouin zone, and a weight factor has to be considered that describes the efficiency of the phonon-magnon coupling for each momentum. The result might be for instance that most of the absorption weight stems from bimagnons at the boundary of the Brillouin zone. The exact form factor depends on the actual structure of the system and the involved phonon. In the case of the 2-leg spin ladders in a trellis configuration, the weight factor is a mixture of

$$F = \omega \sin^4(k/2) \quad (3.20)$$

and of a k -independent term [201]. The \sin^4 term renders the infrared absorption to be more sensitive to $k = \pi$ excitations of the two magnons. Further details on the relevant phonon modes and the according weight factors are presented by Nunner et al. in reference [201] (see also section 5.3.2).

The theoretical line shapes for different spin values in a 2D square-lattice Heisenberg AF are reproduced from reference [12] in figure 3.5. This plot offers a first understanding of the according spectra. In the classical case of $S \rightarrow \infty$, the two-magnon absorption reproduces the density of states and diverges at the upper cutoff at $2E_m$, where E_m is the maximum magnon energy located at the zone boundary. Attractive quantum interactions between the two magnons are switched on by reducing the spin value. The spectral weight is shifted to lower frequencies, and a resonance peak is formed. Since the peak is located within the two-magnon continuum, there is no real bound state of magnons. Increasing the interaction strength, i.e. reducing the spin value further, pulls the resonance to frequencies where the continuum background is small. Thereby the resonance peak sharpens, and for the limiting case of $S = 1/2$ it can be viewed as an *almost* bound state of two magnons, which here is called a “bimagnon”.

In chapter 5 we discuss the infrared absorption of undoped spin ladders. The appropriate description of the magnetic excitations is rather given in terms of triplets than in terms of magnons. Thus technically one has to deal with two-triplet-plus-phonon absorption. It will be shown that undoped spin ladders indeed exhibit a *real* bound state of two triplets, which produces even *two* separate peaks in the optical conductivity. There are as well high-energy sidebands, that can unambiguously be attributed to the two-triplet continuum.

Chapter 4

Experimental Setup

The basic principle of optical spectroscopy as illustrated in figure 4.1 is quite easy. The question to start with is always the same: how much light is transmitted through the sample and / or how much light gets reflected back within a certain range of frequencies. The knowledge of $R(\omega)$ and $T(\omega)$ directly yields the important response functions (see section 3.1) like the optical conductivity $\sigma(\omega)$ or the dielectric function $\varepsilon(\omega)$.

4.1 Fourier Spectroscopy

Dispersive spectrometers used to be the standard tool for optical spectroscopy. They employ fixed slits and rotating gratings (or prisms) to scan the different frequencies one by one. But in the infrared and particularly in the far-infrared range Fourier spectrometers took over since computers got fast enough to perform the necessary Fourier transform. An important advantage compared to dispersive methods is speed. All available frequencies get measured within one run that usually takes no longer than a second. This is known as the *multiplex* or *Fellgett* advantage: Compared to dispersive spectrometers, the signal-to-noise ratio improves proportional to \sqrt{m} , where m is the number of measured frequency intervals in a complete spectrum. In addition, more intensity hits the detector, which can cause the difference between “measurable” and “non-measurable”. Dispersive

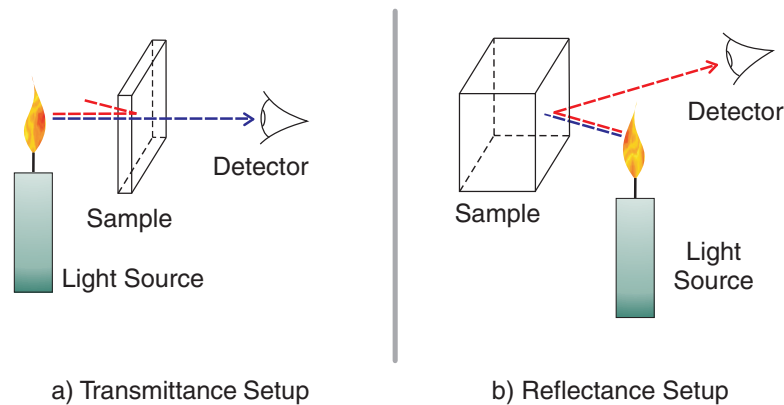


Figure 4.1: Rudimentary experiments in optical spectroscopy.

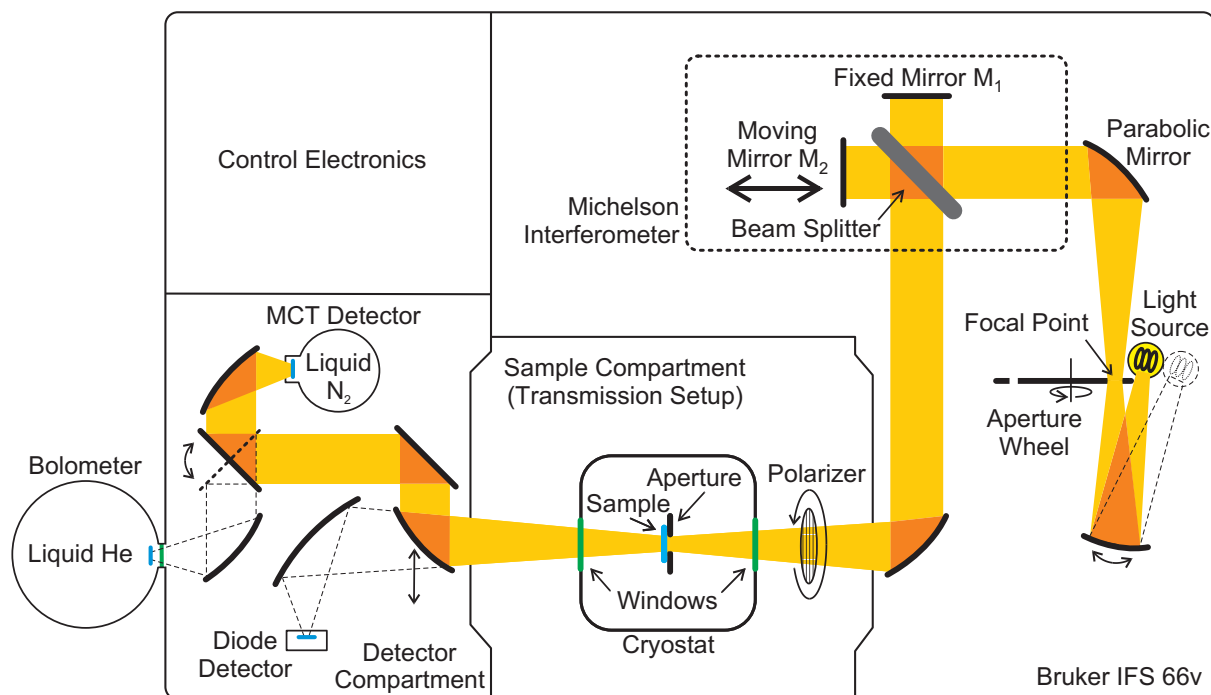


Figure 4.2: Sketch of the Bruker IFS 66v spectrometer. Dashed lines indicate alternative optical paths. An insert with six additional mirrors can be placed into the sample compartment to enable reflectance measurements.

spectrometers have to use narrow linear slits in order to reach a reasonable resolution. Fourier spectrometers can use circular entrance apertures, which waste less area of the incoming beam. This is known as the *throughput* or *Jacquinot* advantage. It is also another reason for larger light intensities yielding a better signal-to-noise ratio, that further reduces the overall measurement time. Sufficient signal is particularly important in the far-infrared regime where intensities of thermal sources are always low. This is due to the spectral shape of the black-body radiation that parabolically reaches zero intensity as the frequency approaches zero. It is also worthwhile to mention the very high available resolution and the almost perfect frequency calibration¹.

Good descriptions of Fourier spectrometers are available in references [188, 202–205] and just the basic principle is presented here. This summary is followed by a more detailed description of the main measurement problems, which are usually not covered by the standard sources.

Figure 4.2 shows a sketch of our spectrometer in transmission configuration. Light from the source gets focussed onto the entrance aperture. The next mirror is parabolic and produces a parallel beam that enters the Michelson interferometer. The light hits the beam splitter that ideally reflects one half of the light whereas the other half can pass through (see figure 4.3). The reflected part of the beam is completely reflected back by the fixed flat mirror M_1 and reaches the beam splitter again. The same happens to the transmitted part of the original beam. Since the corresponding mirror M_2 can be moved back and forth with high precision, the travelling distance of the two partial beams can

¹Usually about 0.01 cm^{-1} , also known as *Connes* advantage.

be chosen to differ by a path difference of δ . When the mirror displacement is equal to x the corresponding optical retardation would accordingly be $\delta = 2x$. Again, ideally half of each beam gets reflected and the other one passes through the beam splitter. This means that finally two partial beams run back to the light source and unfortunately are lost. The other two partial beams leave the interferometer, and as long as coherence is given they will interfere with each other. This is an important point since thermal light sources emit incoherent light. That means that the phase relation of different wave packets is statistical. Substantial interference can only take place when every wave packet is split up and finally superposes a retarded part of the very same packet. Accordingly, δ may not exceed the *total* length of an average wave train by too far. The common meaning of the coherence length is misleading in this context because it only measures the length over which the *main* interferences occur. This length is by orders of magnitude smaller than the usable path difference (see figure 4.4c).

Real beam splitters provide transmittances T and reflectances R that differ from the ideal value of $1/2$. But $R + T = 1$ is always true as long as the absorption is negligible. When the mirror moves back and forth, the average intensity that reaches the sample is proportional to $2RT$ because both partial rays get transmitted and reflected once (see figure 4.3). The maximum value of $1/2$ is only attainable when $R = T = 1/2$. The average value of the lost intensity is proportional to $R^2 + T^2$ since one partial ray is transmitted

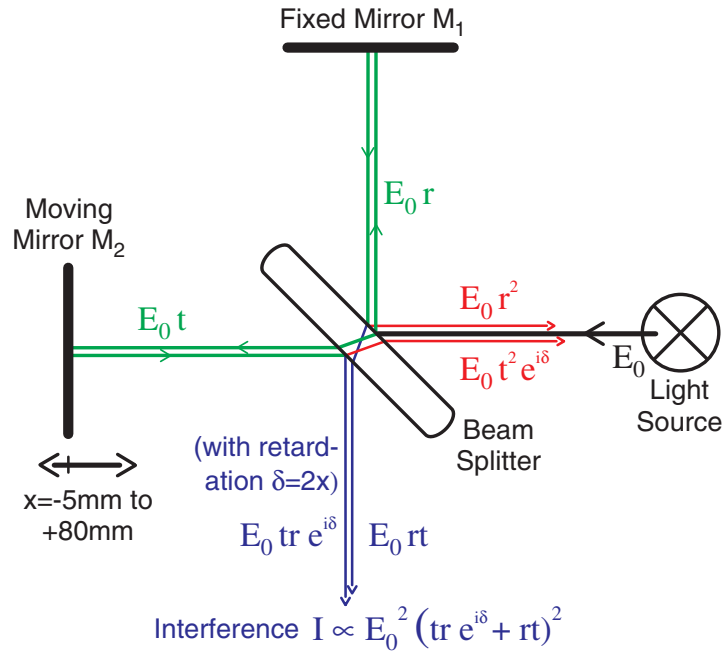


Figure 4.3: Sketch of the Michelson interferometer unit. The primary intensity from the light source (thick line) is proportional to E_0^2 , where E_0 is the amplitude of the electric field. This intensity is split into two parts that strike the mirrors M_1 and M_2 , respectively. Both the beams hit the beam splitter again, and finally there are four beams that leave the interferometer. Two of these run towards the sample. The other two beams are lost. Here, r and t denote the Fresnel coefficients of the beam splitter ($r = E_i/E_r$, where E_i and E_r are the amplitudes of the incident and reflected field, respectively), in contrast to $R = I_i/I_r$.

twice whereas the other one gets reflected twice. Of course the total intensity leaving the interferometer is proportional to unity, which simply means that no light vanishes. For every given position of the mirror, i.e. *without* averaging over time, the intensities depend on the optical retardation between the partial beams. For monochromatic light there will subsequently occur constructive and destructive interference.

Afterwards the light traverses a linear polarizer followed by a vacuum window and gets focussed onto the sample inside the cryostat². The sample is glued to a circular copper aperture with silver paste and can be cooled down to 4 K as well as heated up to 800 K. Next there is a second window and after several mirrors the light finally gets focussed onto the detector. It is important that the pressure inside the cryostat is at least below 10^{-5} mbar before cooling down the sample. Then the cryo-pump effect reduces the pressure further down to less than 10^{-6} mbar. If the pressure before cooling was poor, a layer of dirt would soon cover the sample surface, since it is one of the coldest spots inside the cryostat. Usually this is not a problem for transmittance measurements, but a layer of ice produces characteristic absorption artefacts above 3000 cm^{-1} that ruin the spectra. The spectrometer itself also is evacuated down to a rough vacuum to get rid of absorption lines of for example carbon dioxide and water vapor.

Within a measurement it is possible to switch between different optical components without breaking the vacuum. This comes in quite handy since any changes are reliably reversible. Computer controlled stepping motors operate mirrors to choose one of three different detectors and also one of two light sources. Upon rotating the aperture wheel several entrance diameters are possible. Finally, the polarizer is computer operated as well. This allows us to automate the search for the orientation of a sample with e.g. tetragonal or orthorhombic symmetry, and within one run both the accessible crystal axes can be measured. To cover the complete possible frequency range, at least five different measurements are necessary. The reason is that for instance the exchange of the beam splitter or the cryostat windows is *not* possible without breaking the vacuum and realigning the optics. The resulting span reaches from the far infrared of 10 cm^{-1} all the way up to the ultraviolet of $55\,000\text{ cm}^{-1}$. In terms of wavelengths this is approximately $\lambda = 1\text{ mm}$ down to $\lambda = 180\text{ nm}$. And to make this small compilation complete, the corresponding energies are 1.2 meV and 6.8 eV.

4.1.1 Calculating the Spectra

The detector doesn't measure the spectrum directly but the so-called interferogram instead. To gain the transmittance and the reflectance of the sample, respectively, further processing is required. The most simple example starts with a laser as a monochromatic light source. The spectrum $S(\omega)$, as illustrated in figure 4.4a (left), consists of a delta function at the frequency ω_0 of the laser. Now let the movable mirror glide with constant velocity from the position of zero optical retardation (i.e. $\delta = 0$) by a distance x . The two beams that leave the interferometer superpose, and constructive as well as destructive interference emerges successively. The resulting signal (right panel of figure 4.4a) is proportional to the cosine function [188]

$$I(x) \propto [1 + \cos(4\pi x/\lambda_0)] . \quad (4.1)$$

²Model "Konti - Kryostat Typ Spektro A" by CryoVac, modified to meet our specifications.

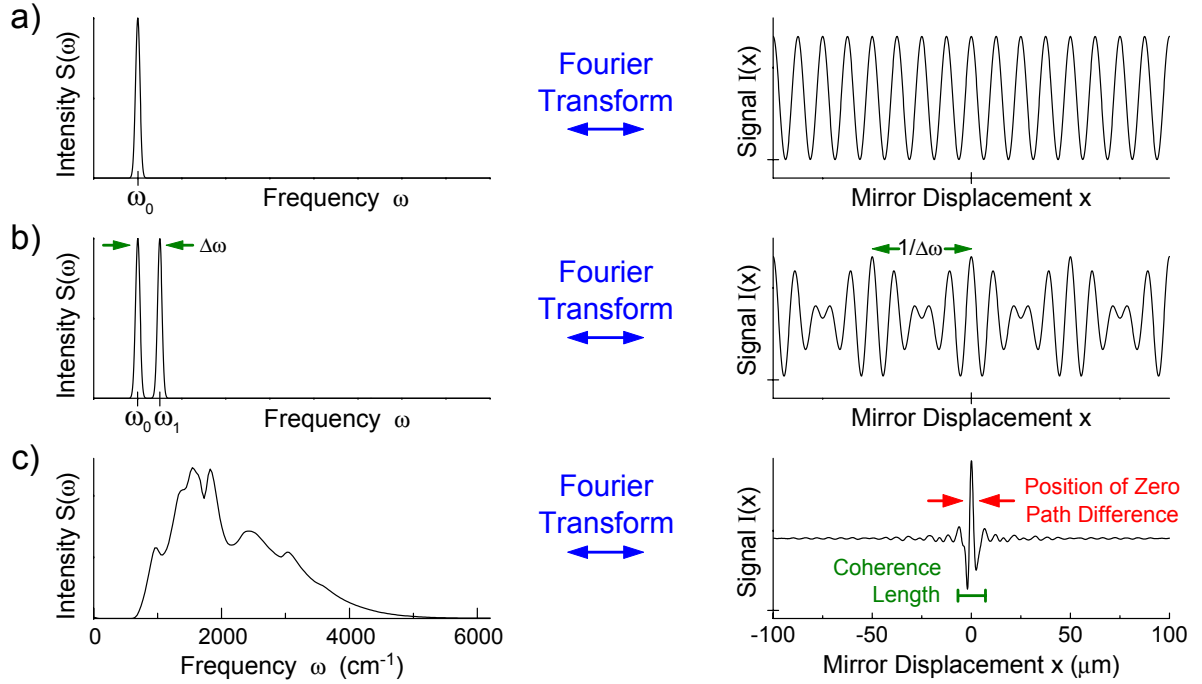


Figure 4.4: Examples of spectra (**left**) and their corresponding interferograms (**right**). **(a)** Spectrum consisting of a single frequency (e.g. laser). The Fourier transform yields a cosine. **(b)** Two frequencies. The Fourier transform consists of a sum of two cosines. **(c)** Measured single-channel spectrum of $\text{La}_{5.2}\text{Ca}_{8.8}\text{Cu}_{24}\text{O}_{41}$ ($E||c$ at 4 K). The interferogram peaks at the position of zero path difference. Just the width of the main fringes is commonly referred to as the coherence length.

This scenario has a practical use because fringes like this indicate the exact position of the moving mirror. Therefore our spectrometer is equipped with a He-Ne laser as additional light source that serves as an accurate sampling clock. In fact, the interferogram $I(x)$ contains all the spectral information and is the cosine Fourier transform of the spectrum $S(\omega)$. In this case that is equivalent to the general Fourier transform because $I(x)$ is an even function. That means that the interferometer performed a *physical* Fourier transform and just the inverse transform is needed to yield the wanted original spectrum $S(\omega)$.

The next step is to add a second laser frequency as shown in the middle panel of figure 4.4. The interferogram gets more complicated because two cosine functions with similar frequencies contribute. If the distance of the laser frequencies scales with $\Delta\omega$, the resulting beats in the interferogram scale as $1/\Delta\omega$. But normal light sources provide continuous spectra. In figure 4.4c a measured transmission spectrum of $\text{La}_{5.2}\text{Ca}_{8.8}\text{Cu}_{24}\text{O}_{41}$ with the electric field parallel to the c axis ($E||c$) is displayed. This is a so-called single-channel (or single-beam) spectrum that, apart from the sample, still depends on the characteristics of the light source, the detector, and all the other optical components within the light path. The corresponding interferogram is dominated by the main maximum I_{max} at the white-light position where the optical retardation is zero. This is the only position at which all frequencies interfere constructively. The main fringes get suppressed after a rather short displacement of the mirror, and the signal oscillates slightly around the average value of

$I_{max}/2$. For $x \rightarrow \infty$ the coherence eventually is lost and the oscillations vanish yielding a constant $I(x) = I_{max}/2$.

In real measurements the maximum displacement Δx_{max} is always limited. This is equivalent to a multiplication of the *real* interferogram by a boxcar function. In case of a monochromatic laser line the inverse Fourier transform doesn't yield a delta function anymore but a $(\sin x/x)$ function instead. This leads to side maxima in the calculated spectra and thus produces artefacts. The achievable resolution increases on extending Δx_{max} , and as a general estimate the minimum resolvable frequency $\delta\omega$ is given by

$$\delta\omega \approx 1/\Delta x_{max} \quad (4.2)$$

with $\delta\omega$ in cm^{-1} . In order to resolve ω_0 from $\omega_1 = \omega_0 + \Delta\omega$, one needs to know the interferogram at least for $x_{max} \geq 1/\Delta\omega$ (see figure 4.4b). The side maxima can be significantly reduced by avoiding an abrupt cutoff. This can be achieved by multiplying the chopped interferogram with an appropriate function that damps the edges. In this way the artefacts vanish at the expense of a slightly broadened instrumental line shape. The whole process is called *apodization*. One of the best performing functions is the three-term Blackmann-Harris function [202]. These efforts yield a highest nominal resolution of $\delta\omega = 0.114 \text{ cm}^{-1}$ for our spectrometer, but in most cases a value of 5 cm^{-1} in the mid-infrared regime is entirely sufficient. The temporal coherence may reduce the maximum resolution since the *total* coherence length of thermal light sources is limited. This causes a so-called self-apodization of interferograms when the optical retardation is greater than the overall length of the average wave packet.

After applying all necessary calculations, the result is the already mentioned single-beam spectrum. But it is quite easy to get the real transmittance and reflectance, respectively. The spectrometer is equipped with a cryostat that can move up and down very accurately over a distance of 3 cm with a stepping motor. A single step is equivalent to a displacement of 70 nm.³ Usually the sample is positioned to within 500 steps ($=35 \mu\text{m}$). In a transmittance setup this allows us to replace the sample with an empty aperture as a reference during the measurement. If the light spot is smaller than the sample aperture, the latter does not influence the spectra, and the ratio of the two single-beam spectra directly yields the transmittance $T(\omega)$:

$$T(\omega) = \frac{S_{\text{sample}}(\omega)}{S_{\text{ref}}(\omega)} . \quad (4.3)$$

In case of a reflectance measurement, a gold or aluminum mirror acts as a reference. It is important to correct the spectrum by multiplying it with the known $R_{\text{ref}}(\omega)$ of the mirror:

$$R(\omega) = \frac{S_{\text{sample}}(\omega)}{S_{\text{ref}}(\omega)} R_{\text{ref}}(\omega) . \quad (4.4)$$

Another important advantage of the movable cryostat shall not remain unmentioned: The cold finger on which the sample is mounted shrinks upon cooling down. Therefore the sample does not reside at the focal point any more and the intensity drops. By moving down the cryostat a bit this can easily be readjusted. In practice, one can move the cryostat and record the intensity for different positions. If the light spot is smaller than the sample aperture, there exists a plateau where the spectrum is not influenced by the sample aperture. The center of this plateau is then chosen for the measurement.

³Of course the slackness is way bigger.

4.1.2 Problems to Take Care of

With Fourier spectroscopy as with any other experimental setup there are numerous sources of errors. Permanent verification of the data consistency is crucial to obtain reliable results.

Polarizers

Since the samples presented in this thesis show orthorhombic symmetry, a polarizer is needed to measure the different crystal axes separately. It is typical for all optical components that the frequency range is limited, and to cover a wide region several polarizers are necessary. Most measurements were carried out with a BaF₂ polarizer. It consists of a BaF₂ substrate and thin aluminum stripes evaporated on one of the surfaces with a grid spacing of 250 nm. In general, the performance is characterized by the two principal transmittances k_1 and k_2 . They are defined as the maximum and minimum transmittance of a single polarizer when it is rotated in a perfectly polarized beam. The general transmittance in perfectly polarized light is

$$T_{\text{single}}(\alpha) = k_1 \cos^2 \alpha + k_2 \sin^2 \alpha, \quad (4.5)$$

where α is the angle between the polarization direction of the incident light and the direction of highest polarizer transmittance. The latter is also referred to as the principal axis. An ideal polarizer would have values of $k_1 = 1$ and $k_2 = 0$. To measure k_1 and k_2 , usually two identical polarizers are placed into an unpolarized beam. In this case the total transmittance in unpolarized light is [206]

$$T_{\text{double}}(\theta) = k_1 k_2 \sin^2(\theta) + \frac{1}{2}(k_1^2 + k_2^2) \cos^2(\theta). \quad (4.6)$$

Here, θ denotes the angle between the principal axes of the two polarizers. Of course both the parameters k_1 and k_2 depend on the frequency, and there is always just a certain frequency window in which k_1 is reasonably high and k_2 small enough at the same time.

The correction of the error that arises from the *wrong*, or unwanted polarization due to k_2 is particularly important when the sample is transparent in one direction and almost opaque in the orthogonal direction. In this case most of the intensity measured in the latter direction is just an artefact. Fortunately, this can be corrected if the extinction ratio k_2/k_1 of the polarizer is known. For that purpose the standard measurement as described above was not applicable since we own just *one* BaF₂ polarizer. However, the strong anisotropy of our samples also implies a possibility to measure the extinction ratio directly. In the telephone-number compounds the onset of electronic excitations is observed at lower frequencies for polarization parallel to the ladders than for the perpendicular directions (see chapter 5.2). Therefore there is a window at high frequencies in which the sample acts as a perfect polarizer.

In figure 4.5 three sets of single-beam ratios are presented. For each sample and each temperature the *c*-axis spectrum has been divided by the corresponding *a*-axis data. One can see clearly that starting from a certain frequency the ratios fall on top of each other. When the ratios become temperature independent, it is straightforward to conclude that all the measured *c*-axis intensity stems from leakage from the *a* axis due to the BaF₂

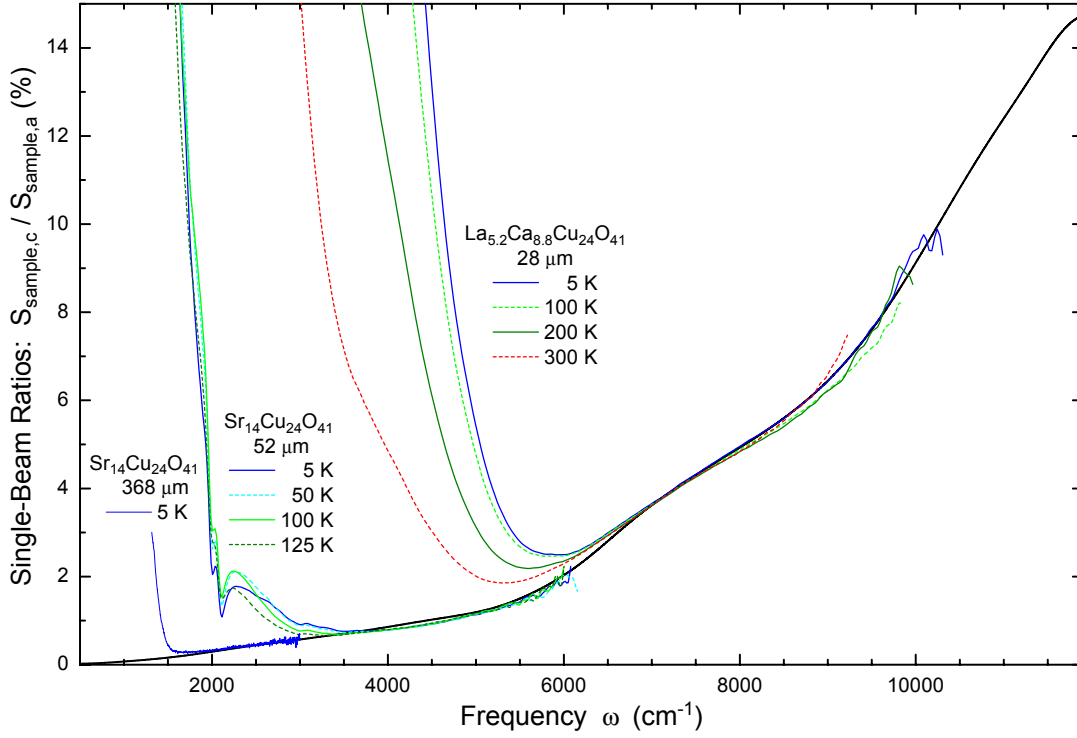


Figure 4.5: Extinction ratio k_2/k_1 of the BaF₂ polarizer (black line). Three sets of exemplary single-beam ratios of the telephone-number compounds are also shown. For several temperatures the c -axis spectra have been divided by the a -axis data. As soon as the c axis is opaque for the respective thickness at high frequencies, the entire intensity for “ $E||c$ ” stems from the unwanted polarization, and the ratios fall on top of each other. Finally lots of measurements for different thicknesses build up the complete extinction ratio. Below $\omega = 1700 \text{ cm}^{-1}$ the ratio is extrapolated.

polarizer. With increasing temperature the onset of charge excitations is observed at lower frequencies, which then allows to determine k_2/k_1 as well down to lower frequencies. Instead of increasing the temperature even higher, a thicker sample also does the job. Accordingly, a very thin sample is needed to cover the high frequency regime. At last, the black curve is the result of seven different measurements including different samples, sample thicknesses, detectors, lamps and beam splitters. It is obvious that the extinction ratio gets worse at higher frequencies, and 12000 cm^{-1} is the upper limit of reasonable operation for the BaF₂ polarizer.

To understand why the black curve indeed is identical to the extinction ratio one has to recall the definitions of k_1 and k_2 . k_2 is the minimum transmittance of the polarizer in a perfectly polarized beam (see equation 4.5). When the c axis of the sample is completely opaque, we get exactly this situation. Actually, the polarizer is located in front of the sample, yet the order with respect to the beam does not matter. This arrangement is sketched in figure 4.6. Thus the ratio k_2/k_1 of the polarizer is equivalent to the ratio of the minimum and maximum intensity, i.e.

$$k_2/k_1 = S_{\text{sample},c}/S_{\text{sample},a} . \quad (4.7)$$

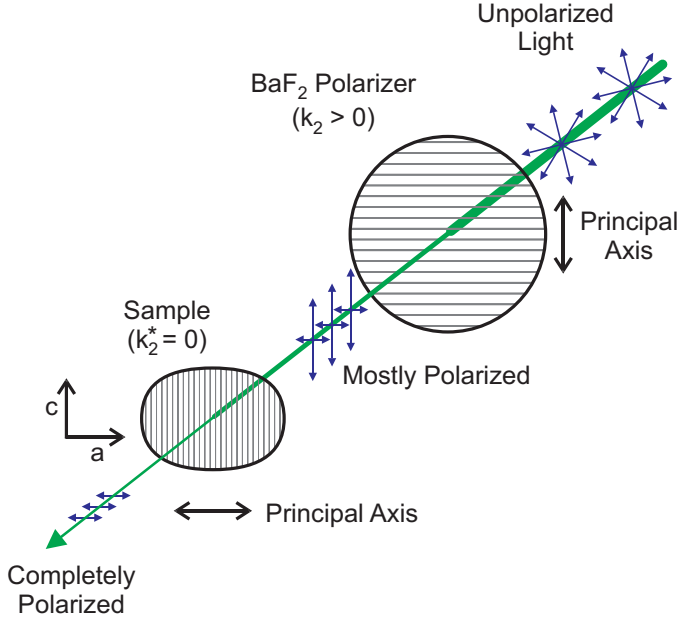


Figure 4.6: Determination of the extinction ratio k_2/k_1 . The light with the electric field parallel to the wires leads to currents and thus gets damped. Since the BaF₂ polarizer provides a $k_2 > 0$, the transmitted light is just *mostly* polarized. In the spin-ladder compounds the ladders along the c direction represent the wires. After traversing the sample, which acts as a perfect polarizer, the dim remaining light is just due to the erroneous k_2 contribution from the polarizer. To measure the k_1 contribution the BaF₂ polarizer needs to be turned by 90°.

The knowledge of the absolute value of the transmittance is only necessary if one wants to determine k_1 and/or k_2 separately but not for the ratio k_2/k_1 . Note that this equation is only true as long as the sample acts as a perfect polarizer and that the c -axis spectrum is non-zero just because of the imperfect BaF₂ polarizer.

Now since the extinction ratio is known, it is possible to correct all measured spectra in order to get rid of the polarizer error. When c and a are the *real* c -axis and a -axis single-beam spectra, respectively, and the index “meas” denotes the *measured* spectra, then

$$c_{\text{meas}} = k_1 c + k_2 a \quad \text{and} \quad a_{\text{meas}} = k_1 a + k_2 c \quad (4.8)$$

in analogy with equation 4.5. The same holds true for the reference spectra ref_c as well as for ref_a . It might be surprising that even the reference spectra show a polarization dependence. The reason is that most of the mirrors inside the spectrometer reflect at non-normal incidence. Therefore a certain polarization direction is preferred, according to the Fresnel equations. Simple rearrangement of equation 4.8 yields e.g. for the c -axis single beams

$$c = \frac{c_{\text{meas}} - (k_2/k_1) a_{\text{meas}}}{k_1 (1 - k_2^2/k_1^2)} \quad \text{and} \quad \text{ref}_c = \frac{\text{ref}_{c,\text{meas}} - (k_2/k_1) \text{ref}_{a,\text{meas}}}{k_1 (1 - k_2^2/k_1^2)}.$$

To calculate the final c -axis transmittance as shown in equation 4.3, c has to be divided by ref_c and the denominator drops out:

$$T_c = \frac{c_{\text{meas}} - (k_2/k_1) a_{\text{meas}}}{\text{ref}_{c,\text{meas}} - (k_2/k_1) \text{ref}_{a,\text{meas}}}. \quad (4.9)$$

The impact of the correction on the transmittance is demonstrated in figure 4.7. The left panel shows T of the a - and c -axis polarization of La_{5.2}Ca_{8.8}Cu₂₄O₄₁. Dashed lines indicate the uncorrected spectra whereas solid lines represent the corrected data. The

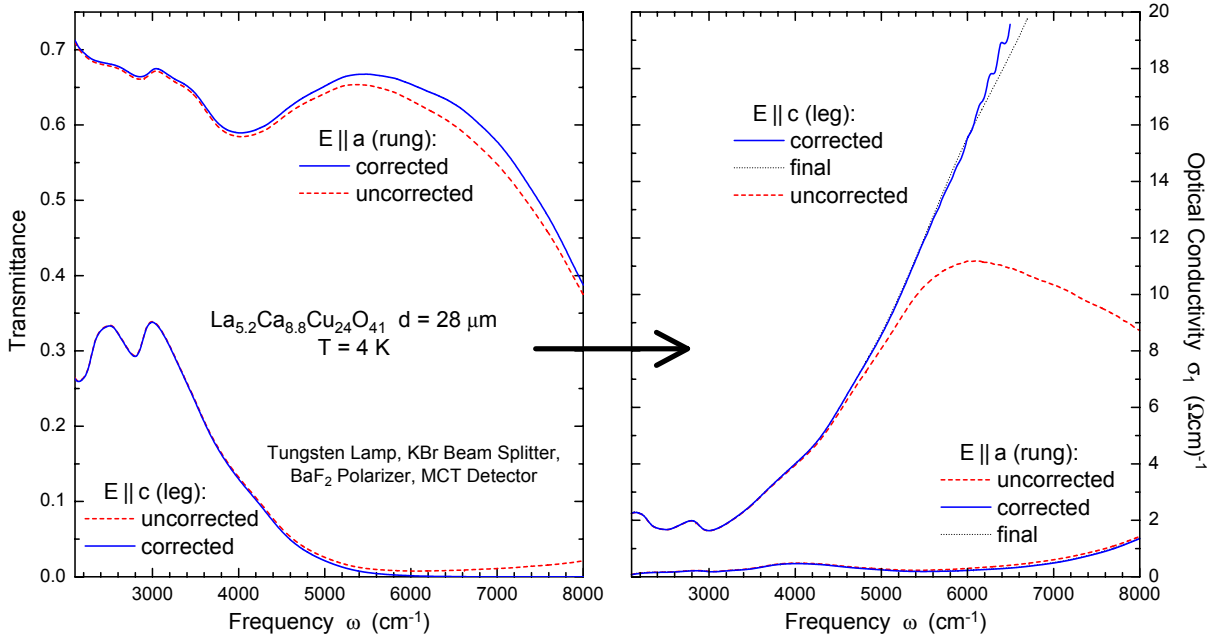


Figure 4.7: The effect of correcting the polarizer error. The **left** panel shows the transmittance of a $d = 28 \mu\text{m}$ thick $\text{La}_{5.2}\text{Ca}_{8.8}\text{Cu}_{24}\text{O}_{41}$ sample at 4 K. Dashed lines indicate the uncorrected spectra whereas solid lines denote the corrected ones. Above 6000 cm^{-1} there is a large impact on the c -axis spectrum, which in fact becomes opaque. The correction gets even more obvious on comparing the calculated conductivities shown in the **right** panel. Black dotted lines show the final conductivities calculated using four sets of different measurements. The high-frequency data above 4600 cm^{-1} stems from a thinner sample of $d = 6 \mu\text{m}$. The excellent agreement between the corrected data of the $28 \mu\text{m}$ sample and of the $6 \mu\text{m}$ sample shows that it is very well possible to correct for the polarizer leakage.

first impression tells that mainly the a axis benefits. Yet the c -axis correction is more dramatic. Above 6000 cm^{-1} the c axis is almost opaque, which is not obvious at all from the uncorrected spectrum. The consequences on the conductivity presented in the right panel hopefully convince the reader. The a -axis data is almost unchanged but the shape of the corrected c -axis spectrum is completely different from the uncorrected one. The right panel also shows the final data sets as dotted black lines. These were calculated using four different measurements including a thinner sample of $d = 6 \mu\text{m}$ and a completely different polarizer. The employed Glan-Taylor polarizing prism has a substantially lower extinction ratio of approximately 1% at frequencies above 5000 cm^{-1} . Since the corrected spectra resemble the final data sets very well, we can conclude that the polarizer problem is greatly reduced.

Interference Fringes

In a transmittance measurement, the surface roughness of the sample has to be smaller than the shortest wavelength of the incident light. Otherwise, scattering might disturb the spectrum particularly at high frequencies. Therefore all the samples presented in

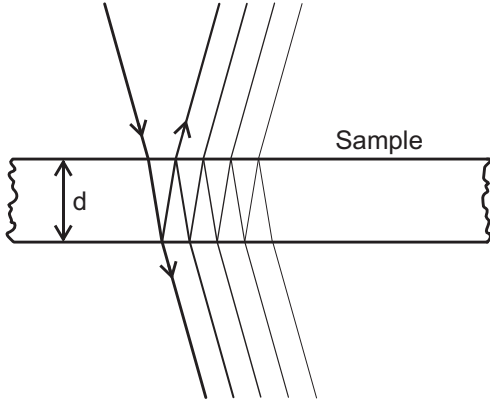


Figure 4.8: Fabry-Perot fringes. Multiple reflections at both the faces of the thin sample lead to interference fringes that overlay the spectrum. The path difference between adjacent beams is approximately $2nd$.

this thesis were polished (see section 4.2). But shiny parallel faces also produce multiple reflections *inside* the sample, which lead to Fabry-Perot interferences (figure 4.8). The resulting fringes reduce the resolution of the measurement. The width $\Delta\omega$ of these fringes broadens by reducing the sample thickness d :

$$\Delta\omega = \frac{1}{2nd} \quad (4.10)$$

with $\Delta\omega$ in cm^{-1} , d in cm, and n being the refractive index. Figure 4.9 demonstrates the problem: In the left panel the thin line denotes a high-resolution measurement of the already mentioned $28 \mu\text{m}$ thick sample of $\text{La}_{5.2}\text{Ca}_{8.8}\text{Cu}_{24}\text{O}_{41}$. The period of the fringes is $\Delta\omega = 75 \text{ cm}^{-1}$. The amplitude becomes smaller when the transmittance gets lower, because the increased absorption inside the sample reduces the effect of multiple reflections. Upon lowering the resolution, the fringes finally disappear (red line). The inset shows a measurement of a $6 \mu\text{m}$ specimen of the same material. Here, $\Delta\omega$ already reaches 380 cm^{-1} and thus all the fine structure of the spectrum is lost.

The right panel contains the interferogram of the single-beam spectrum that was used to calculate the high-resolution transmittance of the $28 \mu\text{m}$ sample. Since the fringes mainly consist of a single frequency, characteristic peaks show up in the interferogram. To avoid the fringes upon reducing the resolution just means cutting the interferogram at the black brackets (see equation 4.2). But the fringes also disappear by exceeding this border by a bit. Because of the used apodization function the peaks still get sufficiently suppressed. This is the reason why a nominal resolution of 60 cm^{-1} already suppresses fringes with a period of 75 cm^{-1} . We got even better results, though, by smoothing the high-resolution spectrum with the use of a fast-Fourier transform. The corresponding thick black curve in the left panel resembles the 60 cm^{-1} data pretty good, but it shows no artefacts as the latter does.

Already at this point the outline of how to accurately determine a complete spectrum becomes clear. To measure the frequencies at which the conductivity is large, a thin sample is necessary. Since at these frequencies the transmittance is low, the fringes are absent. To measure the missing parts of the spectrum with low conductivity a thicker sample has to be prepared. Then the high transmittance is lowered, and again the amplitude of the fringes is low. In addition, the period of the fringes is small due to equation 4.10, and therefore the resolution is higher. Section 6.2 for instance describes how the a -axis

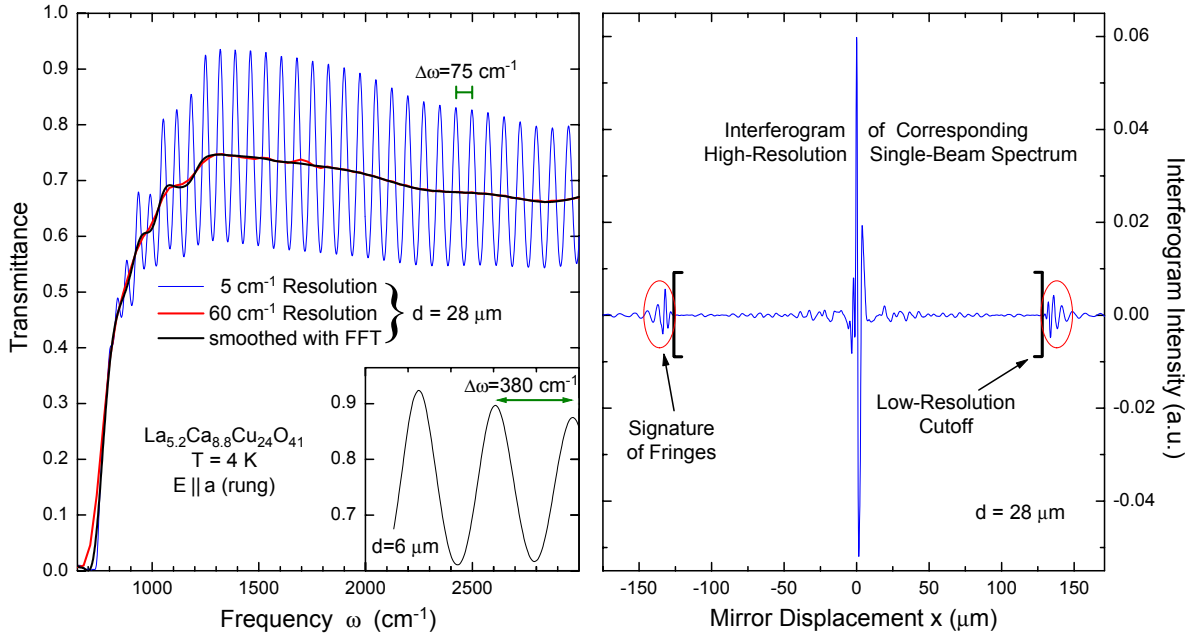


Figure 4.9: **Left** panel: High-resolution transmittance of a $28\ \mu\text{m}$ thick sample of $\text{La}_{5.2}\text{Ca}_{8.8}\text{Cu}_{24}\text{O}_{41}$ (thin line). The period of the fringes is $\Delta\omega = 75\ \mu\text{m}$. The low-resolution spectrum shows no fringes anymore. Smoothing the first spectrum with a fast-Fourier transform yields a slightly better result (thick black line). The inset shows the transmittance of a $6\ \mu\text{m}$ thick specimen with quite large fringes of $380\ \text{cm}^{-1}$. **Right** panel: Measured interferogram of the corresponding high-resolution single-beam spectrum ($d = 28\ \mu\text{m}$). The signatures of the fringes are quite characteristic, and by cutting the interferogram the fringes disappear.

spectrum of $\text{Sr}_{14}\text{Cu}_{24}\text{O}_{41}$ is built up of measurements using three samples with different thicknesses of $d = 20, 52$, and $368\ \mu\text{m}$. After all, there also is an advantage of the whole fringe phenomenon. If transmittance and reflectance are known, the fringes act as a very accurate probe for the sample thickness. Especially for thin samples of less than $50\ \mu\text{m}$ this determination is more reliable than the measurement with a microscope.

Frequency Doubling

The absolute effect of ghost spectra at the double frequency on the transmittance is rather small. But as with the polarizer problem the conductivity is strongly affected. This effect is not to be mistaken for the so-called aliasing [202, 203], which is well taken care of and not described here.

The left panel of figure 4.10 again shows transmittance data of the $28\ \mu\text{m}$ sample of $\text{La}_{5.2}\text{Ca}_{8.8}\text{Cu}_{24}\text{O}_{41}$. The fringes are smoothed away, and the polarizer error is corrected. The c -axis data at 4 and 400 K measured with an infrared globar and a near-infrared tungsten lamp overlap very well at low frequencies. The resemblance of the 4 K data even extends to higher frequencies. The 400 K spectra, though, disagree above $3000\ \text{cm}^{-1}$. The globar spectrum shows additional intensity with clearly visible fringes. This is surprising since the main fringes already got filtered. Strictly speaking, the period of the new fringes

is exactly doubled compared to the main fringes. This is the reason why the additional fringes survived the smoothing procedure and there is a strong hint towards a frequency-doubling problem.

To go one step further, the right panel of figure 4.10 shows the uncorrected single-beam spectrum of the 400 K transmittance measured with the globar (black line). Only the interesting part is plotted. Also presented is the same spectrum but with all frequencies multiplied by two. Afterwards the result got scaled down to match the excess intensity of the original data. One can see quite clearly that above approximately 3200 cm^{-1} the shapes of the two spectra are very similar. In particular the fringes are identical. Thus the original spectrum contains a small contribution of the erroneous frequency-doubled data.

It is obvious that this erroneous contribution is only observable when there is lots of intensity that is mirrored into a region of low intensity. This is the case for the 400 K globar data. The inset of the right panel shows the complete corresponding single-beam spectrum (solid line) with high intensity around 1500 cm^{-1} and low intensity above 3000 cm^{-1} . The tungsten spectrum (dotted line) has considerably less intensity below

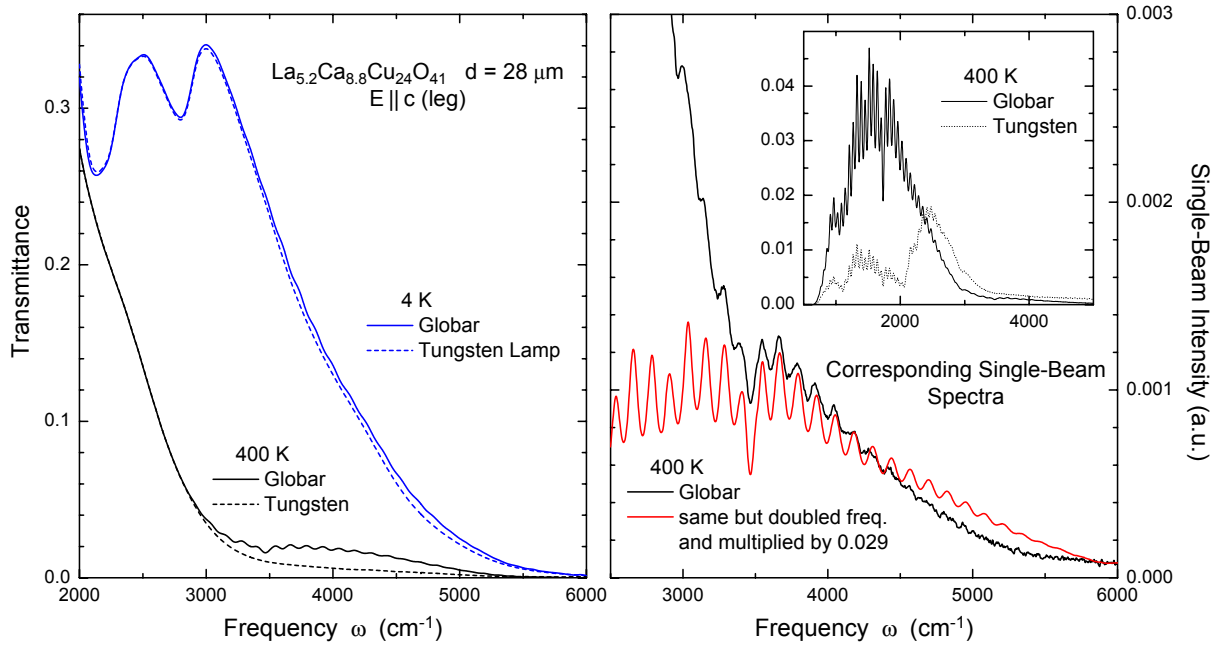


Figure 4.10: The problem of frequency doubling. **Left** panel: Smoothed transmittance of $\text{La}_{5.2}\text{Ca}_{8.8}\text{Cu}_{24}\text{O}_{41}$ (c axis, $d = 28\text{ }\mu\text{m}$) at 4 and 400 K. In particular at 400 K the high-frequency parts measured with globar (solid) and tungsten lamp (dashed) disagree. The globar data shows additional intensity and fringes twice as broad as the filtered main fringes. **Right** panel: Corresponding 400 K single-beam spectrum measured with the globar. The data is unsmoothed, and just the interesting region is plotted. Also shown is the same data but stretched via frequency doubling with subsequent down-scaling. The fringes in the two spectra match. The inset shows the complete globar single-beam spectrum along with the tungsten spectrum (dotted). Due to the overall shape the latter doesn't entail erroneous contributions.

2000 cm^{-1} . This explains why the tungsten data in the left panel is almost unaffected by the frequency-doubling problem, whereas in the case of the globar data the frequency-doubled contribution at $\omega \geq 2 \times 1500\text{ cm}^{-1}$ is comparable to the real intensity at $\omega \geq 3000\text{ cm}^{-1}$. The shapes of the 4 K spectra are less critical for both lamps since the real intensity at $\approx 3000 - 5000\text{ cm}^{-1}$ is much larger than the erroneous frequency-doubled contribution. Fortunately, there is no need to correct the globar spectra, which actually would be a difficult task. Below 3000 cm^{-1} the agreement of the data sets is excellent, and above this frequency the globar data is sort of dispensable. But the problem is always very likely to occur when there is a sharp drop of intensity in any spectrum. This may lead to serious artefacts in the optical conductivity.

The only remaining task is to explain why frequency doubling occurs at all. Basically, this is a common problem with grating spectrometers due to second-order reflections. Yet here the reason is a completely different one. As described in section 4.1 and in the corresponding figure 4.3, the two partial beams that leave the interferometer have a path difference of δ . Afterwards, these beams hit several faces like the polarizer, the first cryostat window, the sample aperture, and of course the sample itself. Every face reflects back a small part of the intensity. Thus each time we get two new partial beams that enter the interferometer for a second time at its actual output. The scene inside the interferometer is equivalent to the already described first passing through of the original beam. That means that one part of the additional intensity runs towards the lamp and causes no trouble. However, the other part leaves the interferometer, again targeted at the sample. Since two separate beams entered, there are *four* ghost beams that leave the interferometer towards the sample. These ghost beams have a retardation with respect to the main beams which is larger than the coherence length. Therefore we only need to consider the interference *within* the four ghost beams. The second and third one of these rays both have a path difference of δ compared to the first new ray. These beams cause no trouble but just add to the overall intensity that reaches the sample.⁴ But the optical retardation of the forth additional beam with respect to the first one is 2δ . This is exactly equal to a doubled frequency in the interferogram and yields the ghost spectrum described above. This becomes clear after recalling, for example, the oscillations due to a unique laser frequency in the interferogram. A single period of a *ghost* laser oscillation would already be completed at half the mirror displacement compared to the main oscillation. And this is equivalent to a second weak laser operating at the double frequency.

As mentioned above, there is a further retardation between the two original beams and the additional ones. Even worse, there are retardations between the different sets of additional beams that originate from the different reflecting faces. But fortunately these path differences are way bigger than δ and by far exceed the coherence length. Therefore the phase information is lost, and no additional interference occurs. This just means that at the time when the additional beams from a certain wave packet reach the detector the original beams from the *same* wave packet are long gone. Accordingly, just the *amplitudes* of the original spectrum and the broadened ghost spectrum add up. Nevertheless it is basically impossible to correct for the ghost spectrum since its line shape is different from the shape of the original spectrum. This is due to the fact that the intensity of the original

⁴The contribution which stems from the reflection of the sample is not present in the reference measurement on an empty aperture, and therefore contributes to a slightly too large transmittance signal.

spectrum is proportional to $(tr e^{i\delta} + rt)^2$, whereas the ghost spectrum is proportional to $(rt^3 + tr^3 e^{i2\delta})^2$ (confer figure 4.3).

Black-Body Radiation

As mentioned above, our cryostat allows us to heat the samples up to 800 K. But at this temperature the sample itself acts as a considerable light source. The global for example, being our standard infrared lamp, also is just a thermal source that operates at a temperature of approximately 1700 K. A fraction of the black-body radiation from the sample directly reaches the detector. Fortunately, this light contribution does not produce an ac detector signal as the beams from the interferometer do and therefore produces no harm. The only effect is to reduce the sensitivity of the detector since the main ac signal is superposed by a dc background. In the worst case the detector may get overloaded. But there also is a contribution that takes the opposite direction and enters the interferometer. The situation then is sort of similar to the frequency-doubling problem described in the previous section. However, now there is no frequency doubling because the extra beams traverse the Michelson unit only once. And beyond all question the extra black-body radiation is completely incoherent with respect to the light from the lamp.

Yet very surprising phenomena may occur. The left panel of figure 4.11 shows several single-beam spectra of a 40 μm thick LaMnO_3 sample in transmission setup at a temperature of 500 K [207]. With decreasing input-aperture size the intensity diminishes. Note that the 1 mm data (dash-dotted line) is divided by 2. But the spectrum measured with the smallest aperture of 0.25 mm shows a very different shape. At frequencies below approximately 1500 cm^{-1} almost all the spectral weight is missing, which is not the case at lower temperatures. During the experiment it is possible to close the input aperture completely. The lamp gets blocked and ideally no oscillating intensity should reach the detector. This is not the case, and the left panel of figure 4.11 shows the measured black-body spectrum with the hot sample as the actual light source. Interestingly, the maximum intensity is located at approximately 1000 cm^{-1} and seems to coincide with the region of maximum suppression in the 0.25 mm spectrum. The first idea may be that destructive interference causes the loss of intensity but, as mentioned above, the sources are completely incoherent.

The corresponding interferograms are plotted in the right panel of figure 4.11. It is not that unusual that the absolute value of the main minimum is larger than that of the main maximum. The reasons are equal to the origin of asymmetrical interferograms in general. For instance none of the sampling positions matches the proper position of zero path difference. On the other hand there are always frequency-dependent phase delays of the optical components. These are e.g. due to the ω dependence of the refractive index $n(\omega)$, which gives rise to frequency-dependent optical path lengths. When the spectrometer is not aligned perfectly, the interfering beams experience different phase delays. That means that for every frequency the position of zero path difference is slightly shifted. Both effects are usually unavoidable and after the Fourier transform they yield a complex spectrum rather than a real one. Each value can be represented either by a sum of real and imaginary part or by the product of modulus (or amplitude) and a phase factor. The so-called Mertz method [208] calculates the phase spectrum and finally the modulus,

which is equal to the proper intensity. When noise is involved, this procedure is superior to computing the amplitude directly. Yet the amplitude of the complex spectrum is only equal to the proper spectrum when there is a single phase error for every frequency.

At this point the problem becomes evident. The intruding beams from the hot sample take a completely different path through the interferometer than the main beams. Again, figure 4.3 helps to demonstrate the situation. The two main beams both *traverse* the beam splitter once. But the two extra beams differ because one of them traverses the beam splitter twice whereas the other one gets reflected twice *without* traversing the beam splitter at all. Thus there is an additional phase shift between the two rays of $2nd$ with respect to the phase shift of the original beams. Here n and d are the refractive index and the thickness of the beam splitter, respectively. The given example of figure 4.11 is kind of extreme since the difference of the phases is almost equal to π . This means that the interferogram of the black-body spectrum has the opposite sign compared to the ones with open input aperture. Since summing up interferograms of different sign is equivalent to a subtraction of spectra it is comprehensible that adding the hot sample as a second

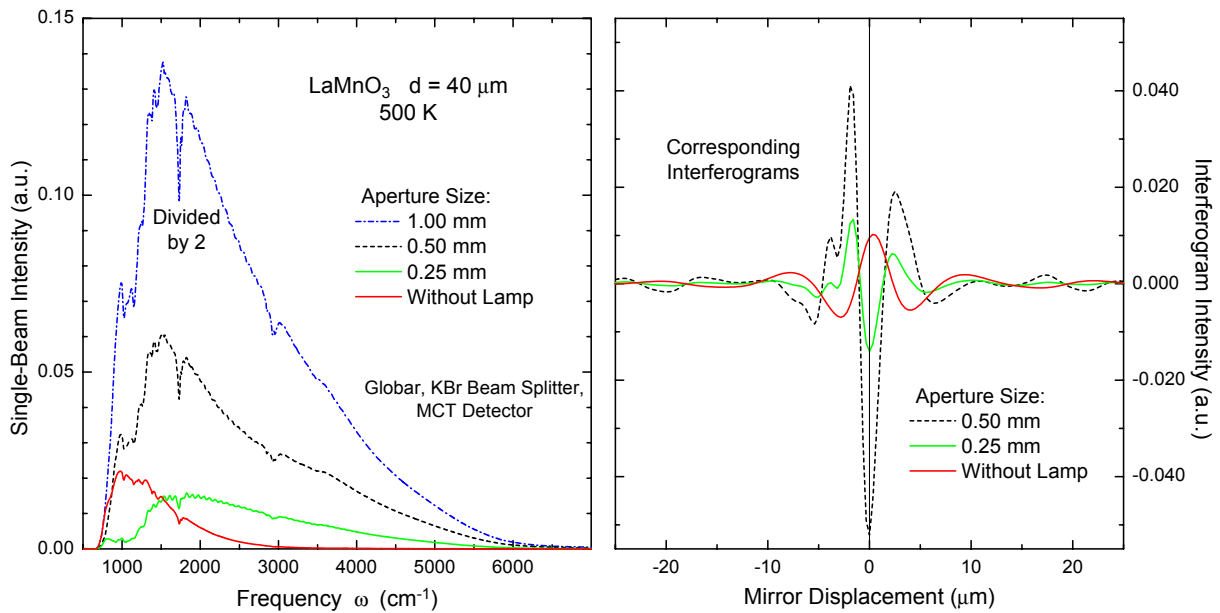


Figure 4.11: Effect of black-body radiation at 500 K [207]. **Left** panel: Single-beam spectra of a $40\ \mu\text{m}$ LaMnO_3 sample in transmittance setup. Note that the 1 mm spectrum is divided by 2. The spectral shape measured with the smallest aperture size of 0.25 mm is very different compared to the other spectra. The measured black-body spectrum of the sample with blocked lamp is also included. Its intensity seems to be identical to the missing weight of the 0.25 mm spectrum. **Right** panel: Corresponding interferograms. The illuminated sample shows minima as main extremal values. The black-body interferogram is more symmetrical and the main extremal value is a maximum. It seems as if this interferogram got multiplied by -1 which is equivalent to an additional phase shift of π between the two interfering beams. But this is just an approximation since the position of the maximum is shifted slightly compared to the main minima of the “illuminated” interferograms.

light source in this case yields less intensity in the final spectrum. The intensity of the erroneous contribution is independent of the chosen entrance aperture. Therefore the error becomes negligible at large entrance apertures. The rule of thumb is: The lower the frequency or the higher the temperature of the sample, the larger the entrance aperture has to be.

The last remaining question concerning the ghost-intensity problems is: Why is this phase-shift problem not relevant for the discussion of the frequency-doubling phenomenon? The corresponding extra beams take the same way through the Michelson unit as the black-body beams. However, the difference is that the former beams are so weak that they have only very little influence on the main spectrum. The effect is only visible in frequency ranges where the main spectrum is almost zero.

Detector Non-Linearity

Some detectors generate a non-linear response with respect to the incident light intensity. Most of the data presented in this thesis was measured with an MCT detector⁵. Unfortunately, of all available detectors the MCT detector is quite prone to this complication. As shown before, the typical interferogram consists of a few main fringes that soon fade, and the details of the spectrum are determined by the small wiggles that follow. These wiggles are not affected by the non-linear response, but the main maximum will be sampled with a too small value. Thus, this error is restricted to a small regime of the interferogram around the position of zero path difference. As a general guideline, narrow features in the interferogram cause broad effects in the corresponding spectrum. The most obvious symptom is a non-zero intensity in a frequency region of the spectrum where actually none is expected. There are two options to make use of such a detector. The first would be not to exceed a certain incident intensity so that the maximum intensity is still within the linear range. Obviously this option yields a poor signal-to-noise ratio. Otherwise the interferogram has to be corrected before executing the Fourier transform.

In figure 4.12 the black solid line represents a corrected single-beam spectrum. The very same interferogram leads to a different spectrum when no linearity correction is carried out. The overall intensity is reduced and there is lots of signal below 1000 cm^{-1} , where there is no weight at all in the corrected spectrum. Even worse, the whole spectral shape below 2100 cm^{-1} is completely wrong. The uncorrected interferogram actually produces negative intensities below this certain frequency that is folded upwards by the phase correction. This becomes clear when the phase correction is also omitted. The dashed line depicts the pure real part of the complex spectrum and in fact, at 2100 cm^{-1} it crosses the x axis. Likewise, the pure imaginary part of the complex spectrum is plotted as dotted line.

The correction for non-linearity is always calculated prior to the Fourier transform of any MCT interferogram. High signal values get amplified insofar that there is no false intensity below 600 cm^{-1} anymore, which is the low-frequency limit of our specific MCT detector.

⁵MCT is short for the narrow-gap semiconductor mercury cadmium telluride: $\text{Hg}_{1-x}\text{Cd}_x\text{Te}$ with $x \approx 0.2$. The detector has to be cooled down to 77 K.

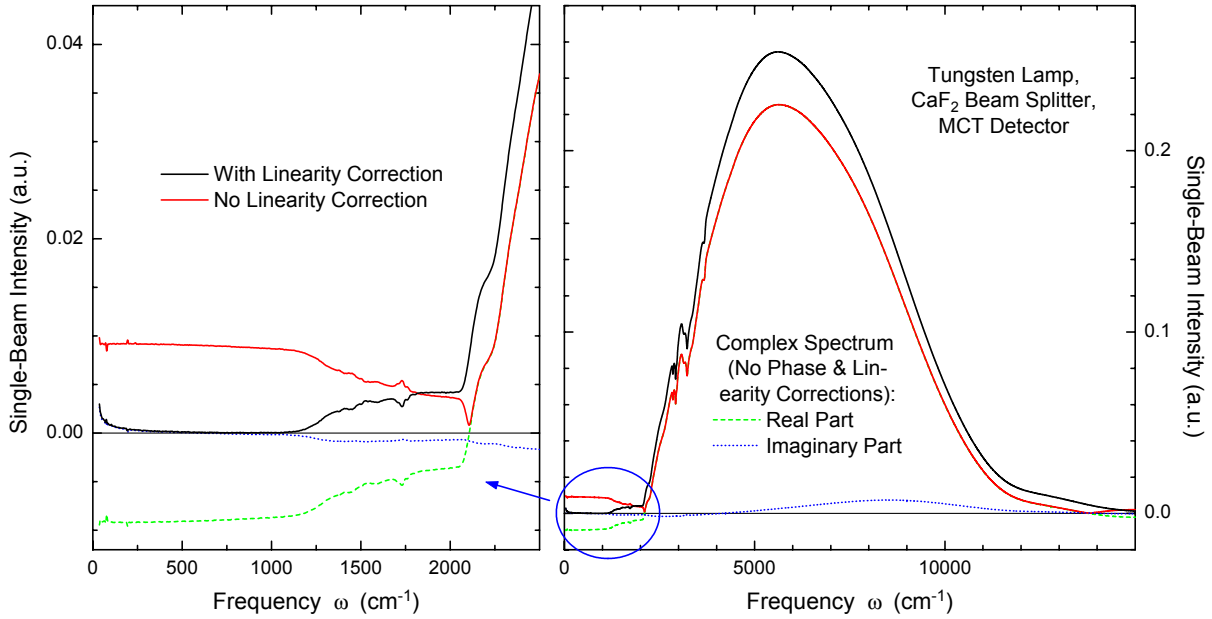


Figure 4.12: Non-linearity of the MCT detector. The **left** panel shows a blow-up of the indicated low-frequency regime. The corrected standard spectrum is plotted as black solid line. The uncorrected spectrum calculated from the identical interferogram is quite different. Also included are the real part (dashed line) and the imaginary part (dotted line) of the complex spectrum without any correction for non-linearity and phase errors. The *positive* values of the real-part spectrum (dashed) agree completely with the corresponding phase-corrected values.

4.2 Sample Preparation

The samples of the spin-ladder compounds discussed in this thesis were grown by U. Ammerahl [6, 7] and M. Hücker ($\text{La}_{5.2}\text{Ca}_{8.8}\text{Cu}_{24}\text{O}_{41}$) with the group of A. Revcolevschi at the Laboratoire de Chimie des Solides, Université Paris-Sud. The single crystals are of very high quality and great detail is given in the PhD thesis of U. Ammerahl [8]. The applied travelling-solvent-floating-zone (TSFZ) method using image furnaces has the advantage that no crucibles are necessary, which tend to contaminate the samples. Also, it is possible to adjust the parameters immediately to prevent anomalies during the crystallization process. The general applicability of the TSFZ method to successfully grow low-dimensional cuprates is discussed in reference [209].

All the used specimens are single crystals as verified with an optical microscope using polarized light. This method serves as a very important test because parasitic phases can be pinpointed down to micrometer dimensions. Moreover, misaligned crystallites are visible in optically anisotropic systems such as spin-ladder compounds. Selected specimens were checked by neutron scattering. Rocking curves, for instance, reproduced the minimal line width of the used triple-axis spectrometer [6]. One of the advantages of neutrons is the small absorption, which allows to probe real bulk properties. Further tests included x-ray powder diffraction, electron microscopy, energy-dispersive x-ray analysis (EDX), and Laue x-ray back-reflection. All these checkups verified the excellent quality of the single crystals.

The oxygen stoichiometry is always a critical parameter with transition-metal oxides. $\text{YBa}_2\text{Cu}_3\text{O}_{6+x}$ probably is one of the most prominent examples since the phase diagram is very sensitive to the precise oxygen content. The maximum superconducting transition temperature T_c of approximately 91 K is only reached close to the optimal doping level of $x = 6.93$. Therefore a verification of the oxygen content of the spin ladders is obvious. But the determination is quite difficult. X-ray and EDX analyses are usually not accurate enough. In reference [8] the results of thermo-gravimetric measurements are presented. Highly sensitive scales weighed powdered samples while the temperature was increased up to 950°C and afterwards lowered to room temperature again. In an H_2/N_2 atmosphere the powder reacted with the hydrogen and the products were analyzed with x-ray scattering. When all products and the loss of mass are known, the oxygen content can be calculated. Figure 4.13 shows that all the examined samples contain a slight amount of excess oxygen. The actual stoichiometry of the samples thus rather corresponds to $\text{A}_{14}\text{Cu}_{24}\text{O}_{42}$. The excess oxygen binds electrons and hence introduces holes. A nominally undoped sample, for instance, corresponds to $\text{A}_{14} = \text{La}_8\text{Ca}_6$, in contrast to $\text{A}_{14} = \text{La}_6\text{Ca}_8$ for an oxygen content of 41. However, the limit of La solubility is reached already close to a La content of five (see page 41). Already at temperatures below 200°C in an atmosphere of 1 bar O_2 , the excess oxygen starts to leave the pulverized samples [8]. But this does not seem to be a problem for our optical measurements. During a transmittance run a sample of $\text{La}_4\text{Ca}_{10}\text{Cu}_{24}\text{O}_{41}$ was measured at a temperature of 230°C in a vacuum of 3×10^{-5} mbar. A cross-check after cooling down again to room temperature revealed no changes of the transmittance. The reason might be that the diffusion is slower in single crystals than in powders.

The grown single-domain rods typically have an elliptical cross-section and a length of 40 - 70 mm. The semi-major axis of usually 5 mm corresponds to the crystallographic a axis whereas the semi-minor axis (usually 4 mm) is parallel to the b axis. The c axis typically does not deviate by more than 10° from the direction of growth. One can conclude that the formation of new atomic layers is easiest along the c axis, which is the

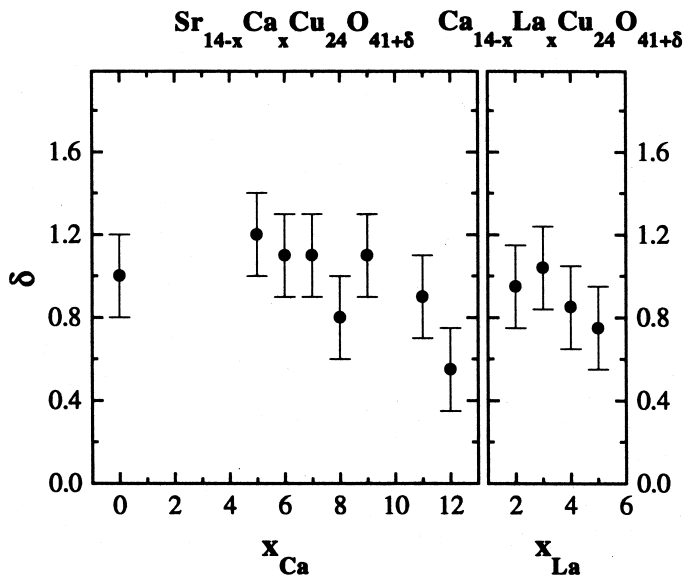


Figure 4.13: Oxygen content of telephone-number compounds grown by Ammerahl et al. with Sr, Ca, and La substitution. All the crystals contain a small amount of excess oxygen. Reproduced from reference [8].

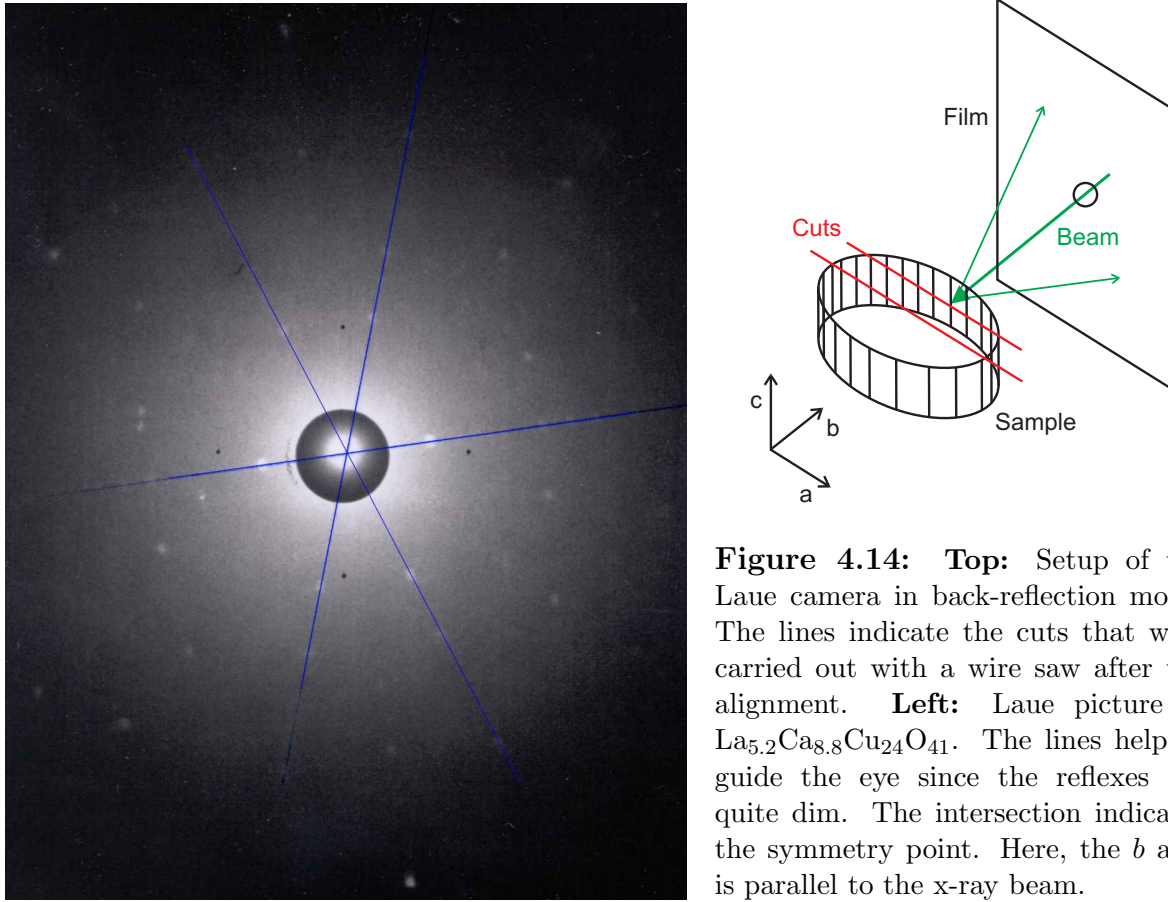


Figure 4.14: Top: Setup of the Laue camera in back-reflection mode. The lines indicate the cuts that were carried out with a wire saw after the alignment. **Left:** Laue picture of $\text{La}_{5.2}\text{Ca}_{8.8}\text{Cu}_{24}\text{O}_{41}$. The lines help to guide the eye since the reflexes are quite dim. The intersection indicates the symmetry point. Here, the b axis is parallel to the x-ray beam.

chain and ladder direction. The planar high- T_c cuprates as well grow slowly along the comparable axis perpendicular to the CuO_2 planes.

Exact cutting and polishing of the samples is simplified quite a bit since the rough orientation of small slices of the original rod is clear just from looking at it. The precise orientation prior to cutting was done by the use of Laue x-ray pictures. The samples were mounted on a goniometer and the only task was to align the main symmetry axis so that it was parallel to the x-ray beam. Figure 4.14 shows a typical Laue picture after successful alignment, i.e. the beam is parallel to the b axis. Also presented is a sketch of the basic setup of the Laue camera. Afterwards, the samples were cut into slices perpendicular to the b axis by a wire saw. Thus the resulting faces are parallel to the ac plane. Only the $\text{Sr}_{14}\text{Cu}_{24}\text{O}_{41}$ crystals made an exception because it is possible to cleave them with a razor blade along the ac plane due to their pronounced anisotropy. Therefore no x-ray aligning and no extra sawing was necessary for $\text{Sr}_{14}\text{Cu}_{24}\text{O}_{41}$.

After cutting, all samples were polished to gain shiny faces. For reflectance samples it is sufficient to treat one surface, but transmittance samples have to be polished on both parallel faces. This is very important to avoid light scattering effects that might disturb the spectra in particular at higher frequencies. Moreover, the polishing process allows us to prepare each sample with the optimal thickness. It was even possible to polish a sample of $\text{La}_{5.2}\text{Ca}_{8.8}\text{Cu}_{24}\text{O}_{41}$ down to a final thickness of $6\text{ }\mu\text{m}$. The used Logitech PM2 machine resembles an old-fashioned record player since the main unit is a heavy rotating

plate with a diameter of 30 cm. It was upgraded with state-of-the-art components to provide high-grade samples. The first step is always to abrade at least $20\text{ }\mu\text{m}$ of the sample to gain a flat homogenous surface. To get a thinner sample, further grinding can be achieved rather fast. This fine-grinding process is called lapping and we typically use an abrasive suspension of $3\text{ }\mu\text{m}$ seized Al_2O_3 particles in water. The lapping plate is made of cast iron because this material is relatively soft. The sample gets gently pressed against the rotating plate by a spring inside the sample holder. The resulting surface is rather coarsely grained. However, no scratches and cracks should be visible at the end of the lapping process because the subsequent polishing provides a very slow removal of material.

The next step is the actual polishing process. Another plate has to be used, which is covered by a polyurethane foam. This material has holes of up to mm sizes. Of course, another suspension with finer particles has to be used, too. A base with a pH value of 10.3 and with suspended quartz crystals of 125 nm diameter provides very good results. In labs for thin-film growth the same setup often comes across to re-polish old substrates. As for thin transmittance samples, both surfaces have to be polished. After the treatment of the first surface the sample is detached and re-glued again to deal with the second surface.

Every material and even every single sample has to be treated in a different way. Especially the contact pressure and the revolution speed are critical parameters. In general, hard materials provide better results than soft and brittle samples. $\text{Sr}_{14}\text{Cu}_{24}\text{O}_{41}$ for instance was not easy to polish because whole layers parallel to the ac plane tended to break off. And sometimes the polishing didn't work out at all for no obvious reason. Maybe the most mysterious case was a specimen of $\text{La}_4\text{Ca}_{10}\text{Cu}_{24}\text{O}_{41}$, that was designated to become

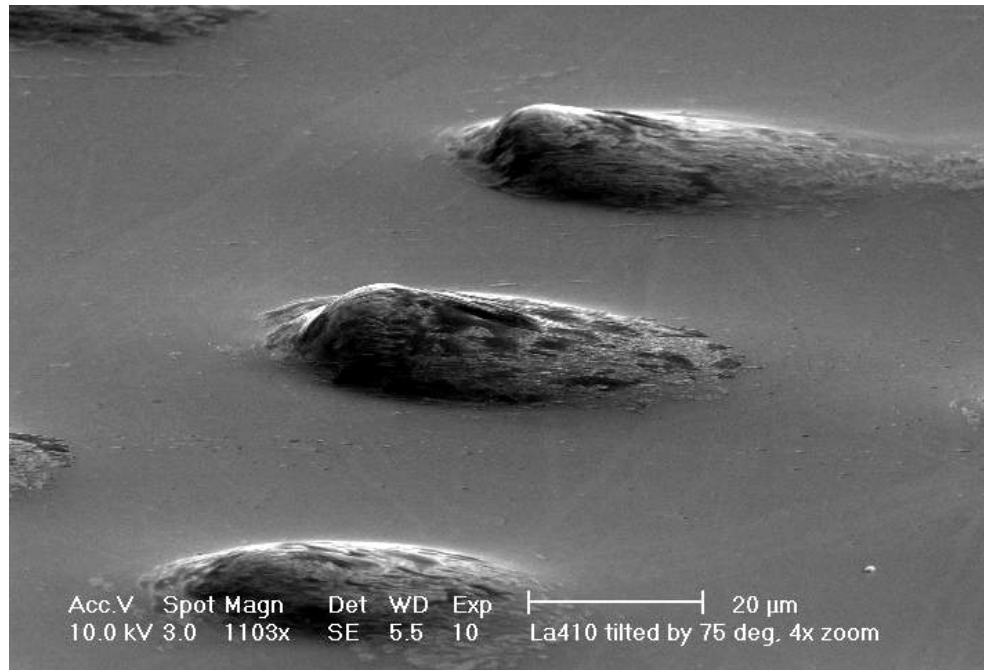


Figure 4.15: Strange bumps on the surface of a $\text{La}_4\text{Ca}_{10}\text{Cu}_{24}\text{O}_{41}$ sample. The picture was taken with a scanning electron microscope [210]. In-between the bumps the area is well polished.

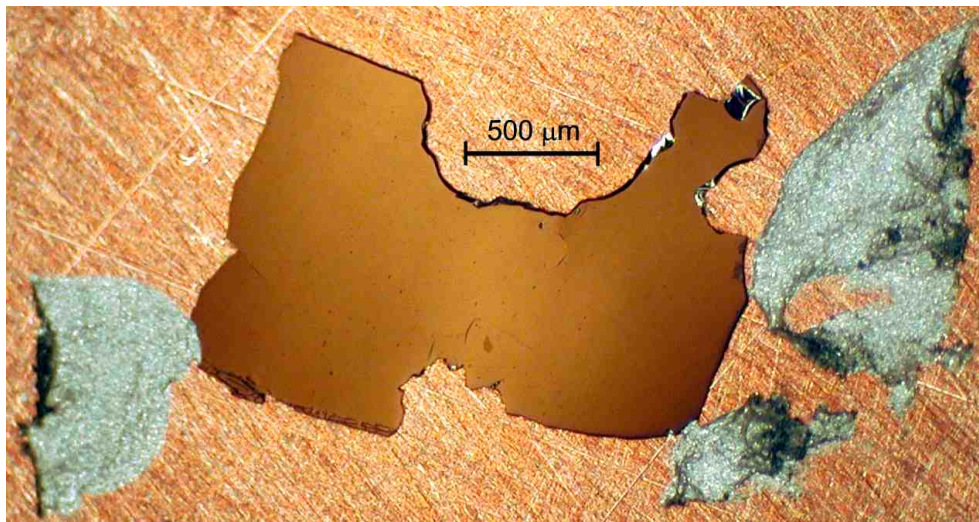


Figure 4.16: Picture of the $6\ \mu\text{m}$ thick transmittance sample of $\text{La}_{5.2}\text{Ca}_{8.8}\text{Cu}_{24}\text{O}_{41}$. Three patches of silver paste hold the specimen in place. The hidden circular aperture hole is located under the left part of the sample and has a diameter of $0.5\ \text{mm}$. The sample itself is of black color. But to make the picture more vivid a second light source was targeted at the sample so that a lot of intensity directly got reflected back.

a transmittance sample. The first surface was easy to polish, and the usual result was achieved. But the second surface withstood all the polishing efforts. Strange bumps of approximately $10\ \mu\text{m}$ height appeared. These bumps reappeared even after completely lapping away the top layer. A second specimen that was cut right next to the former one from the same crystal suffered the same problem. Figure 4.15 shows a picture taken with a scanning electron microscope [210]. The whole area of the sample was covered with comparable structures. An EDX analysis [211] yielded that the bumps basically have the same stoichiometry as the sample. It is quite surprising, though, that the area *between* the bumps was quite flat. The situation didn't change even by removing more material than the total height of the bumps. These two specimens were beyond remedy but fortunately no other sample was lost due to this strange problem.

After polishing, the samples have to be glued onto an aperture. The rather thick reflectance samples are easy to handle but the situation gets quite difficult when extremely thin transmittance samples have to be fastened. The $6\ \mu\text{m}$ thick sample of $\text{La}_{5.2}\text{Ca}_{8.8}\text{Cu}_{24}\text{O}_{41}$ that has already been mentioned above surely was the biggest challenge since it would break immediately by wrong handling. Figure 4.16 illustrates how this sample is glued to a transmittance aperture of $0.5\ \text{mm}$ with silver paste. This adhesive provides good thermal contact and works even for our highest possible temperature of $800\ \text{K}$. Great care is necessary because the paste tends to creep underneath the sample when the consistency is too fluid. The apertures for transmittance measurements are just slices of copper with circular holes. Aligning the spectrometer in a transmittance setup is not too difficult. Yet for reflectance measurements a simple circular aperture won't work. Copper flats parallel to the sample surface would add some false intensity. Therefore we use $4\ \text{mm}$ thick copper slices and conical holes instead, so that the surface right next to the sample is tilted. This works very well for large samples, where the light spot can be

chosen to be smaller than the sample aperture. It is extremely important that the reference mirror is perfectly parallel to the sample. Otherwise, sample and reference signal are not at maximum for the same spectrometer alignment, and at least the absolute value of the spectrum is wrong. Currently an evaporator is set up which will allow to evaporate a thin film of gold in-situ onto the sample surface. This film acts as a reference mirror that perfectly matches the sample area and the sample alignment. For this technique the sample itself is typically glued to a cone to avoid any parallel surfaces nearby.

Summary: Fourier spectrometers are powerful tools to measure optical transmittance and reflectance data accurately from the far infrared all the way up to ultraviolet frequencies. However, some caution is necessary to avoid the many problems successfully that like to cloud the results. We are lucky to have access to high-quality single crystals. Aligning, cutting, and polishing are by now well established procedures in our lab. It was even possible to prepare a 6 μm thick transmittance sample with both sides brightly polished.

Chapter 5

Bound States and Continuum in Undoped Ladders

This chapter picks up the discussion started in section 2.3.3, where the triplet dispersion of two-leg spin-1/2 ladders has been introduced. But the excitation spectrum provides further contributions since, for instance, the simultaneous excitation of two triplets yields a continuum of states. Due to the gap in the elementary triplet dispersion, also the continuum exhibits a gap. In such spin systems with gapped excitation spectra it is particularly tempting to look for bound states. Without continua that span the energy range down to zero, one may expect to find sharp features stemming from bound states. An example discussed already in section 2.2.2 is the alternating Heisenberg chain in which bound states indeed are present [17]. Therefore it does not come as a surprise that bound states in gapped two-leg ladders were in fact predicted theoretically by several groups [16–23]. In general, suitable techniques to probe bound-state peaks include, for instance, inelastic neutron scattering, Raman scattering, and infrared absorption, the tool of choice presented in this thesis. In this chapter, the first observation of a bound state in spin ladders is presented [24, 212, 213]. The measurements were performed on the system $\text{La}_y\text{Ca}_{14-y}\text{Cu}_{24}\text{O}_{41}$, which permits to reduce the amount of charge carriers and thus provides essentially undoped spin ladders. The spectra are compared with several recent theoretical calculations, and the excellent agreement between experiment and theory allows us to extract a unique set of coupling constants. In this context, strong evidence for the importance of the cyclic exchange J_{cyc} is given [26].

5.1 First Predictions

The bottom of a two-magnon continuum was already discussed in 1994 by Barnes et al. [78]. Johnston et al. calculated not only the elementary triplet dispersion for different coupling ratios, as presented in figure 2.23 on page 35, but they also presented the according lower boundary of the two-triplet continuum [133]. The plot is reproduced in figure 5.1 and shows data from isotropic coupling up to $J_{\parallel}/J_{\perp} = 2$. One can see that the elementary triplet branch is lying within the two-triplet continuum over much of the Brillouin zone. However, more striking was the forecast of bound states of two triplets. Such an excitation is sketched in figure 5.2 for the strong-coupling limit. The illustration

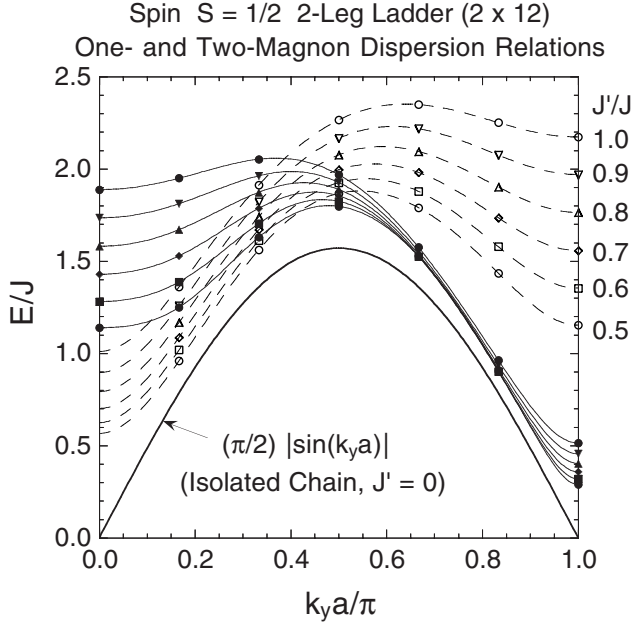


Figure 5.1: Lower boundary of the two-triplet continuum plotted as dashed lines with open symbols. The data sets for various coupling ratios were calculated using the Lanczos algorithm. Solid lines with full symbols represent the corresponding one-triplet dispersion. These branches are identical to the ones from figure 2.23, and again the notation $J = J_{\parallel}$ as well as $J' = J_{\perp}$ is used. The wave vector k_y is parallel to the legs. Reproduced from reference [133].

in the dimer scenario is more instructive than the corresponding spinon counterpart of the chain limit. Two triplets are excited on adjacent rungs and form a bound two-particle state. As a reason for the actual attraction one might visualize that one triplet may take advantage of the perturbation of the spin background by the other one. Moreover, in the depicted case the triplets have antiparallel spins, which cures the AF exchange between the rungs. One has to keep in mind, though, that naive pictures like this should not be strained too much and just give a rough idea of the underlying mechanism.

Like in the alternating Heisenberg chain, again two different excitations of bound states are possible, namely a singlet branch with spin zero and also a triplet branch that is slightly higher in energy. There exists no actual *bound* state with $S = 2$ since the interaction is repulsive in this channel. Nevertheless a solution exists, yet only with energies above the upper edge of the two-triplet continuum. Thus the binding energy is negative, and this state is called “anti-bound”.

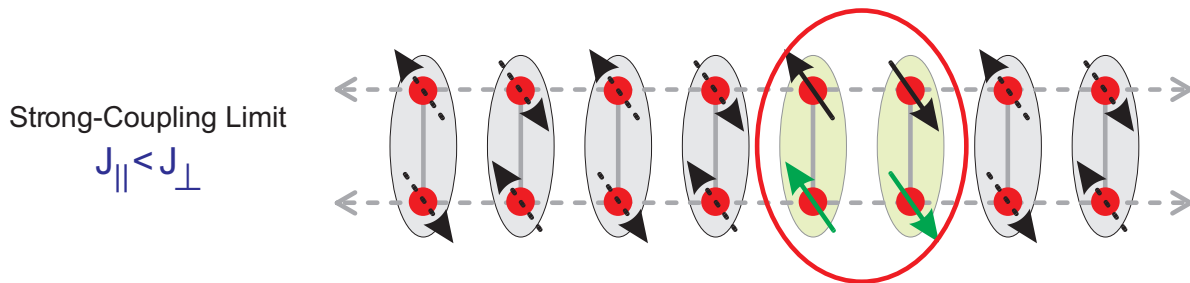


Figure 5.2: Rough sketch of a two-triplet bound state in the strong-coupling limit. Two triplets excited on neighboring rungs are bound together. In the drawn case, the spins of the triplets are antiparallel ($S_{tot} = 0$), and therefore AF interaction between the triplets leads to a positive binding energy.

Damle and Sachdev found both types of bound states in the strong-coupling limit by expansion in powers of J_{\parallel}/J_{\perp} for the ladder Hamiltonian [18]. The $S = 1$ channel can in principle be observed with inelastic neutron scattering. They present a bound-state dispersion that only exists for a limited range of wave vectors k . Beyond this range the binding energy vanishes. Since this energy is the distance between the bound-state branch and the continuum located above, this means that the bound-state dispersion “enters” the continuum. But within the continuum the two triplets can simply dissociate. Due to the attractive interaction there still might appear a resonance within the continuum.

Sushkov and Kotov also studied the strong-coupling limit but extended the parameter range by calculating both bound states for the coupling ratio $J_{\parallel}/J_{\perp} = 0.5$ [19]. The excitation spectrum is reproduced in the left panel of figure 5.3. The solid lines are the elementary triplet branch and the lower edge of the continuum. The dot-dashed curve represents the singlet bound state that leaves the continuum above $k \approx 2\pi/5$. As stated above, the binding energy in the triplet channel is weaker than in the singlet channel. Therefore the triplet bound state, which is drawn as dashed line, is located closer to the

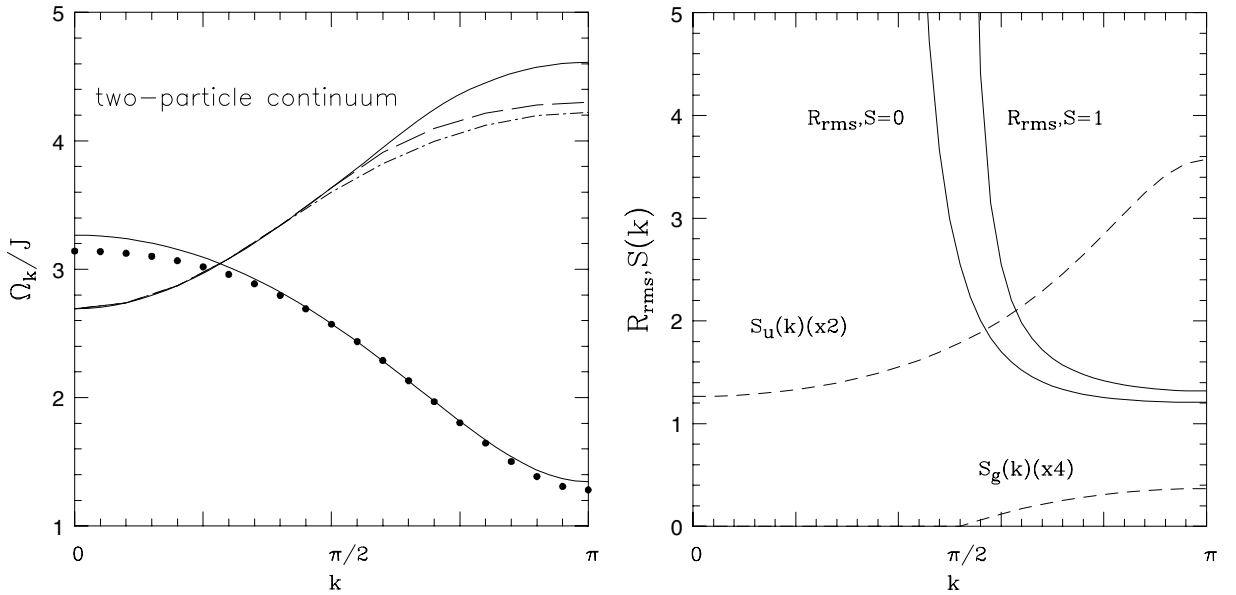


Figure 5.3: **Left:** Excitation spectrum of the ladder for $J_{\parallel}/J_{\perp} = 0.5$. Here the leg coupling is denoted as J . The lower solid line is the elementary triplet branch. For comparison, it is accompanied by data points from reference [214]. The upper solid line stands for the lower edge of the two-triplet continuum. At higher wave vectors the two types of bound states emerge. The bound state with $S = 0$ (dot-dashed) exhibits a larger binding energy than the corresponding $S = 1$ state (dashed) located above. **Right:** Solid lines represent the sizes, or coherence lengths, of the singlet and triplet bound states. Also included are the dynamical structure factors (dashed). The upper line corresponds to the elementary triplet (“ungerade”), the lower one to the $S = 1$ bound state (“gerade”). Note the different scaling factors of 2 and 4. Reproduced from reference [19].

continuum boundary and emerges later, i.e. above $k \approx \pi/2$.¹ Further interesting results calculated by Sushkov and Kotov are the *size* of the bound state and the expected neutron intensities [19]. Both quantities are reproduced in the right panel of figure 5.3. Here the solid lines denote the sizes for both types of bound states in units of the lattice spacing, again for $J_{\parallel}/J_{\perp} = 0.5$. The extensions increase with decreasing binding energy, which is to be expected since the states gradually become unbound. Moreover, the triplet excitations are “larger” than the singlet ones at the same value of k . Except for wave vectors very close to the threshold, the bound states in both channels have typical sizes of just a few lattice spacings.

The neutron intensity is directly proportional to the dynamical structure factor (see footnote on page 16), which is drawn as dashed lines in the right panel of figure 5.3. The upper line represents the intensity of the elementary triplet (S_u , “ungerade”), whereas the lower line stands for the $S = 1$ bound state (S_g , “gerade”). The experimental signal of the $S = 1$ bound state is about 20 times weaker than for the elementary triplet [19]. What is more, the bound-state energies are quite high in cuprate ladders, which renders the quest for this state quite challenging by means of neutrons. The structure factor of the $S = 0$ bound state is zero in the considered neutron channel of $S = 1$. This simply means that for its detection other techniques like e.g. Raman scattering or infrared absorption have to be applied. Raman is sensitive just to $k = 0$ excitations at the zone center, though, while the bound state only emerges at higher momenta. By the simultaneous excitation of a phonon, infrared absorption can very well access this region. Therefore this probe has been the best candidate to actually verify bound states in ladders, as presented below.

A further study of the excitation spectrum was undertaken by Trebst et al. in 2000 [22] and continued by Zheng et al. in reference [23]. For the first time, bound-state properties of spin ladders were obtained from strong-coupling expansions up to higher order. The presented method uses orthogonal transformations to map the original Hamiltonian onto an effective Hamiltonian.² Starting from the dimerized ground state, the authors calculated series in J_{\parallel}/J_{\perp} up to order 7 for the singlet bound state, and up to order 12 for the $S = 1$ and $S = 2$ channels. The reason why the singlet series is computed to lower order than the other bound states is that the singlet has the same quantum numbers as the ground state, which leads to a more elaborate procedure. The dispersions for the coupling ratio of $J_{\parallel}/J_{\perp} = 0.2$ are reproduced in the left panel of figure 5.4. The qualitative features are comparable to the former results of figure 5.3 (see also figure 5.5). The three types of bound states, namely the singlet, triplet, and the antibound quintuplet, evolve at some critical wave vectors below and above the continuum, respectively. It is useful to define an *anti*binding energy as the energy difference between the upper edge of the continuum and the $S = 2$ quintuplet. Both binding and antibinding energies show a maximum at $k = \pi$. Thus it is interesting to see how these energies evolve at this very wave vector

¹In a subsequent paper of Kotov et al. an AF diagonal exchange was included [20]. The additional frustration apparently leads to many-particle bound states at low energies. These new excitations become more and more favorable as J_{diag} increases and might, at some point, completely dominate the excitation spectrum. However, without frustration Kotov et al. speculate that not even a three-particle bound state exists in the strong-coupling limit.

²This approach is distinct but similar to the flow-equation method that uses continuous unitary transformations. The latter technique was refined by Knetter and Uhrig to investigate the dimerized chain [92] and the Shastry-Sutherland model [215]. In the next sections our data of the telephone-number compounds will be interpreted on grounds of new flow-equation results of the same group.

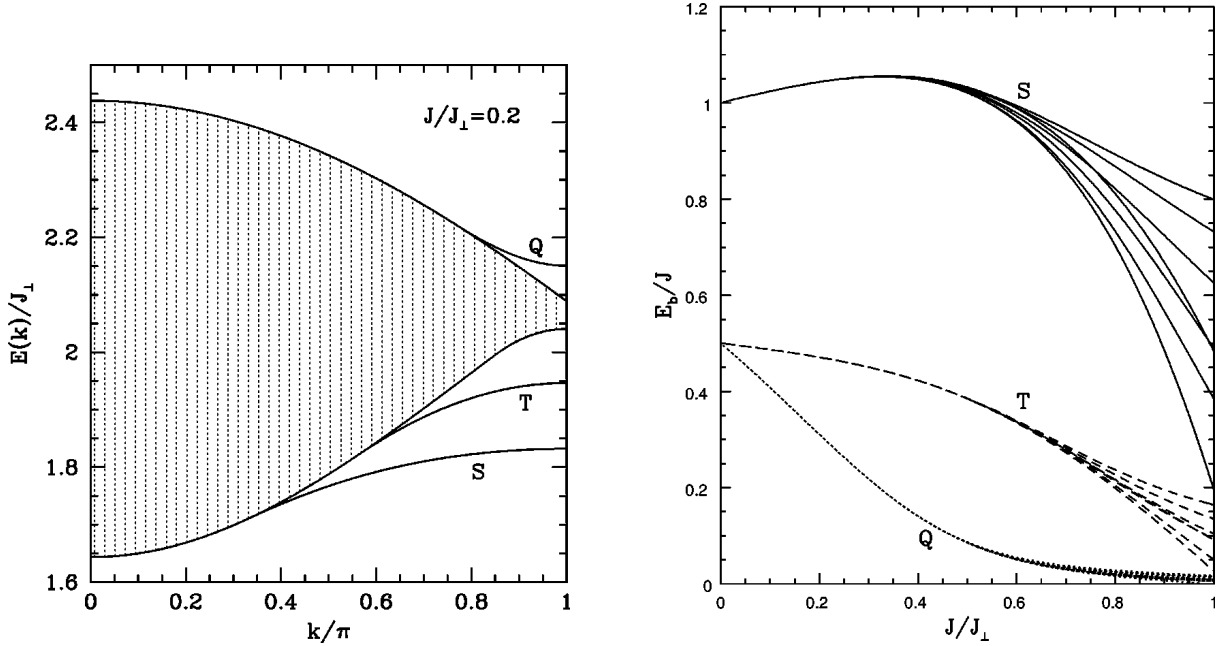


Figure 5.4: **Left:** Excitation spectrum for $J_{\parallel}/J_{\perp} = 0.2$ based on high-order expansions. Note that the leg coupling again is denoted as J and that the elementary triplet is omitted in the plot. S and T are the singlet and triplet bound states, respectively. The quintuplet antibound state above the dotted continuum is labelled as Q . **Right:** Binding and antibinding energies E_b/J_{\parallel} at $k = \pi$ versus the coupling ratio J_{\parallel}/J_{\perp} . Several different approximations to the expansion series are included. Reproduced from reference [23].

upon increasing the coupling ratio J_{\parallel}/J_{\perp} . The corresponding plot is shown in the right panel of figure 5.4. Several different extrapolations are included that demonstrate the uncertainty away from the strong-coupling limit. The binding energy of the singlet (S) in units of J_{\parallel} increases up to $J_{\parallel}/J_{\perp} \approx 0.4$, whereas otherwise all the energies decrease with increasing coupling ratio. Note that for the quintuplet (Q) actually a negative binding energy is plotted.

The first calculations of the impact of bound states on the infrared absorption of ladder compounds were reported by Jurecka and Brenig in 2000 [21]. They used first-order strong-coupling expansions and employed the phonon-assisted bimagnon absorption developed by Lorenzana and Sawatzky [11, 12] (see section 3.3). Yet the term “two-triplet” absorption would be better suited in this case since magnons usually refer to spin-wave excitations. At first, Jurecka and Brenig calculated the dispersion relations and again find the continuum as well as bound states with $S = 0, 1$ and 2 . But the latter two bound states are not optically active, and only the continuum and the singlet bound state can contribute to the infrared absorption. The dispersions are shown in the left panel of figure 5.5. Note the scaling of the energy axis with λ being the coupling ratio J_{\parallel}/J_{\perp} . This kind of rescaling was necessary to gain expressions that just depend on the wave vector k . Apart from that, the main features are again comparable to the other results of Sushkov et al. [19] (figure 5.3) and Zheng et al. (figure 5.4). The binding energy is largest at $k = \pi$, and the $S = 1$ bound state is located in-between the singlet dispersion and the lower edge of the continuum. Moreover, the antibound state with $S = 2$ emerges

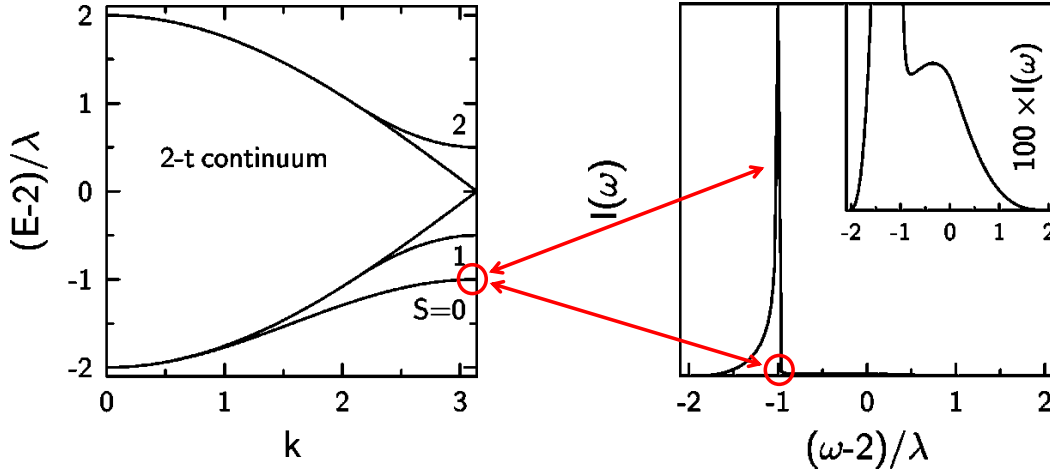


Figure 5.5: **Left:** Two-triplet continuum and the dispersion of the three types of bound states with $S = 0, 1$, and 2 for the strong coupling limit. λ is equal to the ratio J_{\parallel}/J_{\perp} . Note the scaling of the energy axis. The local maximum in the $S = 0$ channel at $k = \pi$ leads to a van Hove singularity in the density of states at the energy $\lambda - 2$. This is the reason for the strong peak in the infrared absorption plotted in the **right** panel. The inset illustrates the small continuum contribution on a magnified scale. Based on reference [21].

above the continuum. Jurecka and Brenig state that their treatment is exact in the limit of $J_{\parallel}/J_{\perp} \ll 1$, yet beyond this limit they expect deviations in particular regarding the positions of the bound states [21].

The next step is to calculate the actual infrared absorption, which is reproduced in the right panel of figure 5.5. Note again the required rescaling of the energy on the x axis. The according choice of the frequency variable implies that zero incoming photon energy corresponds to the point $-2/\lambda$ on the x axis. This point is off the plotted range as soon as $\lambda < 1$, which is necessary in the considered strong-coupling regime. Therefore the plotted range just represents the frequency window in which absorption occurs. The figure demonstrates that the singlet bound state in fact does have a profound impact on the spectrum that is dominated by a sharp bound-state peak. In general, for dispersive excitations the spectral intensity is proportional to the integrated density of states. Consequently, when there is a singularity in the density of states, such as at a band minimum or maximum, one expects a peak in the intensity. This kind of pole is called van Hove singularity, and here the bound state exhibits a local maximum exactly at the boundary of the Brillouin zone, i.e. at $k = \pi$, with the corresponding energy of $2 - \lambda$. The added arrows in figure 5.5 are supposed to demonstrate that the peak in the absorption spectrum occurs exactly at the energy of the band maximum. The inset in the right panel focuses on the remaining spectral weight. It shows a maximum at the center of the two-triplet continuum, but the intensity is very small compared to the main peak. Actually, the largest part of the spectral weight is lying within the bound state only for $J_{\parallel} \ll J_{\perp}$, the continuum is much stronger if J_{\parallel} and J_{\perp} are comparable. In order to describe our experimental data on the telephone-number compounds, the theory had to be pushed to the latter regime and to the inclusion of J_{cyc} . This has been achieved by the groups of Uhrig from the University of Cologne and Kopp from the University of Augsburg (see below).

5.2 Experimental Results

Our primary intention to study spin ladders was actually not to look out for bound states. At first, we were rather interested to find features similar to the challenging mid-infrared spectra of the undoped 2D cuprates in a comparable but easier system. The absorption of undoped $\text{YBa}_2\text{Cu}_3\text{O}_6$ (YBCO), for instance, exhibits a main resonance peak, that is well understood in terms of phonon-assisted bimagnon absorption within spin-wave theory. Yet there is a further broad contribution with significant spectral weight at higher frequencies. Spin-wave theory fails to describe these additional features [14], that e.g. are not apparent in the 2D $S = 1$ system La_2NiO_4 [194]. This suggests that the additional intensity in the $S = 1/2$ 2D cuprates may have its origin in quantum fluctuations which go beyond spin-wave theory (for more details, see discussion in section 3.3). Indeed we found a similar high-frequency contribution in the ladders, that we can attribute unambiguously to the two-triplet continuum. What is more, we found *two* distinct peaks below the continuum. Initially, this double peak contradicted the *single* sharp peak stemming from a bound state as predicted by Jurecka and Brenig [21]. Not until new calculations by the theoretical groups of Uhrig et al. in Cologne as well as Kopp et al. in Augsburg were accomplished, we were finally able to describe the *double* peak as due to a *single* bound state.

First we wanted to study nominally undoped samples of $\text{La}_y\text{Ca}_{14-y}\text{Cu}_{24}\text{O}_{41}$, which corresponds to a La content of $y = 6$. Single-phase crystals of this composition could not be synthesized, though. Ammerahl et al. speculated that the solubility limit of La is somewhere between $y = 5.6$ and 6 [7], as pointed out on page 41. However, high-quality samples with $y = 5.2, 5$, and 4 were available, that on average contain merely 0.8, 1, and 2 holes per formula unit. Our results for the magnetic contribution to $\sigma(\omega)$ stemming from the ladders (see below) is almost unaffected by the three different La contents. Thus we consider the *ladders* to be undoped for the systems at hand. This assumption is well supported by the x-ray absorption data from Nücker et al., which shows that for these low doping levels all holes are located within the chain subsystem [9].

In order to determine the optical conductivity $\sigma(\omega)$, we measured both transmittance and reflectance data between 500 and 12000 cm^{-1} on our Fourier spectrometer. With the use of polarizers and since the samples were cut accordingly, we were able to measure with the electric field parallel to the legs (c axis) and parallel to the rungs (a axis), respectively. The spectra show an electronic background at high frequencies. To gain the pure magnetic contribution to $\sigma(\omega)$, we had to subtract this background for both polarizations. Afterwards, the results were compared with the mentioned new calculations to identify the excitations and to extract, for instance, the proper set of exchange couplings. It turned out that inclusion of a cyclic exchange into the model Hamiltonian solves most of the remaining inconsistencies. The measurement of the b -axis transmittance of $\text{La}_1\text{Sr}_{13}\text{Cu}_{24}\text{O}_{41}$ meets expectations and demonstrates that perpendicular to the ladder sheets the conductivity is very low and almost featureless. Thus we saw no sign of magnetic absorption along this crystallographic direction.

5.2.1 Reflectance

Unlike in other optical studies on, for instance, phonons or the electronic structure, it is not sufficient to measure reflectance spectra alone to gain insight into infrared absorption

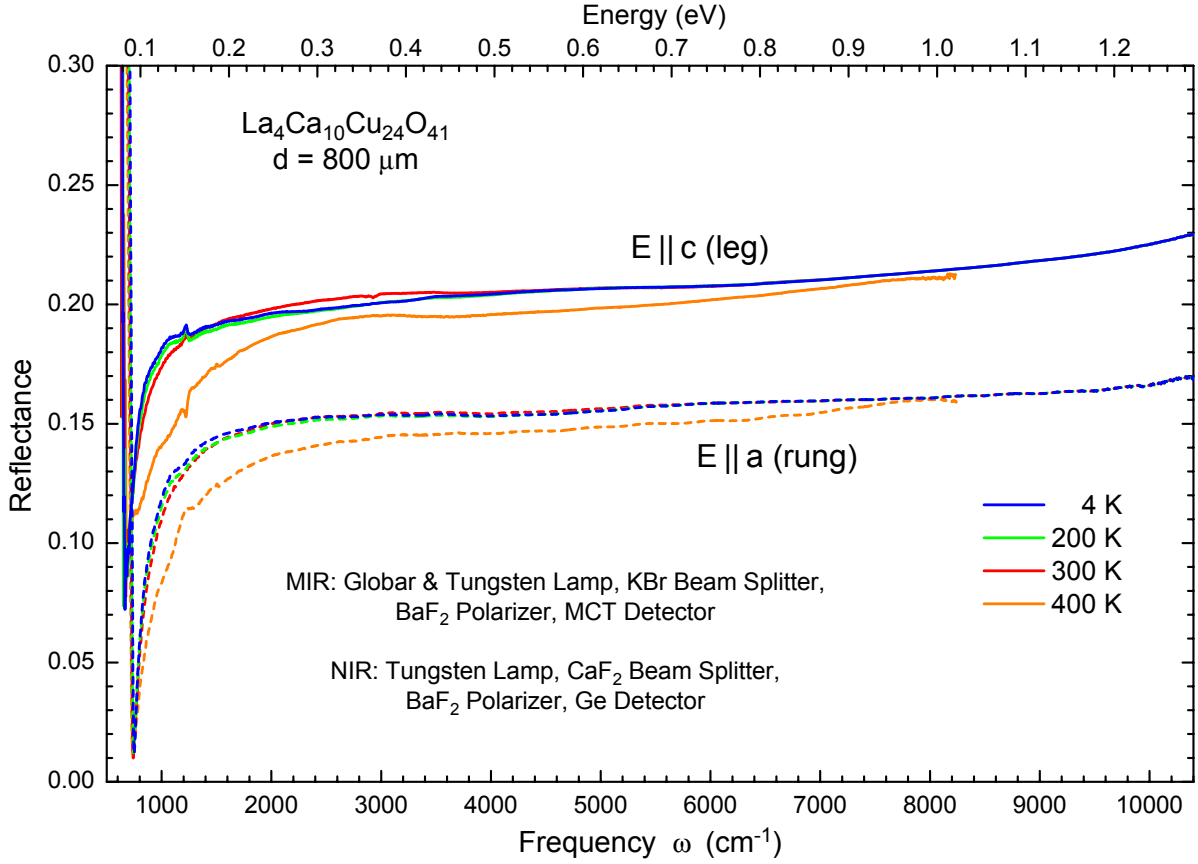


Figure 5.6: Mid-infrared reflectance of a 0.8 mm thick sample of $\text{La}_4\text{Ca}_{10}\text{Cu}_{24}\text{O}_{41}$, showing the range between the phonons and the charge-transfer gap (confer figure 2.32). Solid lines denote the c -axis polarization of the electric field, and dashed lines stand for the perpendicular polarization $E||a$. Apart from the strong phonon feature at about 600 to 700 cm^{-1} , the spectra are almost flat. The little spikes at 1220 cm^{-1} are measurement artefacts. There is no appreciable temperature dependence up to room temperature.

of magnetic excitations. The spectral intensity is so weak that the only chance is to study systems in which the magnetic contribution is located in a frequency window without other sources of absorption. The large exchange couplings in the studied Cu^{2+} ladders shift the magnetic peaks well above the highest phonons. In addition, the undoped compounds are highly insulating so that there is no Drude peak that hides the small magnetic features. And finally, the apparent charge-transfer excitations are located at higher energies. Hence we deal with a frequency range of very small optical conductivity, i.e. small values of the extinction coefficient $k(\omega)$ (order of 10^{-3}). Since the reflectance $R(\omega)$ is given by

$$R(\omega) = \frac{(n(\omega) - 1)^2 + k^2(\omega)}{(n(\omega) + 1)^2 + k^2(\omega)}, \quad (5.1)$$

with n being the index of refraction ($n \approx 2.5$), $R(\omega)$ is almost completely insensitive to small absorption features. Accordingly, a subsequent Kramers-Kronig transformation does not reveal such small features. This is the reason why we have to study the trans-

mittance of thin samples. Together with the reflectance we directly get $\sigma(\omega)$ without any Kramers-Kronig transform, as pointed out in section 3.1.

The measured $R(\omega)$ spectra of a 0.8 mm thick sample of $\text{La}_4\text{Ca}_{10}\text{Cu}_{24}\text{O}_{41}$ are plotted in figure 5.6 for several temperatures between 4 and 400 K. The data sets were calibrated against a gold mirror. A total of two different detectors, two beam splitters, and two lamps was used in three different runs. The high-frequency part above $\approx 6000 \text{ cm}^{-1}$ was measured just at room temperature but was merged also to the low temperature data. This procedure is reasonable, though, since above $\approx 4000 \text{ cm}^{-1}$ there is no temperature dependence in $R(\omega)$ up to 300 K. This is not the case for $T = 400 \text{ K}$ anymore, and therefore just the low-frequency data up to $\approx 8000 \text{ cm}^{-1}$ was used. As expected, the shape is quite featureless and characteristic for the weak absorption regime below the gap of an insulator. At about 600 to 700 cm^{-1} one can see the Cu–O bond-stretching phonon mode. The pronounced dip in $R(\omega)$ denotes the longitudinal eigenfrequency ω_L of this phonon mode, which is about 85 cm^{-1} lower in frequency along the c axis than along the a axis (at $T=4 \text{ K}$: $\omega_{dip}^a \approx 750 \text{ cm}^{-1}$, $\omega_{dip}^c \approx 665 \text{ cm}^{-1}$). At higher frequencies, the reflectance is more or less flat. The different absolute values of the two polarization directions reflect the difference in n , namely $n_a \approx 2.3$ and $n_c \approx 2.6$ above the phonon. It is obvious that a Kramers-Kronig analysis would not reveal any small magnetic contribution in this very frequency window.

5.2.2 Transmittance

A completely different picture emerges from the corresponding transmittance data within the same frequency range. Figure 5.7 shows $T(\omega)$ for two different doping levels. The data of $\text{La}_4\text{Ca}_{10}\text{Cu}_{24}\text{O}_{41}$ is plotted in the top panel. A $d = 60 \text{ }\mu\text{m}$ thick slice was measured, which had been cut parallel to the ac plane, and both faces had been thoroughly polished. The MIR transmittance spectrum³ was calibrated against an empty aperture. Fringes with a small amplitude occurred, which nonetheless were smoothed away.⁴ The upper and slightly thicker lines represent the a -axis polarization. Since in general the conductivity along the rungs is lower than along the legs, $T_a(\omega)$ is *larger* than $T_c(\omega)$ (thin lines). It is quite obvious that these spectra reveal by far more detail than the reflectance. In particular the temperature dependence is quite large. The steep drop below 1000 cm^{-1} is due to the same bond-stretching phonon that was already apparent in $R(\omega)$. Accordingly, along the c axis the phonon feature again appears approximately 90 cm^{-1} lower in frequency than along the a axis. The drop at high frequencies is quite different for both polarizations. The onset of electronic absorption suppresses the c -axis transmittance quite effectively above $\approx 4000 \text{ cm}^{-1}$. Above 5000 cm^{-1} , there is basically no intensity left after the correction of the polarizer error (see page 69). Along the a axis the suppression sets in less drastically, and there is still some transmittance left at the highest measured frequency of 8000 cm^{-1} . In particular, at 5000 cm^{-1} $T_a(\omega) > 50\%$ at 4 K, and $T_c(\omega) = 0$ within experimental accuracy. This is a very nice verification of the single-crystalline nature of the sample.

At this point, a note on the absolute values of $T(\omega)$ is necessary. Using the transmittances along with $R(\omega)$ to calculate the optical conductivity, there sometimes occurs

³Global as light source, KBr beam splitter, BaF₂ polarizer, and MCT detector.

⁴The unsmoothed data is shown in the left panel of figure 5.8.

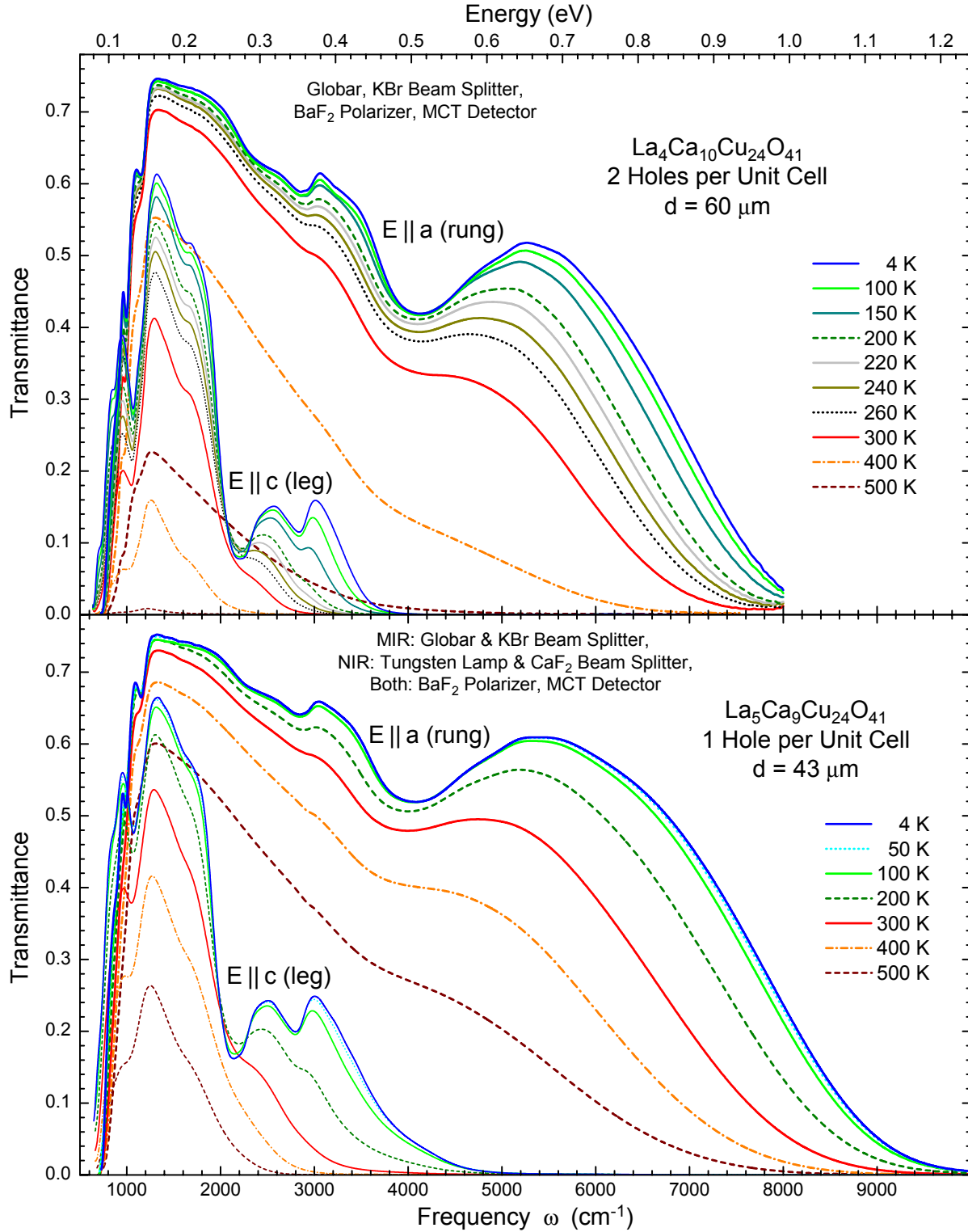


Figure 5.7: Mid-infrared transmittance of a $60 \mu\text{m}$ thick sample of $\text{La}_4\text{Ca}_{10}\text{Cu}_{24}\text{O}_{41}$ (**top**; multiplied by 0.96 to avoid negative values of $\sigma_1(\omega)$, see text) and a $d = 43 \mu\text{m}$ sample of $\text{La}_5\text{Ca}_9\text{Cu}_{24}\text{O}_{41}$ (**bottom**; multiplied by 0.95) for various temperatures. Thick lines denote a-axis polarization, c-axis data is plotted as thin lines. The 500 K spectra are not as accurate as the other temperatures since black-body-radiation problems cannot be ruled out (see page 77).

the problem of nonphysical negative values of $\sigma_1(\omega)$. The problem is most likely when $T(\omega)$ is large, i.e. $\sigma_1(\omega)$ is very small. Thus especially the high values of $T_a(\omega)$ at low temperatures are prone to produce a negative σ_1 . A reasonable remedy is to scale down *all* the transmittances of a data set by a few percent, acknowledging that our absolute values are typically a bit too high. This small inaccuracy is systematic, and we suspect the non-linearity of the MCT detector to be the reason (see page 79). Another possible explanation is that some of the light which initially is reflected on the sample surface traverses through the interferometer a second time and then contributes to the transmittance signal (see page 76). This contribution is absent in the reference measurement. The data of $\text{La}_4\text{Ca}_{10}\text{Cu}_{24}\text{O}_{41}$ had to be multiplied by 0.96 to avoid negative optical conductivities. Note that this does not affect our interpretation and the conclusions we draw from the data, since this small correction does not affect the peak frequencies and has only a small effect on the line shape. Even the spectral weight is changing by only a few percent, since this multiplication has the strongest effect for very small values of σ_1 .

Already from these spectra some remarkable features are obvious between the phonon and the electronic background. In the c axis there are two distinct dips located at around 2200 and 2800 cm^{-1} , respectively. It makes sense to discuss dips in $T(\omega)$ since they indicate absorption. Therefore in the optical conductivity the dips will reappear as peaks. In $T_a(\omega)$ there are also some striking dips. A double dent appears at almost the same frequencies as the c -axis counterparts, and there is a further broad feature at $\approx 4100 \text{ cm}^{-1}$. It is rather difficult to tell if such a peak also shows up in $T_c(\omega)$ because the electronic background already damps the transmittance at the relevant frequencies. But two remedies are possible to answer this question. First, one could measure a thinner sample that yields an overall higher $T(\omega)$, or one could measure a different sample doped with less holes.

In the bottom panel of figure 5.7 we tried both. In $\text{La}_5\text{Ca}_9\text{Cu}_{24}\text{O}_{41}$ the nominal amount of holes is cut in half, leaving just one hole per unit cell. Moreover, the sample with $d = 43 \text{ }\mu\text{m}$ is about 30% thinner than the former one. Note that $T(\omega)$ depends exponentially on d (see equations 3.13 to 3.15). The transmittance at 8000 cm^{-1} remains still large along the a axis for low temperatures. Therefore we did not only measure with the MIR setup but in addition replaced the lamp and the beam splitter⁵ to measure up to 10 000 cm^{-1} . The fringes were smoothed away (see right panel of figure 5.8), and both data sets were merged together. Afterwards, all spectra were multiplied by 0.95 to prevent nonphysical negative values of $\sigma_1(\omega)$. Note that the measured temperatures differ for both samples. The qualitative shapes of the spectra are almost identical to the former ones. The characteristic dips are shifted to lower frequencies. This softening can be attributed to increased lattice constants since La^{3+} is larger than Ca^{2+} , resulting in reduced exchange coupling parameters. The total transmittance is higher, which is quite obvious from comparing the 500 K spectra. Most of the increase certainly stems from the smaller thickness, though. The doping effect on the electronic background is not as big as expected. This will become clearer in the discussion of the optical conductivity in the next section because the dependence on the sample thickness drops out.

Usually, the spectra were measured with a resolution of 5 cm^{-1} . At this high resolution, though, interference fringes emerge that can exhibit quite large amplitudes. All

⁵Tungsten lamp and CaF_2 beam splitter; also referred to as VIS setup in the following.

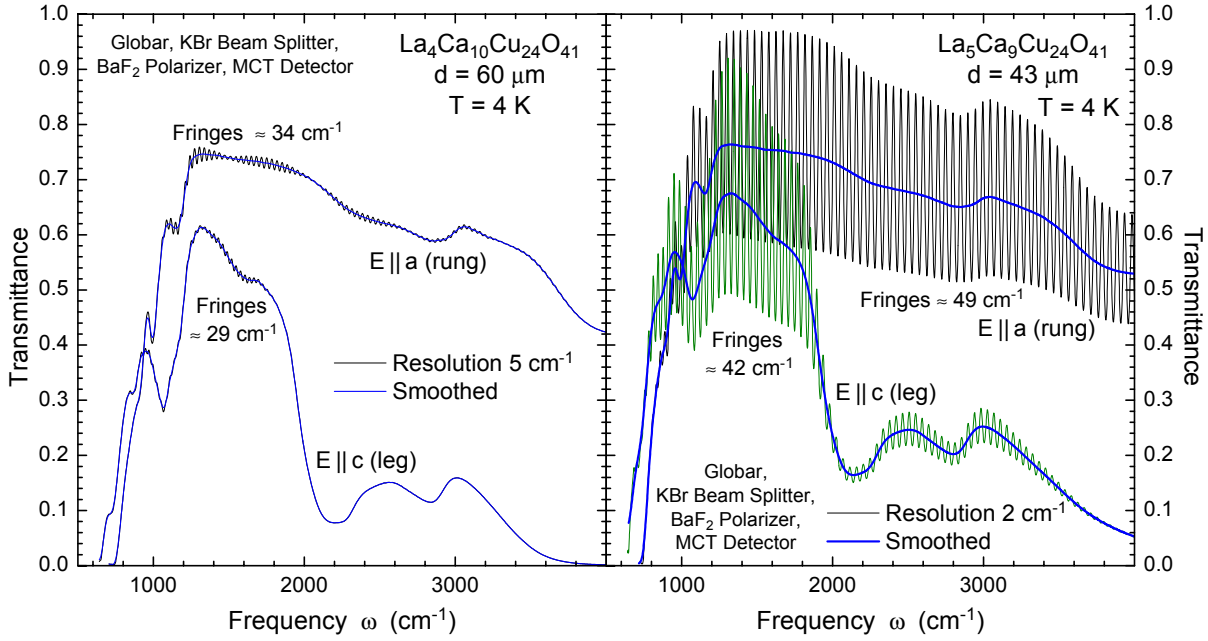


Figure 5.8: Comparison of the interference fringes at 4 K of both specimens from Fig. 5.7. **Left** panel: $\text{La}_4\text{Ca}_{10}\text{Cu}_{24}\text{O}_{41}$ measured with a resolution of 5 cm^{-1} . The unusually small amplitudes of the fringes are most probably caused by slightly misaligned surfaces. The smaller fringe period along the c axis is due to the higher index of refraction. The corresponding smoothed spectra are included in both panels. **Right** panel: $\text{La}_5\text{Ca}_9\text{Cu}_{24}\text{O}_{41}$ exhibits typical fringes with huge amplitudes. The plotted 4 K data was measured with a high resolution of 2 cm^{-1} (other temperatures: 5 cm^{-1}). Merging of different data sets is usually difficult *before* smoothing because typically the fringe amplitudes are very sensitive to the spectrometer alignment.

the presented spectra were smoothed to get rid of these fringes. This is very important because otherwise the calculation of the optical conductivity would yield non-physical results. The fringes stem from multiple reflections within the sample and strongly depend on the thickness, showing a period of $\Delta\omega = (2nd)^{-1}$. Thus the only important benefit for us is actually to determine the proper thickness with higher accuracy compared to the microscope. But there is a considerable difference between both samples. While the fringes of the $\text{La}_4\text{Ca}_{10}\text{Cu}_{24}\text{O}_{41}$ specimen are more or less negligible, the $\text{La}_5\text{Ca}_9\text{Cu}_{24}\text{O}_{41}$ sample exhibits fringes with huge amplitudes. In figure 5.8 the unsmoothed data sets of both samples at 4 K are plotted next to each other. As pointed out before (see page 72), interference effects due to multiple reflections are always present in samples with flat and parallel faces. As annoying as the fringes are at frequencies where the transmittance is high, they are a sign of high-quality samples. Since the polishing process turned out equally good for both samples, the low-amplitude fringes of $\text{La}_4\text{Ca}_{10}\text{Cu}_{24}\text{O}_{41}$ arose most probably because the surfaces were not perfectly parallel. The smoothing process with a Fourier filter turns out unproblematic, but of course the resolution gets reduced. The smoothed data sets are also included in figure 5.8. Fortunately, the width of the features we are interested in (above $\approx 1500\text{ cm}^{-1}$) is large compared to the fringe period, so that

we do not lose any relevant information here. In cases where we were interested in sharp features, we measured thick samples, which both reduces the amplitude and the period of the fringes (see section 6.2).

After completion of the described measurements, we received a large single crystal of $\text{La}_{5.2}\text{Ca}_{8.8}\text{Cu}_{24}\text{O}_{41}$. In this system the nominal amount of holes is reduced even further to 0.8 per unit cell, and so far no single-phase crystals with less doping are available to us.⁶ As this system was the most promising one to reveal the complete magnetic absorption even along the c axis, we measured not just one sample but two distinct ones with different thicknesses. The first one with $d = 28 \mu\text{m}$ was already thinner than the former samples. Our $d = 6 \mu\text{m}$ thin sample, though, extended the frequency range to approximately 9000 cm^{-1} for the c axis and even up to 12000 cm^{-1} for the a axis. The transmittance of the $28 \mu\text{m}$ specimen is plotted in the upper panel of figure 5.9. Two data sets were measured with the globar and the tungsten lamp within a single run.⁷ At first, the polarizer error got corrected. Here also the a -axis spectra were treated, although the effect on σ_a is rather small (see figure 4.7). Afterwards, the fringes were smoothed out in both data sets. For the subsequent merging procedure, it is often necessary to adjust the higher-frequency measurement by a few percent to get good overlap between the data sets. However, the a -axis data of the tungsten lamp had to be scaled down by no more than 1.3%. The c -axis data sets fitted even right away and were as well merged between 2000 and 3000 cm^{-1} . Afterwards, all merged spectra were multiplied by 0.97 to avoid negative values of $\sigma_1(\omega)$ later on.

The second sample of $\text{La}_{5.2}\text{Ca}_{8.8}\text{Cu}_{24}\text{O}_{41}$ could be polished down to $6 \mu\text{m}$ and was measured without any kind of substrate (see figure 4.16 on page 84). The sample was cut from the same rod as the former one and measured with the NIR setup, i.e. tungsten lamp, CaF_2 beam splitter, BaF_2 polarizer, and the MCT detector. Like usual, the polarizer error was corrected and the fringes were smoothed out. The results are shown in the bottom panel of figure 5.9, and the differences in $T(\omega)$ compared to the thicker sample are quite striking. The overall transmittance is of course higher, which is particularly obvious along the c axis. As expected, the $\sigma_1(\omega)$ spectra match quite well (see below). The characteristic dips discussed above, which are ascribed to the magnetic absorption, are less pronounced. This shows that small absorptions are not easy to observe when the sample is very thin. Also the effective resolution suffers as the fringes, which were again smoothed, exhibit a huge period of 380 cm^{-1} (see figure 4.9 on page 74). But the intention of this measurement was to get information at those frequencies where the electronic background is already rather strong. For instance, the dip along the c axis at 3500 cm^{-1} gets very pronounced at high temperatures. This reveals the continuum contribution, which is hard to see in the $28 \mu\text{m}$ data.

⁶Of course, the determination of the real doping level is not that easy. First, the oxygen amount influences the doping, and our samples typically do show some excess oxygen of $\delta < 0.9$ (see figure 4.13 on page 81). In the second place, the formula $\text{X}_{14}\text{Cu}_{24}\text{O}_{41}$ does not represent the true stoichiometry of the incommensurate compounds. What is more, the real ratio of the two incommensurate subcells will change for different La contents. And to complicate things further, in the considered range about $y = 5$ some disorder in the chains occurs, as pointed out on page 41. But since all specimens were grown under similar conditions, the oxygen contents are comparable. And we still expect, on average, less holes for $y = 5.2$ than for $y = 5$ and 4 .

⁷Other components: MCT detector and KBr beam splitter. Confer also figure 4.10 on page 75, where the same data is shown in the context of the frequency-doubling effect.

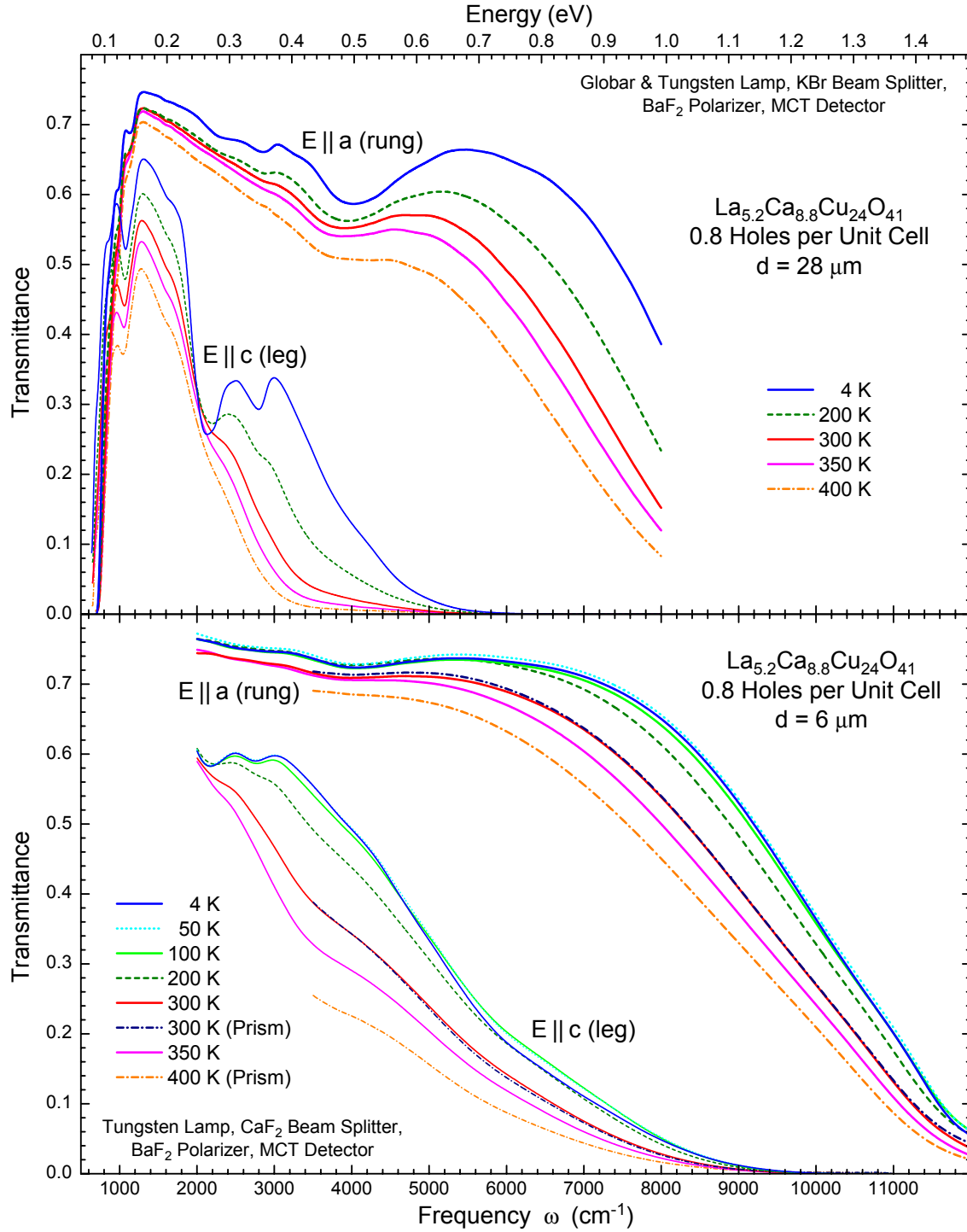


Figure 5.9: Infrared transmittance of $\text{La}_{5.2}\text{Ca}_{8.8}\text{Cu}_{24}\text{O}_{41}$. **Top** panel: $d = 28 \mu\text{m}$ sample. Two data sets measured with globar and tungsten lamp were corrected for the polarizer error, smoothed, merged together, and afterwards multiplied by 0.97 to avoid $\sigma_1(\omega) < 0$. **Bottom** panel: $d = 6 \mu\text{m}$ sample. Note that the plotted spectra are not scaled down. This was done later in order to merge the $\sigma(\omega)$ data of both panels for each available temperature separately. Exemplary, four spectra measured with the prism polarizer are included (dash-dotted). The 300 K spectra demonstrate the excellent agreement of the data obtained with the Glan-Taylor polarizer and the corrected data measured with the BaF_2 polarizer.

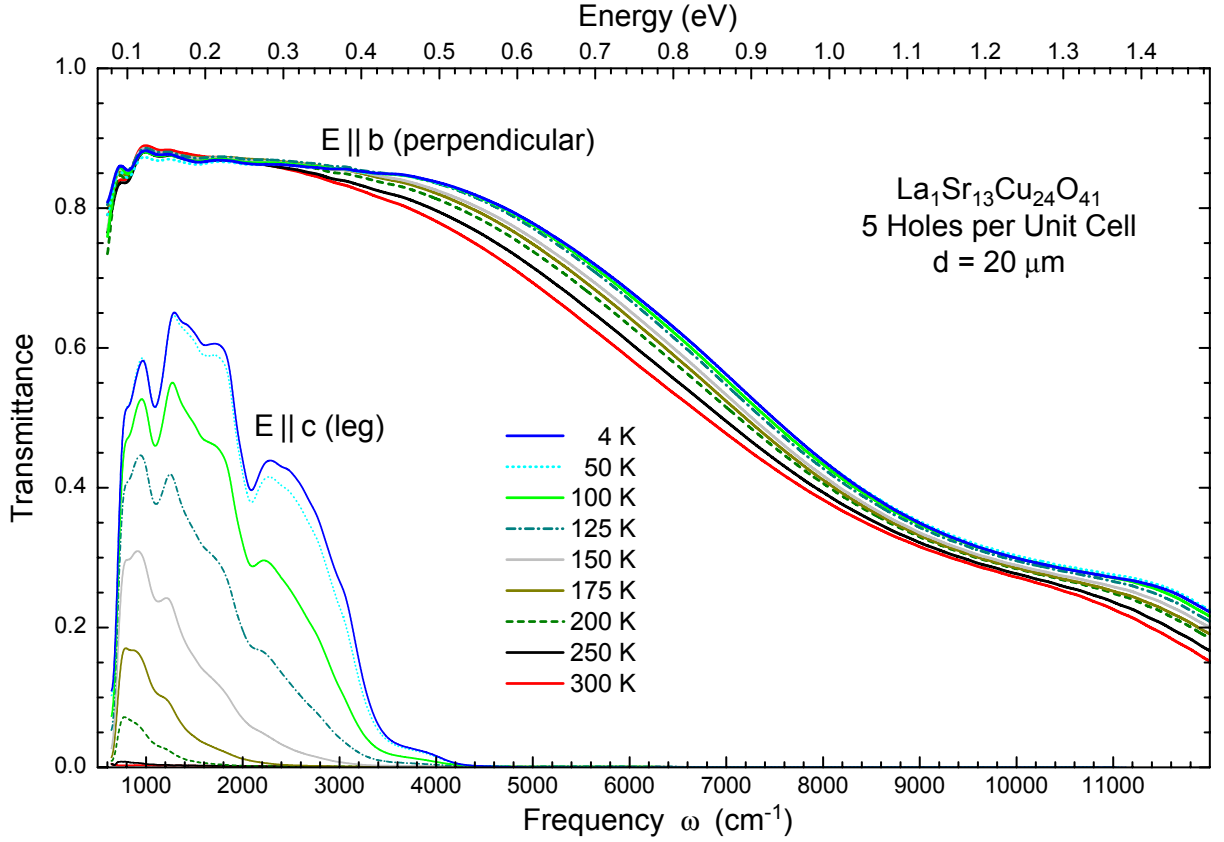


Figure 5.10: Infrared transmittance of $\text{La}_1\text{Sr}_{13}\text{Cu}_{24}\text{O}_{41}$ with $E||b$ (thick lines) and $E||c$ (thin lines). The b -axis transmittance perpendicular to the ladder planes is large and rather featureless. Moreover, the temperature dependence is small compared to the c -axis data.

We performed a further measurement on the thin sample with a different polarizer. We are confident to have the correction of the BaF_2 polarizer under good control, but at high ω we get large extinction ratios of more than 6% (cf. figure 4.5 on page 70). The analysis is very sensitive to this correction when it comes to the subtraction of the electronic background. Therefore we used a Glan-Taylor polarizing prism with a specified extinction ratio of 10^{-5} to check the highest frequencies. The agreement between the Glan-Taylor data and the corrected BaF_2 data is convincing (see the 300 K spectra). To maintain clarity just four exemplary spectra are included in the bottom panel of figure 5.9 as dash-dotted lines.

For comparison, figure 5.10 presents the b -axis transmittance of $\text{La}_1\text{Sr}_{13}\text{Cu}_{24}\text{O}_{41}$, i.e. the electric field is polarized perpendicular to the ladder planes. Note that this compound is intrinsically doped with nominally five holes per unit cell. The effects of charge-carrier doping on the infrared spectra are discussed in more detail later on in section 6.2. Along the b direction the magnetic coupling constants are negligible. Hence one does not expect any noticeable magnetic features in contrast to the c -axis spectra, which are also plotted in figure 5.10. Even though this sample contains more holes and even though this $d = 20 \mu\text{m}$ sample is more than three times thicker than the $d = 6 \mu\text{m}$ sample of undoped $\text{La}_{5.2}\text{Ca}_{8.8}\text{Cu}_{24}\text{O}_{41}$, the b -axis transmittance is larger than the already high a -axis trans-

mittance in the bottom panel of figure 5.9. Along with the small temperature dependence, this clearly demonstrates that a magnetic contribution to the optical conductivity can be neglected for polarization perpendicular to the ladders.

5.2.3 Optical Conductivity

The next step is to take the measured transmittance and reflectance spectra to calculate the real part $\sigma_1(\omega)$ of the optical conductivity. For all of the three different systems ($y=4$, 5, and 5.2) we used the same $R(\omega)$ measured on the $d = 800 \text{ } \mu\text{m}$ $\text{La}_4\text{Ca}_{10}\text{Cu}_{24}\text{O}_{41}$ sample. We expect just negligible effects on σ_1 since the reflectance is rather featureless and does not even depend much on the temperature. The spectrum is that of an insulator and we assume basically no changes by going from $y = 4$ to $y = 5.2$, at least not beyond our experimental accuracy.⁸ All the magnetic features that we are interested in arise solely from the transmittance spectra and are quite insensitive to a possible slight shift of $R(\omega)$. In addition, not for all the needed temperatures $R(\omega)$ was measured. But again, there is no error arising from using e.g. the $T = 4 \text{ K}$ reflectance along with the $T = 100 \text{ K}$ transmittance as there is essentially no change in $R(\omega)$ below 200 K (see figure 5.6). We measured no reliable 500 K reflectance, which is the reason why we refrain from presenting σ_1 data for this temperature.

The calculated spectra for $y = 4$ and 5 are plotted in figure 5.11. Note that both panels are scaled identically to simplify the comparison. Below 1000 cm^{-1} there is the steep increase in σ_1 due to the phonon in each spectrum. The values along the a axis around 1500 cm^{-1} never become negative, which had to be ensured by the discussed scaling down of $T(\omega)$ by 4 to 5%. At the high-frequency limit of the measurements, the electronic background increases strongly with temperature. The overall weight of this background is larger in the higher-doped $\text{La}_4\text{Ca}_{10}\text{Cu}_{24}\text{O}_{41}$, and the onset is shifted to lower frequencies. This can be most easily observed by comparing the 400 K spectra. It is important to take a look at the absolute values of σ_1 . Within the measured frequency window, the conductivity is $< 10 (\Omega\text{cm})^{-1}$. This is by orders of magnitude smaller than the Kramers-Kronig data of, e.g., Osafune et al. in figures 2.32 and 2.33. Hence the high sensitivity of our approach is corroborated, and an electronic background of $10 (\Omega\text{cm})^{-1}$ is still to be considered as very small. In the next section we describe how we subtract this contribution in order to gain the magnetic absorption. It is obvious that this task will be a lot easier for the a axis than for the c axis since the available fitting range is larger. In fact, especially for $\text{La}_4\text{Ca}_{10}\text{Cu}_{24}\text{O}_{41}$ the magnetic peak at about 4000 cm^{-1} along the c axis cannot be discriminated unambiguously from the background.

As mentioned before, the dips in $T(\omega)$ are now clearly visible as absorption peaks. Both samples exhibit quite similar spectra. Most distinct are the double peaks between 2000 and 3000 cm^{-1} along the c axis (thin lines), which do not exceed $2.5 (\Omega\text{cm})^{-1}$ below 300 K. The upper peak vanishes rapidly upon increasing temperature. The lower peak is still visible at 400 K, but the amplitude is strongly reduced. The third peak at about $3500\text{--}4000 \text{ cm}^{-1}$ for $E||c$ is hard to see in the data of $\text{La}_4\text{Ca}_{10}\text{Cu}_{24}\text{O}_{41}$ (upper panel) because reliable data is only available up to $\approx 7 (\Omega\text{cm})^{-1}$, which corresponds to 4000 cm^{-1} at 4 K.

⁸This is supported by the reflectance of $\text{Sr}_{14}\text{Cu}_{24}\text{O}_{41}$ as shown in figure 6.5 on page 145. At temperatures below the melting of the charge order in the chains, the spectrum is very similar to that of $\text{La}_4\text{Ca}_{10}\text{Cu}_{24}\text{O}_{41}$.

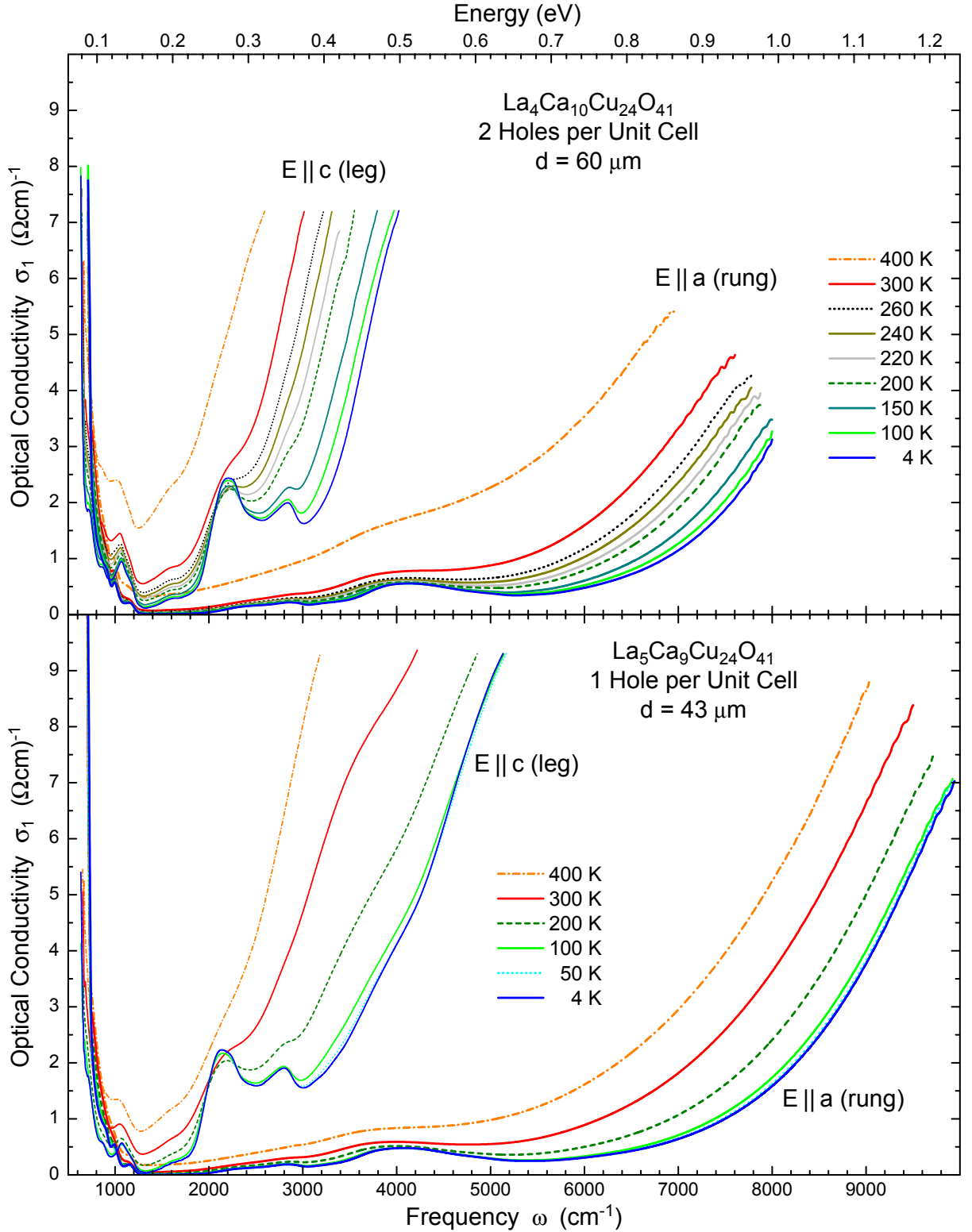


Figure 5.11: Optical conductivity $\sigma_1(\omega)$ of $\text{La}_4\text{Ca}_{10}\text{Cu}_{24}\text{O}_{41}$ (top) and $\text{La}_5\text{Ca}_9\text{Cu}_{24}\text{O}_{41}$ (bottom). For both samples the reflectance of $\text{La}_4\text{Ca}_{10}\text{Cu}_{24}\text{O}_{41}$ has been used (figure 5.6). Thick lines denote the a -axis polarization, and thin lines mark the c axis. Both panels are equally scaled to simplify the comparison.

This cutoff is directly correlated with the vanishing transmittance in the upper panel of figure 5.7. Yet in the $\text{La}_5\text{Ca}_9\text{Cu}_{24}\text{O}_{41}$ data one can see a bump at about $3500\text{--}4000\text{ cm}^{-1}$ that obviously gains weight with temperature. A more detailed view will be possible in the isolated magnetic absorption of $\text{La}_{5.2}\text{Ca}_{8.8}\text{Cu}_{24}\text{O}_{41}$ as presented below. Along the a axis, the magnetic peaks have less intensity, but the third peak at around 4000 cm^{-1} is clearly visible due to the smaller background.

There are two more features to mention. First, the small peak for $E||c$ at approximately 1050 cm^{-1} . We attribute it to a two-phonon excitation since the two-phonon regime ranges up to $2 \times \omega_{dip}^c \approx 1330\text{ cm}^{-1}$ (see section 5.2.1). In principle, the two-triplet continuum starts at two times the gap energy of 280 cm^{-1} [25, 216] plus the necessary phonon energy, which is approximately $2 \times 280\text{ cm}^{-1} + 600\text{ cm}^{-1} = 1160\text{ cm}^{-1}$. This is close to the peak, but the magnetic intensity at this boundary is very low as discussed below. Thus for a magnetic origin, the weight would be too high at this low frequency.

The second feature is the small step around $1400\text{--}1600\text{ cm}^{-1}$. This step is more interesting since it might very well have a magnetic origin. It is definitely located at a frequency that is too high for a two-phonon excitation. A three-phonon excitation cannot be excluded, though. The weight would be an order of magnitude smaller than for a typical two-phonon excitation, which is consistent with the data. However, also another scenario is possible since we as well expect a contribution from the *three-triplet* continuum ($S_{\text{tot}} = 0$). The candidate with lowest energy is the excitation of three triplets with 280 cm^{-1} each, along with the symmetry breaking phonon of $\omega_{\text{phonon}} \approx 600\text{ cm}^{-1}$, yielding $\approx 1440\text{ cm}^{-1}$ as a lower boundary. The lowest-lying triplet is located at wave vector $k = \pi$. Thus the excitation of three triplets again corresponds to a $k = \pi$ excitation, which is the momentum we are most sensitive to by means of phonon-assisted bimagnon absorption (see below).

With the samples of $\text{La}_4\text{Ca}_{10}\text{Cu}_{24}\text{O}_{41}$ and $\text{La}_5\text{Ca}_9\text{Cu}_{24}\text{O}_{41}$ no higher conductivities than $10\text{ }(\Omega\text{cm})^{-1}$ could be measured. This range was expanded by the measurements of $\text{La}_{5.2}\text{Ca}_{8.8}\text{Cu}_{24}\text{O}_{41}$. In particular the thin sample of $6\text{ }\mu\text{m}$ allowed us to measure as high as $60\text{ }(\Omega\text{cm})^{-1}$. The top panel of figure 5.12 shows the complete data sets that were calculated from four different $T(\omega)$ measurements. Of course it was necessary to do some fine tuning to get consistent spectra without artefacts in the corresponding merging intervals. Our standard procedure is to take the low-frequency data measured with the MIR setup and subsequently merge the other spectra until we get to the high-frequency measurements. Typically, the only adjustment of the MIR data is some down-scaling to avoid negative σ_1 . The thickness of each sample is another parameter that enters the calculation of σ_1 . Nevertheless, the thickness d was *never* adjusted to get better overlaps, and always the correct value calculated from the fringes was used. The only adjustments were multiplications of the transmittance data. Apart from a few exceptions above 300 K , the necessary factors did not exceed a few percent, which certainly is in the range of our experimental precision in the MIR and above. If the overlap was still not satisfactory, the only other adjustment we allowed us to perform was the multiplication of the calculated conductivities by a few percent. The complete list of all the used factors and merging ranges is not presented here but can of course be provided upon request.

Apart from the increased range of frequencies and hence better access to the electronic contribution, the $\text{La}_{5.2}\text{Ca}_{8.8}\text{Cu}_{24}\text{O}_{41}$ data is very similar to the previously presented data. Due to the enlarged scale of the plot, the magnetic peaks are difficult to make out in the

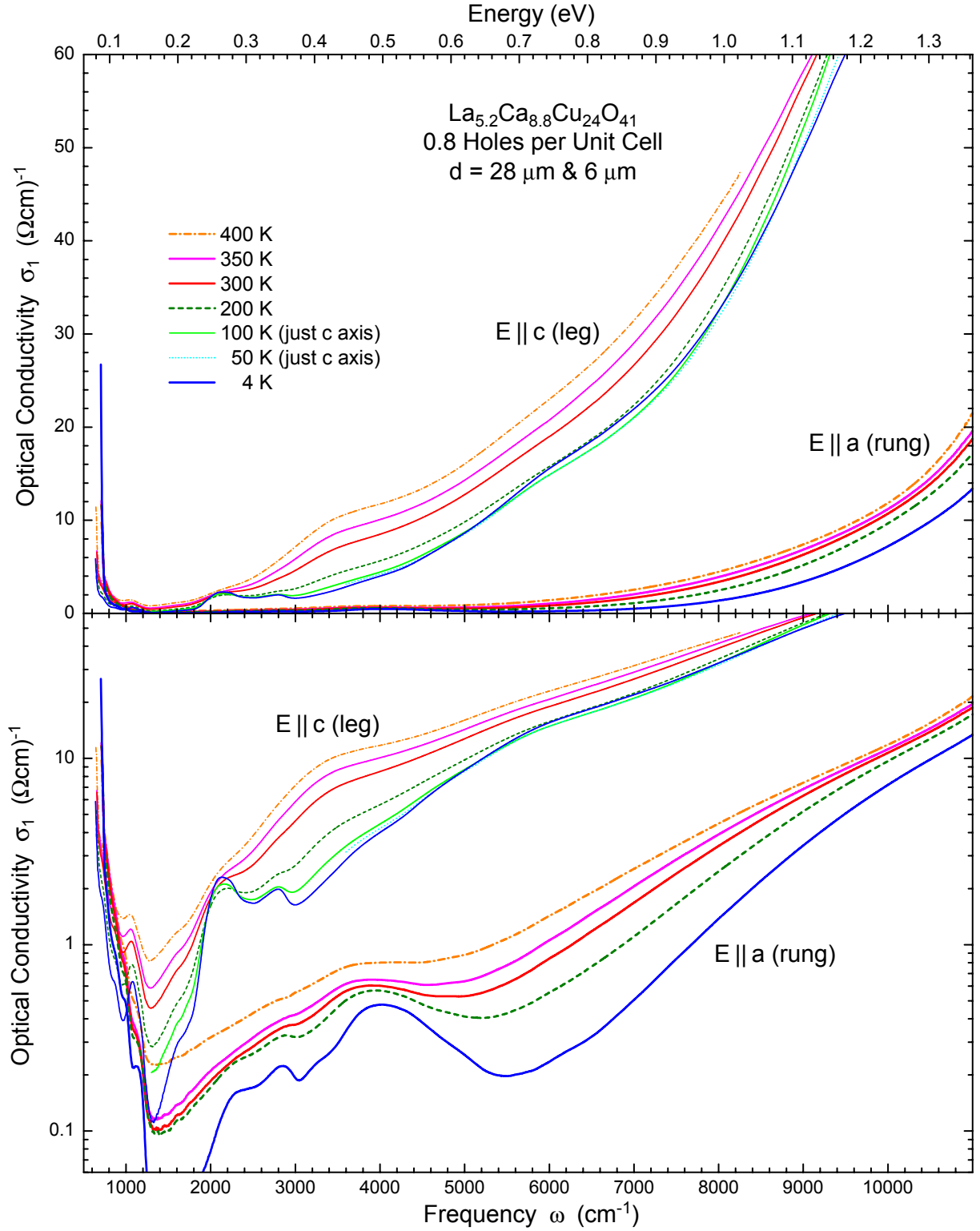


Figure 5.12: Optical conductivity of $\text{La}_{5.2}\text{Ca}_{8.8}\text{Cu}_{24}\text{O}_{41}$. **Top** panel: Data on a linear scale that reaches up to $60\ (\Omega\text{cm})^{-1}$. Note that the measurements were not performed over the entire frequency range for $T = 50$ and $100\ \text{K}$. **Bottom** panel: Same data on a logarithmic scale to emphasize the magnetic features.

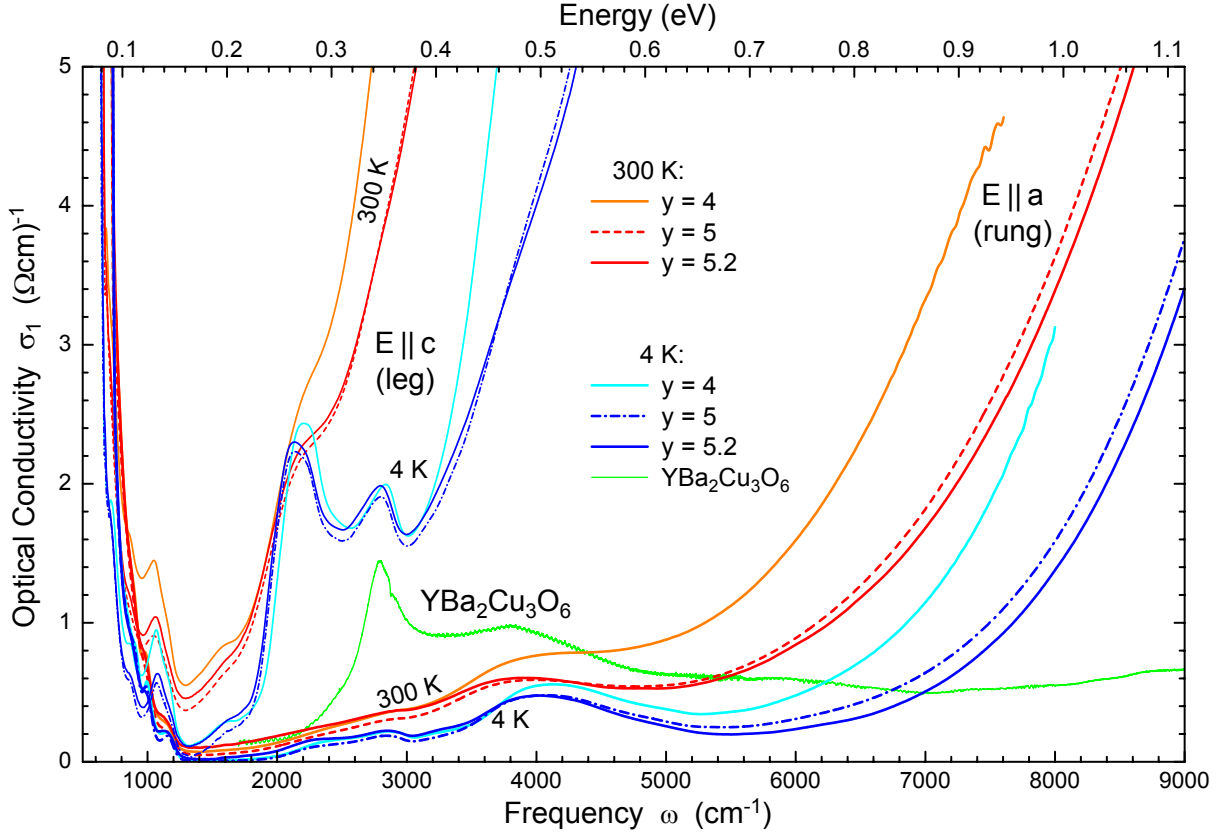


Figure 5.13: Comparison of the optical conductivity of $\text{La}_y\text{Ca}_{14-y}\text{Cu}_{24}\text{O}_{41}$ for $y = 4, 5$ (dashed), and 5.2 at $T = 4$ and 300 K. Again, thin lines denote the polarization $E||c$, and spectra for $E||a$ are drawn as thick lines. With increasing La content there is a decrease and blueshift of the background, whereas the magnetic peaks between 2000 and 3000 cm^{-1} exhibit a small redshift. Apart from that, the spectra are essentially unchanged. Bimagnon-plus-phonon absorption of $\text{YBa}_2\text{Cu}_3\text{O}_6$ [14] is presented for comparison.

top panel of figure 5.12. Therefore the same data is plotted on a logarithmic scale in the bottom panel. Another important information from this type of display is that a simple exponential function does not fit the background reliably.

At last, figure 5.13 enables a direct comparison between the three differently doped systems. Just two exemplary temperatures are included, namely 4 and 300 K. The main information from this plot is that for all doping levels the spectra are more or less equal. This demonstrates the reproducibility of cutting and polishing, and the reliability of the actual measurements and of the data analysis. The main difference between the data sets is the weight of the background. In $\text{La}_4\text{Ca}_{10}\text{Cu}_{24}\text{O}_{41}$ this contribution is obviously enhanced, which is consistent with the doubled average hole concentration compared to $\text{La}_5\text{Ca}_9\text{Cu}_{24}\text{O}_{41}$. The differences between $\text{La}_5\text{Ca}_9\text{Cu}_{24}\text{O}_{41}$ and $\text{La}_{5.2}\text{Ca}_{8.8}\text{Cu}_{24}\text{O}_{41}$ are only marginal as expected from the little change in doping. But still, at high frequencies the background is indeed larger in $\text{La}_5\text{Ca}_9\text{Cu}_{24}\text{O}_{41}$ than in $\text{La}_{5.2}\text{Ca}_{8.8}\text{Cu}_{24}\text{O}_{41}$. Thus it is verified that in the studied doping regime the background correlates with the average amount of holes in the system.

Increasing the La content from $y = 4$ to 5 causes a blueshift of the background, but at the same time the magnetic peaks between 2000 and 3000 cm^{-1} show a redshift. We attribute this redshift to a decrease of the exchange constants caused by an increase of the lattice parameters since La is larger than Ca. The redshift is most obvious for the peak at $\approx 2100 \text{ cm}^{-1}$ within the double feature for polarization $E||c$. We will demonstrate below how the position of these two peaks can be used to determine the actual exchange couplings. The little bump at around 1400-1600 cm^{-1} along the c axis, that was discussed above, is most pronounced for $y = 4$ but nonetheless visible in the other samples as well. The position seems to be basically unaffected. The reason why in $\text{La}_4\text{Ca}_{10}\text{Cu}_{24}\text{O}_{41}$ the structure is more pronounced is most likely that the dominating double peak is slightly shifted to higher frequencies. Thus the small peak is better separated from the main peaks. In figure 5.13 also the optical conductivity of undoped $\text{YBa}_2\text{Cu}_3\text{O}_6$ is plotted. The data is from reference [14] and represents a typical example of the phonon-assisted bimagnon absorption spectrum of undoped 2D cuprates [11, 12]. In fact, the resemblance to our data provided a first motivation to interpret the MIR absorption peaks in $\text{La}_y\text{Ca}_{14-y}\text{Cu}_{24}\text{O}_{41}$ as magnetic excitations. Note that in the studied ladders both the exchange constants and the relevant Cu–O bond-stretching phonon frequencies are comparable to those found in the 2D cuprates [24].

5.2.4 Subtraction of the Electronic Background

To be able to discuss the actual magnetic absorption, we first have to subtract the electronic background. The origin of the background is not really clarified so far. An obvious assumption would be interband excitations of charge-transfer type. Osafune et al. [168] found a charge-transfer gap of around 2 eV ($\approx 16\,000 \text{ cm}^{-1}$) at room temperature as presented in figure 2.32 on page 46. It is not obvious, though, why there should be an onset of absorption already at such low frequencies as 6000 cm^{-1} for $E||a$ and even 3000 cm^{-1} for $E||c$. One possible explanation is that the system is actually not undoped (i.e. not half-filled), but that there is a small amount of doped holes which are localized by e.g. impurities. These holes might result from oxygen non-stoichiometry, which simultaneously may play the role of the localizing impurities. The binding energy along the legs may be lower since the gain in kinetic energy is larger.

Predictions of the actual shape of σ_1 in the vicinity of an excitation gap are quite challenging. The case of conventional band insulators, for instance, is well understood [189]. The most simple type of excitations occurs if the maximum of the valence band and the minimum of the conduction band of a semiconductor have the same wave vector. Then a so-called direct gap is present, and in the absence of interactions, lattice imperfections, and at vanishing temperature there is no absorption for energies smaller than the gap energy E_{gap} . In order to calculate the absorption just above this energy, one has to consider the dimension of the actual system.⁹ In the three-dimensional case one gets a square-root dependence of the imaginary part of the dielectric function [189], i.e.

$$\varepsilon_2 \propto \frac{1}{\omega^2} \sqrt{\hbar\omega - E_{\text{gap}}}. \quad (5.2)$$

⁹Here and in the following we neglect a possible dependence of the matrix element on the energy or on the momentum.

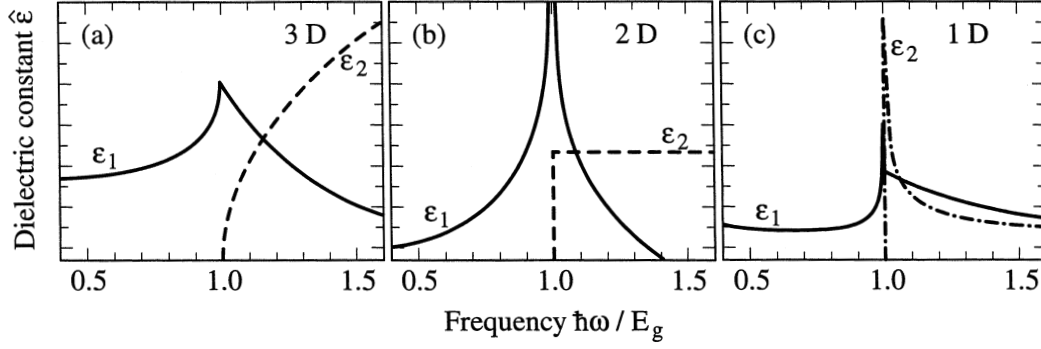


Figure 5.14: Frequency dependence of ε_1 and ε_2 of a semiconductor near the band gap E_g with direct transition for 1, 2, and 3 dimensions. Reproduced from reference [189] and rearranged.

The factor of $1/\omega^2$ may be considered to be mainly constant in the direct vicinity of the gap. Thus it is indeed the square-root behavior that dominates $\varepsilon_2(\omega)$ close to E_{gap} . This does not change for the real part of the optical conductivity, which is directly related to ε_2 according to

$$\sigma_1(\omega) = \frac{\omega}{4\pi} \varepsilon_2(\omega). \quad (5.3)$$

Again, the additional factor of ω does not change the overall shape near E_{gap} . Therefore both σ_1 and ε_2 will exhibit a square-root onset. For systems in which the energy depends only on two components of the wave vector, ε_2 exhibits a step from zero to a constant value at the energy E_{gap} . Finally, in one dimension a singularity in the density of states leads as well to a singularity of the absorption,

$$\varepsilon_2 \propto \frac{1}{\omega^2} \frac{1}{\sqrt{\hbar\omega - E_{gap}}}. \quad (5.4)$$

All three cases are depicted in figure 5.14.

In a large number of semiconductors, the energy maximum of the valence band and the minimum of the conduction band are not located at the same momentum. In this case the gap is called *indirect*. Due to momentum conservation, indirect optical transitions are only possible when the excitation of a phonon is involved. At finite temperatures the phonon states are already populated and annihilation processes are also possible. In 3D, the energy dependence of an indirect optical transition is different from the square-root behavior found for a direct transition. In fact one gets

$$\varepsilon_2(\omega) \propto N_p (\hbar\omega - E_{gap} \mp E_{ph})^2 \quad (5.5)$$

for $\hbar\omega \geq E_{gap} \pm E_{ph}$ [189]. Now the absorption is strongly temperature dependent, reflecting the phonon population factor N_p . The scenario gets more complicated when the Coulomb interaction between the excited electron and the remaining hole leads to exciton states. These bound electron-hole pairs have an energy smaller than E_{gap} . Transitions to these levels may lead to a series of well defined absorption peaks below the absorption

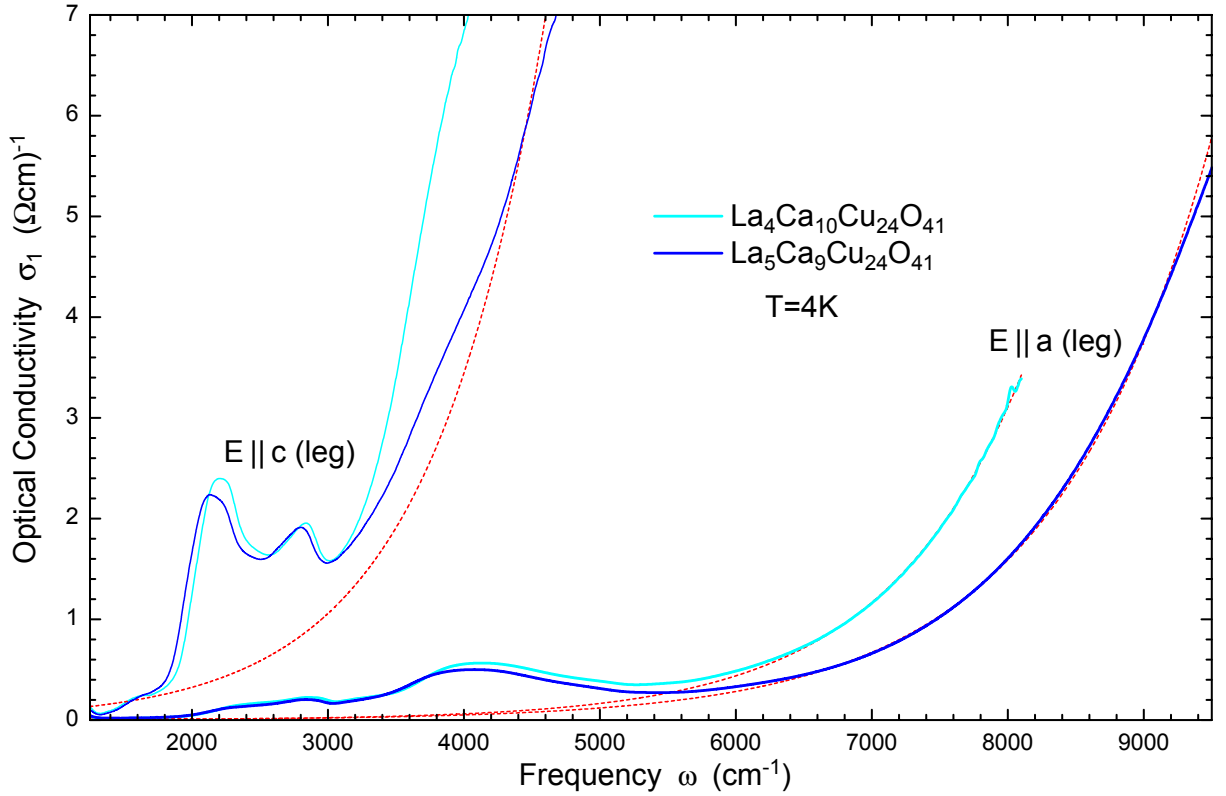


Figure 5.15: Optical conductivity of $\text{La}_4\text{Ca}_{10}\text{Cu}_{24}\text{O}_{41}$ and $\text{La}_5\text{Ca}_9\text{Cu}_{24}\text{O}_{41}$ at 4 K along with exponential fits (dashed lines). The fitting range was $\omega > 6500 \text{ cm}^{-1}$ for $E||a$ and $\omega > 4500 \text{ cm}^{-1}$ for $E||c$. The data is identical to the one presented in reference [24].

onset discussed so far. But especially when E_{gap} is small it is also possible that the different energy levels merge into a continuum.

The correct shape of a realistic absorption onset is already very difficult for conventional semiconductors. However, the case we have to deal with in the ladder compounds is rather described by a Mott-Hubbard insulator with considerable on-site Coulomb repulsion. First calculations for the 1D case of a (half-filled) Mott-Hubbard chain were recently published [217–219]. At half filling, the absorption exhibits a square-root dependence [217, 218]

$$\sigma_1(\omega) \propto \sqrt{\hbar\omega - E_{\text{gap}}}. \quad (5.6)$$

Reference [219] focusses on the influence of Mott-Hubbard excitons on σ_1 , which are also called holon-antiholon pairs.

But there are many effects that can significantly change the absorption spectrum in real crystals, for instance long-range parts of the Coulomb interaction, the actual lattice structure, interchain couplings, and disorder [218]. That means for us that there is no guideline to choose a proper function to fit the background, in particular since it is not clear whether the background is indeed the onset of interband excitations or rather due to e.g. localized carriers. Our first attempt was to use exponential functions as presented in reference [24]. The corresponding data is reproduced in figure 5.15. Dashed lines

indicate the exponential fits for $\omega > 6500 \text{ cm}^{-1}$ (a axis) and $\omega > 4500 \text{ cm}^{-1}$ (c axis). At that time the measurements on $\text{La}_{5.2}\text{Ca}_{8.8}\text{Cu}_{24}\text{O}_{41}$ had not been performed, and hence we were lacking reliable high-conductivity data above $\approx 8 (\Omega\text{cm})^{-1}$. The fits of the a -axis spectra are already convincing, and after subtraction of the background, $\sigma_a(\omega)$ is nearly identical for La contents $y = 4$ and 5. This corroborates the assumption that the ladders are basically undoped. The background subtraction for $E||c$ was difficult, though, and we refrain from presenting fits for $\text{La}_4\text{Ca}_{10}\text{Cu}_{24}\text{O}_{41}$. Due to the uncertainty in $\text{La}_5\text{Ca}_9\text{Cu}_{24}\text{O}_{41}$, the precise shape and spectral weight of the third magnetic peak at $\approx 4000 \text{ cm}^{-1}$ could not be determined unambiguously. In addition, below 1600 cm^{-1} the fit intersects the measured data. Nevertheless, the quality of these initial fits for both polarizations was clearly sufficient to verify the singlet bound state in the undoped telephone-number compounds in reference [24].

Afterwards, the $\text{La}_{5.2}\text{Ca}_{8.8}\text{Cu}_{24}\text{O}_{41}$ data allowed us to refine the fitting. It turned out that for $E||a$ Gaussian fits to the background provide even better results than the exponential ones, and this kind of fits was presented in reference [213]. We used the equation

$$\sigma_{\text{back}}(\omega) = A e^{-(\omega - \omega_c)^2 / 2\omega_o^2}. \quad (5.7)$$

The center of the Gaussian peak is given by ω_c . This position of the maximum is always beyond our measured frequency range. We just use the initial rise of this function. The amplitude is denoted by A , and ω_0 describes the width. From what was said above, we cannot provide an explanation why exactly this function provides excellent fits. Figure 5.16 shows the spectra of the a -axis polarization. In the top panel the data is plotted on a large scale along with the according Gaussian fits. The fit range was 8000 to $10\,500 \text{ cm}^{-1}$, where the magnetic contribution is definitely negligible ($8000 \text{ cm}^{-1} \approx 8J$, see below). The fits are drawn as thin black lines, and above $\approx 7000 \text{ cm}^{-1}$ the agreement with the measured data is excellent. The actual magnetic regime below this frequency is better visible in the middle panel, where the same data is plotted on a smaller scale. To calculate the actual magnetic contribution, we subtracted these fits from the spectra. In the bottom panel of figure 5.16 the results are presented. Note the small scale of this plot. The main peak at around 4000 cm^{-1} does not exceed $0.6 (\Omega\text{cm})^{-1}$, which is a remarkable demonstration of the sensitivity of our measurements. And what is more, between 7000 cm^{-1} and $10\,000 \text{ cm}^{-1}$ the calculated spectra do not exceed $\pm 0.05 (\Omega\text{cm})^{-1}$. This nicely verifies that there is no magnetic absorption above 7000 cm^{-1} and that the Gaussian fits entirely describe the background for $E||a$ in this frequency range.

At 4 K, there are basically three magnetic peaks. Within the double-peak structure, the lower peak at $\approx 2300 \text{ cm}^{-1}$ is less pronounced than the upper peak at $\approx 2850 \text{ cm}^{-1}$. At around 4000 cm^{-1} , a broad peak with large amplitude is centered. This peak surely dominates the spectra and gains weight upon increasing temperature. The maximum shifts slightly to lower frequencies and is located below 3700 cm^{-1} at 400 K. The lowest peak smears out soon at higher temperatures, and already at room temperature it is almost absent. The upper one of the double peak is still visible at 400 K. We will show below that the broad peak stems from the two-triplet continuum, whereas the double peak is a signature of the bound state. Note that the onset of absorption is located between

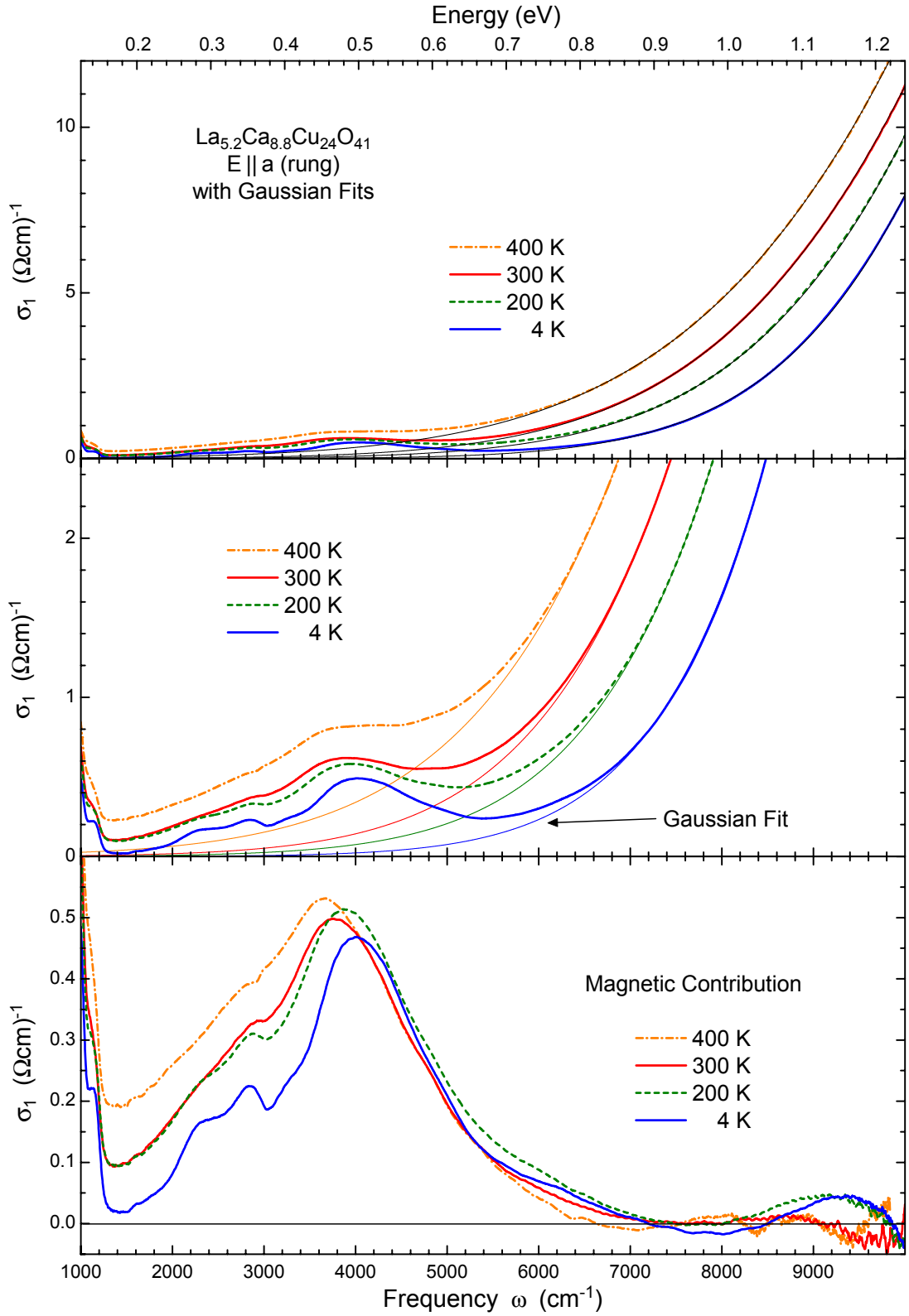


Figure 5.16: Subtraction of the electronic background of σ_1 in $\text{La}_{5.2}\text{Ca}_{8.8}\text{Cu}_{24}\text{O}_{41}$ for polarization $E \parallel a$. **Top** panel: σ_1 on a large scale with Gaussian fits (thin black lines, fit range 8000 to 10500 cm^{-1}). **Middle** panel: Same data on a smaller scale. **Bottom** panel: The fits were subtracted from the spectra to obtain the magnetic contribution. Note the extremely small σ_1 scale and the vanishing magnitude above 7000 cm^{-1} .

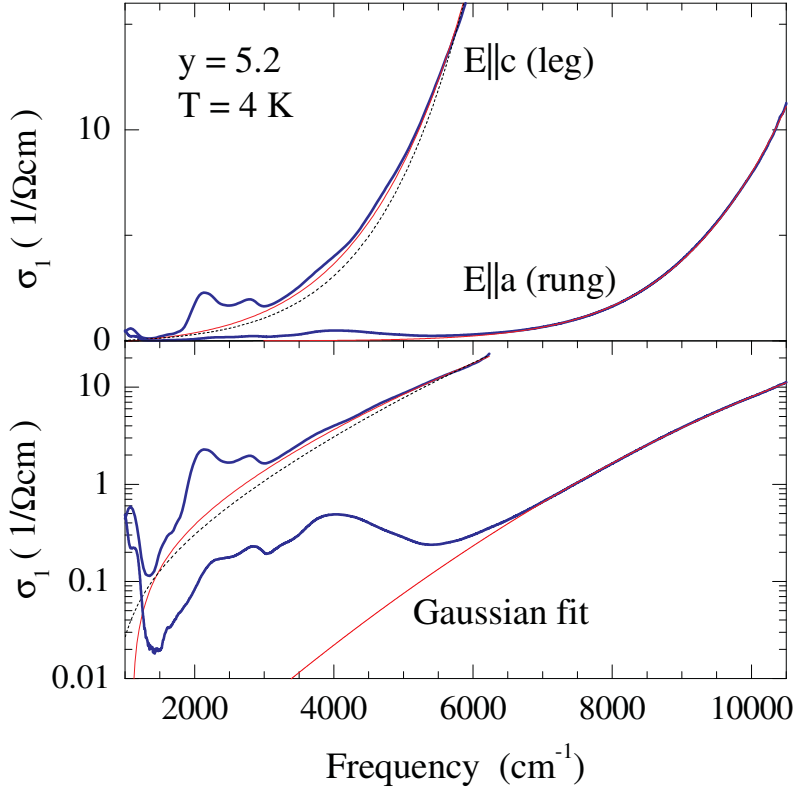


Figure 5.17: Optical conductivity of the $d = 28 \mu\text{m}$ sample of $\text{La}_{5.2}\text{Ca}_{8.8}\text{Cu}_{24}\text{O}_{41}$ at 4 K. In the **top** panel the data is plotted on a linear scale while in the **bottom** panel the same data is shown on a logarithmic scale. Thin lines denote the Gaussian fits for both polarizations. For $E||c$ we could not find unambiguous fits and thus showed two different curves to demonstrate the uncertainty. Already presented in reference [213].

1400 and 1600 cm^{-1} , similar to the above discussed case of the c axis data, where this feature was tentatively ascribed to the onset of phonon-assisted three-triplet absorption.

The extraction of the magnetic features for $E||c$ was more difficult. The exponential fits presented in reference [24] were not appropriate any more as soon as the $d = 28 \mu\text{m}$ data of $\text{La}_{5.2}\text{Ca}_{8.8}\text{Cu}_{24}\text{O}_{41}$ was available. Then we used Gaussian fits just like for $E||a$. We presented such Gaussian fits for both polarizations in reference [213]. However, for $E||c$ we still could not provide unambiguous fits and showed two different Gaussian fits to demonstrate the uncertainty. The corresponding plot of reference [213] is reproduced in figure 5.17. After the $6 \mu\text{m}$ data was available, we found another way to achieve better fits, which was necessary to describe an additional broad bump located at about 6000 cm^{-1} (see figures 5.18 and 5.19). We used a fit function consisting of a quadratic part for the high frequencies and an additional small Gaussian term, i.e.

$$\sigma_{\text{back}}(\omega) = A_1 e^{-(\omega - \omega_{c1})^2/2\omega_o^2} + A_2 (\omega - \omega_{c2})^2. \quad (5.8)$$

The frequency ω_{c2} describes where the parabola sets in, and the strength is given by A_2 . The part of the parabola below the minimum for $\omega < \omega_{c2}$ was omitted. In the top and

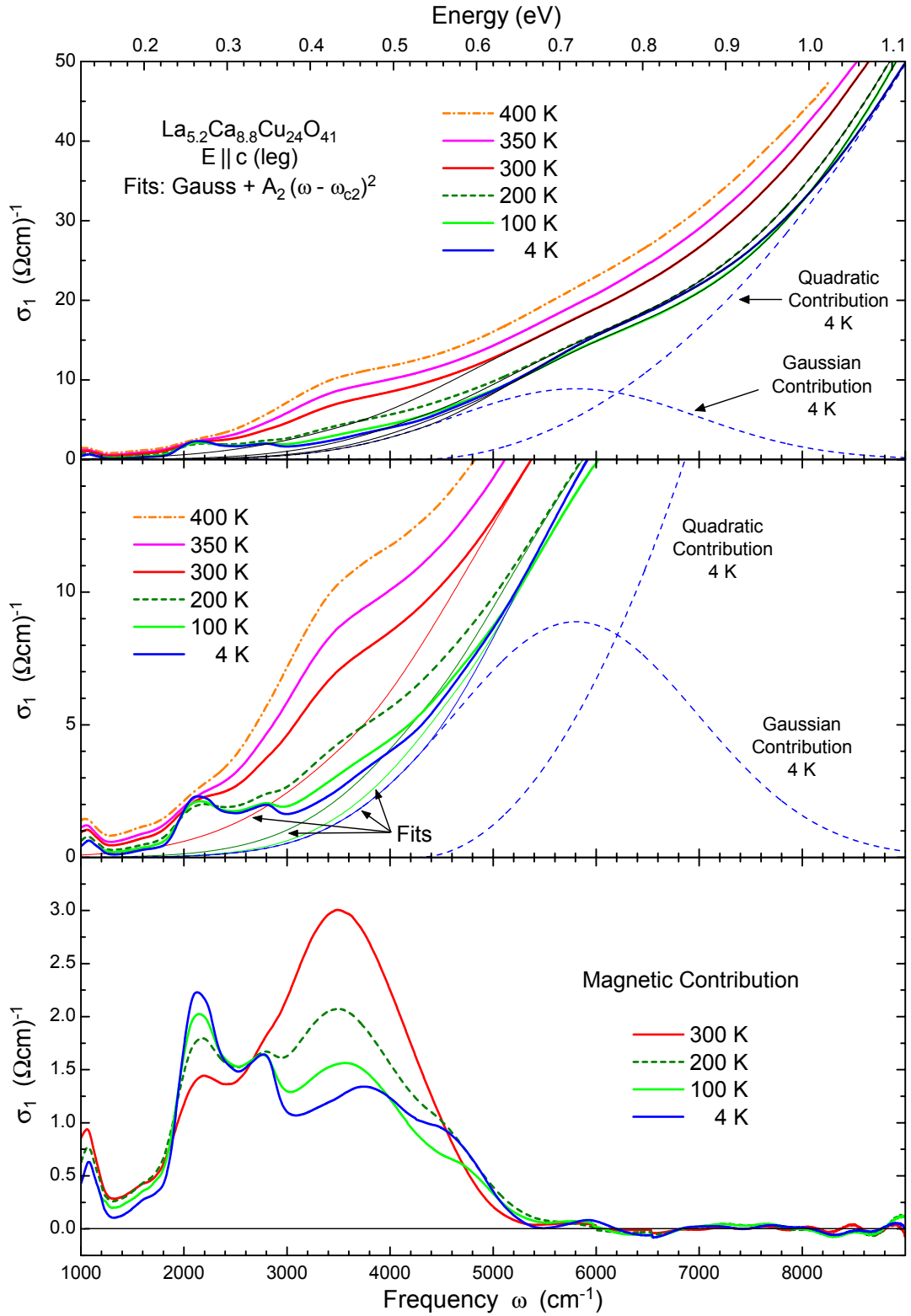


Figure 5.18: Subtraction of the electronic background of $\text{La}_{5.2}\text{Ca}_{8.8}\text{Cu}_{24}\text{O}_{41}$ for $E \parallel c$. **Top** panel: σ_1 on a large scale along with the fits (thin black lines). Dashed lines denote the two components of the 4 K fit. **Middle** panel: Same data on a smaller scale to visualize the magnetic features. **Bottom** panel: The fits were subtracted from the spectra to obtain the magnetic contribution. Note the small σ_1 scale and the vanishing magnitude above 5500 cm^{-1} , which demonstrates the quality of the fits.

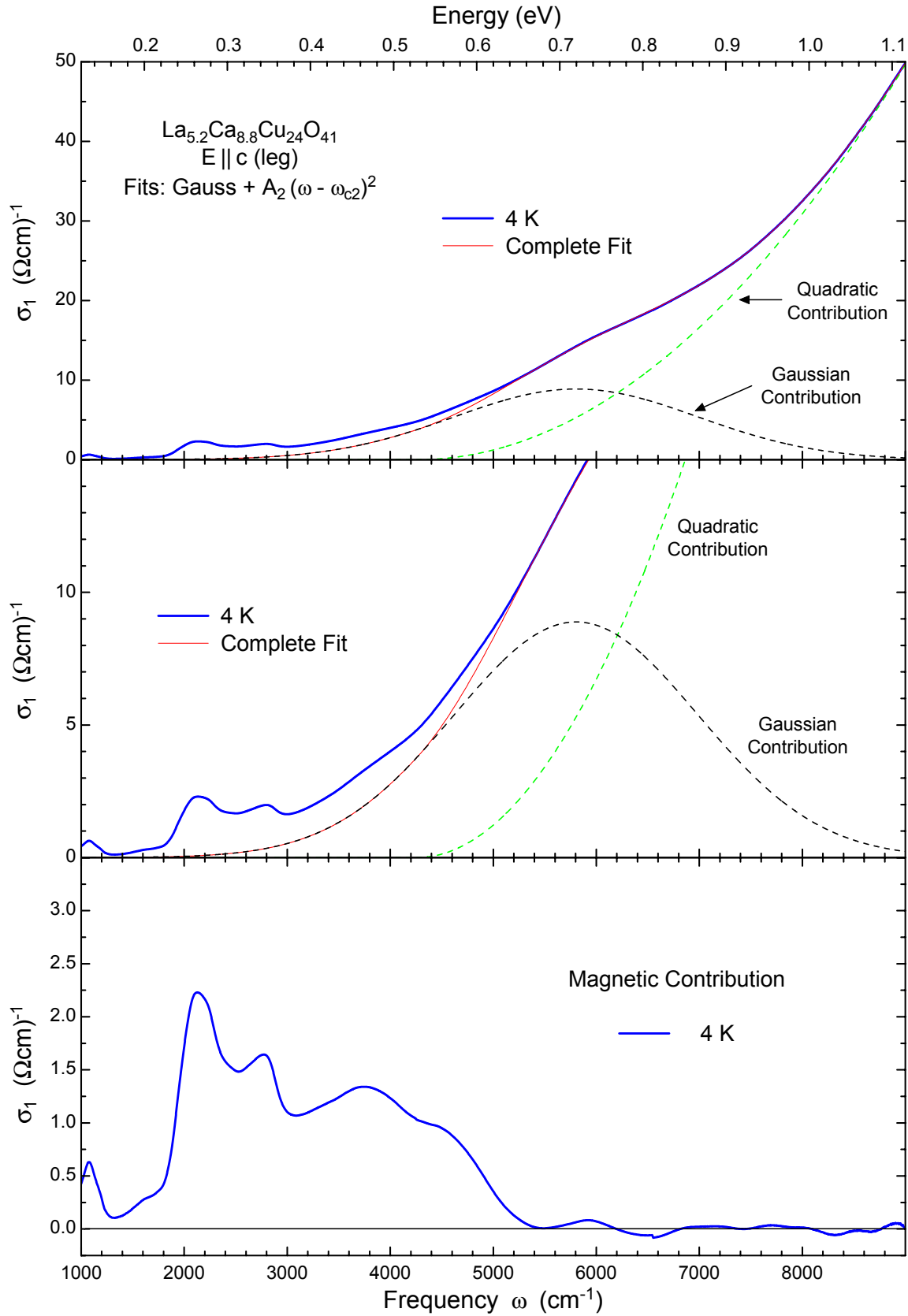


Figure 5.19: Subtraction of the electronic background of $\text{La}_{5.2}\text{Ca}_{8.8}\text{Cu}_{24}\text{O}_{41}$ for $E \parallel c$. This plot is equivalent to figure 5.18, but just the 4 K data is included for clarity.

middle panel of figure 5.18 the c axis spectra of $\text{La}_{5.2}\text{Ca}_{8.8}\text{Cu}_{24}\text{O}_{41}$ are plotted together with the combined fits. As an example, for $T = 4$ K the two terms of the fit are included separately as dashed lines. For clarity, the same plot is shown again with just the 4 K data in figure 5.19. The Gaussian term is used to fit the additional broad bump located at around 6000 cm^{-1} , that does not occur for $E||a$. We don't expect this contribution to have any magnetic origin since the frequency and the strength are too large. It is true that $\text{La}_{5.2}\text{Ca}_{8.8}\text{Cu}_{24}\text{O}_{41}$ is mainly undoped but there are still nominally 0.8 holes per unit cell, which presumably reside in the chains. What is more, the excess oxygen provides further holes. We can only speculate about the influence of these charge carriers. The dc resistivity is very high and thus one might conjecture that e.g. some sort of trapping mechanism is responsible for the broad peak. Anyhow, our primary aim at this point is to deduce the magnetic contribution to σ_1 , and the fits work well.

Apart from the Gaussian contribution at lower frequencies, the main part of these fits at higher frequencies consists of the parabola, especially above 6500 cm^{-1} . We could have also used a second large Gaussian peak like for $E||a$. But in fact, from all the possible theoretical candidates to describe the onset of a charge-transfer gap, a parabola seems to be more likely than the rising part of a large Gaussian peak. What is more, just two parameters are needed for the parabola, which is one less compared to a further Gaussian peak. In the bottom panels of figures 5.18 and 5.19, the magnetic spectra are presented, again calculated by subtracting the fits from the original σ_1 data. Like for the a axis, the high frequency parts of these calculated spectra provide a direct probe for the fitting quality. Here, between 5500 and 8900 cm^{-1} the difference between original data and the fits does never exceed $0.1 (\Omega\text{cm})^{-1}$ although the original values reach as high as $55 (\Omega\text{cm})^{-1}$. All the according fitting parameters are given in table 5.1.¹⁰

The magnetic contribution to σ_1 (σ_{mag}) shows some similarities to the according a -axis spectra of figure 5.16. At 4 K, there are again the two lower peaks which are slightly

	$A_1 (\Omega\text{cm})^{-1}$	$\omega_{c1} (\text{cm}^{-1})$	$\omega_o (\text{cm}^{-1})$	$A_2 (\Omega\text{cm})^{-1}$	$\omega_{c2} (\text{cm}^{-1})$
4 K	8.8842	5804.17	1181.78	2.2027×10^{-6}	4254.10
100 K	10.041	5785.60	1183.97	2.7383×10^{-6}	4652.80
200 K	9.6706	5638.46	1247.78	2.4917×10^{-6}	4385.86
300 K	8.8280	5260.08	1409.73	1.9358×10^{-6}	3586.96

Table 5.1: Complete set of parameters, according to equation 5.8, for the fits shown in figures 5.18 and 5.19.

¹⁰Actually, we also used the later presented DMRG data (figure 5.31) to obtain the presented fits. This was very useful since the two peaks of the continuum (bottom panels of figures 5.18 and 5.19) overlap with the broad Gaussian contribution (middle panel). Hence it is not possible to fit the background separately, unlike the case of $E||a$. With the help of the DMRG data we obtained the position and the width of two additional Gaussian peaks that describe the continuum. These four parameters were afterwards used as fixed values for the complete fitting function. Hence this function included a total of three Gaussians and the parabola. But there were only two new fitting parameters since just the amplitudes of the continuum peaks were allowed to vary. The complete function was then fitted to the spectra above 3300 cm^{-1} where the contribution of the bound-state peaks is negligible. Afterwards, only the described broad Gaussian and the parabola of equation 5.8 were used for the subtraction of the background.

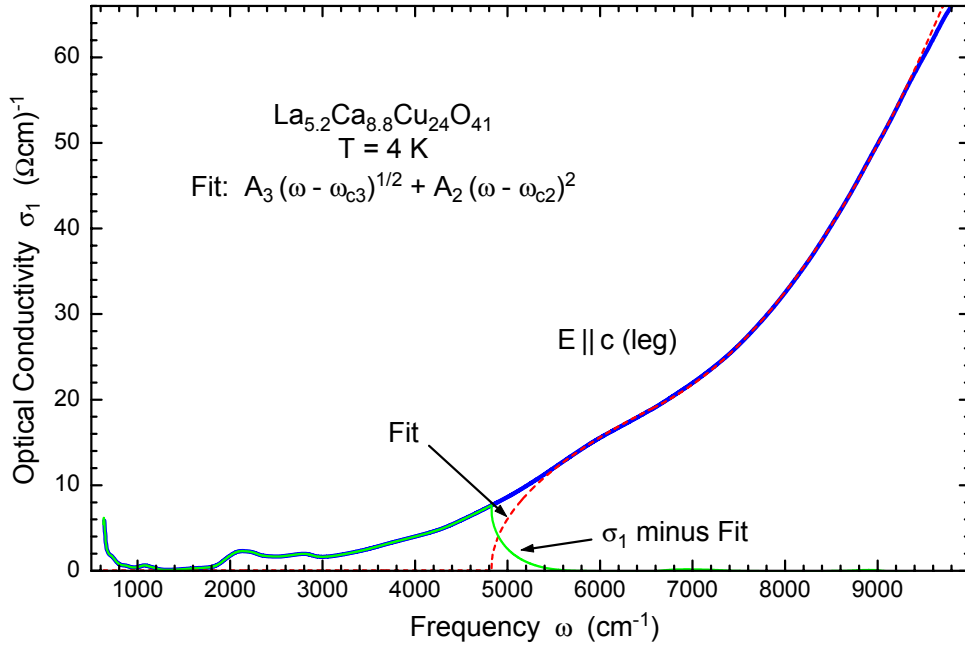


Figure 5.20: Optical conductivity of $\text{La}_{5.2}\text{Ca}_{8.8}\text{Cu}_{24}\text{O}_{41}$ at 4 K for $E||c$. The fit includes a square-root onset together with a parabola. The data above 5500 cm^{-1} is well described, but the actual onset is poorly fitted, resulting in an unrealistic cusp after subtraction of the fit.

redshifted to ≈ 2140 and 2770 cm^{-1} . The broad upper peak shows more structure than for $E||a$ and in fact rather consists of two separate peaks. Upon increasing the temperature, also for $E||c$ the lowest peak at 2140 cm^{-1} loses weight, whereas the broad upper peaks gain weight and lose the fine structure at 300 K. At 2670 cm^{-1} there is a so-called isosbestic point where all spectra of the different temperatures cross. In general, such a feature suggests that there is a transfer of spectral weight from one component to another without an attendant change in the line shape of either component [220]. But the upper peaks obviously gain more weight than the lower ones lose.

As pointed out above, there is a resemblance to the in-plane spectra of undoped $\text{YBa}_2\text{Cu}_3\text{O}_6$ [14, 110]. Upon heating from 4 to 300 K, the main resonance peak at lower frequencies broadens, and at the same time the weight of the high-frequency sideband increases (see figure 3.2 on page 58). The sideband contribution is beyond the scope of conventional spin-wave theory and most likely due to strong quantum fluctuations [14].

The presented fitting procedure is certainly not unique. For instance, we tried to replace the broad Gaussian by a square-root contribution. This was motivated by the expected square-root onset in 1D Mott-Hubbard insulators as discussed above. In figure 5.20 the 4 K data of $\text{La}_{5.2}\text{Ca}_{8.8}\text{Cu}_{24}\text{O}_{41}$ is shown for $E||c$ together with the corresponding fit (dashed line). Thus in principle it is possible to replace the Gaussian by a square-root function. But the actual onset below 5000 cm^{-1} is not described realistically. One might still think of other mechanisms that may lead to some sort of smearing out of the onset. However, this path does not promise to yield better fits of the electronic background than the procedure presented above.

were also presented in references [24, 212, 213]. More detail on the actual computations was given by Knetter et al. in reference [224]. The technique itself is described extensively in reference [92].

A third approach by Nunner et al. [26] is based on the density-matrix renormalization group method (DMRG), which was developed by White in 1992 [225, 226]. A general introduction is given in reference [227]. This method allows to treat fairly large 1D systems with high accuracy and has thus substantially accelerated the progress in the numerical treatment of low-dimensional quantum systems. One shortcoming is that it is mainly applicable to one-dimensional systems, or equivalently systems with short-range interactions. Another point worth mentioning is the limited frequency resolution. The calculation of dynamic correlation functions such as the optical conductivity has become possible only recently by the development of the dynamical DMRG [218, 228]. The DMRG is a refined numerical real-space renormalization-group method.¹² Renormalization-group techniques make use of an iterative truncation of the Hilbert space and try to progressively eliminate unimportant degrees of freedom (usually high-energy eigenstates). They start from a small system which can be handled rigorously, then renormalize the Hamiltonian by projecting onto an effective Hamiltonian, keeping only a truncated Hilbert space, and then increase the system size and reiterate the procedure. The DMRG uses an optimal projection by selecting a reduced set of basis states via density matrices and truncates the Hilbert space by keeping only the eigenstates of the density matrix with the largest weight, i.e. not the high-energy eigenstates are projected out, but the unlikely ones.

For our purpose, which is the comparison of experiment and theory, the major advantage of the DMRG is that it incorporates 100% of the spectral weight of $\sigma_1(\omega)$, and not only the two-triplet contribution. Moreover, Nunner et al. additionally investigated the influence of a cyclic exchange J_{cyc} [26] (see section 2.3.2). These results will be presented in section 5.3.2, for the time being J_{cyc} is omitted. Very recently, the influence of J_{cyc} has also been studied within the CUT approach [163].

5.3.1 Jordan-Wigner Fermions and Continuous Unitary Transformations

We first concentrate on the two techniques using Jordan-Wigner fermions and continuous unitary transformations.¹³ Both methods are controlled in the sense that they become exact on $J_{\parallel}/J_{\perp} \rightarrow 0$. The strong-coupling limit with triplets as elementary excitations is the appropriate starting point. For instance, the excitations of the ladder cannot be constructed perturbatively from free spinons in the uncoupled limit since the rung coupling is a relevant perturbation [16, 221]. This is illustrated by the fact that the excitation spectrum remains gapped for any non-zero J_{\perp} . Very important is the intermediate coupling regime for $J_{\parallel} \approx J_{\perp}$ because we expect such ratio in the telephone-number compounds. But this isotropic regime is difficult to reach and requires elaborate calculations. In fact, comparing the results for the dispersion of the elementary triplet, the agreement between both approaches is excellent for $J_{\parallel}/J_{\perp} \leq 0.6$. In figure 5.22 the triplet dispersion is

¹²A momentum space DMRG was recently set up [229], but it converges reasonably only in weak-coupling regimes.

¹³This section is largely based on references [24, 213].

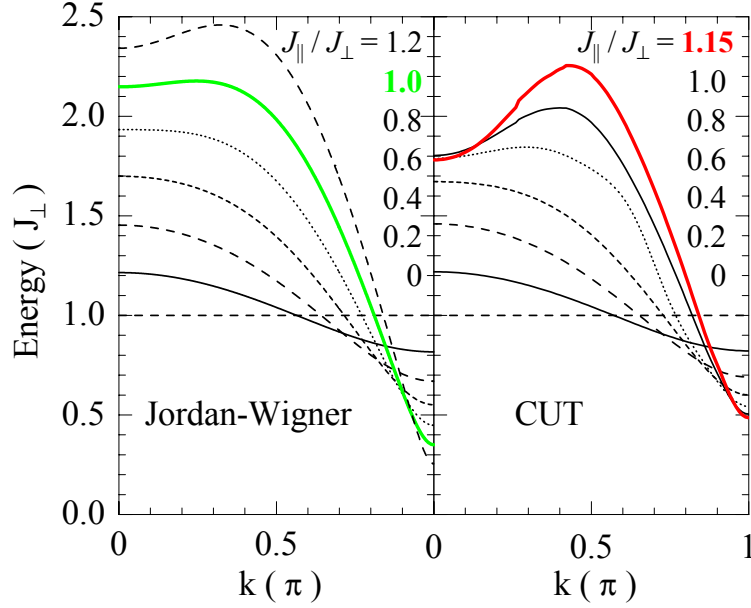


Figure 5.22: Comparison of the elementary triplet dispersion of the Jordan-Wigner (left) and of the CUT approach (right). Different curves are plotted for coupling ratios $0 \leq J_{\parallel}/J_{\perp} \leq 1.2$. The agreement is excellent for $J_{\parallel}/J_{\perp} \leq 0.6$. Thick lines denote the ratio that provided the best fits to our $\text{La}_{5.2}\text{Ca}_{8.8}\text{Cu}_{24}\text{O}_{41}$ data. Already presented in reference [213].

shown for different coupling ratios. For each theory, the thick line denotes the coupling ratio that offers the best description of our $\text{La}_{5.2}\text{Ca}_{8.8}\text{Cu}_{24}\text{O}_{41}$ data. One can see that with increasing J_{\parallel}/J_{\perp} the bandwidth of the dispersion strongly increases. In addition, a maximum emerges at momentum $k \lesssim 0.4\pi$.

The two-triplet excitation energies for the isotropic case $J_{\parallel} = J_{\perp}$ are plotted in figure 5.23. The data of the left panel is identical to the CUT results of reference [224]. Shown are the dispersion of the elementary triplet and the two-triplet continuum. The triplet branch reproduces previous results very well [133, 230]. Also included are the two different two-triplet bound states with $S = 0$ and 1. The overall shape qualitatively resembles the spectra presented earlier (figures 5.3, 5.4, 5.5). However, the continuum and especially the $S = 0$ bound state exhibit more structure. In fact, after leaving the continuum above $k \approx 0.3\pi$, there is a maximum near $\pi/2$. Also there is a considerable dip at $k = \pi$. This has been unnoted so far because it occurs only for $J_{\parallel}/J_{\perp} \gtrsim 0.5$. Hence there will clearly be two separate van Hove singularities in the density of states, corresponding to the maximum and the minimum of the dispersion of the $S = 0$ bound state. We can reckon on *two* absorption peaks stemming from the $S = 0$ bound state. The right panel of figure 5.23 shows the according excitation spectrum based on the Jordan-Wigner transformation (solid lines). The agreement between both techniques is good although there are some deviations in the absolute values. The symbols connected by dashed and dotted lines in the right panel denote the results of dynamical DMRG for a ladder with $N = 80$ sites [26]. This third approach is discussed in section 5.3.2, but it is obvious that the agreement with the CUT data is excellent.

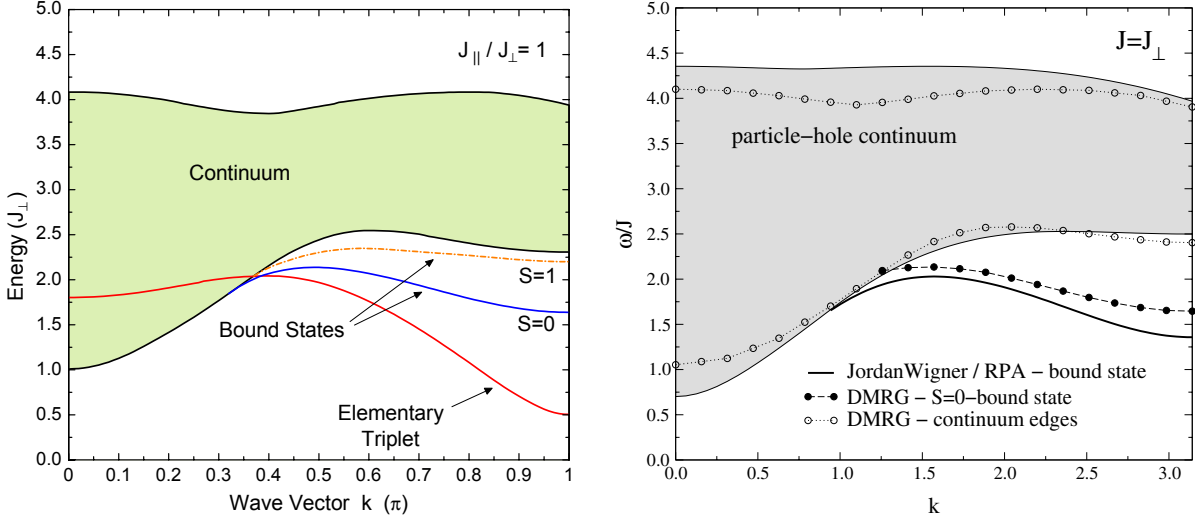


Figure 5.23: Band edges of the two-triplet continuum and $S = 0$ bound-state energies for an isotropic coupling ratio $J_{\parallel}/J_{\perp} = 1$. In both panels there is a considerable dip in the bound-state dispersion at $k = \pi$. **Left** panel: Results of the perturbative CUT computations. Also included are the elementary triplet and the $S = 1$ bound state (dash-dotted). The data is from reference [224]. **Right** panel: Jordan-Wigner results (solid); here J means J_{\parallel} . Symbols connected by dashed and dotted lines represent DMRG data (see section 5.3.2) for $J_{\parallel} = J_{\perp}$. Here, $J_{cyc} = 0$ in all calculations. Reproduced from reference [221].

In order to determine the optical conductivity, one needs to calculate the momentum-resolved spectral densities of the $S_{tot} = 0$ channel. The evolution of the two-triplet contribution to these spectral densities from $J_{\parallel}/J_{\perp} = 0.2$ to 1 is plotted for both theories in figure 5.24 for $E||c$. Afterwards, the optical conductivity as given in figure 5.25 is obtained by integrating these k -resolved curves. A weight factor of

$$F = \sin^4(k/2) \quad (5.9)$$

is needed to account for the proper coupling to the involved phonon.¹⁴ To compare the spectra with experimental data, one has to add the energy of the involved symmetry-breaking phonon as a constant shift of the energy scale. Afterwards, it is also necessary to multiply the densities by the frequency ω [213].

In the following, the k -resolved spectra of figure 5.24 and their implications on the derived conductivity spectra of figure 5.25 are described. For the smallest ratio of

¹⁴In general, one has to consider the dependence of the exchange constants both on the external electric field \mathbf{E} of the photon and on the displacements \mathbf{u} of the oxygen atoms, as discussed in section 3.3. Thus $J_{\parallel,\perp} \equiv J_{\parallel,\perp}(\mathbf{E}, \mathbf{u})$ [11, 12, 14]. The phonons modulate the inter-site hopping and the on-site energies on both Cu and O sites. A momentum-dependent weight factor emerges that influences the line shape of the spectrum. Here, the weight factor is a mixture of the mentioned \sin^4 term [140] and a k -independent term. For simplicity, we consider only the dominant \sin^4 term and Einstein phonons with a typical frequency of $\omega_{ph} = 600 \text{ cm}^{-1}$, as is common for the cuprates. Our findings depend only very weakly on the precise phonon energy [24]. Further details on the relevant phonon modes and the according weight factors are presented by Nunner et al. in reference [201], see also section 5.3.2.

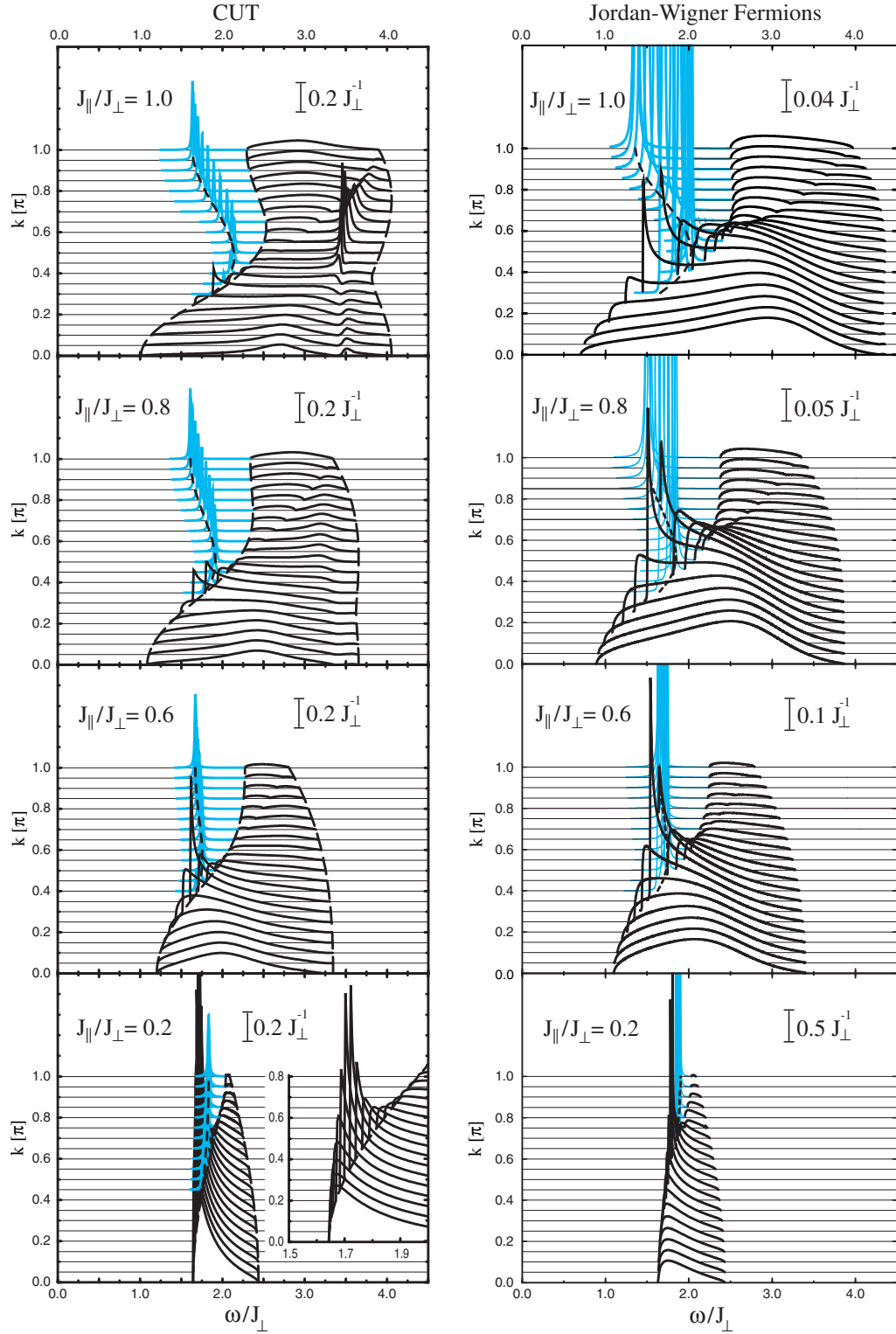


Figure 5.24: Momentum dependence of the two-triplet spectral densities with $S_{tot} = 0$ for $E||c$. Calculations were performed with continuous unitary transformations (**left**) and Jordan-Wigner fermions (**right**) for $0.2 \leq J_{||}/J_{\perp} \leq 1$. The k -resolved weights of both theories agree within 25% (note the different scalings). Light curves represent the bound state (divided by 16 and artificially broadened by $J_{\perp}/100$ in the left panels). Black curves denote the continuum. Inset: enlarged view of the continuum, the bound state is not shown here. Already presented in reference [213].

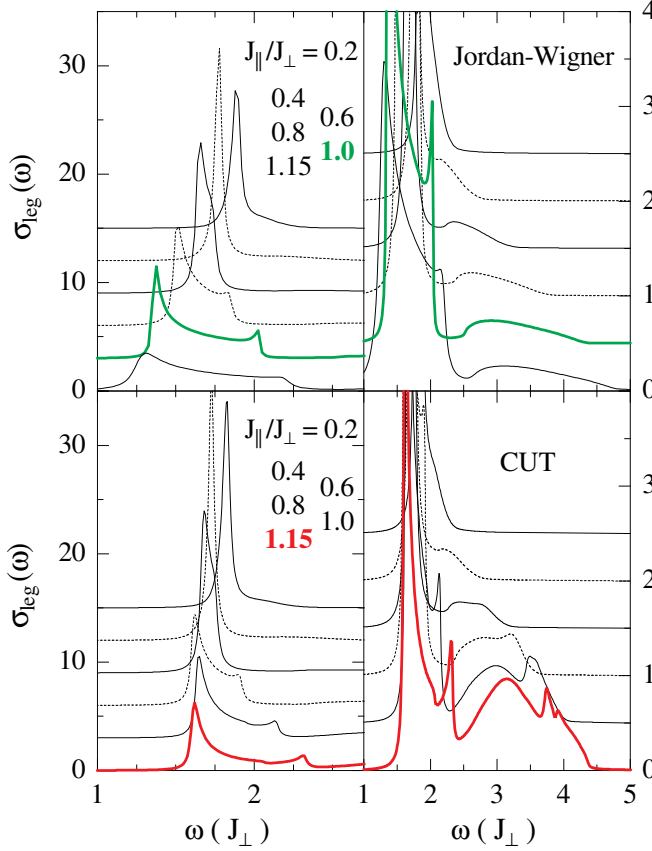


Figure 5.25: Comparison of the optical conductivity for $E||c$ calculated with Jordan-Wigner fermions (**top** panels) and with continuous unitary transformations (**bottom**) for $0.2 \leq J_{||}/J_{\perp} \leq 1.15$. The **left** panels focus on the bound state, whereas the **right** panels emphasize the two-triplet continuum on enlarged scales. For clarity, the curves were shifted with respect to each other by $3 (\Omega\text{cm})^{-1}$ in the left and $0.5 (\Omega\text{cm})^{-1}$ in the right panels. For each theory, the thick lines denote the coupling ratio that offers the best description of the bound state in σ_1 of $\text{La}_{5.2}\text{Ca}_{8.8}\text{Cu}_{24}\text{O}_{41}$. For comparison with experiment, the phonon frequency still has to be added (here: 600 cm^{-1}). Already presented in reference [213].

$J_{||}/J_{\perp} = 0.2$, the elementary triplet shows only little dispersion (confer figure 5.22). Hence the two-particle continuum is rather narrow and the spectral weight is piled up at the bottom of the continuum (black lines in figure 5.24) for small momenta k . With increasing k , the width of the continuum is further reduced due to the cosine-like shape of the elementary triplet dispersion. Thus the interaction between two triplets is strong enough to form a bound state (light lines) below the continuum. For small coupling ratios of $J_{||}/J_{\perp}$ the bound state reaches its maximum energy at the Brillouin zone boundary. This produces a *single* sharp peak in σ_1 that will dominate the absorption spectrum as shown in the left panels of figure 5.25. With increasing coupling ratio the bound state acquires a strong dispersion, and for $J_{||}/J_{\perp} \gtrsim 0.5$ it shows a maximum in the middle of the Brillouin zone at $k \approx \pi/2$ as well as a minimum at $k = \pi$ (compare also figure 5.23). Since both features give rise to van Hove singularities in the density of states, there are now *two* peaks in σ_1 . This means that the dominant peak observed for $J_{||}/J_{\perp} = 0.2$ splits into two with increasing $J_{||}$ (left panels of figure 5.25).

Now the evolution of the continuum with increasing $J_{||}/J_{\perp}$ in figure 5.24 is discussed. At small k , the spectra are broadened strongly by the increase of the continuum width. Therefore, the $k = 0$ Raman response shows a sharp peak for small $J_{||}/J_{\perp}$ and a broad band for isotropic couplings (see reference [231] for more details). For large momenta one can observe the opposite, i.e., the features within the continuum become stronger and more pronounced with increasing coupling ratio. For $J_{||}/J_{\perp} = 1$ the CUT result (top left panel of figure 5.24) shows additional pronounced features within the high-energy part of the continuum [224]. The appearance of these features is related to the existence of the dip in the dispersion of the elementary triplet at small k (figure 5.22). Precursors of these

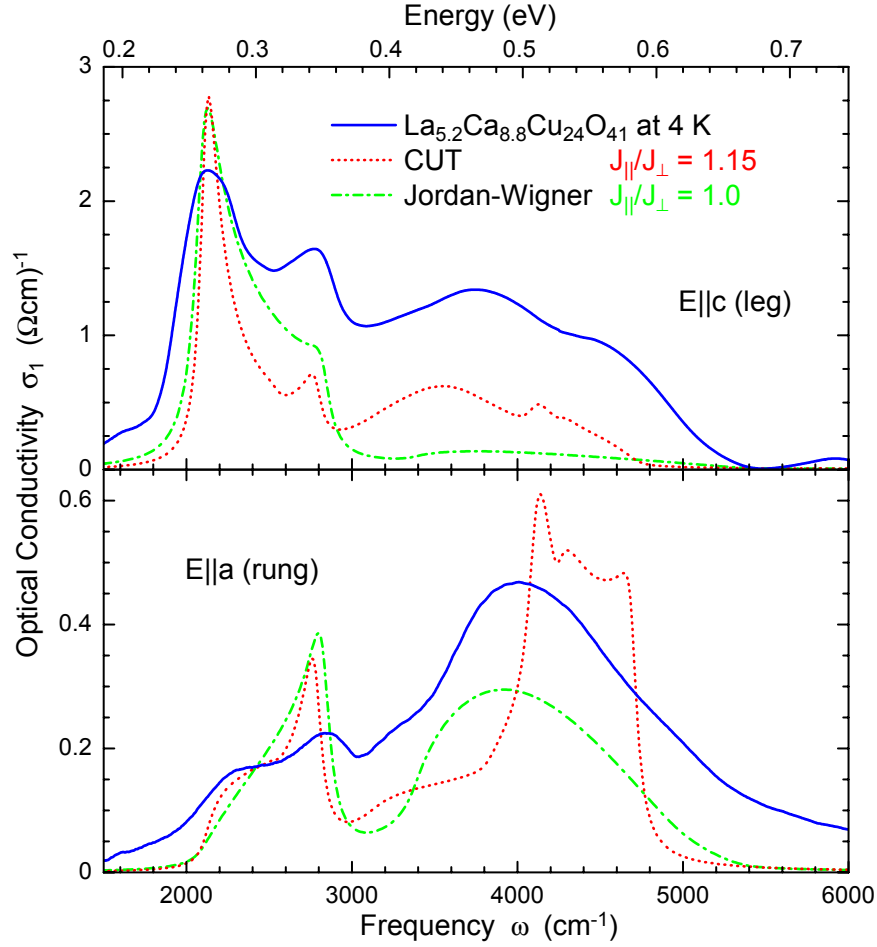


Figure 5.26: Comparison of experiment and theory. The magnetic contribution to the optical conductivity of $\text{La}_{5.2}\text{Ca}_{8.8}\text{Cu}_{24}\text{O}_{41}$ at 4 K is plotted with solid lines. The **top** panel shows the spectrum for polarization $E||c$; **bottom** panel: $E||a$. The Jordan-Wigner spectra (dash-dotted) were calculated using $J_{||}/J_{\perp} = 1.0$ and $J_{||} = 1100 \text{ cm}^{-1}$. Dotted lines denote the CUT results for $J_{||}/J_{\perp} = 1.15$ and $J_{||} = 1080 \text{ cm}^{-1}$. For both calculations a phonon frequency of 600 cm^{-1} was used.

features are present in the CUT spectra for $J_{||}/J_{\perp} = 0.8$ where the dip in the dispersion is only small. The Jordan-Wigner data does not show such features.

Now the calculated spectra are compared with our data of $\text{La}_{5.2}\text{Ca}_{8.8}\text{Cu}_{24}\text{O}_{41}$ at 4 K in figure 5.26. The electronic background has been subtracted as discussed in the previous section. The two peaks at 2140 and 2770 cm^{-1} for $E||c$ as well as the corresponding two peaks for $E||a$ can unambiguously be identified with the two van Hove singularities in the density of states stemming from the $S = 0$ bound state. The lower peak corresponds to the bound-state energy at the boundary of the Brillouin zone, i.e. $E(k = \pi)$. The other peak at higher energy is due to the maximum of the bound-state dispersion E_{max} at about $k \approx \pi/2$ (see figure 5.27). These two energies determine the two free magnetic parameters $J_{||}$ and J_{\perp} . In principle, the experimental σ_1 is well described by both theories for $J_{||}/J_{\perp} = 1$ and $J_{||} \approx 1020 - 1100 \text{ cm}^{-1}$ as presented in reference [24]. At that time there were no CUT spectra available for coupling ratios $J_{||}/J_{\perp} > 1$. The quantitative

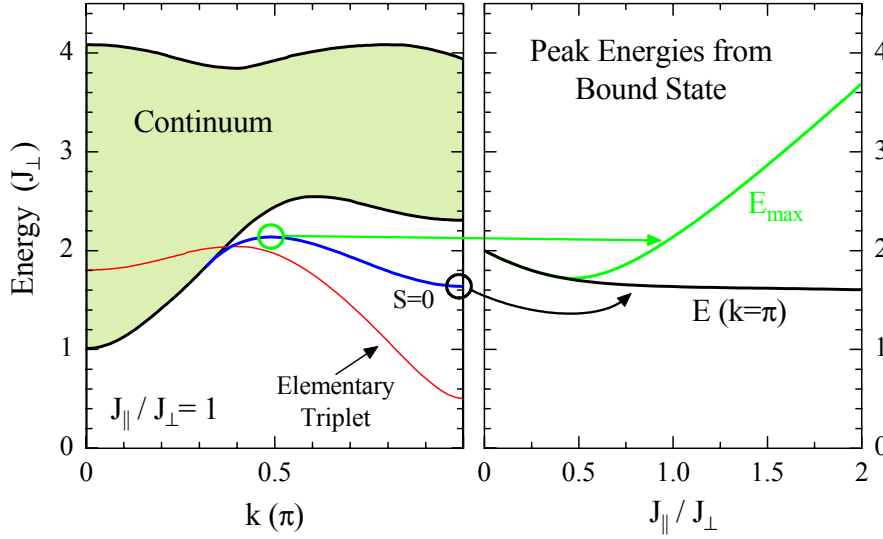


Figure 5.27: Determination of the coupling ratio. In the **left** panel the data is equal to the CUT results of figure 5.23. In the **right** panel the energies of the two bound-state peaks are plotted against the coupling ratio. Below the ratio of $J_{\parallel}/J_{\perp} \approx 0.5$, there is just a single peak. Already presented in reference [24].

analysis could already be pushed a step further, though, based on the values of E_{max} and $E(k = \pi)$ computed by extrapolated perturbation within the CUT formalism. In general, energies can be extrapolated much more accurately than spectral densities. The according evolution of both energies with respect to J_{\parallel}/J_{\perp} is plotted in the right panel of figure 5.27. The lower peak shows only little dependence on the coupling ratio within the relevant regime. The upper peak strongly depends on the actual coupling ratio, though. This allowed us to pinpoint J_{\parallel} and J_{\perp} , yielding $J_{\parallel} \approx 1080 \text{ cm}^{-1}$ and a slightly larger ratio of $J_{\parallel}/J_{\perp} \approx 1.15$. In figure 5.26 the more recent CUT results for exactly these predicted couplings are plotted. Jordan-Wigner calculations for different coupling ratios did not improve the agreement further, and thus the optimal parameters are still $J_{\parallel}/J_{\perp} = 1.0$ and $J_{\parallel} = 1100 \text{ cm}^{-1}$. This 15% discrepancy reflects the differences between the two theories that were already present in the dispersion of the elementary triplet (see figures 5.22 and 5.23).

Our interpretation of the experimental features is confirmed by the good agreement between theory and experiment concerning the line shape of the bound states. Excellent justification for this interpretation is also provided by the selection rule stemming from reflection symmetry about the a axis (RSa). Both theories show that the bound singlet at $k = \pi$ is *even* under RSa. But the excitations at $k = \pi$ are *odd* under RSa for $E||a$ and *even* for $E||c$. It can be shown that the weight of the bound state varies as $(k - \pi)^2$ for $E||a$, whereas it is prevailing for $E||c$. This means that near the zone boundary at $k = \pi$ there is a strong reduction of weight for $E||a$ [24]. This can be seen in figure 5.28, where the k -resolved spectra for both polarizations are compared. In the top panel for $E||a$, there is indeed no weight left at $k = \pi$. That is not the case for the opposite polarization in the bottom panel. Since the van Hove singularity at $k = \pi$ produces the *lower* peak in σ_1 , this explains why the lower peak for $E||a$ is reduced to a weak shoulder.

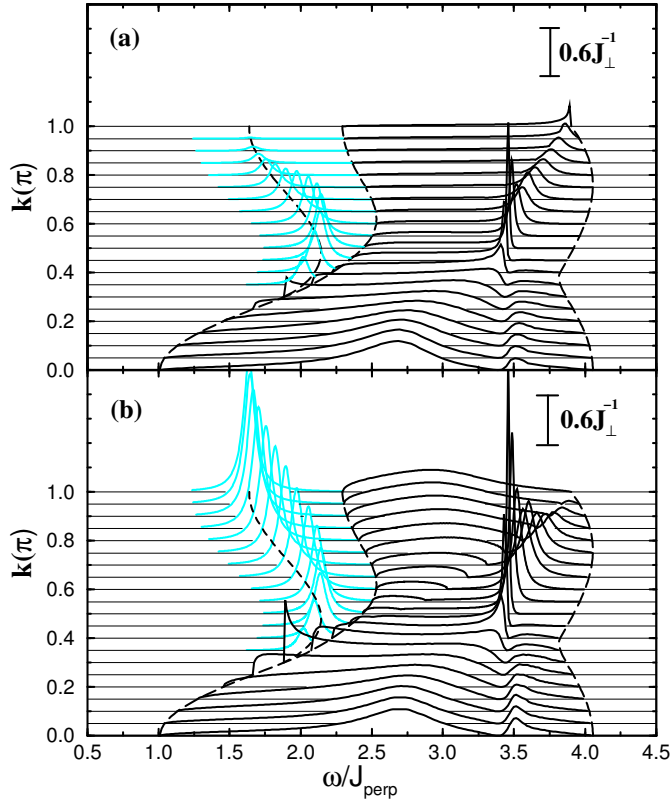


Figure 5.28: Comparison of the k -resolved spectra for both polarizations. This CUT data was computed for $J_{\parallel}/J_{\perp} = 1$. In the **top** panel ($E||a$) there is a strong reduction of the bound-state weight at $k = \pi$. The other polarization (**bottom** panel, $E||c$) does not show such a decrease. The data of the bottom panel corresponds to the upper left panel of figure 5.24. Note that here the continuum in (b) is multiplied by 4. In both panels, the bound state is not scaled down, but an increased broadening of $J_{\perp}/20$ was used. Reproduced from reference [224].

Shortcomings of the theory are the overestimation of the spectral weight of the 2800 cm^{-1} peak for $E||a$ and that the onset of σ_1 around 2000 cm^{-1} is sharper than observed experimentally. However, the agreement is better than one may have expected since we neglected both the frustrated coupling between neighboring ladders and in particular the cyclic exchange. A finite inter-ladder coupling produces a dispersion of the bound state along k_a and thereby broadens the features in σ_1 . This may also explain the smearing out of the onset at 2000 cm^{-1} . Moreover, both theories describe only the two-triplet contribution, i.e. processes with more than two triplets are missing. This explains in particular the discrepancy in the continuum range. The three-triplet contribution with $S_{tot} = 0$ may also explain the low-frequency onset, as discussed above (each of the three triplets with $k = \pi$ and an energy corresponding to the spin gap).

A ratio of $J_{\parallel}/J_{\perp} \approx 1$ seems to be in conflict with several former results of other techniques, proposing $J_{\parallel}/J_{\perp} \gtrsim 1.5$ (see section 2.3.2 and the discussion in reference [133]). Such a rather small value of J_{\perp} is suggested by the small spin gap of 280 cm^{-1} , observed by means of neutron scattering [25, 216]. The according gap energies stemming from our results are considerably larger by a factor of around 1.5 (see figure 5.22). We can clearly exclude $J_{\parallel}/J_{\perp} > 1.2$ from our presented analysis.¹⁵ But recently it was pointed out that the neutron data is as well consistent with an isotropic exchange $J_{\parallel}/J_{\perp} \approx 1 - 1.1$ and $J_{\parallel} \approx 900 \text{ cm}^{-1}$, if a cyclic exchange of $J_{cyc} \approx 0.15J_{\perp}$ is taken into account [25, 216].¹⁶

¹⁵This is valid for $J_{cyc} = 0$.

¹⁶Note that there are several different definitions of J_{cyc} in the literature. In particular it is important whether a factor of 2 is included in the definition or not (see also reference 22 in reference [163]).

Adding a finite cyclic exchange term reduces the gap at $k = \pi$ and washes out the dip in the triplet dispersion at small momenta [25, 26, 231]. Furthermore, J_{cyc} weakens the attractive interaction between two rung triplets. These two changes, reduction of the dip and of the attractive interaction, render the theoretical predictions closer to the experimental findings of optical spectroscopy [26, 231]. In the next section, the DMRG study with included J_{cyc} clearly verifies these expectations.

Now the broad peak at around 4000 cm^{-1} in figure 5.26 is addressed, which is identified unambiguously as the continuum of two and more triplets by comparison with the theoretical results. The main discrepancies are the underestimation of the spectral weight by both calculations for $E||c$ and the line shape of the CUT result for the a axis. The underestimation of the weight is explained by the fact that both theories include only the two-triplet contribution, whereas higher-order contributions are missing. These correspond to $\approx 20 - 30\%$ of the total spectral weight [224]. In the calculated spectra of figure 5.25 for $E||c$, the CUT results for $J_{||}/J_{\perp} \geq 0.8$ display a second peak above $\omega \approx 3J_{\perp}$ in the high-energy continuum. The experimental data (figure 5.26) also shows two peaks in the continuum for the same polarization, independent of the precise background correction. Yet the experimental peaks are located at higher energies, and they are further apart from each other. On inclusion of J_{cyc} the calculated peaks will be shifted to higher energies since the attractive interaction is weakened. So we identify the two experimental peaks with the two theoretical ones even though their shape and mutual distance are not in perfect agreement. The DMRG study presented in the next section supports this interpretation.

At last, we want to note that the position, spectral weight, and the shape of the continuum shows a striking similarity with the high-energy band observed in undoped 2D cuprates like $\text{YBa}_2\text{Cu}_3\text{O}_6$ (see figure 5.13). As discussed in section 3.3, the main resonance peak is due to an *almost* bound state and well described in terms of phonon-assisted bimagnon absorption in the frame of spin-wave theory [11, 12]. However, the high-energy peak at 3800 cm^{-1} is absent in this approach. It has been suggested that the high-energy weight in 2D $S=1/2$ compounds is due to strong quantum fluctuations that go beyond spin-wave theory [14]. The intriguing similarity of the high-energy continuum of the $S=1/2$ quasi-1D ladder $(\text{La,Ca})_{14}\text{Cu}_{24}\text{O}_{41}$ to the 3800 cm^{-1} peak of YBCO strongly indicates that the high-energy weight of YBCO is indeed a signature of strong quantum fluctuations.

5.3.2 DMRG Results: Continuum and the Influence of a Cyclic Exchange

The agreement of our data with the discussed two theoretical studies is excellent and clearly proves the existence of a bound state in the undoped telephone-number compounds. But there remain some discrepancies. A consistent description of both peaks of the bound state in $\sigma_1(\omega)$ and of the spin gap could not be obtained with a model that contains only the couplings $J_{||}$ and J_{\perp} . This will be resolved in the following by inclusion of the cyclic exchange J_{cyc} into the model Hamiltonian. Moreover, the DMRG results largely improve the description of the high-energy continuum since the coupling of the photon to

excitations of more than two triplets is taken into account as well.¹⁷ Actually, only the inclusion of J_{cyc} allows to obtain an almost perfect agreement with the experimentally determined line shape.¹⁸

A cyclic coupling emerges as a correction to the Heisenberg Hamiltonian in order t^4/U^3 from a t/U expansion of the one-band Hubbard model [144]. It is expected to be the dominant correction within the more realistic three-band description of the CuO_2 planes of the 2D cuprates because in this case the cyclic permutation of four spins on a plaquette can take place without double occupancy [145] (see also section 2.3.2). The similarity of the CuO_2 plaquettes in the 2D planes and the spin ladders suggests an equal relevance of J_{cyc} for our analysis of the ladders. The actual calculations to study the influence of J_{cyc} on σ_1 were performed by Nunner et al. [26] using the dynamical density-matrix renormalization group (dynamical DMRG).

The complete Hamiltonian including the cyclic exchange reads

$$\begin{aligned} \mathcal{H} = & J_{\perp} \sum_i \mathbf{S}_{i,l} \mathbf{S}_{i,r} + J_{\parallel} \sum_i (\mathbf{S}_{i,l} \mathbf{S}_{i+1,l} + \mathbf{S}_{i,r} \mathbf{S}_{i+1,r}) \\ & + J_{cyc} \sum_i \frac{1}{4} (\mathbf{P}_{(i,l)(i,r)(i+1,r)(i+1,l)} + \mathbf{P}_{(i,l)(i,r)(i+1,r)(i+1,l)}^{-1}) \end{aligned} \quad (5.10)$$

where the index i refers to the rungs, and (l, r) label the two legs. The cyclic permutation operator \mathbf{P}_{1234} is given by

$$\begin{aligned} \mathbf{P}_{1234} + \mathbf{P}_{1234}^{-1} = & 4(\mathbf{S}_1 \mathbf{S}_2)(\mathbf{S}_3 \mathbf{S}_4) + 4(\mathbf{S}_1 \mathbf{S}_4)(\mathbf{S}_2 \mathbf{S}_3) - 4(\mathbf{S}_1 \mathbf{S}_3)(\mathbf{S}_2 \mathbf{S}_4) \\ & + \mathbf{S}_1 \mathbf{S}_2 + \mathbf{S}_3 \mathbf{S}_4 + \mathbf{S}_1 \mathbf{S}_4 + \mathbf{S}_2 \mathbf{S}_3 + \mathbf{S}_1 \mathbf{S}_3 + \mathbf{S}_2 \mathbf{S}_4. \end{aligned} \quad (5.11)$$

The consideration of J_{cyc} primarily renormalizes the coupling strengths J_{\parallel} and J_{\perp} in the Hamiltonian. The only new contribution is a repulsive interaction between local triplets on neighboring rungs. The strongest effect on the excitation spectrum is a reduction of the binding energy of the bound state, i.e. the energy difference between the bound state and the lower edge of the continuum. The energy of the entire elementary triplet dispersion is reduced, including the spin-gap energy at $k = \pi$. In figure 5.29a the elementary triplet dispersion is shown for an 80-site ladder with isotropic coupling $J_{\parallel} = J_{\perp}$ and different values of J_{cyc} . The shape of this excitation branch remains qualitatively unchanged. The strongest suppression affects the spin gap at $k = \pi$ and the maximum near $k \approx 0.3\pi$. Even for $J_{cyc}/J_{\perp} = 0.3$ the local minimum at $k = 0$ is still present. The inset shows the rapid decrease of the spin gap for a larger range of J_{cyc} . Figure 5.29b demonstrates the effect on the lower edge of the two-triplet continuum (open symbols) and on the bound state (full symbols). Corresponding to the one-triplet dispersion, the lower edge of the continuum shifts down on increasing J_{cyc} . Due to the mentioned additional

¹⁷The photon couples to two spins on neighboring sites. Locally, at maximum two triplets can be annihilated and two can be generated. By Bogoliubov transformations the local triplets can be expressed in terms of the true excitations, i.e. dressed triplets, the true excited eigenstates. The annihilation and creation operators mix so that also three or four dressed triplets can be generated. Higher-order vertex corrections lead to the generation of even more than four triplets, which however do not yield an important contribution.

¹⁸This section is largely based on reference [26] by Nunner, Brune, Kopp, Windt and Grüninger. We are much obliged to the fruitful collaboration with the Augsburg theory group.

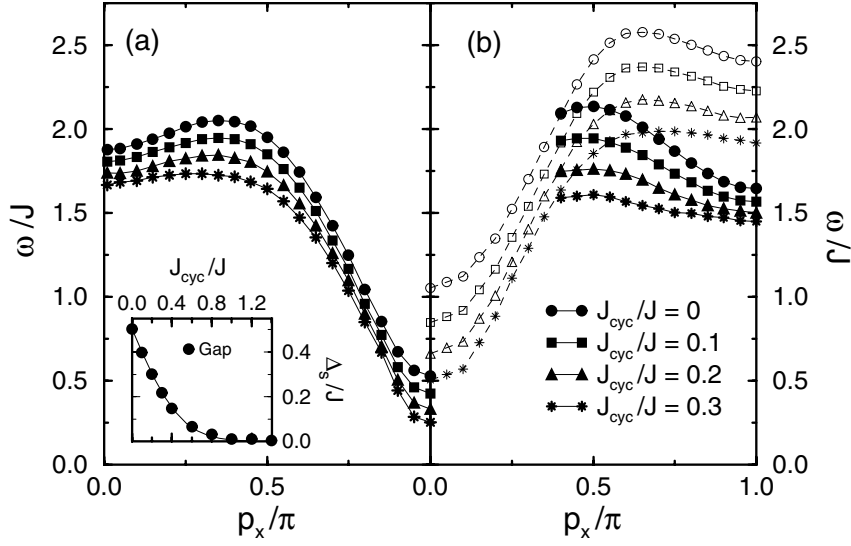


Figure 5.29: DMRG results for an 80-site ladder with $J_{\parallel} = J_{\perp}$ and several values of J_{cyc} . Here J means J_{\parallel} . **Left** panel: Dispersion of the elementary triplet. The inset shows the evolution of the spin gap for a large range of J_{cyc} . These values are extrapolated to an infinite ladder. **Right** panel: Lower edge of the two-triplet continuum (open symbols) and the $S = 0$ bound state (full symbols). Reproduced from reference [26].

repulsion between neighboring triplets, the binding energy is reduced. As a consequence, the width of the bound-state dispersion decreases dramatically. This width is obviously very sensitive to the magnitude of J_{cyc} and hence provides a suitable probe to check for the actual size of J_{cyc} once the ratio J_{\parallel}/J_{\perp} is known.

In order to determine the proper set of exchange couplings for $\text{La}_{5.2}\text{Ca}_{8.8}\text{Cu}_{24}\text{O}_{41}$, the frequencies of the two bound-state peaks in σ_1 were calculated. In figure 5.30a the according values of ω_{max} (full symbols) and ω_{min} (open symbols) are plotted for different sets of couplings. The corresponding values of the spin gap Δ_s are shown in figure 5.30b. In the range depicted in the figure, these values may be approximated within 5% by [26]

$$\omega_{min} \approx 1.64 J_{\perp} - 0.54 J_{cyc} , \quad (5.12)$$

$$\omega_{max} \approx 0.61 J_{\perp} - 1.87 J_{cyc} + 1.53 J_{\parallel} , \text{ and} \quad (5.13)$$

$$\Delta_s \approx 0.48 J_{\perp} - 0.84 J_{cyc} . \quad (5.14)$$

One can also rewrite the equations as

$$J_{\perp} \approx 0.75 \omega_{min} - 0.48 \Delta_s , \quad (5.15)$$

$$J_{\parallel} \approx 0.23 \omega_{min} + 0.65 \omega_{max} - 1.60 \Delta_s , \text{ and} \quad (5.16)$$

$$J_{cyc} \approx 0.57 J_{\perp} - 1.19 \Delta_s \approx 0.43 \omega_{min} - 1.46 \Delta_s . \quad (5.17)$$

Thus in principle, the three experimental values of ω_1 and ω_2 from our infrared spectra and $\Delta_s \approx 280 \text{ cm}^{-1}$ from neutron scattering [25, 216] are sufficient to determine the three exchange couplings J_{\parallel} , J_{\perp} and J_{cyc} . But ω_1 and ω_2 also depend on the actual phonon frequency ω_{ph} of the involved symmetry-breaking phonon. That means that

$$\omega_1 = \omega_{min} + \omega_{ph}^{p=\pi} \text{ and} \quad (5.18)$$

$$\omega_2 = \omega_{max} + \omega_{ph}^{p \approx \pi/2} . \quad (5.19)$$

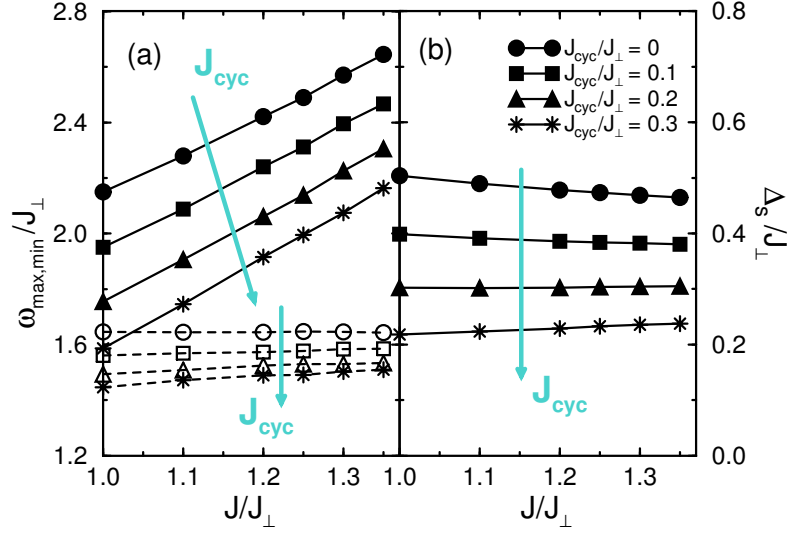


Figure 5.30: Left panel: Frequencies ω_{max} (full symbols) and ω_{min} (open symbols) of the two peaks stemming from the two local extremals of the bound-state dispersion (see figure 5.29b). The values are plotted as a function of J_{\parallel}/J_{\perp} for different ratios J_{cyc}/J_{\perp} . All results have been extrapolated to an infinite ladder. **Right panel:** Corresponding values of the spin gap Δ_s . Reproduced from reference [26].

The very momenta of the excited phonons are necessary to ensure a total momentum of zero since infrared light provides only negligible momenta. Thus we have to know not only the phonon frequency but also the phonon dispersion for an accurate analysis. Fortunately it is possible to make use of the relative insensitivities of Δ_s and ω_{min} on the coupling ratio J_{\parallel}/J_{\perp} . This allows us to determine the value of J_{cyc} without the consideration of ω_2 and thus omits any effect of a possible dispersion of the optical phonon. A cautious estimate of the Cu-O bond-stretching phonon frequency at the zone boundary yields $\omega_{ph}^{p=\pi} = (600 \pm 100) \text{ cm}^{-1}$. The according results presented in reference [26] are

$$\begin{aligned} J_{\parallel}/J_{\perp} &\approx 1.25 - 1.35, \\ J_{\perp} &\approx 950 - 1100 \text{ cm}^{-1}, \text{ and} \\ J_{cyc}/J_{\perp} &= 0.20 - 0.27. \end{aligned} \tag{5.20}$$

For the determination of the ratio J_{\parallel}/J_{\perp} , a reasonable phonon dispersion of $\pm 50 \text{ cm}^{-1}$ was allowed.

So far, just the position of the bound-state peaks and the size of the spin gap entered the analysis. But even the overall line shape of $\sigma_1(\omega)$ can be reproduced with the given set of parameters. This is demonstrated in figure 5.31 where our data of $\text{La}_{5.2}\text{Ca}_{8.8}\text{Cu}_{24}\text{O}_{41}$ is compared to DMRG results for $J_{\parallel}/J_{\perp} = 1.30$, $J_{\perp} = 1000 \text{ cm}^{-1}$ and $J_{cyc}/J_{\perp} = 0.20$. Note that for the polarization $E||c$ in the top panel there are two contributions to the DMRG spectrum, where the legs are excited in-phase ($p_y = 0$) or out-of-phase ($p_y = \pi$). The in-phase mode (squares) contains the coupling to two and four bare triplets and thus includes the bound state. The out-of-phase mode reflects the coupling to three bare triplets and hence contributes only to the high-frequency continuum. Note that in the notation used in reference [26], where the spin operators are represented by rung singlets

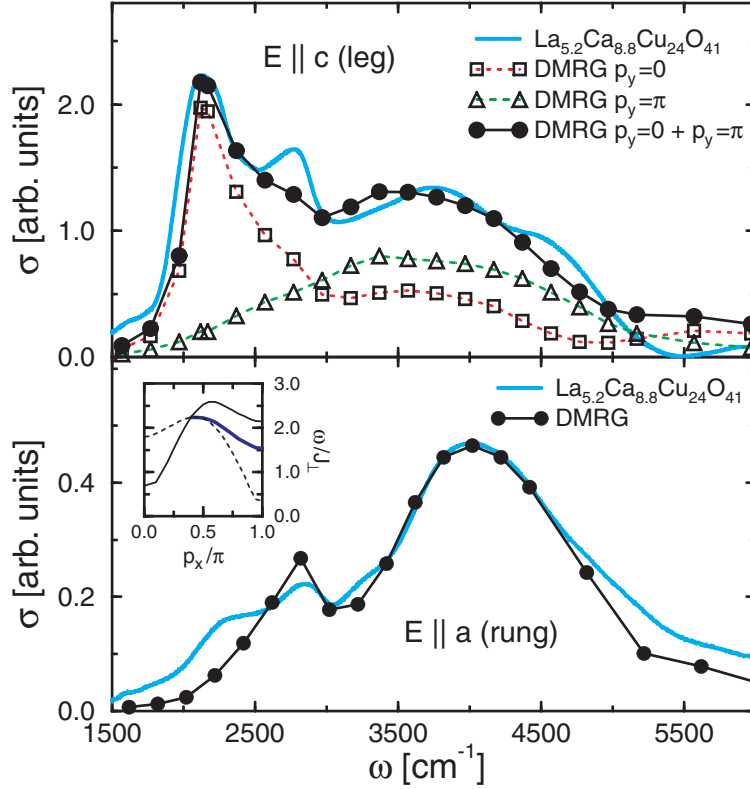


Figure 5.31: Comparison of the $\text{La}_{5.2}\text{Ca}_{8.8}\text{Cu}_{24}\text{O}_{41}$ data at 4 K (solid line) with the results of dynamical DMRG (full symbols) for an 80-site ladder. The parameters are $J_{\parallel}/J_{\perp} = 1.30$, $J_{\perp} = 1000 \text{ cm}^{-1}$, $J_{\text{cyc}}/J_{\perp} = 0.20$, and a finite broadening of $0.1J_{\perp}$. In the **top** panel for $E||c$ a phonon frequency of $\omega_c = 570 \text{ cm}^{-1}$ was used, whereas for $E||a$ in the **bottom** panel $\omega_a = 620 \text{ cm}^{-1}$ (see text). In the top panel there are two contributions to the calculated σ_1 (open symbols), where the two legs are excited in-phase and out-of-phase with each other. The subtraction of the electronic background from the experimental spectra is discussed in section 5.2.4. The **inset** shows the dispersion of the elementary triplet, the lower edge of the two-triplet continuum, and the $S = 0$ bound state for the above mentioned exchange parameters. Reproduced from reference [26].

and rung triplets, light does not couple to excitations of more than four bare triplets. The DMRG results thus correspond to 100% of the spectral weight. For $E||a$ in the bottom panel of figure 5.31, σ_1 only contains the coupling to two-triplet excitations¹⁹, and the lower bound-state peak is reduced by the selection rule as discussed above. For $E||a$ there is almost perfect agreement, in particular concerning the line shape of the continuum, whereas for $E||c$ there are some minor deviations at the highest frequencies. However, as discussed in the previous section the experimental uncertainty due to the subtraction of the electronic background certainly exceeds these deviations. Also within the bound-state regime at lower frequencies, the agreement with our data is better than before. Actually, the position of both peaks has been used to gain the proper exchange couplings in the first place. The upper bound-state peak for $E||c$ is more pronounced in the measured

¹⁹On a single rung, the photon may annihilate a bare triplet and create another one, which can amount to the creation of two (or an even number) of dressed triplets (see also footnote on page 127).

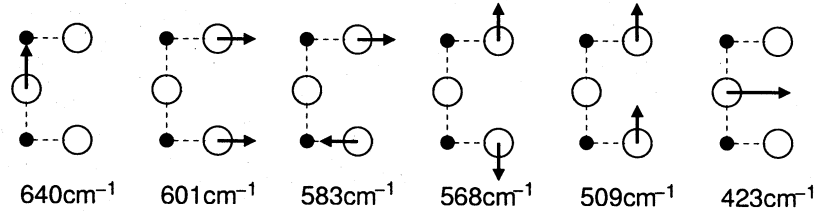


Figure 5.32: Displacement patterns and energies of the optical phonons in the ladder subcell of $\text{La}_y\text{Ca}_{14-y}\text{Cu}_{24}\text{O}_{41}$ at $k = 0$. Black dots are the Cu atoms, whereas large open circles denote the O atoms. Reproduced from reference [201]. Note that in reference [201] the sketches of the bending modes at 568 and 509 cm^{-1} were erroneously exchanged.

data, which is similar to the situation of the lower peak for the rung polarization. Nunner et al. [26] propose that both effects are related to the actual form factors of the relevant optical phonons.

A more detailed discussion of the corresponding phonon characteristics is given by Nunner et al. in reference [201]. Based on a shell model the calculations yield the dispersion and the form factor of each phonon mode. The results also explain the 50 cm^{-1} difference in the assumed phonon frequencies ω_a^{ph} and ω_c^{ph} (figure 5.31). For $E||a$ the 640 cm^{-1} mode depicted in figure 5.32 provides the strongest contribution to σ_1 . For the other polarization, the modes with 601 and 568 cm^{-1} are dominant. The according mean value of these two modes is 585 cm^{-1} . The actual frequencies used to calculate σ_1 of figure 5.31 were $\omega_a = 620 \text{ cm}^{-1}$ and $\omega_c = 570 \text{ cm}^{-1}$, which are hence convincingly verified. Experimentally, the frequency of the upper bound state is $\approx 60 \text{ cm}^{-1}$ higher in σ_a than in σ_c .

Any spectrum calculated with vanishing cyclic coupling did not reach the agreement with experiment as the presented data with $J_{cyc}/J_{\perp} = 0.2$. This demonstrates the importance of this exchange term. Actually, the line shape calculated on the basis of the model Hamiltonian 5.10 does agree so convincingly with our data, that Nunner et al. [26] can claim to have identified the minimal model that yields the relevant magnetic properties of undoped $S = 1/2$ cuprate ladders. This is corroborated by the recent CUT results of Schmidt et al. [163], who found an excellent description of the two-triplet Raman data of $\text{La}_6\text{Ca}_8\text{Cu}_{24}\text{O}_{41}$ for the parameters given by Nunner et al. in reference [26]. Note that in this CUT calculation a slightly different definition of the exchange parameters has been used. Very similar values of J_{cyc} have been reported for the 2D cuprates [148], which demonstrates the fundamental role of this term. One might speculate that such a sizable cyclic spin-exchange term will have significant consequences for superconductivity in the doped spin ladders [5], since magnetic and pairing correlations are considered as closely related phenomena [2].

Summary: The magnetic contribution to the optical conductivity of the undoped telephone-number compounds $\text{La}_y\text{Ca}_{14-y}\text{Cu}_{24}\text{O}_{41}$ was clearly reproduced by three different approaches. The three main peaks could be unambiguously attributed to the $S = 0$ bound state and to the multi-triplet continuum. Thus we provide the first experimental verification of a bound state in spin ladders, and the coupling constants could be derived. The actual line shape of σ_1 is nicely reproduced as well as the spin gap measured with neutron scattering by incorporating $J_{cyc}/J_{\perp} = 0.2$. Therefore the minimal model was

identified which captures all relevant magnetic properties. Table 5.2 summarizes the exchange couplings from the three presented theoretical studies that provided best fits to our data at 4 K.

	J_{\parallel}/J_{\perp}	J_{\perp} (cm ⁻¹)	J_{cyc}/J_{\perp}	ω_{ph} (cm ⁻¹)
Jordan-Wigner Fermions (no J_{cyc})	1.0	1100	-	600
CUT (no J_{cyc})	1.15	940	-	600
Dynamical DMRG (with J_{cyc})	1.30	1000	0.20	570 (c), 620 (a)

Table 5.2: Summary of the coupling ratios stemming from the comparison of our data with the three theoretical results. In the case of DMRG, different phonon frequencies were used for the two polarizations. In the first two rows, $J_{cyc} = 0$ was assumed. However, a consistent description of $\sigma(\omega)$ and the spin gap requires a finite value of J_{cyc} .

5.3.3 Resemblance to the $S=1$ Chain

In this section a further way of describing the $S = 1/2$ two-leg ladder is presented.²⁰ The starting point was our empirical result that with increasing temperature the line shape and the weight of the continuum contribution for polarization along the legs are changing drastically. This can be clearly seen in the bottom panel of figure 5.18, where the magnetic part of σ_1 for $E||c$ is shown. At 300 K the weight of the double-peak structure of the bound state is reduced considerably. The continuum weight is strongly increased, and only a single broad peak remains in contrast to the *two* continuum peaks at 4 K. Unfortunately, calculations of the temperature dependence of the phonon-assisted magnetic absorption are available only for the $S = 1/2$ chain [233].

Empirically we find that the 300 K spectrum of the two-leg ladder $\text{La}_{5.2}\text{Ca}_{8.8}\text{Cu}_{24}\text{O}_{41}$ resembles the expectations for an $S = 1$ chain at $T = 0$ (see below). As a first idea that supports such resemblance, one might think of thermally excited triplets in the strong coupling limit of $J_{\perp} \gg J_{\parallel}$. The triplets are located next to each other on the rungs of the ladder and thus form a “chain” of spin-1 entities (see figure 5.33).²¹ For a rough

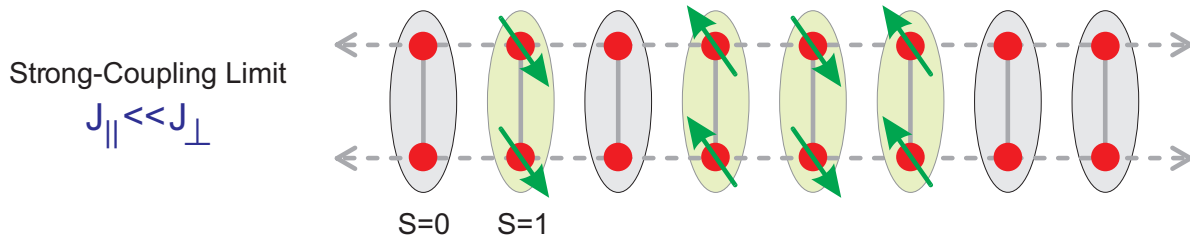


Figure 5.33: Naive picture of the similarity of a thermally excited $S = 1/2$ ladder to a $S = 1$ Haldane chain.

²⁰This section is largely based on discussions with Tamara Nunner from the University of Augsburg [232] and with Kai Schmidt from the Cologne theory group.

²¹Antiferromagnetic chains with integer spin exhibit a so-called Haldane gap as discussed on page 16.

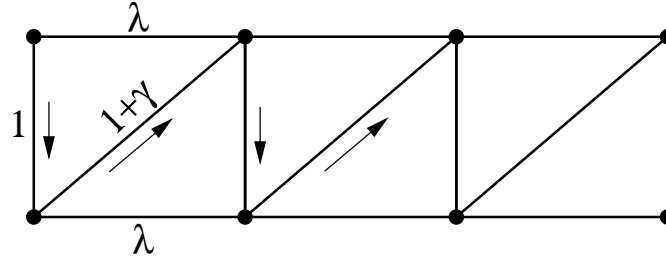


Figure 5.34: The generalized spin-1/2 ladder with an additional diagonal coupling $1 + \gamma$. The arrows denote the succession of the sites in order to map this system onto a single chain with nearest- and next-nearest-neighbor interactions. The latter exchange is denoted by λ and causes frustration for $\lambda > 0$. The nearest-neighbor interaction alternates between 1 and $1 + \gamma$. Reproduced from reference [234].

estimate we consider a set of isolated singlets with a triplet energy gap of $\Delta = 400$ K, which corresponds to the ladder spin gap of 280 cm^{-1} . At $T = 300$ K the Boltzmann distribution $n(T) = 3 \exp(-\Delta/k_B T) / [1 + 3 \exp(-\Delta/k_B T)]$ results in an occupation probability of 44% for a triplet state.

Nevertheless, even at zero temperature there is a real similarity between both model systems as pointed out by White in reference [235]. White introduced continuous transformations between the $S = 1$ Heisenberg chain and the $S = 1/2$ Heisenberg ladder in such way that there is no phase transition along the mapping path. The actual mapping can be demonstrated by means of the *generalized* ladder as depicted in figure 5.34. The arrows indicate the zigzag path that represents a chain. In this picture of a chain, the coupling denoted by λ is equivalent to a next-nearest-neighbor coupling that causes frustration. The nearest-neighbor coupling alternates between 1 and $1 + \gamma$. The case of the isotropic Heisenberg ladder is obtained for $\lambda = 1$ and $\gamma = -1$. Then there is no diagonal exchange, and the rung and leg couplings are equal. The phase diagram for this kind of generalized ladder was analyzed by Brehmer et al. in reference [234]. The according phase diagram is reproduced in figure 5.35. The line with $\gamma = 0$ describes the uniform chain with frustration due to the next-nearest-neighbor interaction λ . Within the interval from $\lambda = 0$ (no frustration) up to the critical frustration of $\lambda_c \approx 0.2412$, the chain is gapless (see section 2.2). Above this point, the chain exhibits an RVB ground state with a spin gap to the first excited state. The Majumdar-Gosh point is reached at $\lambda = 0.5$, where the ground state is a product of nearest-neighbor singlets without any long-range bonds. Apart from the gapless line for $\gamma = 0$ and $\lambda < \lambda_c$, all other systems within the phase diagram are gapped. The dashed lines indicate at which momentum the spin gap is located. Above the upper line this is at $k = 0$, and below the lower line the gap is present at the zone boundary. The Heisenberg ladder belongs to this region. Both boundaries are accompanied by a disorder line where the spin-spin correlations become incommensurate in real space. Just the upper line belonging to the $k = 0$ boundary is plotted. Hence the lower disorder line is missing in figure 5.35 since its exact position could not be calculated.

Interesting to us is the case of $\gamma \rightarrow -\infty$. This means that an infinite ferromagnetic coupling along the diagonals forces the diagonal spins to be parallel and to form effective $S = 1$ units (see figure 5.36). Thus the system is equivalent to an $S = 1$ Haldane chain

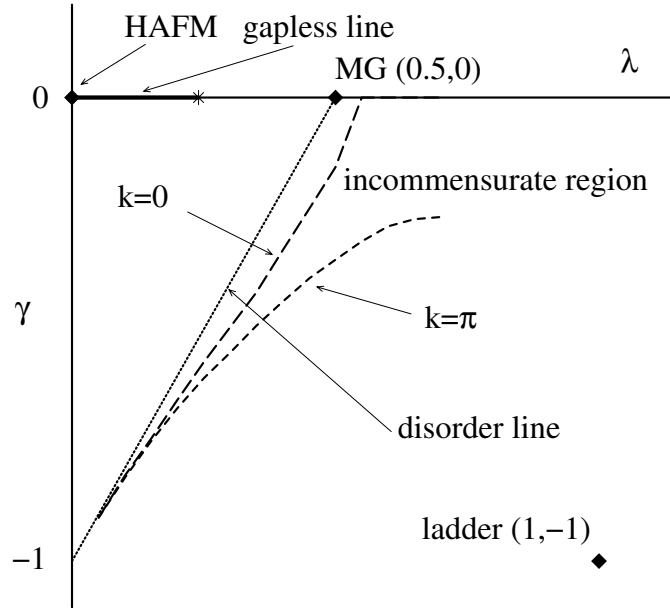


Figure 5.35: Phase diagram of the generalized ladder with the couplings depicted in figure 5.34. The interval of the line $\gamma = 0$ for $0 < \lambda < \lambda_c \approx 0.2412$ is gapless, and the remaining part of the diagram is gapped. Above the dashed line labelled as $k = 0$ the gap is located at momentum zero, below the lower dashed line it is at $k = \pi$, just as for the isotropic ladder at $\lambda = 1$ and $\gamma = -1$. Below the disorder line the region starts where the correlations become incommensurate in real space. The lower boundary of this incommensurate region is *not* included since the exact position could not be determined. For $\gamma \rightarrow -\infty$ one approaches the $S = 1$ Haldane chain. Reproduced from reference [234].

along the leg axis with an effective coupling constant [234, 235] of

$$J_{\text{eff}} = \frac{1 + 2\lambda}{4}, \quad (5.21)$$

where $1 + 2\lambda$ sums up the three exchange paths between neighboring triplets on the diagonals, namely twice along the legs and once across a rung. The factor $1/4$ is due

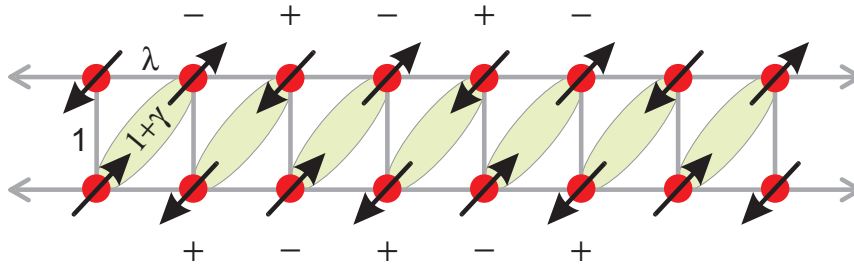


Figure 5.36: A strong ferromagnetic diagonal coupling ($\gamma \rightarrow -\infty$) drives the generalized ladder to the limit of the $S = 1$ Haldane chain with $S = 1$ units on the diagonals. The “+” and “-” signs illustrate the phase on each site for an excitation with $(k_x, k_y) = (\pi, \pi)$.

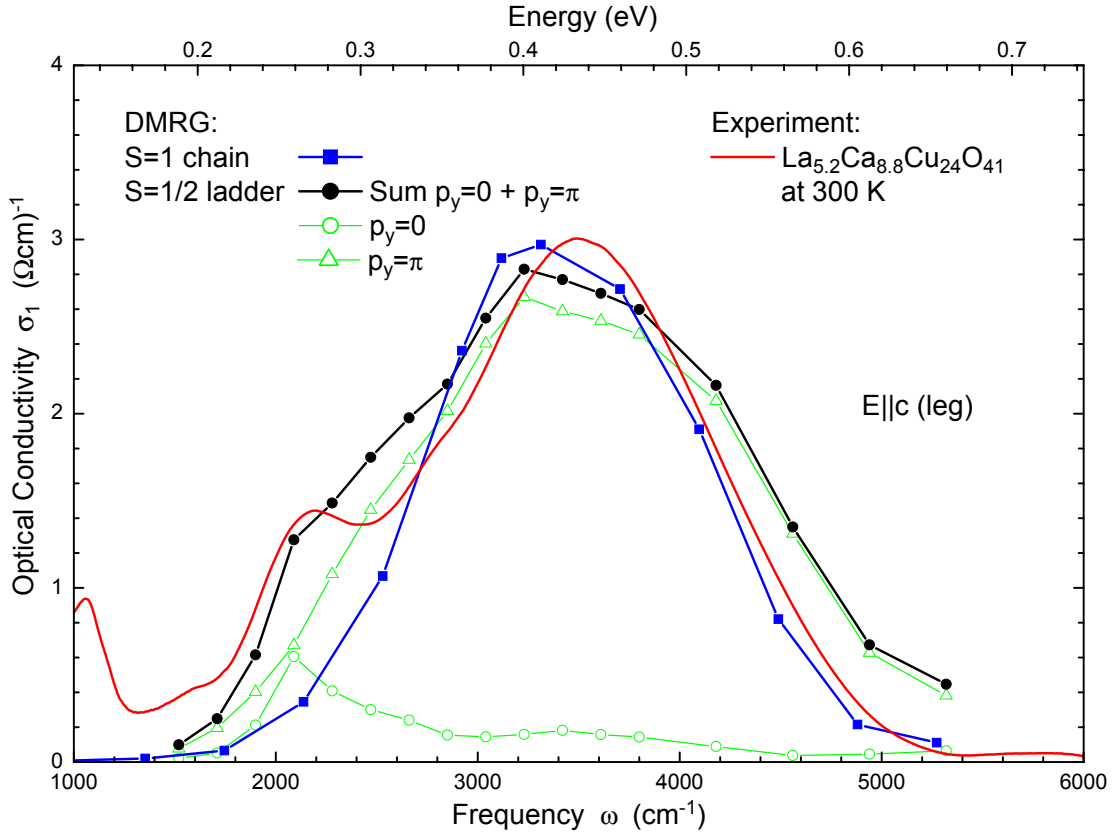


Figure 5.37: Comparison of the magnetic contribution to σ_1 of $\text{La}_{5.2}\text{Ca}_{8.8}\text{Cu}_{24}\text{O}_{41}$ at 300 K for polarization $E||c$ (solid line) with two different calculations. Full squares represent DMRG data for the $S = 1$ chain with effective coupling $J_{\text{eff}} = (J_{\perp} + 2J_{\parallel})/4$ by Nunner et al. [236]. The used values are $J_{\parallel}/J_{\perp} = 1.15$, $J_{\perp} = 950 \text{ cm}^{-1}$, and $\omega_{ph} = 570 \text{ cm}^{-1}$, hence $J_{\text{eff}} \approx 784 \text{ cm}^{-1}$. Open symbols stand for the DMRG data of the ladder as presented in the previous section. The relative weight of the $p_y = \pi$ contribution (open triangles) has been increased by a factor of 10.5 compared to the $p_y = 0$ contribution (open circles). The sum (full circles) reproduces the measured line shape well.

to the effective spin of 1 compared to the original $S = 1/2$.²² The important result of White was that this picture even holds for *vanishing* diagonal coupling, i.e. $\gamma = -1$. The probability of finding a pair of spins along a diagonal that forms a triplet state is still 96.2% in an isotropic ladder with $\gamma = -1$ and $\lambda = 1$. This surprisingly high number reflects the strong AF short-range correlations and indicates that even the isotropic ladder is “not too far” from the $S = 1$ chain [235]. In fact, both systems are in the same gapped phase.

In figure 5.37 the magnetic contribution to σ_1 of $\text{La}_{5.2}\text{Ca}_{8.8}\text{Cu}_{24}\text{O}_{41}$ at 300 K is plotted for $E||c$ (solid line). The dominating feature is the strong peak at 3500 cm^{-1} . This peak evolved from the double-peak continuum, which is present at 4 K (see figure 5.18). At the same time, the relative weight of the bound-state peaks decreases upon heating. The

²²The Hamiltonian contains products of two spin operators, hence the effective coupling J_{eff} incorporates the factor $(1/2)^2 = 1/4 \times 1^2$.

upper peak originally located around 2770 cm^{-1} is almost unrecognizable, and also the lower peak at 2140 cm^{-1} becomes weaker. The squares in figure 5.37 denote DMRG results calculated by Nunner et al. [236] for an $S = 1$ chain. For comparison with the data of $\text{La}_{5.2}\text{Ca}_{8.8}\text{Cu}_{24}\text{O}_{41}$ we evaluate the effective coupling constant J_{eff} using equation 5.21, which in our case reads

$$J_{\text{eff}} = \frac{J_{\perp} + 2J_{\parallel}}{4}. \quad (5.22)$$

Here we neglect the cyclic exchange for the sake of simplicity. The actual parameters used in figure 5.37 were thus chosen according to our results for $J_{\text{cyc}} = 0$, i.e. $J_{\parallel}/J_{\perp} = 1.15$ and the proper c -axis phonon frequency of 570 cm^{-1} . However, we reduced the absolute values of both couplings by 5%, and thus set $J_{\perp} = 950 \text{ cm}^{-1}$. This slight reduction of the exchange parameters can be interpreted as a softening of the magnetic system due to the thermal expansion of the lattice. We obtain $J_{\text{eff}} = 3.3J_{\perp}/4 \approx 784 \text{ cm}^{-1}$. The good agreement with the measured line shape is indeed surprising and supports the picture of the resemblance of the $S = 1$ chain and the $S = 1/2$ two-leg ladder at high temperatures. Nevertheless we do not want to stretch this analogy too far. For instance, the remnant of the bound-state structure at around 2100 cm^{-1} can certainly not be captured by such a mapping. In the following we try to shed some light on the similarity of the spectra.

The DMRG calculations for the $S = 1/2$ two-leg ladder presented in the previous section yield two contributions to the total intensity. The in-phase part ($p_y = 0$) contains the coupling to two and four bare triplets (see footnote on page 127). Therefore it includes the bound-state intensity and also the two-triplet continuum. The out-of-phase part ($p_y = \pi$), though, reflects the broad three-triplet continuum [26] (once again, see footnote on page 127). Interestingly, we found that it is possible to describe the 300 K data rather well if the relative weight of the $p_y = \pi$ contribution (open triangles) is increased by a factor of 10.5 compared to the $p_y = 0$ part. The corresponding sum is denoted by full circles in figure 5.37, where we have used $J_{\parallel}/J_{\perp} = 1.3$, $J_{\text{cyc}}/J_{\perp} = 0.2$, and a reduced absolute value of $J_{\perp} = 950 \text{ cm}^{-1}$ (see above). This suppression of the $p_y = 0$ channel (open circles) is necessary in order to reproduce the strongly reduced relative weight of the bound state. We certainly have overestimated this suppression since a finite-temperature calculation will probably show a transfer of spectral weight from the bound state into the continuum, in particular from the upper peak which shows a smaller binding energy. Nevertheless we are confident that the out-of-phase contribution dominates at high temperatures. This can be explained by the specific form of this three-triplet process, which annihilates one bare triplet and creates two other ones.²³ The weight of this contribution thus vanishes when no bare triplets are present in the ground state, and it is expected to grow when the number of triplets increases at higher temperatures [232].

The resemblance of the $S = 1/2$ two-leg ladder and the $S = 1$ chain thus boils down to the similarity of the $p_y = \pi$ contribution and the spectrum of the $S = 1$ chain. At $p_y = \pi$, the two legs of the ladder are excited out-of-phase. Considering the generalized ladder depicted in figure 5.36, a scenario in terms of an $S = 1$ chain certainly requires that the bonds which connect neighboring triplets are excited in-phase. This is the case at $(p_x, p_y) = (\pi, \pi)$, where p_x denotes the momentum along the legs. Note that the spectra of phonon-assisted magnetic absorption are dominated by the contribution from $p_x = \pi$,

²³These triplets account mainly for the creation of three dressed triplets.

which finally may explain the similarity between the $p_y = \pi$ part and the spectrum of the $S = 1$ chain.

Summary: In $\text{La}_{5.2}\text{Ca}_{8.8}\text{Cu}_{24}\text{O}_{41}$ we find a growth of spectral weight of the continuum with increasing temperature. This effect is more pronounced for polarization $E||c$, where also the line shape is strongly affected. At 300 K, the line shape for $E||c$ resembles the DMRG result for an $S = 1$ Haldane chain, illustrating the close relationship between the two model systems. Good agreement with the experimental data is also obtained if the relative weight of the $p_y = \pi$ contribution to $\sigma_1(\omega)$ of the $S = 1/2$ ladder is increased. The relationship between this $p_y = \pi$ contribution and the spectrum of the $S = 1$ chain has been discussed.

Chapter 6

Doped Ladders

The successful study of the undoped ladders in the previous chapter directly leads to the question of what happens upon hole doping. In $\text{Sr}_{14}\text{Cu}_{24}\text{O}_{41}$, for instance, there are nominally six holes per formula unit, but most of them are expected to reside within the chains [9] (see also section 2.4.2). Therefore this compound offers the interesting opportunity to investigate the interplay of spin and charge degrees of freedom in the two subcells.

The optical spectra of $\text{Sr}_{14}\text{Cu}_{24}\text{O}_{41}$ are similar to the undoped telephone-number compounds with respect to the bound state. Again we find the double-peak structure that has been identified to stem from the bound state. Yet there are additional features, which are not present in the undoped crystals. Certainly the most striking difference is that the lower bound-state peak is split into a sharp double-peak structure. In general, we find more features over most of the frequency range. The evolution of these features is studied by comparing the spectra with the data of less-doped $\text{La}_1\text{Sr}_{13}\text{Cu}_{24}\text{O}_{41}$ and with $\text{Sr}_{11}\text{Ca}_3\text{Cu}_{24}\text{O}_{41}$. Although the latter compound also exhibits six holes per unit cell, presumably more holes are present in the ladders than in those of $\text{Sr}_{14}\text{Cu}_{24}\text{O}_{41}$. Also in the case of Raman spectroscopy a remarkable change of the line shape was reported from $\text{La}_6\text{Ca}_8\text{Cu}_{24}\text{O}_{41}$ to $\text{Sr}_{14}\text{Cu}_{24}\text{O}_{41}$ [237, 238].

Based on these interesting features in both the infrared and the Raman spectra of $\text{Sr}_{14}\text{Cu}_{24}\text{O}_{41}$, we have developed an explanation in terms of a modulation of the exchange coupling in the ladder by the charge order in the chains. We worked on this interpretation in close collaboration with Götz Uhrig and Kai Schmidt from the theory department of the University of Cologne. The sharpening of the two-triplet Raman peak has been described recently by Schmidt et al. within this scenario [163]. Preliminary results for the infrared absorption will be presented here. This scenario assumes that the ladders of $\text{Sr}_{14}\text{Cu}_{24}\text{O}_{41}$ are still undoped at low temperatures.

However, it cannot be excluded that some holes indeed are located within the ladder subcell. Troyer et al. studied this lightly doped ladder by means of exact diagonalization and found bound pairs of holes even in the limit of isotropic coupling [239]. They also find a new kind of triplet excitation at lower energies that is not present in the undoped ladder. We speculate that some features in the infrared spectra might arise from this new kind of excitation.

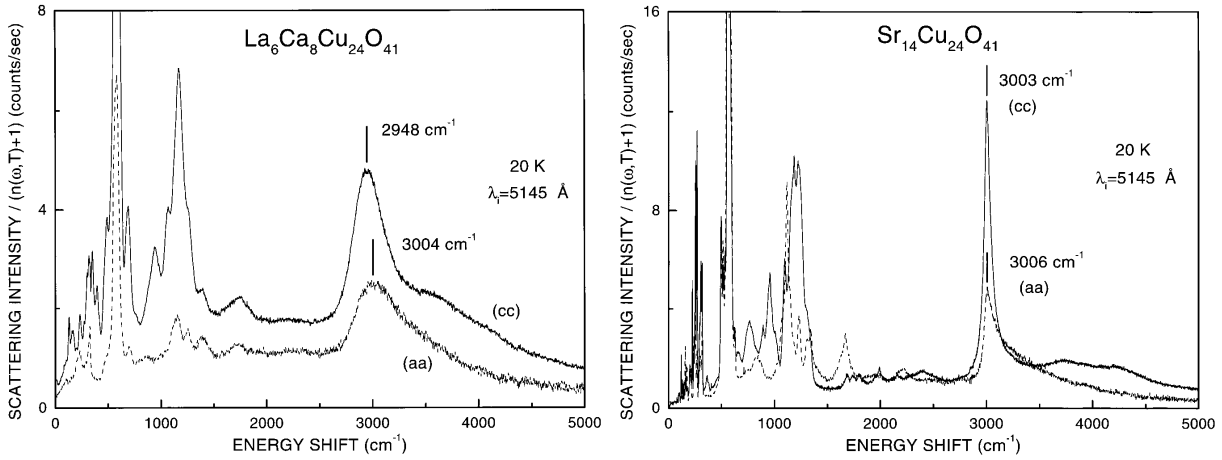


Figure 6.1: Raman spectra of $\text{La}_6\text{Ca}_8\text{Cu}_{24}\text{O}_{41}$ (left) and $\text{Sr}_{14}\text{Cu}_{24}\text{O}_{41}$ (right) for polarizations $E||c$ and $E||a$ of both the incident and scattered light at 20 K. Reproduced from reference [237].

6.1 Sharp Raman Peak in $\text{Sr}_{14}\text{Cu}_{24}\text{O}_{41}$

Sugai and Suzuki measured the Raman scattering of $\text{Sr}_{14}\text{Cu}_{24}\text{O}_{41}$ and $\text{La}_6\text{Ca}_8\text{Cu}_{24}\text{O}_{41}$ with polarizations $E||c$ and $E||a$ for both incident and scattered light [237].¹ At around 3000 cm^{-1} there are strong peaks caused by two-triplet excitations. In the undoped compound $\text{La}_6\text{Ca}_8\text{Cu}_{24}\text{O}_{41}$, this Raman line is rather broad with slightly different positions for both polarizations, as can be seen in the left panel of figure 6.1. Schmidt et al. found good agreement with theoretical results using continuous unitary transformations [163, 231]. Evidence was found that the Heisenberg model is not sufficient to describe the data. But the inclusion of a cyclic exchange term with $J_{cyc} \approx 0.2J_{\perp}$ remedies most of the deviations between experiment and theory [163]. A very different line shape was found in $\text{Sr}_{14}\text{Cu}_{24}\text{O}_{41}$, though. In this compound the two-triplet peak is notably sharper, and it occurs at the same frequency for both polarizations (right panel of figure 6.1) [237, 238].

The sharp Raman peak in $\text{Sr}_{14}\text{Cu}_{24}\text{O}_{41}$ is surprising compared to the rather broad two-magnon peak observed in the 2D cuprates [240], which still causes controversial discussions. Gozar et al. question that quantum fluctuations are responsible for the broad feature in the 2D cuprates since in the quasi-1D ladders even stronger fluctuations should produce a by far broader line shape than measured in $\text{Sr}_{14}\text{Cu}_{24}\text{O}_{41}$ [238]. Schmidt et al. challenge this interpretation by providing a clear explanation for the sharp Raman peak [163]. The main idea is that the charge order in the chains has an influence on the exchange coupling within the ladder. Usually, the different periodicity of ladders and chains as well as their mutual influence are not considered.

What is more, charge ordering in the chains of $\text{Sr}_{14-x}\text{Ca}_x\text{Cu}_{24}\text{O}_{41}$ occurs as long as the Ca content is not too high. This effect was reported by several groups using neutron diffraction [113, 169], x-ray scattering [170], thermal expansion [171], and dc resistivity measurements [159] (see also section 2.4.3). Further support was presented by Kataev et

¹Ammerahl et al. speculate that a La content of $y = 6$ is already beyond the solubility limit [7]. See also pages 41 and 81.

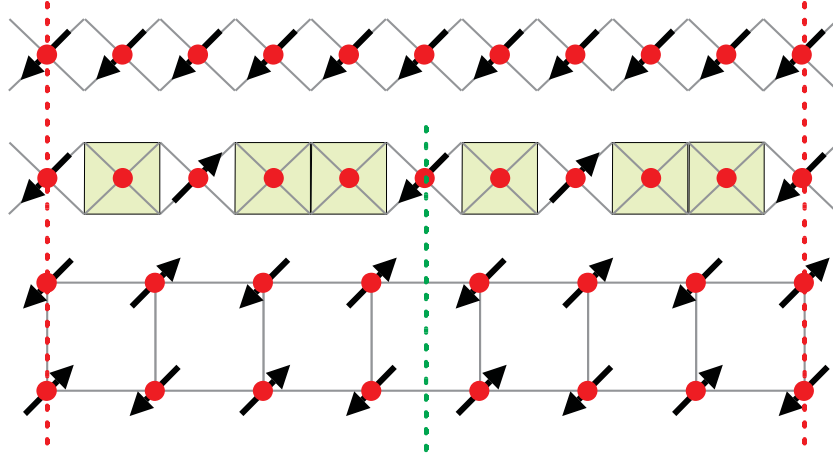


Figure 6.2: Sketch of the superstructure in the chains and ladders along the c axis. 10 chain units in the top row approximately match 7 ladder units in the bottom row. This induces a structural modulation in the ladders with a wave vector $Q_S = c_{\text{ladder}}/c_{\text{chain}} = 10/7 = 3/7 + 1$ in reciprocal lattice units of the ladder. The charge ordering in $\text{Sr}_{14}\text{Cu}_{24}\text{O}_{41}$ produces an additional superstructure with $Q_{\text{CO}} = 2/7$, corresponding to a periodicity of $5 \cdot c_{\text{chain}}$. A possible visualization of such an ordering is shown in the middle row (cf. figure 2.14 on page 24). Filled squares represent Zhang-Rice singlets. Reproduced from reference [163].

al. who studied single crystals with Ca contents from $x = 0$ to 12 by means of electron spin resonance (ESR) [10]. They found the onset of charge order in the chains at $T_{\text{CO}} = 200$ K for $x = 0$, 170 K ($x = 2$), and 80 K ($x = 5$). There was no signature of charge ordering for larger Ca contents. A recent x-ray diffraction measurement by Fukuda et al. provides evidence that the charge order in the chains of $\text{Sr}_{14}\text{Cu}_{24}\text{O}_{41}$ exhibits a periodicity of five chain units [172]. Thus one may expect an additional modulation of the exchange coupling in the *ladders* of $\text{Sr}_{14}\text{Cu}_{24}\text{O}_{41}$ below $T_{\text{CO}} = 200$ K. Due to this modulation the ladders show the same superstructure as the chains, which produces a back-folding of the dispersion of the elementary triplet. New gaps arise at the crossing points, which drastically influences the Raman line shape. Schmidt et al. again use continuous unitary transformations to calculate the according spectra with the necessary high resolution [163]. A cyclic spin exchange was included since its relevance for the telephone-number compounds is by now clearly established.

The presence of the chains produces seven inequivalent ladder rungs per formula unit of the composite structure, as sketched in figure 6.2. The corresponding modulation of the ladders is characterized by the wave vector $Q_S = 10/7 = 3/7 + 1$ in reciprocal lattice units of the ladder. In the magnetic subsystem of the ladders, wave vectors are only meaningful modulo unity. Therefore the wave vectors $Q_S = 10/7$ and $Q_S = 3/7$ are equivalent. The main effect is a slight shift of the oxygen ions within the chains, which induces a modulation of the Madelung potentials within the ladders and thus also of the exchange couplings. An estimate of the amplitude of the modulation yields that also the second harmonic $2Q_S = 6/7$ has to be considered [163]. The additional modulation stemming from the charge ordering on the chains below $T_{\text{CO}} \approx 200$ K is described by the wave vector $Q_{\text{CO}} = c_{\text{ladder}}/5 \cdot c_{\text{chain}} = 2/7$.

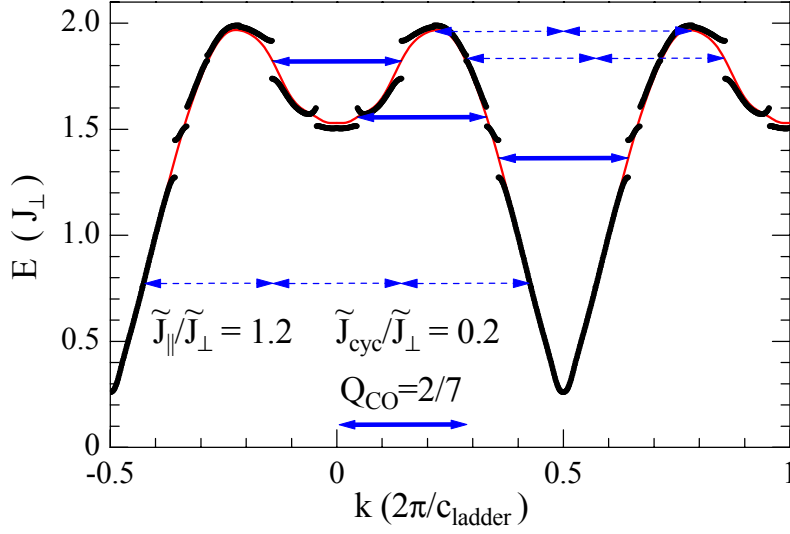


Figure 6.3: Dispersion of the elementary triplet with (thick black lines) and without (thin line) a charge-order modulation of 15%. The corresponding wave vector of $Q_{CO} = 2/7$ is denoted by the arrows. Dashed arrows indicate higher-order contributions. Reproduced from reference [163].

For the actual calculation of the Raman spectra Schmidt et al. use the set of coupling constants found by the DMRG analysis of Nunner et al., which has been described in section 5.3.2 [26]. The couplings have to be scaled to match the definition of Schmidt et al. since the definition of the cyclic exchange term slightly differs from the one in equation 5.10. The values for undoped $\text{La}_{5.2}\text{Ca}_{8.8}\text{Cu}_{24}\text{O}_{41}$ in the new notation read $\tilde{J}_{\parallel}/\tilde{J}_{\perp} = 1.2$, $\tilde{J}_{\text{cyc}}/\tilde{J}_{\perp} = 0.2$, and $\tilde{J}_{\perp} = 1150 \text{ cm}^{-1}$ [163]. Figure 6.3 shows the dispersion of the elementary triplet with and without a 15% modulation due to the charge ordering, i.e. with the wave vector $Q_{CO} = 2/7$. Notable gaps open wherever Q_{CO} links equal energies $E(k) = E(k + Q_{CO})$ of the unmodulated ladder. Smaller gaps open for higher-order processes, e.g. for $E(k) = E(k + 2Q_{CO})$. Thus the energies at which gaps open depend decisively on the wave vector of the modulation.

In figure 6.4 the calculated Raman spectra are compared with the experimental data of Sugai and Suzuki [237]. The calculated broad Raman response of the unmodulated ladder (bottom panel) is in good agreement with the measured data of $\text{La}_6\text{Ca}_8\text{Cu}_{24}\text{O}_{41}$ (middle panel). In particular, the large width of the Raman line reflects the width of the two-triplet continuum at $k = 0$ as depicted in figure 5.28 on page 125. Note that the excellent description of the peak position obtained for the parameter set of section 5.3.2 [26] clearly verifies these parameters. The next step is to examine the effect of a modulation on the line shape. The occurrence of gaps produces van Hove singularities in the density of states that produce new peaks in the Raman spectra. Raman scattering only measures excitations with total momentum $k_{\text{tot}} = 0$. Thus the spectra reflect the excitation of two triplets with opposite momenta $k_1 = -k_2$ and equal energies $E(k_1) = E(-k_2)$. Therefore a gap at E_{gap} leads to a corresponding feature in the spectrum at $2E_{\text{gap}}$. For the structural modulations with wave vectors $Q_S = 3/7$ and $6/7$ these effects are rather small, as can be seen in the middle panel of figure 6.4. However, a drastic effect occurs if $2E_{\text{gap}}$ coincides with the broad peak of the unmodulated ladder. In this case the opening of the gap

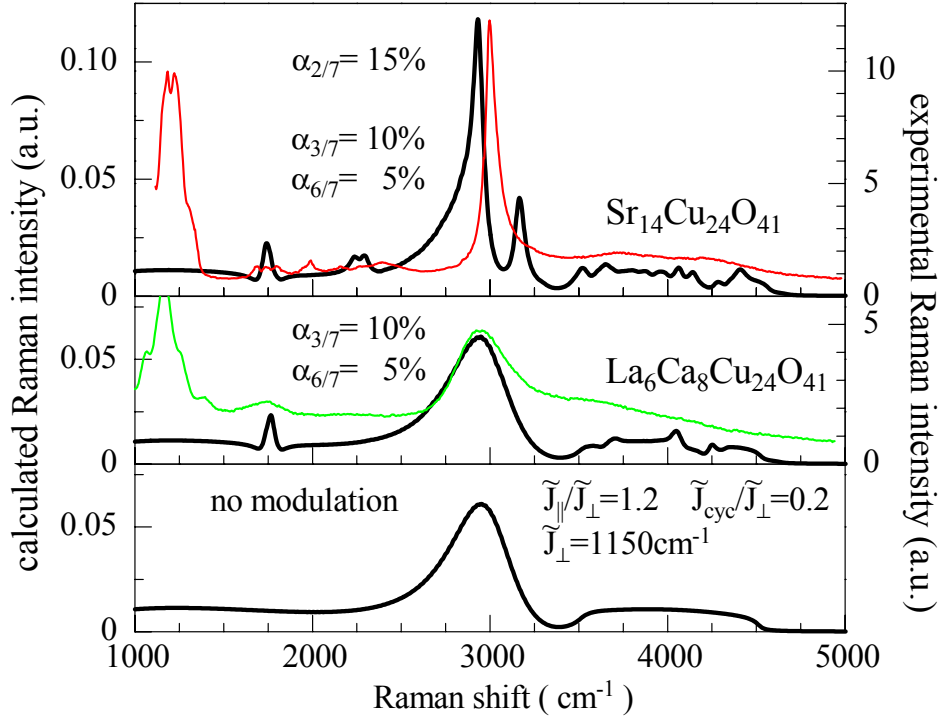


Figure 6.4: Theoretical (thick lines) and experimental (thin lines, $T = 20$ K) Raman spectra of spin ladders for cc polarization. For the calculations the exchange couplings of $\tilde{J}_{\parallel}/\tilde{J}_{\perp} = 1.2$, $\tilde{J}_{cyc}/\tilde{J}_{\perp} = 0.2$, and $\tilde{J}_{\perp} = 1150 \text{ cm}^{-1}$ were used. The **bottom** panel shows the theoretical spectrum without any modulation. In the **middle** panel the structural modulations with $Q_S = 3/7$ and $6/7$ are included. The thin line denotes the measured $\text{La}_6\text{Ca}_8\text{Cu}_{24}\text{O}_{41}$ data [237]. Finally, in the **top** panel also the charge-order modulation with $Q_{CO} = 2/7$ is included in the calculated spectrum. Here the thin line represents the $\text{Sr}_{14}\text{Cu}_{24}\text{O}_{41}$ data [237]. Reproduced from reference [163].

leads to a redistribution of a large part of the spectral weight. For the used exchange couplings a gap opens at approximately 3100 cm^{-1} , which is slightly above the Raman peak of the unmodulated ladder. Hence the charge-order modulation piles up a large part of the high-frequency weight on top of the peak. A sharp feature arises, that agrees very well with the experimental line shape of $\text{Sr}_{14}\text{Cu}_{24}\text{O}_{41}$ [237, 238] (upper panel of figure 6.4). The exact position can be reproduced by a 2% increase of J_{\perp} . But for a conclusive determination an independent, precise result of J_{\parallel} and J_{cyc} in $\text{Sr}_{14}\text{Cu}_{24}\text{O}_{41}$ is necessary [163]. This can be provided by an analysis of our infrared data.

Note that the couplings used for the calculations were determined independently, namely from our infrared spectra of the undoped ladder. Thus the agreement with the measured Raman spectra in terms of the line shape and the position of the main peak provides strong evidence for the underlying concept of modulations. In particular, a charge order with a periodicity of $5 \cdot c_{\text{chain}}$ supports the view that at low temperatures almost all six charge carriers per formula unit are located in the chains (see figure 6.2). A further argument arises from the polarization dependence. According to reference [231], the peak positions for the two polarizations should be different as soon as a cyclic exchange is involved. This is the case in $\text{La}_6\text{Ca}_8\text{Cu}_{24}\text{O}_{41}$ [237], but the sharp peak in $\text{Sr}_{14}\text{Cu}_{24}\text{O}_{41}$ is

found at $\approx 3000 \text{ cm}^{-1}$ for *both* polarizations [237, 238]. But in the scenario of modulated couplings the peak position is determined by the position and the size of the gap. Hence the coincidence of the peak position for both polarizations despite $J_{cyc} > 0$ supports the proposed modulation scenario. Moreover, it becomes clear why the sharp peaks in the measured spectra are only visible below $\approx 200 \text{ K}$, since at this temperature the charge ordering sets in.

6.2 Infrared Spectra of $\text{Sr}_{14}\text{Cu}_{24}\text{O}_{41}$

Infrared absorption is also restricted to $k_{tot} = 0$ excitations, but since the phonon participating in the phonon-assisted magnetic absorption provides momentum according to $0 = k_{tot} = k_{phonon} + k_{magnons}$, it rather measures a weighted average of the magnetic $S = 0$ spectrum over the whole Brillouin zone (see section 3.3). Thus the Raman calculations for $k = 0$ presented above are just the first step to describe the infrared absorption spectra. The according computations by Schmidt et al. are currently in progress, and therefore we can only present preliminary results. But at first our infrared spectra of $\text{Sr}_{14}\text{Cu}_{24}\text{O}_{41}$ are presented.

Figure 6.5 shows the reflectance data for polarization $E||c$ (top panel) and $E||a$ (bottom panel). Below $T_{CO} = 200 \text{ K}$ the spectra are very similar to the spectra of $\text{La}_4\text{Ca}_{10}\text{Cu}_{24}\text{O}_{41}$ in figure 5.6. But there is a considerable change above this temperature in particular for $E||c$. Due to the melting of the charge order in the chains, the conductivity increases giving rise to a metallic Drude contribution. Therefore the reflectance in the low-frequency part of the spectra strongly increases (confer figure 3.1 on page 55). The data shows that, as expected, the increase of charge mobility is larger along the c axis than along the a axis.

In addition, the transmittance was measured on a total of three different samples. In figure 6.6 the results of the $d = 52 \text{ }\mu\text{m}$ sample are plotted in the top panel. At 4 K the spectra are still similar to, for instance, the $\text{La}_4\text{Ca}_{10}\text{Cu}_{24}\text{O}_{41}$ transmittance data in the top panel of figure 5.7. However, the absolute values of $\text{Sr}_{14}\text{Cu}_{24}\text{O}_{41}$ are smaller although the sample is approximately 15% thinner. At 4 K there is a reduction of $T_a(\omega)$ below 2200 cm^{-1} compared to the higher temperatures. A similar reduction was reported in very low-doped YBCO and attributed to a localization of polaronic charge carriers at low temperatures [110]. The effect is very small in the present case. It is comparable to what has been observed in those samples of YBCO which represent the lowest hole doping that can actually be achieved. Such doping levels are usually considered as “undoped” for all practical purposes. So far, $\text{Sr}_{14}\text{Cu}_{24}\text{O}_{41}$ is the only telephone-number compound measured by our group for which we could verify such a reduction of $T_a(\omega)$ at low temperatures.

Note that for $E||c$ the fringes were not smoothed away for $d = 52 \text{ }\mu\text{m}$. This is important to ensure the necessary resolution in order to resolve e.g. the new double dip above 2000 cm^{-1} . These unsmoothed spectra were used later on for the calculation of σ_c in the low-frequency regime. The double-dip feature is less pronounced in the $d = 20 \text{ }\mu\text{m}$ data as plotted in the bottom panel of figure 6.6 since here the fringes were smoothed also for $E||c$. At least up to 150 K these spectra were used for the calculation of σ_c only above 2500 cm^{-1} .

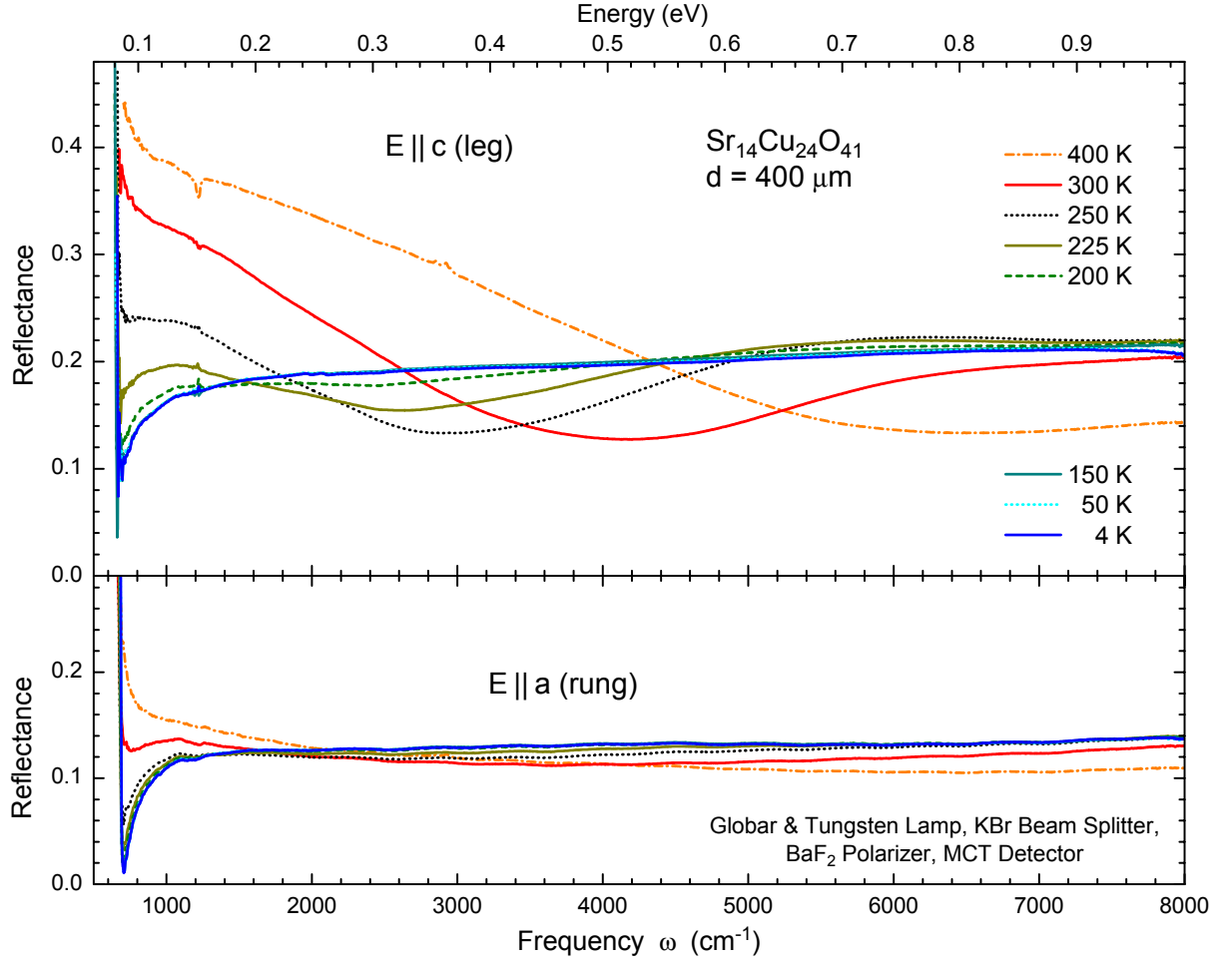


Figure 6.5: Mid-infrared reflectance of a $400\ \mu\text{m}$ thick sample of $\text{Sr}_{14}\text{Cu}_{24}\text{O}_{41}$. The **top** panel shows the spectra for $E \parallel c$, whereas the $E \parallel a$ data is plotted in the **bottom** panel. Above $T_{\text{CO}} = 200\ \text{K}$ a metallic contribution emerges in particular for $E \parallel c$. The little spikes at $1220\ \text{cm}^{-1}$ and the $2900\ \text{cm}^{-1}$ features at $400\ \text{K}$ are measurement artefacts. See figure 5.6 on page 94 for a comparison with the reflectance data of $\text{La}_4\text{Ca}_{10}\text{Cu}_{24}\text{O}_{41}$.

For both samples there is a drastic difference to the spectra of the undoped compounds. Upon increasing the temperature the transmittance gets strongly suppressed. Above $190\ \text{K}$ for $E \parallel c$ and above $220\ \text{K}$ for $E \parallel a$ it was not possible to measure any spectrum because the samples became opaque. The mobile charge carriers above the charge-order temperature of $T_{\text{CO}} \approx 200\ \text{K}$ cause too much absorption. Yet below this temperature we are particularly interested in the apparent new fine structure of the spectra. Since the fringe amplitudes of the presented a -axis data were too large to omit the smoothing procedure, we measured a rather thick sample to gain high-resolution spectra. In figure 6.7 the transmittance of a $d = 368\ \mu\text{m}$ thick sample is plotted. The values for $E \parallel c$ are very small and thus not used for the calculation of σ_c . For the other polarization, though, there are interesting features around $2000\ \text{cm}^{-1}$ that could not be resolved before. Already above $4000\ \text{cm}^{-1}$ the sample became opaque, and above $160\ \text{K}$ no transmittance could be measured at all. Since the absolute values of $T(\omega)$ are not higher than 20%,

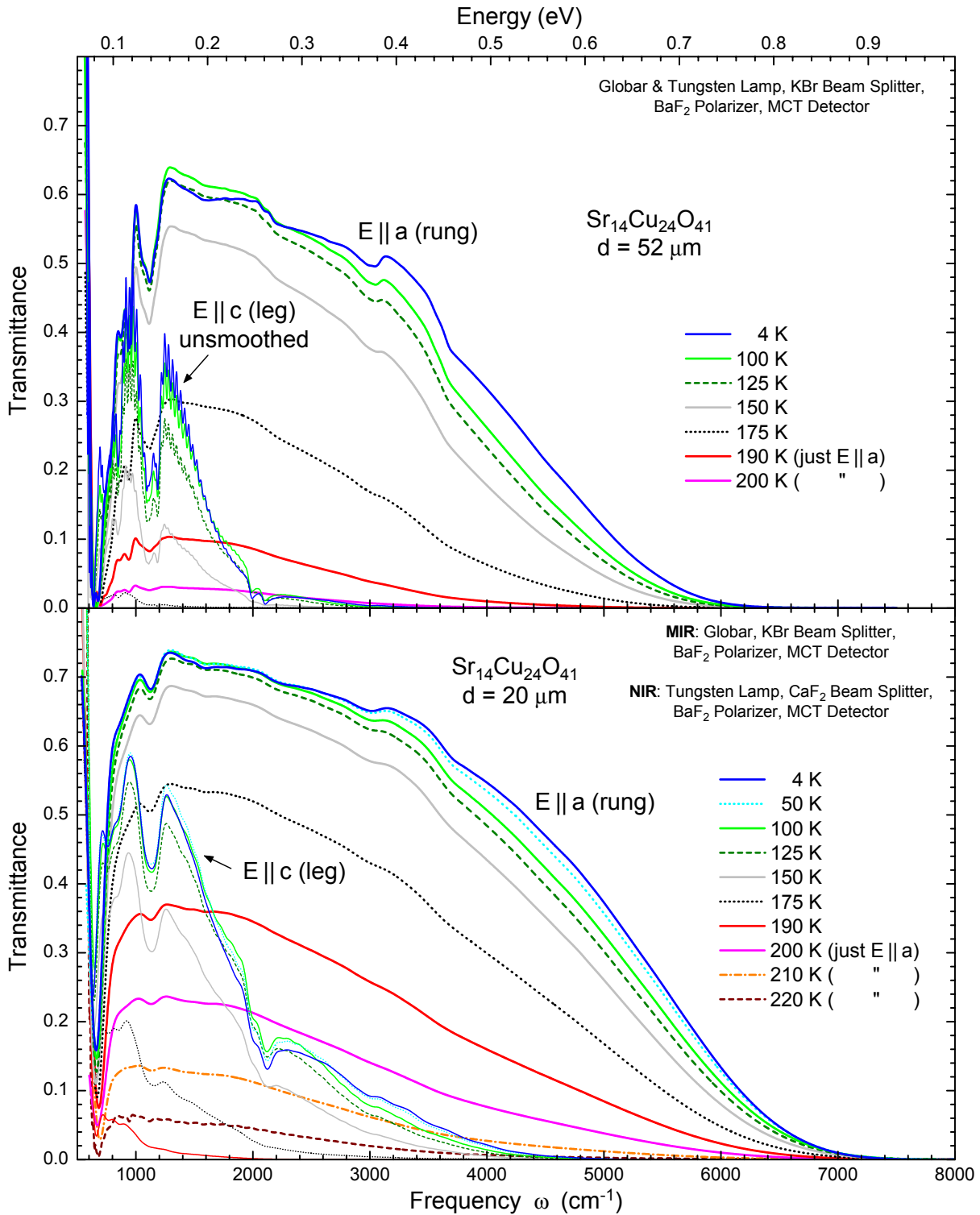


Figure 6.6: Mid-infrared transmittance of $\text{Sr}_{14}\text{Cu}_{24}\text{O}_{41}$ with $T_{\text{CO}} = 200$ K. All spectra were corrected for the polarizer error (see page 69). Apart from the $E \parallel c$ data (thin lines) of the $d = 52 \mu\text{m}$ sample (**top** panel), all spectra were smoothed to get rid of the fringes. For the $d = 20 \mu\text{m}$ sample (**bottom** panel) it was possible to obtain spectra up to a slightly higher temperature of 220 K. Only a -axis data (thick lines) could be determined for the highest temperatures. Note that no down-scaling was necessary to ensure positive values of σ_1 .

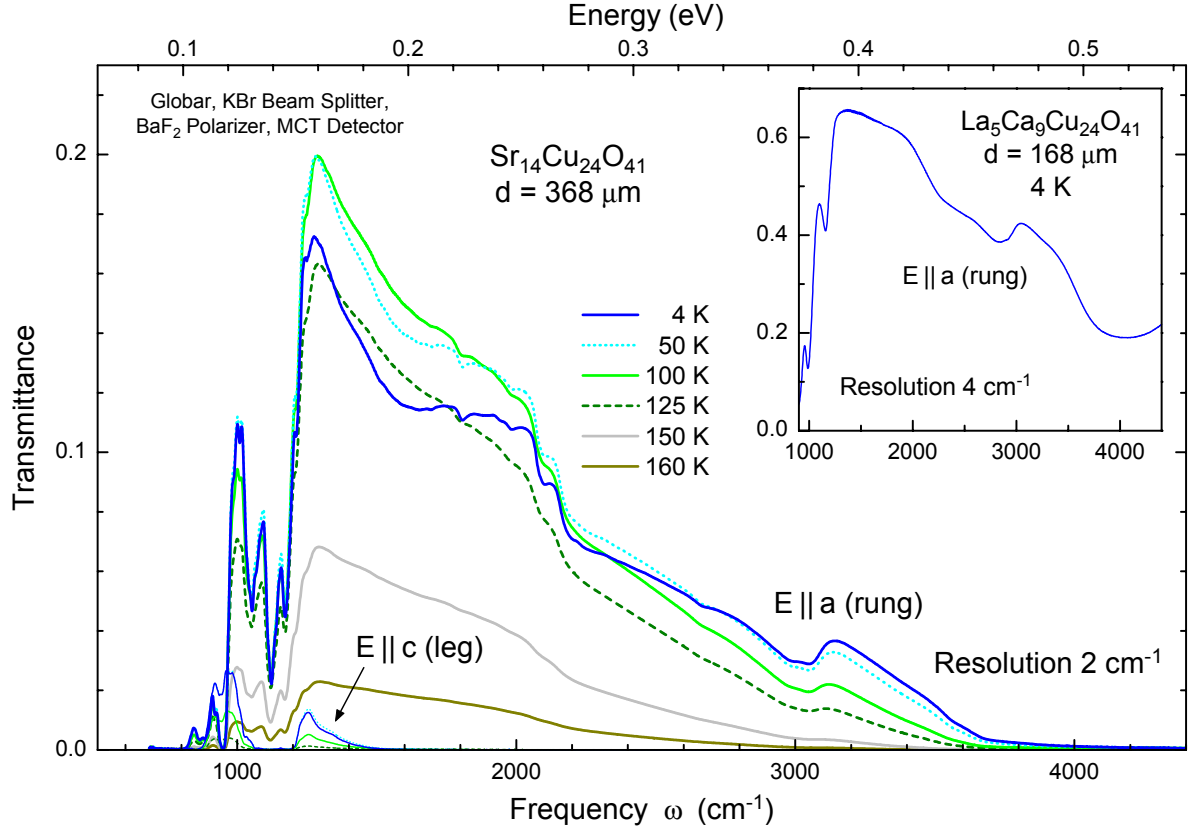


Figure 6.7: Transmittance of a $d = 368 \mu\text{m}$ thick sample of $\text{Sr}_{14}\text{Cu}_{24}\text{O}_{41}$. The c axis is almost opaque even at 4 K. Since no fringes are present, no smoothing is necessary. The resolution of the spectra is 2 cm^{-1} . To demonstrate that there is no fine structure in the undoped compounds, the inset shows $T(\omega)$ of a $d = 168 \mu\text{m}$ sample of $\text{La}_5\text{Ca}_9\text{Cu}_{24}\text{O}_{41}$ for $E||a$ at 4 K. The data is also unsmoothed and measured with a resolution of 4 cm^{-1} .

no fringes occurred in the spectra. Hence the presented data is completely unsmoothed and measured with a high resolution of 2 cm^{-1} . The above mentioned reduction of $T_a(\omega)$ below $\approx 2200 \text{ cm}^{-1}$ at low temperatures is clearly visible, in excellent agreement with the data of the $d = 52 \mu\text{m}$ sample.

The calculated optical conductivity is shown in figure 6.8. The c -axis data in the top panel exhibits a prominent double-peak structure above 2000 cm^{-1} instead of the rather broad lower bound-state peak of the undoped ladders (see also top panel of figure 6.9). Just the two thinner samples with $d = 52$ (unsmoothed) and $20 \mu\text{m}$ (smoothed) were used. Already above 125 K, σ_1 increases considerably, and 190 K was the highest temperature for which a spectrum could be measured. This supports that the charge-order temperature in $\text{Sr}_{14}\text{Cu}_{24}\text{O}_{41}$ indeed is located at $T_{\text{CO}} \approx 200 \text{ K}$. The spectra for $E||a$ are plotted in the bottom panel of figure 6.8. Here the unsmoothed data of the $368 \mu\text{m}$ sample was used for the lowest frequencies. Similar to the other polarization, an increase of σ_1 above 125 K can be observed. But on this scale it is not possible to see any fine structure. Therefore the interesting regime is plotted on an enlarged scale in the bottom panel of figure 6.9. The 4 K spectrum also reveals a double structure of

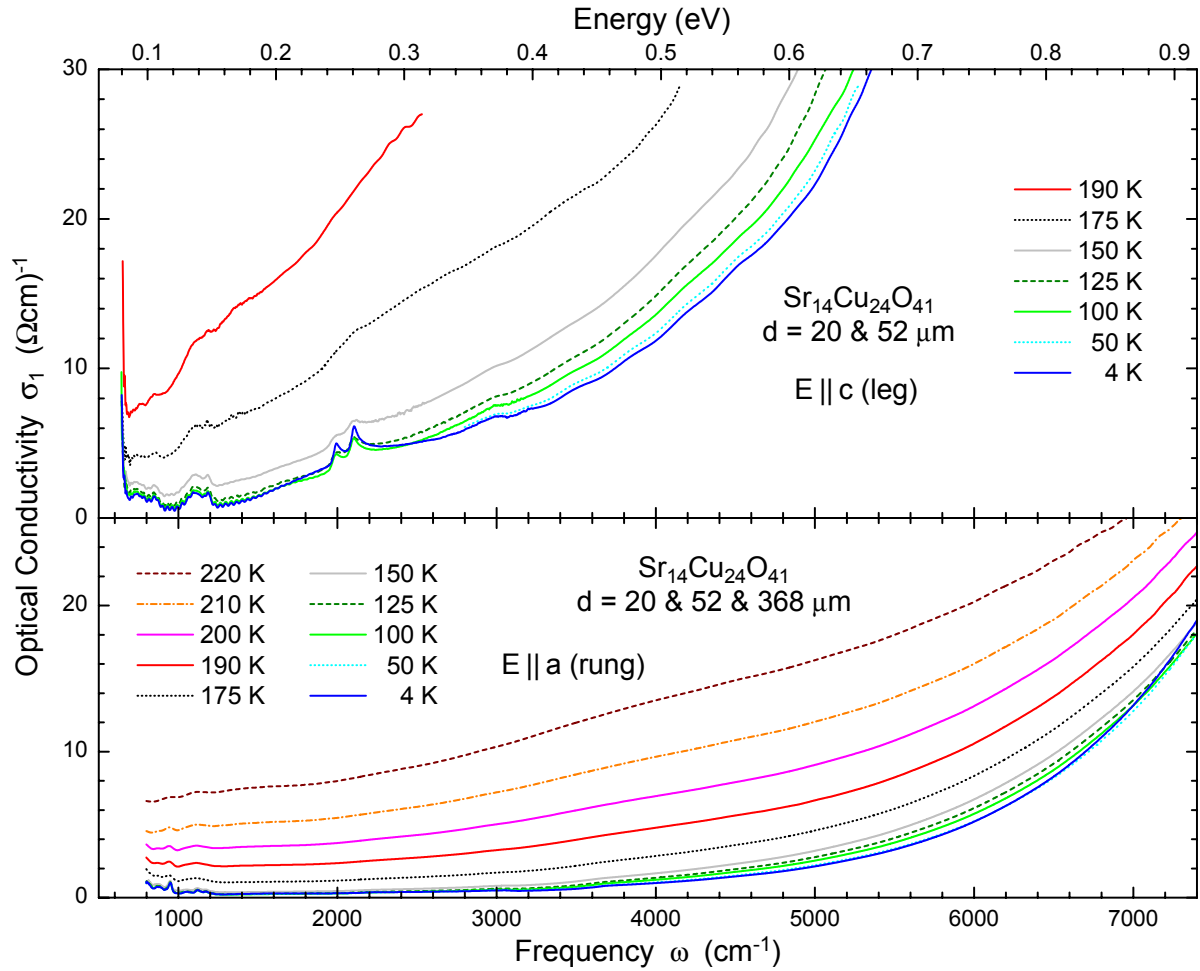


Figure 6.8: Optical conductivity of $\text{Sr}_{14}\text{Cu}_{24}\text{O}_{41}$ for polarization $E \parallel c$ (**upper** panel) and $E \parallel a$ (**bottom** panel). The transmittance data of the samples with $d = 20$ and $52 \mu\text{m}$ were used for both polarizations, whereas the $d = 368 \mu\text{m}$ sample was used only for $E \parallel a$.

the lower bound-state peak at $\approx 2100 \text{ cm}^{-1}$, similar to the case of $E \parallel c$. But there are further small features, as for instance the peak at $\approx 1810 \text{ cm}^{-1}$ below the bound-state peaks and another one in-between the bound-state peaks at $\approx 2670 \text{ cm}^{-1}$. Also the upper bound-state peak at $\approx 3000 \text{ cm}^{-1}$ is split in two peaks.

Now it is interesting to compare the fine structure in $\text{Sr}_{14}\text{Cu}_{24}\text{O}_{41}$ with the results of other telephone-number compounds. Figure 6.10 shows not only the almost undoped compounds $\text{La}_{5.2}\text{Ca}_{8.8}\text{Cu}_{24}\text{O}_{41}$ and $\text{La}_4\text{Ca}_{10}\text{Cu}_{24}\text{O}_{41}$ but also the doped² compounds $\text{La}_1\text{Sr}_{13}\text{Cu}_{24}\text{O}_{41}$ and $\text{Sr}_{11}\text{Ca}_3\text{Cu}_{24}\text{O}_{41}$. The latter two systems were measured by Puchalla and will be presented shortly in reference [241]. The undoped samples show much broader features compared to the doped ones. The presented spectra of the undoped samples exhibit a reduced resolution since the fringes were smoothed. However, there is definitely no such fine structure that was lost due to the smoothing. This can be easily seen in figure

²The term “doped” here means that there are nominally 5 (6) holes per formula unit in $\text{La}_1\text{Sr}_{13}\text{Cu}_{24}\text{O}_{41}$ ($\text{Sr}_{11}\text{Ca}_3\text{Cu}_{24}\text{O}_{41}$). Whether there are holes in the ladders is not clear a priori.

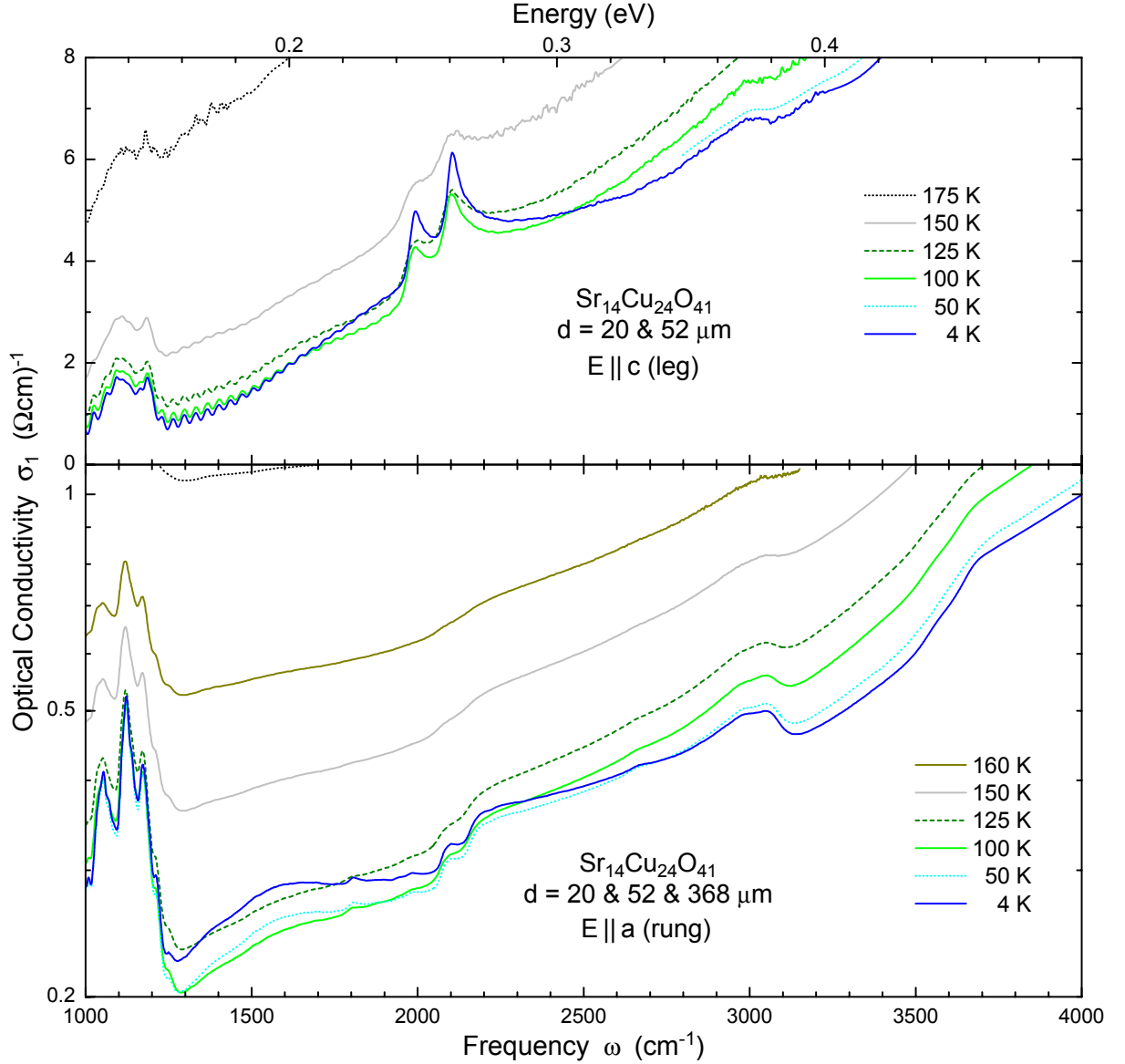


Figure 6.9: Optical conductivity of $\text{Sr}_{14}\text{Cu}_{24}\text{O}_{41}$ for $E \parallel c$ (**top**) and for $E \parallel a$ (**bottom**) on enlarged scales to reveal the fine structure. In this regime the resolution for $E \parallel a$ is 2 cm^{-1} . For $E \parallel c$ the resolution is 5 cm^{-1} only below $\approx 2500 \text{ cm}^{-1}$. Note the logarithmic σ_1 scale in the bottom panel.

5.8 on page 98 where smoothed and unsmoothed spectra are compared. In addition, the inset of figure 6.7 shows $T(\omega)$ of a $d = 168 \mu\text{m}$ sample of $\text{La}_5\text{Ca}_9\text{Cu}_{24}\text{O}_{41}$ for $E \parallel a$ at 4 K. This spectrum does not show significant fringes due to the large thickness, and thus no smoothing was necessary. The resolution of the presented spectrum is 4 cm^{-1} , and there is no fine structure.

The doped sample of $\text{La}_1\text{Sr}_{13}\text{Cu}_{24}\text{O}_{41}$ nominally exhibits already five holes per formula unit. This clearly enhances the electronic background but the bound-state peaks for both polarizations are almost as broad as in the undoped samples. But there are first precursors of the sharpening that occurs for $\text{Sr}_{14}\text{Cu}_{24}\text{O}_{41}$. For instance the lower bound-state peak

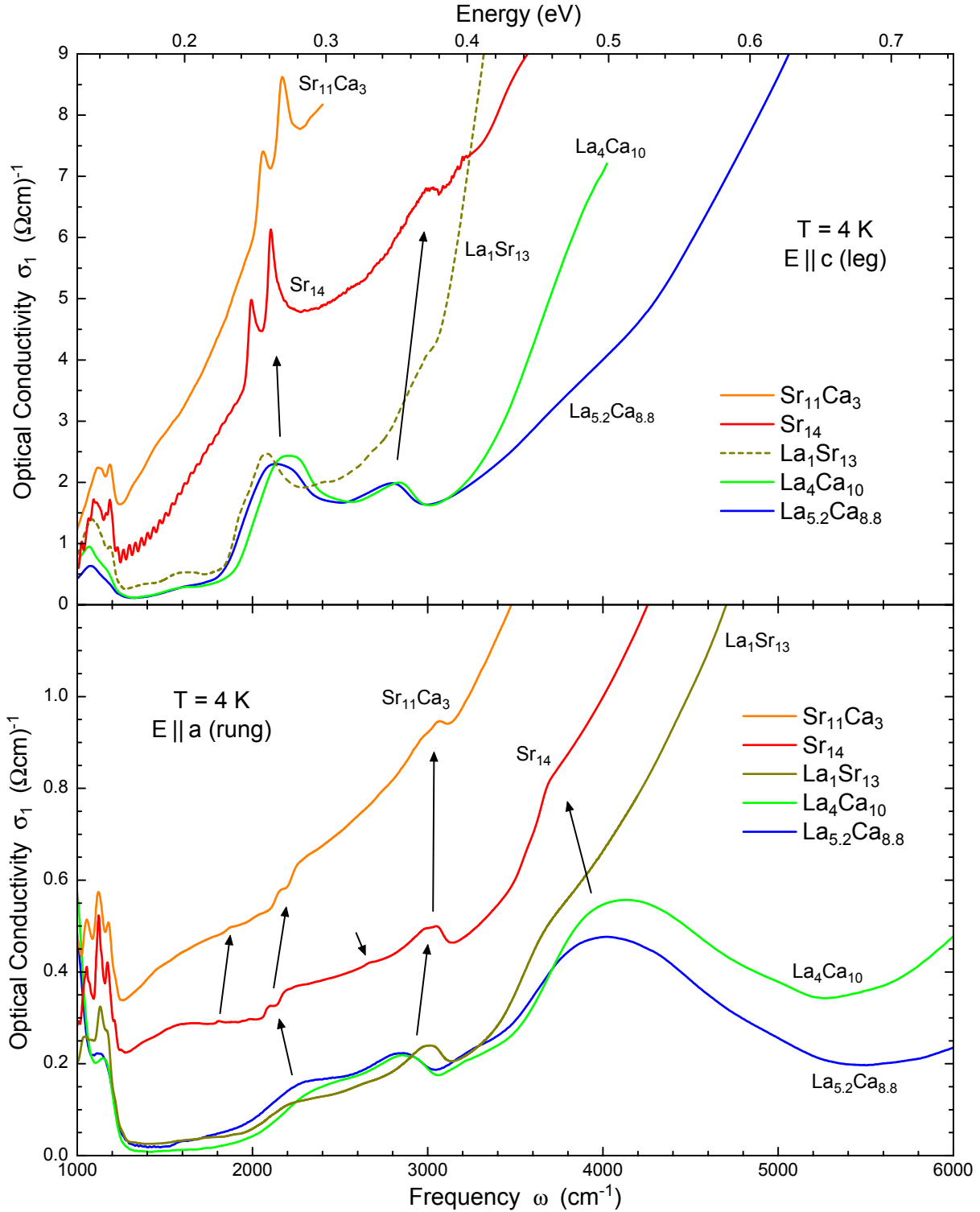


Figure 6.10: Comparison of the magnetic fine structure in the spectra of different telephone-number compounds at 4 K. The undoped $\text{La}_{5.2}\text{Ca}_{8.8}\text{Cu}_{24}\text{O}_{41}$ and $\text{La}_4\text{Ca}_{10}\text{Cu}_{24}\text{O}_{41}$ show broad peaks, whereas the intermediate system $\text{La}_1\text{Sr}_{13}\text{Cu}_{24}\text{O}_{41}$ [241] exhibits first precursors. Finally, in $\text{Sr}_{14}\text{Cu}_{24}\text{O}_{41}$ and $\text{Sr}_{11}\text{Ca}_3\text{Cu}_{24}\text{O}_{41}$ [241] similar sharp peaks occur for $E \parallel c$ (**upper** panel), and there is further fine structure for $E \parallel a$ (**bottom** panel).

for $E||c$ (upper panel of figure 6.10) is less rounded and clearly exhibits a slight shoulder at the low-frequency side. And for the other polarization $E||a$ (bottom panel) the upper bound-state peak is slightly sharper and shifted up to 3000 cm^{-1} . Also the feature in-between the bound-state peaks can be seen at around 2630 cm^{-1} . The strong double feature in $\text{Sr}_{14}\text{Cu}_{24}\text{O}_{41}$ for $E||c$ is very similar to the sharpening observed in the Raman data. $\text{Sr}_{11}\text{Ca}_3\text{Cu}_{24}\text{O}_{41}$ shows basically the same feature. The nominal doping is the same as for $\text{Sr}_{14}\text{Cu}_{24}\text{O}_{41}$, but substituting Ca for Sr is expected to move holes from the chains to the ladders and to hinder charge order in the chains. In fact, the electronic background is the highest of all presented compounds. The slight rounding compared to $\text{Sr}_{14}\text{Cu}_{24}\text{O}_{41}$ might be attributed to disorder induced by Ca. Also along the a axis the magnetic features are very similar for $\text{Sr}_{11}\text{Ca}_3\text{Cu}_{24}\text{O}_{41}$ and $\text{Sr}_{14}\text{Cu}_{24}\text{O}_{41}$. Even the small peak below the bound state is present in both compounds. Almost all the features are shifted up by around 60 cm^{-1} in $\text{Sr}_{11}\text{Ca}_3\text{Cu}_{24}\text{O}_{41}$. This has to be expected since Ca is smaller than Sr, which causes an increase of the exchange couplings.

Apart from the modulation effects discussed below, another possible explanation for the sharper features in the samples without La might simply be that La substitution induces disorder into the crystal structure as described in section 2.4.2. In this scenario the splitting of the lower bound-state peak for $E||c$ might stem from the *two* relevant phonons that are involved in the absorption process along this axis (see figure 5.32 on page 131). But the distance between the peaks is $\approx 110\text{ cm}^{-1}$ in both $\text{Sr}_{14}\text{Cu}_{24}\text{O}_{41}$ and $\text{Sr}_{11}\text{Ca}_3\text{Cu}_{24}\text{O}_{41}$, which is considerably larger than the difference of $30 - 60\text{ cm}^{-1}$ between the phonon modes as calculated by Nunner et al. [201].

By using equations 5.15 to 5.17 on page 128 derived from the DMRG analysis of section 5.3.2, it is possible to deduce the exchange parameters from the positions of the bound-state peaks. For $\text{La}_1\text{Sr}_{13}\text{Cu}_{24}\text{O}_{41}$ one can easily determine the frequency of the lower bound-state peak for $E||c$. The upper bound-state peak is easier to determine for $E||a$. For the other parameters we have used identical values as for the analysis of $\text{La}_{5.2}\text{Ca}_{8.8}\text{Cu}_{24}\text{O}_{41}$, i.e. $\omega_{ph}^c = 570\text{ cm}^{-1}$, $\omega_{ph}^a = 620\text{ cm}^{-1}$ [201], and $\Delta_s = 280\text{ cm}^{-1}$ [25, 216]. The same procedure can be applied to $\text{Sr}_{14}\text{Cu}_{24}\text{O}_{41}$ and $\text{Sr}_{11}\text{Ca}_3\text{Cu}_{24}\text{O}_{41}$. As long as the origin of the double peaks is not finally clarified, it is reasonable to use the mean values of the two frequencies. The calculated couplings are summarized in table 6.1. Note that the used equations are only accurate within 5% as long as $J_{||}/J_{\perp} \leq 1.35$. But there still is a clear tendency that away from the undoped compounds the ratio $J_{||}/J_{\perp}$ increases. For a detailed statement on J_{cyc} a more accurate analysis is necessary. Especially measurements of the gap energies for different dopings would be helpful.

To check if there are in fact modulation effects in the optical conductivity as there are in the Raman spectra, one has to analyze the bound-state dispersion and the two-triplet continuum. Just to give an idea, in figure 6.11 the DMRG result for the excitation spectrum is plotted that was calculated by Nunner et al. [26]. Similar to figure 6.3, some exemplary modulation vectors are included. Again gaps will open wherever the modulation wave vectors link equal energies. Like before, $Q = 2/7$ denotes the effect of the charge ordering in the chains, and the structural modulation is described by $Q = 3/7$ along with the overtone $Q = 6/7$. The latter wave vector is equivalent to $Q = |6/7 - 1| = 1/7$. The according calculations by Schmidt et al. are currently in progress. Preliminary results for the infrared spectra are available as plotted in figure 6.12. Again continuous unitary transformations were used, but the cyclic exchange is not included so far. Thus the

	ω_{min}^c (cm ⁻¹)	ω_{max}^a (cm ⁻¹)	J_{\parallel}/J_{\perp}	J_{\perp} (cm ⁻¹)	J_{cyc}/J_{\perp}
La _{5.2} Ca _{8.8} Cu ₂₄ O ₄₁	1570	2230	1.31	1040	0.26
La ₄ Ca ₁₀ Cu ₂₄ O ₄₁	1635	2265	1.28	1090	0.27
La ₁ Sr ₁₃ Cu ₂₄ O ₄₁	1510	2390	1.46	1000	0.24
Sr ₁₄ Cu ₂₄ O ₄₁	1480	2395	1.48	980	0.23
Sr ₁₁ Ca ₃ Cu ₂₄ O ₄₁	1545	2410	1.44	1020	0.25

Table 6.1: Coupling constants of various telephone-number compounds determined via equations 5.15 to 5.17 on page 128. ω_{min}^c was determined for $E||c$ and ω_{max}^a for $E||a$. The subtracted phonon frequencies are 570 and 620 cm⁻¹, respectively [26, 201]. Note that there are several sources of inaccuracies in this determination. First, the proper peak positions are not easy to find in the spectra. Next, the phonon frequencies are not exactly known and were assumed to be constant for all compounds. The dispersion of the phonons was neglected, and the relative difference between a - and c -axis polarization is not known in detail for every compound. The same holds true for the spin gap, which was assumed to be constant: $\Delta_s = 280$ cm⁻¹ [25, 216]. At last, the used equations are only valid within 5% below the ratio of $J_{\parallel}/J_{\perp} = 1.35$ [26].

coupling ratio $J_{\parallel}/J_{\perp} = 1.15$ was assumed according to our previous results (see table 5.2 on page 132). The bound-state peaks are shown for $E||a$ (left panel) and $E||c$ (right panel) for 5% modulation of J_{\parallel} with the three different wave vectors. Note that the spectra are shifted with respect to each other. One can see that indeed fine structure is introduced by the modulations. However, the exact shape of the underlying dispersion is important. And since the cyclic exchange is not included so far, the precise positions of the new peaks are about to change. But a clear tendency can be seen. The higher the wave vector of the modulation, the higher is the frequency of the induced structure, which is apparent

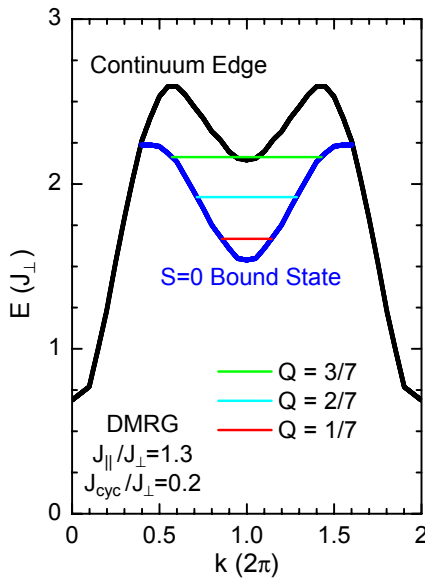


Figure 6.11: $S = 0$ bound state and lower edge of the two-triplet continuum, according to the unmodulated DMRG results of Nunner et al. [26]. Some exemplary modulation wave vectors are included. Wherever these vectors link equal energies of the dispersion of the bound state, gaps will open. Effects in which the continuum participates are more complex. The wave vectors $Q = 3/7$ and $1/7$ stem from the structural modulation of the ladders, whereas $Q = 2/7$ is due to the additional charge order in the chains.

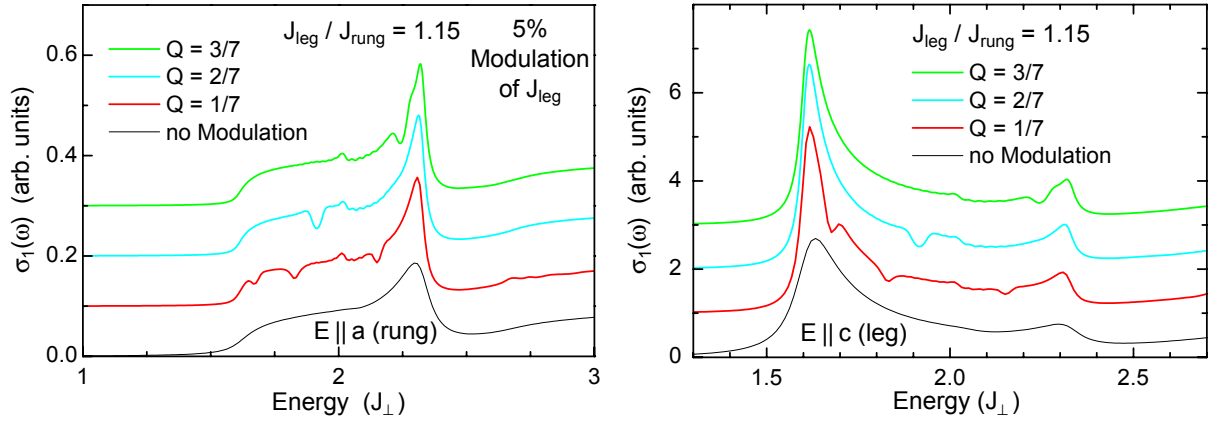


Figure 6.12: Preliminary results for the optical conductivity in the bound-state range as calculated by Schmidt and Uhrig using CUT. A 5% modulation of J_{\parallel} with the three different wave vectors is included for $E \parallel a$ (left) and $E \parallel c$ (right). The unmodulated spectra are shown as thin black lines. For readability the spectra are shifted with respect to each other. There is no J_{cyc} included so far.

from figure 6.11. Therefore the structural modulation with $Q = 3/7$ causes new features only close to the upper bound-state peak. The charge-order modulation is responsible for the peaks in-between the main peaks, and the overtone with $Q = 1/7$ of the structural modulation produces features over the whole range of the main peaks.

However, there is no influence on the line shape below the lower main peak. But we do observe a new peak within that region in $\text{Sr}_{14}\text{Cu}_{24}\text{O}_{41}$ and in $\text{Sr}_{11}\text{Ca}_3\text{Cu}_{24}\text{O}_{41}$ (see figures 6.9 and 6.10). So we are lead to search for further explanations. We cannot rule out that a certain amount of holes is present in the ladders. Nücker et al. found 0.8 holes in the ladders per formula unit in $\text{Sr}_{14}\text{Cu}_{24}\text{O}_{41}$ at room temperature [9] (see figure 2.28). Low-temperature x-ray absorption data is unfortunately not available so far. Thus it is interesting to ask what kind of impact doped holes have on the magnetic excitations. Troyer et al. studied the properties of lightly doped ladders by means of exact diagonalization of clusters with 20 sites [239]. They found evidence of hole pairing and a modified d -wave RVB state in agreement with e.g. the mean-field study of Sigrist et al. [4]. This pairing is responsible for the theoretically predicted occurrence of superconductivity. The basic mechanism of such pairing of holes can easily be visualized in the strong-coupling limit. When a single hole is introduced into the ladder, it breaks up a singlet and leaves an unpaired spin next to the hole on the same rung. If there are two holes nearby, they can share a common rung and thus reduce the number of broken spin singlets.

Apart from the triplet dispersion that continuously evolves away from the undoped spin liquid, Troyer et al. find a new type of triplet excitation that involves the breakup of a hole pair. A possible sketch of such an excitation is attempted in figure 6.13. In the upper panel the holes reside on neighboring rungs, which is expected for an isotropic ladder [239]. This is in contrast to the limit of $J_{\perp} \gg J_{\parallel}$, where both holes reside on the same rung. A singlet is formed by the remaining spins. During the new excitation the holes become unbound, and a triplet is excited. Interestingly, this excitation is lower in

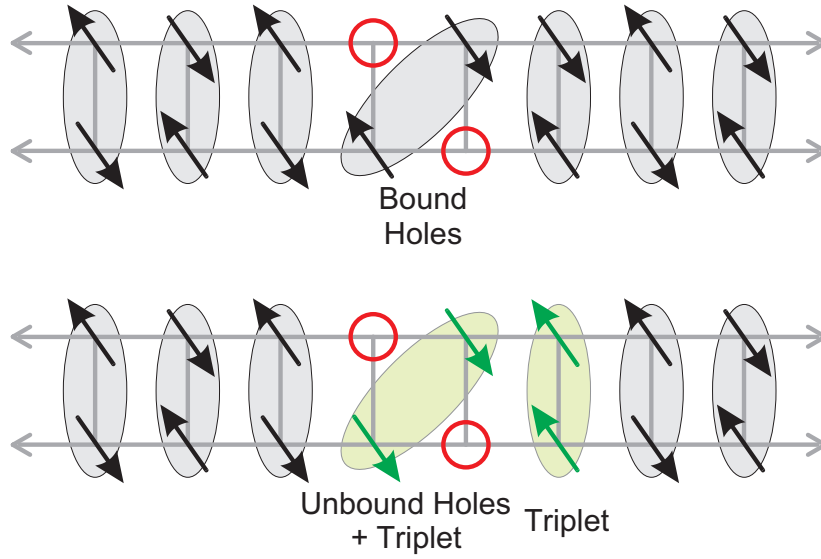


Figure 6.13: Possible sketch of the new low-energy excitation in lightly doped ladders. The **top** panel shows a bound pair of holes on adjacent rungs, which is expected for the isotropic ladder [239]. The other two spins on these rungs build a singlet. In the **bottom** panel this singlet is excited to a triplet, and at the same time the holes become unbound. For excitation with light it is necessary to create another triplet in order to obtain $S = 0$.

energy than a “purely magnetic” triplet excitation, where the holes are not involved [239]. This does not only hold in the strong coupling limit but also all the way up to isotropic couplings $J_{\parallel}/J_{\perp} = 1$. A second triplet is needed for infrared absorption in order to obtain $S = 0$ (bottom panel).

The two types of triplet excitations have different contributions to the dynamical structure factor. Most of the weight stems from the conventional triplet branch, and there is very little weight in the low-energy excitation [239]. This scenario might explain the spectra of $\text{Sr}_{14}\text{Cu}_{24}\text{O}_{41}$ and $\text{Sr}_{11}\text{Ca}_3\text{Cu}_{24}\text{O}_{41}$ (figures 6.9 and 6.10). We mainly see the same signature of the bound states as in the undoped ladders. The additional fine structure might partially be explained by modulation effects. But at least the low-energy peaks at $\approx 1810 \text{ cm}^{-1}$ in $\text{Sr}_{14}\text{Cu}_{24}\text{O}_{41}$ and $\approx 1870 \text{ cm}^{-1}$ in $\text{Sr}_{11}\text{Ca}_3\text{Cu}_{24}\text{O}_{41}$ for $E||a$ can most likely not be attributed to the modulation. We speculate that the new low-energy mode might be a candidate for this feature. Further calculations are necessary to verify this idea.

Finally, also an interpretation in terms of phonons cannot be ruled out. If the splitting of the lower bound-state peak is due to the contribution of different phonon modes, then it is possible that contributions involving lower-energy phonons give rise to the weak features below the main peaks. Note that a superposition of contributions from different phonons will smear out features caused by modulation effects.

Summary: In the following the main findings in the mid-infrared spectra of doped telephone-number compounds are outlined.

- The lower bound-state peak for $E||c$ becomes a sharp double peak in $\text{Sr}_{14}\text{Cu}_{24}\text{O}_{41}$ and $\text{Sr}_{11}\text{Ca}_3\text{Cu}_{24}\text{O}_{41}$. In $\text{La}_1\text{Sr}_{13}\text{Cu}_{24}\text{O}_{41}$ a precursor of such splitting is present.

- This might be due to modulation effects stemming (i) from charge order in the chains or (ii) from the incommensurate crystal structure. In the La-substituted compounds there is no charge order, and the crystal structure is disordered.
- Another possible explanation is that the *two* relevant phonons for $E||c$ produce the two peaks. In the La-substituted compounds the disordered structure broadens this double peak.
- The lower bound-state peak also splits in two for $E||a$ in $\text{Sr}_{14}\text{Cu}_{24}\text{O}_{41}$ and $\text{Sr}_{11}\text{Ca}_3\text{Cu}_{24}\text{O}_{41}$, although not as spectacular as for $E||c$.
 - Again modulation effects or a second relevant phonon might explain this feature.
- The additional fine structure below the bound state for $E||a$ in $\text{Sr}_{14}\text{Cu}_{24}\text{O}_{41}$ and $\text{Sr}_{11}\text{Ca}_3\text{Cu}_{24}\text{O}_{41}$ might stem from the low-energy mode described by Troyer et al. [239], but also a phononic origin cannot be ruled out.
- In $\text{Sr}_{14}\text{Cu}_{24}\text{O}_{41}$ there is a small peak in-between the bound-state peaks, which can possibly be explained by modulation effects.
- The low-temperature feature in $\text{Sr}_{14}\text{Cu}_{24}\text{O}_{41}$ at $\approx 1600 \text{ cm}^{-1}$ for $E||a$
 - might be due to localized polaronic charge carriers as in very low-doped YBCO
 - or to the low-energy mode described by Troyer et al. [239].
- The electronic background increases from $\text{La}_y\text{Ca}_{14-y}\text{Cu}_{24}\text{O}_{41}$ to $\text{Sr}_{14}\text{Cu}_{24}\text{O}_{41}$ to $\text{Sr}_{11}\text{Ca}_3\text{Cu}_{24}\text{O}_{41}$. Nevertheless, at 4 K there always remains a gap for electronic excitations of $\Delta \geq 100 \text{ meV}$.
- From the positions of the bound-state peaks we estimated the coupling constants.

Chapter 7

Conclusions

Within the scope of this thesis the mid- and near-infrared absorption of undoped and doped telephone-number compounds $(\text{Sr},\text{La},\text{Ca})_{14}\text{Cu}_{24}\text{O}_{41}$ was measured in the range between 600 and 12 000 cm^{-1} , which corresponds to wavelengths from 17 to 0.8 μm . This study presents the first determination of the magnetic contribution to the optical conductivity of spin ladders. A comparison between experiment and new theoretical calculations provides a comprehensive understanding of the magnetic spectrum of the undoped compounds.

A Fourier spectrometer was put into operation. To be able to study the weak magnetic contribution to the spectra, it was necessary to measure not only the reflectance but in particular the transmittance of thin samples. When both quantities are available for a given frequency, it is directly possible to calculate the optical conductivity without the use of Kramers-Kronig transforms. Although the samples are highly insulating, sample thicknesses of down to 6 μm had to be prepared. This was necessary in order to allow for the subtraction of the electronic background, which becomes apparent in the mid-infrared range.

The reflectance spectrum of the (almost) undoped sample of $\text{La}_4\text{Ca}_{10}\text{Cu}_{24}\text{O}_{41}$ is rather featureless as is common for the weak-absorption regime below the gap of an insulator. A strong phonon peak is apparent in the low-frequency part of the spectrum. But there are no indications of any magnetic excitations, which demonstrates that reflectance measurements with subsequent Kramers-Kronig analysis are not appropriate to reveal very weak absorption features. In contrast, the transmittance data shows a lot of structure and strongly depends on the temperature as well as on the polarization of the light.

The derived magnetic contribution to the optical conductivity of $\text{La}_y\text{Ca}_{14-y}\text{Cu}_{24}\text{O}_{41}$ at 4 K was clearly reproduced by three different theoretical approaches in the frame of phonon-assisted two-triplet absorption. The group of Uhrig et al. from the University of Cologne used continuous unitary transformations (CUT), whereas the group of Kopp et al. from the University of Augsburg performed both a Jordan-Wigner calculation and a density-matrix-renormalization-group (DMRG) study. The excellent agreement between theory and experiment allows to attribute the two main peaks between 2000 and 3000 cm^{-1} to a bound state of two triplets. There is a resemblance to the undoped 2D cuprates, which show a single sharp peak in the same frequency range that stems from an *almost* bound state. In the spin ladders *true* bound states were already predicted by several groups, but we were able to present the first experimental verification.

In the 2D cuprates there is a high-frequency contribution which still causes discussion. However, a similar feature in the undoped spin ladders could unambiguously be attributed to a multi-triplet continuum by comparison with the mentioned theoretical calculations. The DMRG study also incorporated a cyclic exchange, that proved to be important to reproduce the complete line shape of the infrared absorption and the spin gap measured by neutron scattering at the same time. We were also able to deduce the proper set of coupling constants. The inclusion of the cyclic exchange into the CUT calculations by Schmidt et al. from the Cologne theory group is currently in progress, and preliminary results are quite similar to the DMRG data of Nunner et al. from the Augsburg group.

With increasing temperature the line shape of the spectra changes considerably. The spectral weight of the continuum strongly increases with temperature, whereas the bound-state peaks lose some weight. This effect is more pronounced for polarization of the light along the leg direction. At 300 K the data resembles the DMRG result of Nunner et al. for an $S = 1$ Haldane chain, which illustrates the close relation between the two model systems. Good agreement with the experimental data at room temperature is also obtained by increasing the relative weight of the out-of-phase contribution to the DMRG results of the $S = 1/2$ ladder. A motivation of this resemblance has been discussed.

The other main part of this thesis was to examine the influence of doping on the infrared spectra of the telephone-number compounds. $\text{Sr}_{14}\text{Cu}_{24}\text{O}_{41}$ was measured, which is intrinsically doped with nominally six holes per formula unit. Yet the holes are expected to reside mainly within the chains of the composite crystals. The major features of the undoped samples can still be observed, but there is an increased electronic background, and additional peaks are present. For polarization along the legs, e.g. the lower bound-state peak is split in two sharp peaks. The same holds for the polarization along the rungs, but the splitting is not as pronounced. For this polarization, a new peak evolves between the lower and the upper bound-state peak, and there are new features below the bound-state peaks.

Several scenarios have been discussed to explain the additional structure. Modulations of the exchange coupling in the ladders due to the incommensurate structure and the charge ordering in the chains nicely explain the difference in the Raman spectra of $\text{Sr}_{14}\text{Cu}_{24}\text{O}_{41}$ and $\text{La}_6\text{Ca}_8\text{Cu}_{24}\text{O}_{41}$. The same mechanism might account for some of the new peaks, namely the splitting of the lower bound-state peak and the structure between both bound-state peaks. The features below the bound state cannot be attributed to modulation effects, and we speculate that a predicted new kind of excitation in lightly-doped ladders might be a candidate. This might also explain the broad absorption feature around 1600 cm^{-1} , which so far is only verified in $\text{Sr}_{14}\text{Cu}_{24}\text{O}_{41}$ for polarization along the rungs. A similar feature in lightly doped $\text{YBa}_2\text{Cu}_3\text{O}_{6+\delta}$ has been attributed to localized polaronic charge carriers. Also the influence of disorder in the crystal structure of $\text{La}_y\text{Ca}_{14-y}\text{Cu}_{24}\text{O}_{41}$ and of the second phonon mode involved in the absorption process for polarization along the legs has been discussed. However, a comprehensive understanding of the phenomena observed in the doped ladders requires further investigations.

Outlook

Recent measurements of $\text{Sr}_{11}\text{Ca}_3\text{Cu}_{24}\text{O}_{41}$ performed in our group by Puchalla show structures very similar to those of $\text{Sr}_{14}\text{Cu}_{24}\text{O}_{41}$. Precursors of the overall sharpening of the

features as compared to the undoped compounds were found also in the intermediate system $\text{La}_1\text{Sr}_{13}\text{Cu}_{24}\text{O}_{41}$. This compound was also measured by Puchalla, and the results will soon be presented in his *Diplomarbeit*. A first analysis of the positions of the bound-state peaks in the Sr-substituted compounds yields basically the same value of the cyclic exchange as in the undoped compounds. Also the coupling along the rungs is unchanged, but the leg coupling increases slightly.

Calculations by Schmidt et al. are currently in progress to incorporate the cyclic exchange as well as the modulation of the exchange coupling into the CUT approach. Preliminary results of the theoretical spectra are promising, but only the final results will allow to verify which of the new peaks stem from modulation effects.

For the future, measurements are planned on the development of the continuum contribution in the Sr-substituted telephone-number compounds. Since the background is large, very thin samples with thicknesses of less than $10\text{ }\mu\text{m}$ have to be prepared. For the study of samples of $\text{Sr}_{14-x}\text{Ca}_x\text{Cu}_{24}\text{O}_{41}$, the transmittance is probably not measurable anymore since the absorption becomes too large. This is due to the vanishing charge order in these samples. Other compounds currently under investigation are the spin-ladder compound SrCu_2O_3 and the corrugated spin-ladder CaCu_2O_3 .

References

The numbers at the end of each entry refer to the corresponding pages of occurrence.

- [1] E. Manousakis, “The spin-1/2 Heisenberg antiferromagnet on a square lattice and its application to the cuprous oxides”, *Rev. Mod. Phys.* **63**, 1 (1991). 3
- [2] E. Dagotto, and T.M. Rice, “Surprises on the Way from One- to Two-Dimensional Quantum Magnets: The Ladder Materials”, *Science* **271**, 618 (1996). 3, 24, 48, 131
- [3] E. Dagotto, J. Riera, and D. Scalapino, “Superconductivity in ladders and coupled planes”, *Phys. Rev. B* **45**, 5744 (1992). 4, 5, 24, 48
- [4] M. Sigrist, T.M. Rice, and F.C. Zhang, “Superconductivity in a quasi-one-dimensional spin liquid”, *Phys. Rev. B* **49**, 12058 (1994). 4, 153
- [5] M. Uehara, T. Nagata, J. Akimitsu, H. Takahashi, N. Môri, and K. Kinoshita, “Superconductivity in the Ladder Material $\text{Sr}_{0.4}\text{Ca}_{13.6}\text{Cu}_{24}\text{O}_{41.84}$ ”, *J. Phys. Soc. Jpn.* **65**, 2764 (1996). 4, 36, 44, 131
- [6] U. Ammerahl, G. Dhalenne, A. Revcolevschi, J. Berthon, and H. Moudden, “Crystal growth and characterization of the spin-ladder compound $(\text{Sr,Ca})_{14}\text{Cu}_{24}\text{O}_{41}$ ”, *J. Crystal Growth* **193**, 55 (1998). 4, 36, 39, 80
- [7] U. Ammerahl, and A. Revcolevschi, “Crystal growth of the spin-ladder compound $(\text{Ca,Lu})_{14}\text{Cu}_{24}\text{O}_{41}$ and observation of one-dimensional disorder”, *J. Crystal Growth* **197**, 825 (1999). 4, 36, 41, 80, 93, 140
- [8] U. Ammerahl, *Einkristallherstellung und physikalische Eigenschaften niedrigdimensionaler Kuprate*, PhD Thesis, GCA-Verlag, Herdecke (2000). 4, 36, 39, 41, 80, 81
- [9] N. Nücker, M. Merz, C.A. Kuntscher, S. Gerhold, S. Schuppler, R. Neudert, M.S. Golden, J. Fink, D. Schild, S. Stadler, V. Chakarian, J. Freeland, Y.U. Idzerda, K. Conder, M. Uehara, T. Nagata, J. Goto, J. Akimitsu, N. Motoyama, H. Eisaki, S. Uchida, U. Ammerahl, and A. Revcolevschi, “Hole distribution in $(\text{Sr,Ca,Y,Lu})_{14}\text{Cu}_{24}\text{O}_{41}$ ladder compounds studied by x-ray absorption spectroscopy”, *Phys. Rev. B* **62**, 14384 (2000). 4, 23, 40, 47, 93, 139, 153
- [10] V. Kataev, K.-Y. Choi, M. Grüninger, U. Ammerahl, B. Büchner, A. Freimuth, and A. Revcolevschi, “Interplay of spin and charge dynamics in $\text{Sr}_{14-x}\text{Ca}_x\text{Cu}_{24}\text{O}_{41}$ ”, *Phys. Rev. B* **64**, 104422 (2001). 4, 41, 43, 141
- [11] J. Lorenzana, and G.A. Sawatzky, “Phonon Assisted Multimagnon Optical Absorption and Long Lived Two-Magnon States in Undoped Lamellar Copper Oxides”, *Phys. Rev. Lett.* **74**, 1867 (1995). 4, 31, 57, 58, 59, 60, 61, 91, 107, 120, 126
- [12] J. Lorenzana, and G.A. Sawatzky, “Theory of phonon-assisted multimagnon optical absorption and bimagnon states in quantum antiferromagnets”, *Phys. Rev. B* **52**, 9576 (1995). 4, 31, 57, 58, 59, 60, 61, 91, 107, 120, 126

- [13] J.D. Perkins, J.M. Graybeal, M.A. Kastner, R.J. Birgeneau, J.P. Falck, and M. Greven, “Mid-Infrared Optical Absorption in Undoped Lamellar Copper Oxides”, *Phys. Rev. Lett.* **71**, 1621 (1993). 4, 57, 58, 59
- [14] M. Grüninger, D. van der Marel, A. Damascelli, A. Erb, T. Nunner, and T. Kopp, “Mid-infrared absorption in $\text{YBa}_2\text{Cu}_3\text{O}_6$: Evidence for a failure of spin-wave theory for spin $1/2$ in two dimensions”, *Phys. Rev. B* **62**, 12422 (2000). 4, 57, 58, 59, 61, 93, 106, 107, 116, 120, 126
- [15] J. Lorenzana, J. Eroles, and S. Sorella, “Does the Heisenberg Model Describe the Multimagnon Spin Dynamics in Antiferromagnetic CuO Layers?”, *Phys. Rev. Lett.* **83**, 5122 (1999). 4, 59
- [16] D.G. Shelton, A.A. Nersesyan, and A.M. Tsvelik, “Antiferromagnetic spin ladders: Crossover between spin $S = 1/2$ and $S = 1$ chains”, *Phys. Rev. B* **53**, 8521 (1996). 5, 26, 87, 118
- [17] G.S. Uhrig, and H.J. Schulz, “Magnetic excitation spectrum of dimerized antiferromagnetic chains”, *Phys. Rev. B* **54**, R9624 (1996). Erratum, *Phys. Rev. B* **58**, 2900 (1998). 5, 20, 87
- [18] K. Damle, and S. Sachdev, “Spin dynamics and transport in gapped one-dimensional Heisenberg antiferromagnets at nonzero temperatures”, *Phys. Rev. B* **57**, 8307 (1998). 5, 87, 89
- [19] O.P. Sushkov, and V.N. Kotov, “Bound States of Magnons in the $S = 1/2$ Quantum Spin Ladder”, *Phys. Rev. Lett.* **81**, 1941 (1998). 5, 87, 89, 90, 91
- [20] V.N. Kotov, O.P. Sushkov, and R. Eder, “Excitation spectrum of the $S = 1/2$ quantum spin ladder with frustration: Elementary quasiparticles and many-particle bound states”, *Phys. Rev. B* **59**, 6266 (1999). 5, 87, 90
- [21] C. Jurecka, and W. Brenig, “Optical absorption of spin ladders”, *Phys. Rev. B* **61**, 14307 (2000). 5, 87, 91, 92, 93
- [22] S. Trebst, H. Monien, C.J. Hamer, Z. Weihong, and R.R.P. Singh, “Strong-Coupling Expansions for Multiparticle Excitations: Continuum and Bound States”, *Phys. Rev. Lett.* **85**, 4373 (2000). 5, 87, 90
- [23] W. Zheng, C.J. Hamer, R.R.P. Singh, S. Trebst, and H. Monien, “Linked cluster series expansions for two-particle bound states”, *Phys. Rev. B* **63**, 144410 (2001). 5, 87, 90, 91
- [24] M. Windt, M. Grüninger, T. Nunner, C. Knetter, K.P. Schmidt, G.S. Uhrig, T. Kopp, A. Freimuth, U. Ammerahl, B. Büchner, and A. Revcolevschi, “Observation of Two-Magnon Bound States in the Two-Leg Ladders of $(\text{Ca}, \text{La})_{14}\text{Cu}_{24}\text{O}_{41}$ ”, *Phys. Rev. Lett.* **87**, 127002 (2001). 5, 87, 107, 109, 110, 112, 117, 118, 120, 123, 124
- [25] M. Matsuda, K. Katsumata, R.S. Eccleston, S. Brehmer, and H.-J. Mikeska, “Magnetic excitations and exchange interactions in the spin- $1/2$ two-leg ladder compound $\text{La}_6\text{Ca}_8\text{Cu}_{24}\text{O}_{41}$ ”, *Phys. Rev. B* **62**, 8903 (2000). 5, 32, 33, 104, 125, 126, 128, 151, 152
- [26] T.S. Nunner, P. Brune, T. Kopp, M. Windt, and M. Grüninger, “Cyclic Spin Exchange in Cuprate Spin Ladders”, *Phys. Rev. B* **66**, 180404(R) (2002). 5, 32, 33, 87, 118, 119, 126, 127, 128, 129, 130, 131, 136, 142, 151, 152
- [27] G.S. Uhrig, and M. Grüninger, “Das Wechselspiel magnetischer Anregungen in Spinflüssigkeiten”, *Physik Journal* **2**, 41 (2003). 5, 9, 14, 20, 21
- [28] Copied from <http://www.leitern.de>, home page of Beckmann-Steigtechnik, Bad Salzuffen, Germany. 5

- [29] L.J. de Jongh, ed., *Magnetic Properties of Layered Transition Metal Compounds*, Kluwer Academic Publishers, Dordrecht (1990). 7, 10
- [30] F. Boersma, W.J.M. de Jonge, and K. Kopinga, “Anisotropic classical chain: Numerical calculations of thermodynamic properties”, *Phys. Rev. B* **23**, 186 (1981). 7, 8
- [31] V. Kataev, K.-Y. Choi, M. Grüninger, U. Ammerahl, B. Büchner, A. Freimuth, and A. Revcolevschi, “Strong Anisotropy of Superexchange in the Copper-Oxygen Chains of $\text{La}_{14-x}\text{Ca}_x\text{Cu}_{24}\text{O}_{41}$ ”, *Phys. Rev. Lett.* **86**, 2882 (2001). 8
- [32] L.J. de Jongh, and R. Block, “On the Exchange Interactions in some 3d-Metal Ionic Compounds”, *Physica B* **79**, 568 (1975). 8
- [33] P.W. Anderson, “Theory of Magnetic Exchange Interactions: Exchange in Insulators and Semiconductors”, *Solid State Physics* **14**, 99 (1963). 8, 37
- [34] J.M. Ricart, R. Dovesi, C. Roetti, and V.R. Saunders, “Electronic and magnetic structure of KNiF_3 perovskite”, *Phys. Rev. B* **52**, 2381 (1995). 9
- [35] N.W. Ashcroft, and N.D. Mermin, *Solid State Physics*, Saunders College Publishing (1976). 9, 52
- [36] G.S. Uhrig, *Niedrigdimensionale Spinsysteme und Spin-Phonon-Kopplung*, Habilitationsschrift, Universität zu Köln (1999). 9, 12, 13, 14
- [37] A. Auerbach, *Interacting Electrons and Quantum Magnetism*, Springer-Verlag, New York (1994). 9
- [38] L. Onsager, “A Two-Dimensional Model with an Order-Disorder Transition”, *Phys. Rev.* **65**, 117 (1944). 10
- [39] N.D. Mermin, and H. Wagner, “Absence of Ferromagnetism or Antiferromagnetism in One- or Two-Dimensional Isotropic Heisenberg Models”, *Phys. Rev. Lett.* **17**, 1133 (1966). 10
- [40] P.C. Hohenberg, “Existence of Long-Range Order in One and Two Dimensions”, *Phys. Rev.* **158**, 383 (1967). 10, 45
- [41] E. Dagotto, and A. Moreo, “Zero-temperature properties of the two-dimensional Heisenberg antiferromagnet: A numerical study”, *Phys. Rev. B* **38**, 5087 (1988). 10
- [42] J.M. Kosterlitz, and D.J. Thouless, “Ordering, metastability and phase transitions in two-dimensional systems”, *J. Phys. C* **6**, 1181 (1973). 10
- [43] J.M. Kosterlitz, “The critical properties of the two-dimensional xy model”, *J. Phys. C* **7**, 1046 (1974). 10
- [44] M.E. Fisher, “The theory of equilibrium critical phenomena”, *Rep. Prog. Phys.* **30**, 615 (1967). 10
- [45] M. Boninsegni, “Ground state of a triangular quantum antiferromagnet: Fixed-node Green-function Monte Carlo study”, *Phys. Rev. B* **52**, 15304 (1995). 11
- [46] P. Lecheminant, B. Bernu, C. Lhuillier, L. Pierre, and P. Sindzingre, “Order versus disorder in the quantum Heisenberg antiferromagnet on the *kagomé* lattice using exact spectra analysis”, *Phys. Rev. B* **56**, 2521 (1997). 11
- [47] C. Waldtmann, H.-U. Everts, B. Bernu, C. Lhuillier, P. Sindzingre, P. Lecheminant, and L. Pierre, “First excitations of the spin 1/2 Heisenberg antiferromagnet on the *kagomé* lattice”, *Eur. Phys. J. B* **2**, 501 (1998). 11
- [48] P.W. Anderson, “Resonating Valence Bonds: A New Kind of Insulator?”, *Mat. Res. Bull.* **8**, 153 (1973). 11
- [49] P.W. Anderson, “The Resonating Valence Bond State in La_2CuO_4 and Superconductivity”, *Science* **235**, 1196 (1987). 11

- [50] S. Liang, B. Doucot, and P.W. Anderson, “Some New Variational RVB-Type Wave Functions for the Spin-1/2 Antiferromagnetic Heisenberg Model on a Square Lattice”, *Phys. Rev. Lett.* **61**, 365 (1988). 11, 12
- [51] H. Bethe, “Eigenwerte und Eigenfunktionen der linearen Atomkette”, *Z. Phys.* **71**, 205 (1931). 13
- [52] R. Orbach, “Linear Antiferromagnetic Chain with Anisotropic Coupling”, *Phys. Rev.* **112**, 309 (1958). 13
- [53] L. Hulthén, “Über das Austauschproblem eines Kristalles”, *Arkiv för Matematik, Astronomi och Fysik* **26A**, 1 (1939). 13
- [54] C.K. Majumdar, and D.K. Ghosh, “On Next-Nearest-Neighbor Interaction in Linear Chain. I”, *J. Math. Phys.* **10**, 1388 (1969). 13
- [55] C.K. Majumdar, and D.K. Ghosh, “On Next-Nearest-Neighbor Interaction in Linear Chain. II”, *J. Math. Phys.* **10**, 1399 (1969). 13
- [56] C.K. Majumdar, “Antiferromagnetic model with known ground state”, *J. Phys. C* **3**, 911 (1970). 13
- [57] I. Affleck, T. Kennedy, E.H. Lieb, and H. Tasaki, “Valence Bond Ground States in Isotropic Quantum Antiferromagnets”, *Commun. Math. Phys.* **115**, 477 (1988). 13
- [58] P.M. van den Broek, “Exact value of the ground state energy of the linear antiferromagnetic Heisenberg chain with nearest and next-nearest neighbor interactions”, *Phys. Lett.* **77A**, 261 (1980). 13
- [59] K. Okamoto, and K. Nomura, “Fluid-dimer critical point in $S = 1/2$ antiferromagnetic Heisenberg chain with next nearest neighbor interactions”, *Phys. Lett. A* **169**, 433 (1992). 13
- [60] S. Eggert, “Numerical evidence for multiplicative logarithmic corrections from marginal operators”, *Phys. Rev. B* **54**, R9612 (1996). 13
- [61] J. des Cloizeaux, and J.J. Pearson, “Spin-Wave Spectrum of the Antiferromagnetic Linear Chain”, *Phys. Rev.* **128**, 2131 (1962). 13, 14, 15
- [62] L.D. Faddeev, and L.A. Takhtajan, “What is the spin of a spin wave?”, *Phys. Lett.* **85A**, 375 (1981). 13
- [63] N. Andrei, and J.H. Lowenstein, “Diagonalization of the Chiral-Invariant Gross-Neveu Hamiltonian”, *Phys. Rev. Lett.* **43**, 1698 (1979). 13
- [64] F.D.M. Haldane, “Nonlinear Field Theory of Large-Spin Heisenberg Antiferromagnets: Semiclassically Quantized Solitons of the 1D Easy-Axis Néel State”, *Phys. Rev. Lett.* **50**, 1153 (1983). 13, 16
- [65] R. Moessner, and S.L. Sondhi, “Resonating Valence Bond Phase in the Triangular Lattice Quantum Dimer Model”, *Phys. Rev. Lett.* **86**, 1881 (2001). 14
- [66] M. Karbach, G. Müller, A.H. Bougourzi, A. Fledderjohann, and K.-H. Mütter, “Two-spinon dynamic structure factor of the one-dimensional $s = 1/2$ Heisenberg antiferromagnet”, *Phys. Rev. B* **55**, 12510 (1997). 15, 16
- [67] M.T. Hutchings, E.J. Samuelsen, and G. Shirane, “Neutron-Diffraction Determination of the Antiferromagnetic Structure of KCuF_3 ”, *Phys. Rev.* **188**, 919 (1969). 16
- [68] S.E. Nagler, D.A. Tennant, R.A. Cowley, T.G. Perring, and S.K. Satija, “Spin dynamics in the quantum antiferromagnetic chain compound KCuF_3 ”, *Phys. Rev. B* **44**, 12361 (1991). 16

- [69] M.T. Hutchings, G. Shirane, R.J. Birgeneau, and S.L. Holt, “Spin Dynamics in the One-Dimensional Antiferromagnet $(\text{CD}_3)_4\text{NMnCl}_3$ ”, *Phys. Rev. B* **5**, 1999 (1972). 16
- [70] D.A. Tennant, T.G. Perring, R.A. Cowley, and S.E. Nagler, “Unbound Spinons in the $S = 1/2$ Antiferromagnetic Chain KCuF_3 ”, *Phys. Rev. Lett.* **70**, 4003 (1993). 16, 17
- [71] H.J. Schulz, “Phase diagrams and correlation exponents for quantum spin chains of arbitrary spin quantum number”, *Phys. Rev. B* **34**, 6372 (1986). 16
- [72] E. Lieb, T. Schultz, and D. Mattis, “Two Soluble Models of an Antiferromagnetic Chain”, *Annals Phys.* **16**, 407 (1961). 17
- [73] I. Affleck, T. Kennedy, E.H. Lieb, and H. Tasaki, “Rigorous results on valence-bond ground states in antiferromagnets”, *Phys. Rev. Lett.* **59**, 799 (1987). 17
- [74] A.W. Garrett, S.E. Nagler, D.A. Tennant, B.C. Sales, and T. Barnes, “Magnetic Excitations in the $S = 1/2$ Alternating Chain Compound $(\text{VO})_2\text{P}_2\text{O}_7$ ”, *Phys. Rev. Lett.* **79**, 745 (1997). 17, 18, 36
- [75] A.V. Prokofiev, F. Bülesfeld, W. Assmus, H. Schwenk, D. Wichert, U. Löw, and B. Lüthi, “Magnetic properties of the low dimensional spin system $(\text{VO})_2\text{P}_2\text{O}_7$: ESR and susceptibility”, *Eur. Phys. J B* **5**, 313 (1998). 17
- [76] D.C. Johnston, J.W. Johnson, D.P. Goshorn, and A.J. Jacobson, “Magnetic susceptibility of $(\text{VO})_2\text{P}_2\text{O}_7$: A one-dimensional spin-1/2 Heisenberg antiferromagnet with a ladder spin configuration and a singlet ground state”, *Phys. Rev. B* **35**, 219 (1987). 17
- [77] R.S. Eccleston, T. Barnes, J. Brody, and J.W. Johnson, “Inelastic Neutron Scattering from the Spin Ladder Compound $(\text{VO})_2\text{P}_2\text{O}_7$ ”, *Phys. Rev. Lett.* **73**, 2626 (1994). 17
- [78] T. Barnes, and J. Riera, “Susceptibility and excitation spectrum of $(\text{VO})_2\text{P}_2\text{O}_7$ in ladder and dimer-chain models”, *Phys. Rev. B* **50**, 6817 (1994). 17, 30, 34, 35, 87
- [79] A.W. Garrett, S.E. Nagler, T. Barnes, and B.C. Sales, “Neutron-scattering study of magnetic excitations in $(\text{VO})_2\text{P}_2\text{O}_7$ ”, *Phys. Rev. B* **55**, 3631 (1997). 17
- [80] R. Valenti, and T. Saha-Dasgupta, “Electronic and magnetic structure of CsV_2O_5 ”, *Phys. Rev. B* **65**, 144445 (2002). 17
- [81] H. Manaka, I. Yamada, M. Tokunaga, T. Yasuhira, and N. Miura, “Magnetization process of the alternating Heisenberg chains with ferromagnetic and antiferromagnetic interactions formed in $(\text{CH}_3)_2\text{CHNH}_3\text{CuCl}_3$ ”, *Physica B* **246-247**, 513 (1998). 17
- [82] N. Elstner, and R.R.P. Singh, “Field-dependent thermodynamics and quantum critical phenomena in the dimerized spin system $\text{Cu}_2(\text{C}_5\text{H}_{12}\text{N}_2)_2\text{Cl}_4$ ”, *Phys. Rev. B* **58**, 11484 (1998). 17, 18
- [83] D.C. Johnston, R.K. Kremer, M. Troyer, X. Wang, A. Klümper, S.L. Bud’ko, A.F. Panchula, and P.C. Canfield, “Thermodynamics of spin $S = 1/2$ antiferromagnetic uniform and alternating-exchange Heisenberg chains”, *Phys. Rev. B* **61**, 9558 (2000). 18
- [84] M. Aïn, J.E. Lorenzo, L.P. Regnault, G. Dhahlenne, A. Revcolevschi, B. Hennion, and T. Jolicoeur, “Double Gap and Solitonic Excitations in the Spin-Peierls Chain CuGeO_3 ”, *Phys. Rev. Lett.* **78**, 1560 (1997). 18, 21, 22
- [85] G. Castilla, S. Chakravarty, and V.J. Emery, “Quantum Magnetism of CuGeO_3 ”, *Phys. Rev. Lett.* **75**, 1823 (1995). 18, 19
- [86] J. Riera, and A. Dobry, “Magnetic susceptibility in the spin-Peierls system CuGeO_3 ”, *Phys. Rev. B* **51**, 16098 (1995). 18, 19
- [87] M.C. Cross, and D.S. Fisher, “A new theory of the spin-Peierls transition with special relevance to the experiments on TTFCuBDT ”, *Phys. Rev. B* **19**, 402 (1979). 18

- [88] J.L. Black, and V.J. Emery, “Critical properties of two-dimensional models”, *Phys. Rev. B* **23**, 429 (1981). 18
- [89] P. Jordan, and E. Wigner, “Über das Paulische Äquivalenzverbot”, *Z. Phys.* **47**, 631 (1928). 18, 117
- [90] M. Hase, I. Terasaki, and K. Uchinokura, “Observation of the Spin-Peierls Transition in Linear Cu^{2+} (Spin-1/2) Chains in an Inorganic Compound CuGeO_3 ”, *Phys. Rev. Lett.* **70**, 3651 (1993). 19, 38
- [91] T. Barnes, J. Riera, and D.A. Tennant, “ $S = 1/2$ alternating chain using multiprecision methods”, *Phys. Rev. B* **59**, 11384 (1999). 19
- [92] C. Knetter, and G.S. Uhrig, “Perturbation theory by flow equations: dimerized and frustrated $S = 1/2$ chain”, *Eur. Phys. J. B* **13**, 209 (2000). 19, 90, 118
- [93] A. Fledderjohann, and C. Gros, “Spin dynamics of dimerized Heisenberg chains”, *Europhys. Lett.* **37**, 189 (1997). 20
- [94] M. Arai, M. Fujita, M. Motokawa, J. Akimitsu, and S.M. Bennington, “Quantum Spin Excitations in the Spin-Peierls System CuGeO_3 ”, *Phys. Rev. Lett.* **77**, 3649 (1996). 21, 22
- [95] H. Kuroe, and T. Sekine, “Raman-scattering study of CuGeO_3 in the spin-Peierls phase”, *Phys. Rev. B* **50**, 16468 (1994). 21
- [96] G. Els, P.H.M. van Loosdrecht, P. Lemmens, H. Vonberg, G. Güntherodt, G.S. Uhrig, O. Fujita, J. Akimitsu, G. Dhalenne, and A. Revcolevschi, “Observation of Three-Magnon Light Scattering in CuGeO_3 ”, *Phys. Rev. Lett.* **79**, 5138 (1997). 21
- [97] G. Els, G.S. Uhrig, P. Lemmens, H. Vonberg, P.H.M. van Loosdrecht, G. Güntherodt, O. Fujita, J. Akimitsu, G. Dhalenne, and A. Revcolevschi, “Dopant-bound spinons in $\text{Cu}_{1-x}\text{Zn}_x\text{GeO}_3$ ”, *Europhys. Lett.* **43**, 463 (1998). 21, 22
- [98] M. Laukamp, G.B. Martins, C. Gazza, A.L. Malvezzi, E. Dagotto, P.M. Hansen, A.C. López, and J. Riera, “Enhancement of antiferromagnetic correlations induced by nonmagnetic impurities: Origin and predictions for NMR experiments”, *Phys. Rev. B* **57**, 10755 (1998). 22
- [99] G.S. Uhrig, F. Schöfeld, M. Laukamp, and E. Dagotto, “Unified quantum mechanical picture for confined spinons in dimerized and frustrated spin $S = 1/2$ chains”, *Eur. Phys. J. B* **7**, 67 (1999). 22
- [100] M. Hase, I. Terasaki, Y. Sasago, K. Uchinokura, and H. Obara, “Effects of Substitution of Zn for Cu in the Spin-Peierls Cuprate, CuGeO_3 : The Suppression of the Spin-Peierls Transition and the Occurrence of a New Spin-Glass State”, *Phys. Rev. Lett.* **71**, 4059 (1993). 22
- [101] S.B. Oseroff, S.-W. Cheong, B. Aktas, M.F. Hundley, Z. Fisk, and L.W. Rupp, Jr., “Spin-Peierls State versus Néel State in Doped CuGeO_3 ”, *Phys. Rev. Lett.* **74**, 1450 (1995). 22
- [102] B. Grenier, J.-P. Renard, P. Veillet, C. Paulsen, R. Calemczuk, G. Dhalenne, and A. Revcolevschi, “Magnetic susceptibility and phase diagram of $\text{CuGe}_{1-x}\text{Si}_x\text{O}_3$ single crystals”, *Phys. Rev. B* **57**, 3444 (1998). 22
- [103] B. Grenier, J.-P. Renard, P. Veillet, C. Paulsen, G. Dhalenne, and A. Revcolevschi, “Scaling in dimer breaking by impurities in CuGeO_3 : A comparative experimental study of Zn-, Mg-, Ni-, and Si-doped single crystals”, *Phys. Rev. B* **58**, 8202 (1998). 22

- [104] G.B. Martins, E. Dagotto, and J.A. Riera, “Rapid suppression of the spin gap in Zn-doped CuGeO_3 and SrCu_2O_3 ”, *Phys. Rev. B* **54**, 16032 (1996). 22
- [105] W.E. Pickett, “Electronic structure of the high-temperature oxide superconductors”, *Rev. Mod. Phys.* **61**, 433 (1989). 23
- [106] S. Uchida, T. Ido, H. Takagi, T. Arima, Y. Tokura, and S. Tajima, “Optical spectra of $\text{La}_{2-x}\text{Sr}_x\text{CuO}_4$: Effect of carrier doping on the electronic structure of the CuO_2 plane”, *Phys. Rev. B* **43**, 7942 (1991). 23, 47
- [107] T. Timusk, and D.B. Tanner, *Infrared Properties of High- T_c Superconductors*, in *Physical Properties of High Temperature Superconductors I*, edited by D. M. Ginsberg, World Scientific Publishing, Singapore (1989). 23
- [108] D.B. Tanner, and T. Timusk, *Optical Properties of High-Temperature Superconductors*, in *Physical Properties of High Temperature Superconductors III*, edited by D. M. Ginsberg, World Scientific Publishing, Singapore (1992). 23
- [109] F.C. Zhang, and T.M. Rice, “Effective Hamiltonian for the superconducting Cu oxides”, *Phys. Rev. B* **37**, 3759 (1988). 23, 41
- [110] M. Grüninger, *Of Spin and Charge in the Cuprates*, PhD Thesis, PrintPartners Ipskamp B.V., Enschede, Netherlands (1999), see also:
<http://www.ub.rug.nl/eldoc/dis/science/m.u.grueninger/index.html>. 23, 47, 55, 116, 144
- [111] J. Voit, “One-dimensional Fermi liquids”, *Rep. Prog. Phys.* **57**, 977 (1994). 23
- [112] T. Lorenz, M. Hofmann, M. Grüninger, A. Freimuth, G.S. Uhrig, M. Dumm, and M. Dressel, “Evidence for spin-charge separation in quasi-one-dimensional organic conductors”, *Nature* **418**, 614 (2002). 23
- [113] L.P. Regnault, J.P. Boucher, H. Moudden, J.E. Lorenzo, A. Hiess, U. Ammerahl, G. Dhalenne, and A. Revcolevschi, “Spin dynamics in the magnetic chain arrays of $\text{Sr}_{14}\text{Cu}_{24}\text{O}_{41}$: A neutron inelastic scattering investigation”, *Phys. Rev. B* **59**, 1055 (1999). 24, 41, 43, 140
- [114] E. Dagotto, “Experiments on ladders reveal a complex interplay between a spin-gapped normal state and superconductivity”, *Rep. Prog. Phys.* **62**, 1525 (1999). 24, 26, 30
- [115] T. Barnes, E. Dagotto, J. Riera, and E.S. Swanson, “Excitation spectrum of Heisenberg spin ladders”, *Phys. Rev. B* **47**, 3196 (1993). 25, 26, 33
- [116] M. Greven, R.J. Birgeneau, and U.-J. Wiese, “Monte Carlo Study of Correlations in Quantum Spin Ladders”, *Phys. Rev. Lett.* **77**, 1865 (1996). 26
- [117] S. Gopalan, T.M. Rice, and M. Sigrist, “Spin ladders with spin gaps: A description of a class of cuprates”, *Phys. Rev. B* **49**, 8901 (1994). 26, 27
- [118] S.R. White, R.M. Noack, and D.J. Scalapino, “Resonating Valence Bond Theory of Coupled Heisenberg Chains”, *Phys. Rev. Lett.* **73**, 886 (1994). 26, 27, 28, 29
- [119] M. Azuma, Z. Hiroi, and M. Takano, “Observation of a Spin Gap in SrCu_2O_3 Comprising Spin-1/2 Quasi-1D Two-Leg Ladders”, *Phys. Rev. Lett.* **73**, 3463 (1994). 27, 29, 30, 31, 33
- [120] Z. Hiroi, M. Azuma, M. Takano, and Y. Bando, “A New Homologous Series $\text{Sr}_{n-1}\text{Cu}_{n+1}\text{O}_{2n}$ Found in the SrO-CuO System Treated under High Pressure”, *J. Solid State Chem.* **95**, 230 (1991). 26, 27
- [121] T.M. Rice, S. Gopalan, and M. Sigrist, “Superconductivity, Spin Gaps and Luttinger Liquids in a Class of Cuprates”, *Europhys. Lett.* **23**, 445 (1993). 26

- [122] C. Sekar, T. Watanabe, and A. Matsuda, “Crystal growth and characterization of the 4-leg spin ladder compound $\text{La}_2\text{Cu}_2\text{O}_5$ ”, *J. Cryst. Growth* **212**, 142 (2000). 27
- [123] C. Sekar, T. Watanabe, A. Matsuda, H. Shibata, Y. Zenitani, and J. Akimitsu, “Crystal growth, structure, and transport properties of the five-leg spin ladder compound $\text{La}_8\text{Cu}_7\text{O}_{19}$ ”, *J. Sol. State Chem.* **156**, 422 (2001). 27
- [124] D. Poilblanc, H. Tsunetsugu, and T.M. Rice, “Spin gaps in coupled t - J ladders”, *Phys. Rev. B* **50**, 6511 (1994). 27
- [125] N. Hatano, and Y. Nishiyama, “Scaling theory of antiferromagnetic Heisenberg ladder models”, *J. Phys. A* **28**, 3911 (1995). 27
- [126] M. Reigrotzki, H. Tsunetsugu, and T.M. Rice, “Strong-coupling expansions for antiferromagnetic Heisenberg spin-1/2 ladders”, *J. Phys.: Condens. Matter* **6**, 9235 (1994). 28, 33
- [127] A.G. Rojo, “Absence of gap for infinite half-integer spin ladders with an odd number of legs”, *Phys. Rev. B* **53**, 9172 (1996). 28
- [128] F.D.M. Haldane, “O(3) Nonlinear σ Model and the Topological Distinction between Integer- and Half-Integer-Spin Antiferromagnets in Two Dimensions”, *Phys. Rev. Lett.* **61**, 1029 (1988). 28
- [129] D.V. Khveshchenko, “Singlet pairing in the double-chain t - J model”, *Phys. Rev. B* **50**, 380 (1994). 28
- [130] G. Sierra, M.A. Martín-Delgado, J. Dukelsky, S.R. White, and D.J. Scalapino, “Dimer-hole-RVB state of the two-leg t - J ladder: A recurrent variational ansatz”, *Phys. Rev. B* **57**, 11666 (1998). 28
- [131] R.M. Noack, S.R. White, and D.J. Scalapino, “Correlations in a Two-Chain Hubbard Model”, *Phys. Rev. Lett.* **73**, 882 (1994). 28
- [132] K. Kojima, A. Keren, G.M. Luke, B. Nachumi, W.D. Wu, Y.J. Uemura, M. Azuma, and M. Takano, “Magnetic Behavior of the 2-Leg and 3-Leg Spin Ladder Cuprates $\text{Sr}_{n-1}\text{Cu}_{n+1}\text{O}_{2n}$ ”, *Phys. Rev. Lett.* **74**, 2812 (1995). 28
- [133] D.C. Johnston, M. Troyer, S. Miyahara, D. Lidsky, K. Ueda, M. Azuma, Z. Hiroi, M. Takano, M. Isobe, Y. Ueda, M.A. Korotin, V.I. Anisimov, A.V. Mahajan, and L.L. Miller, “Magnetic Susceptibilities of Spin-1/2 Antiferromagnetic Heisenberg Ladders and Applications to Ladder Oxide Compounds”, *cond-mat/0001147* (2000). 29, 31, 33, 34, 35, 87, 88, 119, 125
- [134] B. Frischmuth, B. Ammon, and M. Troyer, “Susceptibility and low-temperature thermodynamics of spin-1/2 Heisenberg ladders”, *Phys. Rev. B* **54**, R3714 (1996). 29, 30
- [135] M. Troyer, H. Tsunetsugu, and D. Würtz, “Thermodynamics and spin gap of the Heisenberg ladder calculated by the look-ahead Lanczos algorithm”, *Phys. Rev. B* **50**, 13515 (1994). 30
- [136] K. Ishida, Y. Kitaoka, Y. Tokunaga, S. Matsumoto, K. Asayama, M. Azuma, Z. Hiroi, and M. Takano, “Spin correlation and spin gap in quasi-1D spin-1/2 cuprate oxides: A ^{63}Cu NMR study”, *Phys. Rev. B* **53**, 2827 (1996). 30
- [137] D.C. Johnston, “Antiferromagnetic exchange in two-leg spin-1/2 ladders”, *Phys. Rev. B* **54**, 13009 (1996). 30, 32
- [138] N. Motoyama, H. Eisaki, and S. Uchida, “Magnetic Susceptibility of Ideal Spin 1/2 Heisenberg Antiferromagnetic Chain Systems, Sr_2CuO_3 and SrCuO_2 ”, *Phys. Rev. Lett.* **76**, 3212 (1996). 30

- [139] H. Suzuura, H. Yasuhara, A. Furusaki, N. Nagaosa, and Y. Tokura, “Singularities in Optical Spectra of Quantum Spin Chains”, *Phys. Rev. Lett.* **76**, 2579 (1996). 30, 58, 59
- [140] J. Lorenzana, and R. Eder, “Dynamics of the one-dimensional Heisenberg model and optical absorption of spinons in cuprate antiferromagnetic chains”, *Phys. Rev. B* **55**, R3358 (1997). 31, 58, 59, 120
- [141] Y. Mizuno, T. Tohyama, and S. Maekawa, “Superexchange interaction in cuprates”, *Phys. Rev. B* **58**, R14713 (1998). 31, 32
- [142] S. Brehmer, H.-J. Mikeska, M. Müller, N. Nagaosa, and S. Uchida, “Effects of biquadratic exchange on the spectrum of elementary excitations in spin ladders”, *Phys. Rev. B* **60**, 329 (1999). 32
- [143] H.J. Schmidt, and Y. Kuramoto, “Four-spin interaction as an effective interaction in high- T_c copper oxides”, *Physica C* **167**, 263 (1990). 32
- [144] A.H. MacDonald, S.M. Girvin, and D. Yoshioka, “ t/U expansion for the Hubbard model”, *Phys. Rev. B* **37**, 9753 (1988). **41**, 2565 (1990). 32, 127
- [145] E. Müller-Hartmann, and A. Reischl, “Derivation of effective spin models from a three band model for CuO_2 -planes”, *Eur. Phys. J. B* **28**, 173 (2002). 32, 127
- [146] M. Roger, J.H. Hetherington, and J.M. Delrieu, “Magnetism in solid ^3He ”, *Rev. Mod. Phys.* **55**, 1 (1983). 32
- [147] M. Roger, and J.M. Delrieu, “Cyclic four-spin exchange on a two-dimensional square lattice: Possible applications in high- T_c superconductors”, *Phys. Rev. B* **39**, 2299 (1989). 32
- [148] R. Coldea, S.M. Hayden, G. Aeppli, T.G. Perring, C.D. Frost, T.E. Mason, S.-W. Cheong, and Z. Fisk, “Spin Waves and Electronic Interactions in La_2CuO_4 ”, *Phys. Rev. Lett.* **86**, 5377 (2001). 32, 131
- [149] A.A. Katanin, and A.P. Kampf, “Spin excitations in La_2CuO_4 : Consistent description by inclusion of ring exchange”, *Phys. Rev. B* **66**, 100403 (2002). 32
- [150] Y. Mizuno, T. Tohyama, and S. Maekawa, “Magnetic Interaction in Insulating Cuprates”, *J. Low Temp. Phys.* **117**, 389 (1999). 32
- [151] Y. Mizuno, T. Tohyama, and S. Maekawa, “Systematic Study of Magnetic Interactions in Insulating Cuprates”, *Physica C* **341-348**, 473 (2000). 32
- [152] R.S. Eccleston, M. Uehara, J. Akimitsu, H. Eisaki, N. Motoyama, and S. Uchida, “Spin Dynamics of the Spin-Ladder Dimer-Chain Material $\text{Sr}_{14}\text{Cu}_{24}\text{O}_{41}$ ”, *Phys. Rev. Lett.* **81**, 1702 (1998). 32, 34, 42
- [153] M. Kato, K. Shiotani, and Y. Koike, “Metal-insulator transition and spin gap in the spin-1/2 ladder system $\text{Sr}_{14-x}\text{A}_x\text{Cu}_{24}\text{O}_{41}$ ($\text{A} = \text{Ba}$ and Ca)”, *Physica C* **258**, 284 (1996). 36, 40
- [154] T. Nagata, M. Uehara, J. Goto, N. Komiya, J. Akimitsu, N. Motoyama, H. Eisaki, S. Uchida, H. Takahashi, T. Nakanishi, and N. Môri, “Superconductivity in the ladder compound $\text{Sr}_{2.5}\text{Ca}_{11.5}\text{Cu}_{24}\text{O}_{41}$ (single crystal)”, *Physica C* **282-287**, 153 (1997). 36, 45
- [155] E.M. McCarron, M.A. Subramanian, J.C. Calabrese, and R.L. Harlow, “The Incommensurate Structure of $(\text{Sr}_{14-x}\text{Ca}_x)\text{Cu}_{24}\text{O}_{41}$ ($0 < x \sim 8$) - A Superconductor Byproduct”, *Mat. Res. Bull.* **23**, 1355 (1988). 36
- [156] T. Siegrist, L.F. Schneemeyer, S.A. Sunshine, J.V. Waszczak, and R.S. Roth, “A New Layered Cuprate Structure-Type, $(\text{A}_{1-x}\text{A}'_x)_{14}\text{Cu}_{24}\text{O}_{41}$ ”, *Mat. Res. Bull.* **23**, 1429 (1988). 36

- [157] M. Isobe, T. Ohta, M. Onoda, F. Izumi, S. Nakano, J.Q. Li, Y. Matsui, E. Takayama-Muromachi, T. Matsumoto, and H. Hayakawa, “Structural and electrical properties under high pressure for the superconducting spin-ladder system $\text{Sr}_{0.4}\text{Ca}_{13.6}\text{Cu}_{24}\text{O}_{41+\delta}$ ”, *Phys. Rev. B* **57**, 613 (1998). 37, 44
- [158] Provided by U. Ammerahl, Universität zu Köln. 37, 38
- [159] S.A. Carter, B. Batlogg, R.J. Cava, J.J. Krajewski, W.F. Peck, Jr., and T.M. Rice, “Hole Doping of the CuO_2 Chains in $(\text{La,Sr,Ca})_{14}\text{Cu}_{24}\text{O}_{41}$ ”, *Phys. Rev. Lett.* **77**, 1378 (1996). 37, 40, 41, 42, 43, 140
- [160] S. Tornow, O. Entin-Wohlman, and A. Aharony, “Anisotropic superexchange for nearest and next-nearest coppers in chain, ladder, and lamellar cuprates”, *Phys. Rev. B* **60**, 10206 (1999). 38
- [161] W. Geertsma, and D. Khomskii, “Influence of side groups on 90° superexchange: A modification of the Goodenough-Kanamori-Anderson rules”, *Phys. Rev. B* **54**, 3011 (1996). 38
- [162] T. Ohta, F. Izumi, M. Onoda, M. Isobe, E. Takayama-Muromachi, and A.W. Hewat, “Modulated Structure of the Composite Crystal $\text{Ca}_{13.6}\text{Sr}_{0.4}\text{Cu}_{24+y}\text{O}_{41+z}$ ”, *J. Phys. Soc. Jpn.* **66**, 3107 (1997). 38, 39, 40, 42
- [163] K.P. Schmidt, C. Knetter, M. Grüninger, and G.S. Uhrig, “Charge-order-induced sharp Raman peak in $\text{Sr}_{14}\text{Cu}_{24}\text{O}_{41}$ ”, *Phys. Rev. Lett.* **90**, 167201 (2003). 39, 118, 125, 131, 139, 140, 141, 142, 143
- [164] M. Matsuda, K. Katsumata, T. Osafune, N. Motoyama, H. Eisaki, S. Uchida, T. Yokoo, S.M. Shapiro, G. Shirane, and J.L. Zarestky, “Magnetic excitations and structural change in the $S = 1/2$ quasi-one-dimensional magnet $\text{Sr}_{14-x}\text{Y}_x\text{Cu}_{24}\text{O}_{41}$ ($0 \leq x \leq 1$)”, *Phys. Rev. B* **56**, 14499 (1997). 39
- [165] A. Frost-Jensen, V. Petříček, F. Krebs-Larsen, and E.M. McCarron, “Importance of True Satellite Reflections in the Analysis of Modulated, Composite Crystal Structures. II. The Structure of $[\text{M}'_2\text{Cu}_2\text{O}_3]_7[\text{CuO}_2]_{10}$, $\text{M}' = \text{Bi}_{0.04}\text{Sr}_{0.96}$ ”, *Acta Cryst.* **B53**, 125 (1997). 39
- [166] Y. Mizuno, T. Tohyama, and S. Maekawa, “Electronic States of Doped Spin Ladders $(\text{Sr,Ca})_{14}\text{Cu}_{24}\text{O}_{41}$ ”, *J. Phys. Soc. Jpn.* **66**, 937 (1997). 40, 46, 47
- [167] R.J. Cava, A.W. Hewat, E.A. Hewat, B. Batlogg, M. Marezio, K.M. Rabe, J.J. Krajewski, W.F. Peck, Jr., and L.W. Rupp, Jr., “Structural anomalies, oxygen ordering and superconductivity in oxygen deficient $\text{Ba}_2\text{YCu}_3\text{O}_x$ ”, *Physica C* **165**, 419 (1990). 40
- [168] T. Osafune, N. Motoyama, H. Eisaki, and S. Uchida, “Optical Study of the $\text{Sr}_{14-x}\text{Ca}_x\text{Cu}_{24}\text{O}_{41}$ System: Evidence for Hole-Doped Cu_2O_3 Ladders”, *Phys. Rev. Lett.* **78**, 1980 (1997). 40, 45, 46, 47, 107
- [169] M. Matsuda, T. Yoshihama, K. Kakurai, and G. Shirane, “Quasi-two-dimensional hole ordering and dimerized state in the CuO_2 -chain layers in $\text{Sr}_{14}\text{Cu}_{24}\text{O}_{41}$ ”, *Phys. Rev. B* **59**, 1060 (1999). 41, 43, 140
- [170] D.E. Cox, T. Iglesias, K. Hirota, G. Shirane, M. Matsuda, N. Motoyama, H. Eisaki, and S. Uchida, “Low-temperature charge ordering in $\text{Sr}_{14}\text{Cu}_{24}\text{O}_{41}$ ”, *Phys. Rev. B* **57**, 10750 (1998). 41, 140
- [171] U. Ammerahl, B. Büchner, L. Colonescu, R. Gross, and A. Revcolevschi, “Interplay between magnetism, charge localization, and structure in $\text{Sr}_{14-x}\text{Ca}_x\text{Cu}_{24}\text{O}_{41}$ ”, *Phys. Rev. B* **62**, 8630 (2000). 41, 140
- [172] T. Fukuda, J. Mizuki, and M. Matsuda, “Periodic hole structure in a spin-chain ladder material $\text{Sr}_{14}\text{Cu}_{24}\text{O}_{41}$ ”, *Phys. Rev. B* **66**, 012104 (2002). 41, 141

- [173] M. Hücker with the group of A. Revcolevschi at the Laboratoire de Chimie des Solides, Université Paris-Sud, France. 41
- [174] K. Kumagai, S. Tsuji, M. Kato, and Y. Koike, “NMR Study of Carrier Doping Effects on Spin Gaps in the Spin Ladder $\text{Sr}_{14-x}\text{A}_x\text{Cu}_{24}\text{O}_{41}$ ($\text{A} = \text{Ca}, \text{Y}, \text{and La}$)”, *Phys. Rev. Lett.* **78**, 1992 (1997). 41, 42
- [175] R.S. Eccleston, M. Azuma, and M. Takano, “Neutron-scattering and susceptibility study of spin chains and spin ladders in $(\text{Sr}_{0.8}\text{Ca}_{0.2})_{14}\text{Cu}_{24}\text{O}_{41}$ ”, *Phys. Rev. B* **53**, 14721 (1996). 42
- [176] K. Magishi, S. Matsumoto, Y. Kitaoka, K. Ishida, K. Asayama, M. Uehara, T. Nagata, and J. Akimitsu, “Spin gap and dynamics in $\text{Sr}_{14-x}\text{Ca}_x\text{Cu}_{24}\text{O}_{41}$ comprising hole-doped two-leg spin ladders: Cu NMR study on single crystals”, *Phys. Rev. B* **57**, 11533 (1998). 42
- [177] H. Mayaffre, P. Auban-Senzier, M. Nardone, D. Jérôme, D. Poilblanc, C. Bourbonnais, U. Ammerahl, G. Dhalenne, and A. Revcolevschi, “Absence of a Spin Gap in the Superconducting Ladder Compound $\text{Sr}_2\text{Ca}_{12}\text{Cu}_{24}\text{O}_{41}$ ”, *Science* **279**, 345 (1998). 43
- [178] T. Mito, K. Magishi, S. Matsumoto, G. Zheng, Y. Kitaoka, K. Asayama, N. Motoyama, H. Eisaki, and S. Uchida, “Study of spin-ladder system under pressure”, *Physica B* **259-261**, 1042 (1999). 43, 45
- [179] S. Katano, T. Nagata, J. Akimitsu, M. Nishi, and K. Kakurai, “Spin Gap in the Hole-Doped Spin Ladder System $(\text{Sr}_{2.5}\text{Ca}_{11.5})\text{Cu}_{24}\text{O}_{41}$: Neutron Inelastic Scattering Study”, *Phys. Rev. Lett.* **82**, 636 (1999). 43, 45
- [180] N. Motoyama, T. Osafune, T. Kakeshita, H. Eisaki, and S. Uchida, “Effect of Ca substitution and pressure on the transport and magnetic properties of $\text{Sr}_{14}\text{Cu}_{24}\text{O}_{41}$ with doped two-leg Cu–O ladders”, *Phys. Rev. B* **55**, R3386 (1997). 45
- [181] T. Nagata, M. Uehara, J. Goto, J. Akimitsu, N. Motoyama, H. Eisaki, S. Uchida, H. Takahashi, T. Nakanishi, and N. Môri, “Pressure-Induced Dimensional Crossover and Superconductivity in the Hole-Doped Two-Leg Ladder Compound $\text{Sr}_{14-x}\text{Ca}_x\text{Cu}_{24}\text{O}_{41}$ ”, *Phys. Rev. Lett.* **81**, 1090 (1998). 45
- [182] S. Katano, T. Nagata, H. Fujino, J. Akimitsu, M. Nishi, and K. Kakurai, “Pressure effects on spin-gap and antiferromagnetism in the hole-doped spin ladder system $\text{Sr}_{2.5}\text{Ca}_{11.5}\text{Cu}_{24}\text{O}_{41}$ ”, *Physica B* **259-261**, 1046 (1999). 45
- [183] T. Osafune, N. Motoyama, H. Eisaki, S. Uchida, and S. Tajima, “Pseudogap and Collective Mode in the Optical Conductivity Spectra of Hole-Doped Ladders in $\text{Sr}_{14-x}\text{Ca}_x\text{Cu}_{24}\text{O}_{41}$ ”, *Phys. Rev. Lett.* **82**, 1313 (1999). 47, 48
- [184] C.C. Homes, T. Timusk, R. Liang, D.A. Bonn, and W.N. Hardy, “Optical Conductivity of c Axis Oriented $\text{YBa}_2\text{Cu}_3\text{O}_{6.70}$: Evidence for a Pseudogap”, *Phys. Rev. Lett.* **71**, 1645 (1993). 47
- [185] B. Ruzicka, L. Degiorgi, U. Ammerahl, G. Dhalenne, and A. Revcolevschi, “Temperature dependence of the anisotropic electrodynamics in the ladder compounds $\text{Sr}_{14-x}\text{Ca}_x\text{Cu}_{24}\text{O}_{41}$ ”, *Eur. Phys. J. B* **6**, 301 (1998). 48
- [186] B. Ruzicka, L. Degiorgi, U. Ammerahl, G. Dhalenne, and A. Revcolevschi, “Optics in the ladder compounds $\text{Sr}_{14-x}\text{Ca}_x\text{Cu}_{24}\text{O}_{41}$ ”, *Physica B* **259-261**, 1036 (1999). 48
- [187] H. Tsunetsugu, M. Troyer, and T.M. Rice, “Singlet stripe phases in the planar t – J model”, *Phys. Rev. B* **51**, 16456 (1995). 48
- [188] H. Kuzmany, *Solid-State Spectroscopy*, Springer-Verlag, Berlin, Heidelberg (1998). 51, 64, 66

- [189] M. Dressel, and G. Grüner, *Electrodynamics of Solids: Optical Properties of Electrons in Matter*, Cambridge University Press, Cambridge (2002). 51, 56, 107, 108
- [190] F. Wooten, *Optical Properties of Solids*, Academic Press, New York (1972). 51, 53, 54, 56
- [191] H.S. Choi, E.J. Choi, and Y.J. Kim, “Temperature dependence of the mid-infrared absorptions in undoped cuprate $\text{Sr}_2\text{CuO}_2\text{Cl}_2$ ”, *Physica C* **304**, 66 (1998). 54, 58
- [192] M. Grüninger, *Infrarot-Transmissions- und Reflexionsvermögen der antiferromagnetischen Phase des Hochtemperatursupraleiters $\text{R}\text{Ba}_2\text{Cu}_3\text{O}_{6+x}$* , Diplomarbeit, Universität Karlsruhe (1994). 54
- [193] P. Grosse, *Freie Elektronen in Festkörpern*, Springer Verlag, Berlin (1979). 56
- [194] J.D. Perkins, D.S. Kleinberg, M.A. Kastner, R.J. Birgeneau, Y. Endoh, K. Yamada, and S. Hosoya, “Infrared optical excitations in La_2NiO_4 ”, *Phys. Rev. B* **52**, R9863 (1995). 57, 58, 59, 93
- [195] J.D. Perkins, R.J. Birgeneau, J.M. Graybeal, M.A. Kastner, and D.S. Kleinberg, “Mid-infrared optical excitations in undoped lamellar copper oxides”, *Phys. Rev. B* **58**, 9390 (1998). 58
- [196] M. Grüninger, J. Münzel, A. Gaymann, A. Zibold, H.P. Geserich, and T. Kopp, “Spin-waves in the mid-infrared spectrum of antiferromagnetic $\text{YBa}_2\text{Cu}_3\text{O}_{6.0}$ ”, *Europhys. Lett.* **35**, 55 (1996). 57, 59
- [197] Y.Y. Wang, F.C. Zhang, V.P. Dravid, K.K. Ng, M.V. Klein, S.E. Schnatterly, and L.L. Miller, “Momentum-Dependent Charge Transfer Excitations in $\text{Sr}_2\text{CuO}_2\text{Cl}_2$ Angle-Resolved Electron Energy Loss Spectroscopy”, *Phys. Rev. Lett.* **77**, 1809 (1996). 59
- [198] V.V. Struzhkin, A.F. Goncharov, H.K. Mao, R.J. Hemley, S.W. Moore, J.M. Graybeal, J. Sarrao, and Z. Fisk, “Coupled magnon-phonon excitations in $\text{Sr}_2\text{CuCl}_2\text{O}_2$ at high pressure”, *Phys. Rev. B* **62**, 3895 (2000). 59
- [199] R. Newman, and R.M. Chrenko, “Optical Properties of Nickel Oxide”, *Phys. Rev.* **114**, 1507 (1959). 60
- [200] Y. Mizuno, and S. Koide, “Vibrationally Induced Electronic Transitions in Crystals of Magnetic Compounds”, *Phys. kondens. Materie* **2**, 166 (1964). 60
- [201] T.S. Nunner, P. Brune, T. Kopp, M. Windt, and M. Grüninger, “Phonon-Assisted Magnetic Absorption of $(\text{La,Ca})_{14}\text{Cu}_{24}\text{O}_{41}$: Contribution of Different Phonon Modes”, *Acta Physica Polonica B* **34**, 1545 (2003). 61, 120, 131, 151, 152
- [202] J. Gronholz, and W. Herres, *Understanding FT-IR Data Processing*, Dr. Alfred Huethig Publishers (1985). 64, 68, 74
- [203] A.E. Martin, *Infrared Interferometric Spectrometers*, Elsevier Scientific Publishing Company, Amsterdam, Oxford, New York (1980). 64, 74
- [204] R.J. Bell, *Introductory Fourier Transform Spectroscopy*, Academic Press, New York (1972). 64
- [205] P.R. Griffiths, and J.A. de Haseth, *Fourier Transform Infrared Spectrometry*, John Wiley & Sons, New York (1986). 64
- [206] Product catalog from Melles Griot, *The Practical Application of Light*, USA (1999). 69
- [207] Measurements by R. Rückamp, Universität zu Köln. 77, 78
- [208] H. Sakai, G.A. Vanasse, and M.L. Forman, “Spectral Recovery in Fourier Spectroscopy”, *J. Opt. Soc. Amer.* **58**, 84 (1968). 77

- [209] A. Revcolevschi, U. Ammerahl, and G. Dhalenne, “Crystal growth of pure and substituted low-dimensionality cuprates CuGeO_3 , La_2CuO_4 , SrCuO_2 , Sr_2CuO_3 and $\text{Sr}_{14}\text{Cu}_{24}\text{O}_{41}$ by the floating zone and travelling solvent zone methods”, *J. Crystal Growth* **198**, 593 (1999). 80
- [210] Measurement by T. Kemen, Universität zu Köln. 83, 84
- [211] Measurements by H. Gottschalk, Universität zu Köln. 84
- [212] M. Grüninger, M. Windt, T. Nunner, C. Knetter, K.P. Schmidt, G.S. Uhrig, T. Kopp, A. Freimuth, U. Ammerahl, B. Büchner, and A. Revcolevschi, “Optical spectroscopy of $(\text{La,Ca})_{14}\text{Cu}_{24}\text{O}_{41}$ spin ladders: comparison of experiment and theory”, *Physica B* **312-313**, 617 (2002). 87, 117, 118
- [213] M. Grüninger, M. Windt, T. Nunner, C. Knetter, K.P. Schmidt, G.S. Uhrig, T. Kopp, A. Freimuth, U. Ammerahl, B. Büchner, and A. Revcolevschi, “Magnetic excitations in two-leg spin 1/2 ladders: experiment and theory”, *J. Phys. Chem. Sol.* **63**, 2167 (2002). 87, 110, 112, 117, 118, 119, 120, 121, 122
- [214] J. Oitmaa, R.R.P. Singh, and Z. Weihong, “Quantum spin ladders at $T = 0$ and at high temperatures studied by series expansions”, *Phys. Rev. B* **54**, 1009 (1996). 89
- [215] C. Knetter, A. Bühler, E. Müller-Hartmann, and G.S. Uhrig, “Dispersion and Symmetry of Bound States in the Shastry-Sutherland Model”, *Phys. Rev. Lett.* **85**, 3958 (2000). 90
- [216] M. Matsuda, K. Katsumata, R.S. Eccleston, S. Brehmer, and H.-J. Mikeska, “Magnetic excitations from the $S = 1/2$ two-leg ladders in $\text{La}_6\text{Ca}_8\text{Cu}_{24}\text{O}_{41}$ ”, *J. Appl. Phys.* **87**, 6271 (2000). 104, 125, 128, 151, 152
- [217] J.M.P. Carmelo, N.M.R. Peres, and P.D. Sacramento, “Finite-Frequency Optical Absorption in 1D Conductors and Mott-Hubbard Insulators”, *Phys. Rev. Lett.* **84**, 4673 (2000). 109
- [218] E. Jeckelmann, F. Gebhard, and F.H.L. Essler, “Optical Conductivity of the Half-Filled Hubbard Chain”, *Phys. Rev. Lett.* **85**, 3910 (2000). 109, 118
- [219] F.H.L. Essler, F. Gebhard, and E. Jeckelmann, “Excitons in one-dimensional Mott insulators”, *Phys. Rev. B* **64**, 125119 (2001). 109
- [220] J.J. McGuire, M. Windt, T. Startseva, T. Timusk, D. Colson, and V. Viallet-Guillen, “Gap in the infrared response of $\text{HgBa}_2\text{Ca}_2\text{Cu}_3\text{O}_{8+\delta}$ ”, *Phys. Rev. B* **62**, 8711 (2000). 116
- [221] T.S. Nunner, and T. Kopp, “Jordan-Wigner approach to dynamic correlations in spin-ladders”, *cond-mat/0210103* (2002). 117, 118, 120
- [222] M. Azzouz, L. Chen, and S. Moukouri, “Calculation of the singlet-triplet gap of the antiferromagnetic Heisenberg model on a ladder”, *Phys. Rev. B* **50**, 6233 (1994). 117
- [223] X. Dai, and Z. Su, “Mean-field theory for the spin-ladder system”, *Phys. Rev. B* **57**, 964 (1998). 117
- [224] C. Knetter, K.P. Schmidt, M. Grüninger, and G.S. Uhrig, “Fractional and Integer Excitations in Quantum Antiferromagnetic Spin 1/2 Ladders”, *Phys. Rev. Lett.* **87**, 167204 (2001). 118, 119, 120, 122, 125, 126
- [225] S.R. White, “Density Matrix Formulation for Quantum Renormalization Groups”, *Phys. Rev. Lett.* **69**, 2863 (1992). 118
- [226] S.R. White, “Density-matrix algorithms for quantum renormalization groups”, *Phys. Rev. B* **48**, 10345 (1993). 118

- [227] I. Peschel, X. Wang, M. Kaulke, and K. Hallberg, eds., *Density-Matrix Renormalization, A New Numerical Method in Physics*, Lecture Notes in Physics Vol. 528, Springer, Berlin (1999). 118
- [228] T.D. Kühner, and S.R. White, “Dynamical correlation functions using the density matrix renormalization group”, *Phys. Rev. B* **60**, 335 (1999). 118
- [229] S. Nishimoto, E. Jeckelmann, F. Gebhard, and R.M. Noack, “Application of the density matrix renormalization group in momentum space”, *Phys. Rev. B* **65**, 165114 (2002). 118
- [230] Z. Weihong, V. Kotov, and J. Oitmaa, “Two-chain spin ladder with frustrating second-neighbor interactions”, *Phys. Rev. B* **57**, 11439 (1998). 119
- [231] K.P. Schmidt, C. Knetter, and G.S. Uhrig, “Raman response in antiferromagnetic two-leg $S = 1/2$ Heisenberg ladders”, *Europhys. Lett.* **56**, 877 (2001). 122, 126, 140, 143
- [232] T.S. Nunner, *Spin Excitations in Low-Dimensional Quantum Antiferromagnets*, PhD Thesis, Universität Augsburg (2003). 132, 136
- [233] E. Gagliano, F. Lema, S. Bacci, J.J.V. Alvarez, and J. Lorenzana, “Optical absorption of CuO_3 antiferromagnetic chains at finite temperatures”, *Phys. Rev. B* **62**, 1218 (2000). 132
- [234] S. Brehmer, A.K. Kolezhuk, H.-J. Mikeska, and U. Neugebauer, “Elementary excitations in the gapped phase of a frustrated $S = 1/2$ spin ladder: from spinons to the Haldane triplet”, *J. Phys.: Condens. Matter* **10**, 1103 (1998). 133, 134
- [235] S.R. White, “Equivalence of the antiferromagnetic Heisenberg ladder to a single $S = 1$ chain”, *Phys. Rev. B* **53**, 52 (1996). 133, 134, 135
- [236] T.S. Nunner, P. Brune, and T. Kopp, private communication. 135, 136
- [237] S. Sugai, and M. Suzuki, “Magnetic Raman Scattering in Two-Leg Spin Ladder $\text{Sr}_{14-x-y}\text{Ca}_x\text{Y}_y\text{Cu}_{24}\text{O}_{41}$ ”, *phys. stat. sol. (b)* **215**, 653 (1999). 139, 140, 142, 143, 144
- [238] A. Gozar, G. Blumberg, B.S. Dennis, B.S. Shastry, N. Motoyama, H. Eisaki, and S. Uchida, “Spin Dynamics of $\text{Sr}_{14}\text{Cu}_{24}\text{O}_{41}$ Two-Leg Ladder Studied by Raman Spectroscopy”, *Phys. Rev. Lett.* **87**, 197202 (2001). 139, 140, 143, 144
- [239] M. Troyer, H. Tsunetsugu, and T.M. Rice, “Properties of lightly doped t - J two-leg ladders”, *Phys. Rev. B* **53**, 251 (1996). 139, 153, 154, 155
- [240] G. Blumberg, P. Abbamonte, M.V. Klein, W.C. Lee, D.M. Ginsberg, L.L. Miller, and A. Zibold, “Resonant two-magnon Raman scattering in cuprate antiferromagnetic insulators”, *Phys. Rev. B* **53**, R11930 (1996). 140
- [241] J. Puchalla, *Optische Spektroskopie magnetischer Anregungen in dotierten Spinleiterverbindungen*, Diplomarbeit, Universität zu Köln (2003). 148, 150

List of Publications

1. **Observation of Two-Magnon Bound States in the Two-Leg Ladders of $(\text{Ca},\text{La})_{14}\text{Cu}_{24}\text{O}_{41}$**
M. Windt, M. Grüninger, T. Nunner, C. Knetter, K.P. Schmidt, G.S. Uhrig, T. Kopp, A. Freimuth, U. Ammerahl, B. Büchner, and A. Revcolevschi
Physical Review Letters **87**, 127002 (2001).
2. **Optical Spectroscopy of Low-Dimensional Quantum Spin Systems**
M. Grüninger, M. Windt, E. Benckiser, T.S. Nunner, K.P. Schmidt, G.S. Uhrig, and T. Kopp
Advances in Solid State Physics **43**, 95 – 112 (2003).
3. **Phonon-Assisted Magnetic Absorption of $(\text{La},\text{Ca})_{14}\text{Cu}_{24}\text{O}_{41}$: Contribution of Different Phonon Modes**
T.S. Nunner, P. Brune, T. Kopp, M. Windt, and M. Grüninger
Acta Physica Polonica B **34**, 1545 – 1548 (2003).
4. **Magnetic excitations in two-leg spin 1/2 ladders: experiment and theory**
M. Grüninger, M. Windt, T. Nunner, C. Knetter, K.P. Schmidt, G.S. Uhrig, T. Kopp, A. Freimuth, U. Ammerahl, B. Büchner, and A. Revcolevschi
Journal of Physics and Chemistry of Solids **63**, 2167 – 2173 (2002).
5. **Cyclic spin exchange in cuprate spin ladders**
T.S. Nunner, P. Brune, T. Kopp, M. Windt, and M. Grüninger
Physical Review B **66**, 180404(R) (2002).
6. **Orbital physics - Experimental quest for orbital waves**
M. Grüninger, R. Rückamp, M. Windt, P. Reutler, C. Zobel, T. Lorenz, A. Freimuth, and A. Revcolevschi
Nature **418**, 39 – 40 (2002).
7. **Optical spectroscopy of $(\text{La},\text{Ca})_{14}\text{Cu}_{24}\text{O}_{41}$ spin ladders: comparison of experiment and theory**
M. Grüninger, M. Windt, T. Nunner, C. Knetter, K.P. Schmidt, G.S. Uhrig, T. Kopp, A. Freimuth, U. Ammerahl, B. Büchner, and A. Revcolevschi
Physica B **312-313**, 617 – 618 (2002).

8. **Infrared and optical properties of pure and cobalt-doped $\text{LuNi}_2\text{B}_2\text{C}$**
M. Windt, J.J. McGuire, T. Rõõm, A. Pronin, T. Timusk, I.R. Fisher, and P.C. Canfield
Physical Review B **65**, 064506 (2002).
9. **Gap in the infrared response of $\text{HgBa}_2\text{Ca}_2\text{Cu}_3\text{O}_{8+\delta}$**
J.J. McGuire, M. Windt, T. Startseva, T. Timusk, D. Colson, and V. Viallet-Guillen
Physical Review B **62**, 8711 – 8714 (2000).
10. **On the nature of the electric-field effect on $\text{YBa}_2\text{Cu}_3\text{O}_{7-\delta}$ grain boundary junctions employing epitaxial SrTiO_3 gate insulators**
M. Windt, H. Haensel, D. Koelle, and R. Gross
Applied Physics Letters **74**, 1027 – 1029 (1999).

Erklärung

Ich versichere, dass ich die von mir vorgelegte Dissertation selbständig angefertigt, die benutzten Quellen und Hilfsmittel vollständig angegeben und die Stellen der Arbeit - einschließlich Tabellen, Karten und Abbildungen -, die anderen Werken im Wortlaut oder dem Sinn nach entnommen sind, in jedem Einzelfall als Entlehnung kenntlich gemacht habe; dass diese Dissertation noch keiner Fakultät oder Universität zur Prüfung vorgelegen hat; dass sie - abgesehen von oben angegebenen Teilpublikationen - noch nicht veröffentlicht worden ist sowie, dass ich eine solche Veröffentlichung vor Abschluss des Promotionsverfahrens nicht vornehmen werde. Die Bestimmungen dieser Promotionsordnung sind mir bekannt. Die von mir vorgelegte Dissertation ist von Prof. Dr. A. Freimuth betreut worden.

Marco Windt

Acknowledgements

At this point I would like to express my gratitude to all who supported me during my work on this thesis and to all who contributed to the enjoyable atmosphere during the last years.

It was Prof. Freimuth who offered me the great opportunity to do optical spectroscopy at the University of Cologne. But he also encouraged me to spend a year abroad to work with Prof. Timusk at the McMaster University in Canada. I really don't want to miss that period, and I'm very grateful for all the experience that Tom Timusk willingly passes on to his students.

Of course most of the teaching workload had to be sustained by Markus Grüninger. Beyond doubt he was indispensable for my thesis and I owe most of the physics I learned during the last years to him. I really enjoyed working with him.

Also very essential to my thesis were all the theorists who did not get tired to improve their techniques over and over again to calculate all the spectra: Götz Uhrig, Kai Schmidt, and Christian Knetter from Cologne as well as Thilo Kopp and Tamara Nunner from Augsburg.

But there were others, too, who tried to answer all my bold questions. I want to start with my office mate Vladik Kataev who often was the first to get asked. In Canada it was Jeff McGuire who not only taught me the first secrets of infrared spectroscopy but also some of the many pitfalls of the English language.

I want to thank Gladys Chan for cookies and proofreading but also, together with Andrzej Borowiec and Sabine Milz, for a wonderful time in Canada. Back in Cologne I was very happy to have Thomas Kemen as my office mate who accompanied me as a good friend during the whole physics program. Silke Schymon is a further good friend I was happy to meet at our institute.

But I don't want to miss out Kostas Kordonis, Sven Kiele, Markus Kriener, Alexander Gößling, Reinhard Rückamp, Eva Benckiser, Christina Hilgers, and Marc Zittartz, whom I wish all the best for the future.

Our machine shop and the electronic shop were responsible for making all the little gadgets that we needed to keep our spectrometer chilly and cosy.

Last but not least I want to thank my parents for all their constant support. And I am very grateful to Tanja, who became my pillar of strength and encouragement.

Abstract

In the framework of this thesis the infrared spectra of two-leg spin ladders were measured. This study presents the first determination of the magnetic contribution to the optical conductivity of spin ladders. A comparison between experiment and new theoretical calculations provided a comprehensive understanding of the magnetic spectrum of the undoped telephone-number compounds $\text{La}_y\text{Ca}_{14-y}\text{Cu}_{24}\text{O}_{41}$.

To be able to study the weak magnetic contribution to the spectra, it was necessary to measure not only the reflectance but in particular the transmittance of thin single crystals. When both quantities are known, one can directly calculate the optical conductivity. The low-temperature spectra were compared with results of three different theoretical approaches in close collaboration with the theory groups of Uhrig et al. from the University of Cologne and of Kopp et al. from the University of Augsburg. The excellent agreement between theory and experiment allowed us to identify the two sharp peaks in the mid-infrared range unambiguously as the signature of a true bound state of two triplets. The occurrence of bound states in spin ladders had been predicted already by several groups, but we provided the first experimental verification. Again by comparison with the theoretical spectra, further spectral weight at higher frequencies was attributed to the multi-triplet continuum. The exchange couplings were derived, and the importance of a four-spin cyclic exchange was demonstrated.

With increasing temperature especially the line shape for polarization along the legs changes considerably. The spectral weight of the continuum strongly grows, whereas the bound-state peaks lose weight. The resemblance between the measured room-temperature data of the $S = 1/2$ ladder and theoretical results for the $S = 1$ Haldane chain was discussed. The corresponding calculations were performed by Nunner et al. from the Augsburg group.

Another main part of this thesis was to examine the influence of doping on the infrared spectra. In the telephone-number compounds the charge carriers are expected to reside mainly within the chains rather than within the ladders. We still observed the same bound-state features in $\text{Sr}_{14}\text{Cu}_{24}\text{O}_{41}$ as in the undoped compounds, but there was additional structure in the spectra. Several scenarios were discussed in order to explain the additional features, including the modulation of the exchange coupling along the legs due to the incommensurate structure and due to the charge order in the chains. Calculations by Schmidt et al. from the Cologne group are currently in progress to clarify the relevance of this mechanism.

Zusammenfassung

Im Rahmen dieser Arbeit wurden Infrarotspektren von Spinleitern gemessen und die erste Bestimmung des magnetischen Beitrags zur optischen Leitfähigkeit präsentiert. Ein Vergleich zwischen Experiment und neuen theoretischen Berechnungen lieferte ein umfassendes Verständnis des magnetischen Spektrums der undotierten Telefonnummer-Verbindungen $\text{La}_y\text{Ca}_{14-y}\text{Cu}_{24}\text{O}_{41}$.

Um den schwachen magnetischen Beitrag der Spektren bestimmen zu können ist es notwendig, nicht nur die Reflexion, sondern insbesondere auch die Transmission von dünnen Einkristallen zu messen. Wenn beide Größen bekannt sind, kann man die optische Leitfähigkeit direkt berechnen. Die Spektren bei tiefen Temperaturen wurden mit den Ergebnissen von drei verschiedenen theoretischen Ansätzen verglichen. Die Rechnungen wurden in den Theorie-Gruppen von Uhrig et al. an der Universität zu Köln und von Kopp et al. an der Universität Augsburg durchgeführt. Die hervorragende Übereinstimmung zwischen Theorie und Experiment ermöglichte uns, die zwei scharfen Peaks im mittleren Infrarot eindeutig einem gebundenen Zustand von zwei Triplets zuzuordnen. Das Auftreten von gebundenen Zuständen in Spinleitern wurde zwar schon von mehreren Gruppen vorhergesagt, aber wir haben den ersten experimentellen Nachweis erbracht. Wiederum im Vergleich mit den theoretischen Spektren konnte das spektrale Gewicht bei höheren Frequenzen dem Vielteilchen-Kontinuum zugeordnet werden. Die Austauschkonstanten wurden bestimmt, und die Bedeutung des zyklischen Vier-Spin-Austausches konnte demonstriert werden.

Mit steigender Temperatur ändert sich die Linienform insbesondere für die Polarisation entlang der Holme. Das spektrale Gewicht des Kontinuums steigt stark an, während die Peaks des gebundenen Zustands an Gewicht verlieren. Die Ähnlichkeit der Raumtemperatur-Daten der $S = 1/2$ Leiter mit dem theoretischen Spektrum der $S = 1$ Haldane-Kette wurde diskutiert. Die entsprechenden Berechnungen wurden in der Augsburger Gruppe von Nunner et al. durchgeführt.

Ein weiterer wichtiger Teil dieser Arbeit war die Untersuchung des Einflusses von Dotierung auf die Infrarotspektren. In den Telefonnummer-Verbindungen werden die meisten Löcher innerhalb der Ketten und nicht in den Leitern vermutet. In $\text{Sr}_{14}\text{Cu}_{24}\text{O}_{41}$ konnten wir die gleichen Merkmale des gebundenen Zustands messen wie in den undotierten Leitern. Es traten allerdings weitere Strukturen in den Spektren auf. Verschiedene Erklärungsansätze wurden diskutiert. Eines dieser Szenarien beinhaltet die Modulation der Austauschkopplung entlang der Leiter durch die inkommensurable Struktur der Verbindung und durch die Ladungsordnung in den Ketten. Entsprechende Rechnungen werden momentan von Schmidt et al. in der Kölner Theorie-Gruppe durchgeführt, um die Bedeutung dieses Mechanismus klären.

Curriculum Vitae

Name		Marco Windt
Wohnsitz		Barthelstr. 85 50823 Köln
Geburtstag		12. März 1972
Geburtsort		Vechta (Niedersachsen)
Staatsangehörigkeit		deutsch
Schule	08/1978 - 07/1984	Schulausbildung in Melle (Niedersachsen)
	08/1984 - 05/1991	Gymnasium Melle
	05/1991	Abitur
Zivildienst	07/1991 - 09/1992	Sozialstation Melle
Studium	10/1992	Beginn des Physikstudiums an der Universität zu Köln
	09/1994	Vordiplom
	12/1996 - 02/1998	Diplomarbeit bei Prof. Gross mit dem Titel „Josephson-Feldeffekttransistoren aus Hochtemperatur-Supraleitern“
	03/1998	Diplom
Promotion	06/1998	Beginn der Promotion bei Prof. Freimuth
	09/1998 - 10/1999	Aufenthalt an der McMaster University in Hamilton (Kanada) bei Prof. Timusk
	11/1999	Rückkehr an die Universität zu Köln